Electronic Thesis and Dissertation Repository

8-21-2019 2:30 PM

Numerical Studies on Hydrodynamics in Various Circulating Fluidization Systems

Zeneng Sun, *The University of Western Ontario*

Supervisor: Zhu, Jesse, *The University of Western Ontario*
Joint Supervisor: Zhang, Chao, *The University of Western Ontario*
A thesis submitted in partial fulfillment of the requirements for the Doctor of Philosophy degree in Chemical and Biochemical Engineering
© Zeneng Sun 2019

Recommended Citation

Abstract

Various circulating fluidized bed (CFB) systems including gas-solid fluidization, liquid-solid fluidization, and gas-liquid-solid three-phase fluidization are numerically studied. With a comprehensive knowledge from the experiments, improved computational fluid dynamic (CFD) models are developed for detailed investigations on a wide operating range in the gas-solid CFB (GSCFB) system. The CFD model developed is also extended to study two new types of fluidized beds, an inverse liquid-solid circulating fluidized bed (ILSCFB) and a bubble induced fluidized bed (BIFB), as a supplement to the experimental work.

Flow structures and transitions from low-density operations to high-density operations in both GSCFB riser and downer are characterized based on numerical results and validated by experimental data. Correlations on the overall bed density in the GSCFB riser and downer under different operating conditions are developed respectively. The solid inlet geometry is found to have profound impacts on the flow structure in the GSCFB riser, which leads to the modifications on the inlet boundary conditions in the CFD model.

A cluster-driven drag model, which includes the information of clusters, is proposed for the simulation of the GSCFB riser. With more realistic physical meanings of the gas-solid interactions provided, a good agreement with the experimental results is also achieved. The clustering effects on the flow development, and solids distribution are discussed based on the numerical results.

The CFD approach is also extended to study an ILSCFB system where light particles are used and validated by experimental results. The flow structures from the CFD simulations in the ILSCFB riser and downer are compared. CFD results show that the flow structure in the ILSCFB is more uniform compared with the GSCFB system. Numerical results also show that the binary particle system in the ILSCFB shares many similarities with the single-particle system.

A three-phase Eulerian-Eulerian CFD model is developed and validated by the experimental results for a newly invented BIFB. Three flow regimes and the corresponding

transition gas velocities in the BIFB are defined based on the experimental and numerical results. Effects form the particle density, solids loading, and superficial gas velocity are also studied.

Keywords

Circulating fluidized bed, numerical study, CFD modelling, gas-solid fluidized bed, gas-liquid-solids fluidized bed, inverse liquid-solid fluidized bed, bubble induced inverse fluidized bed, particle cluster, high-density/low-density operation, flow structure

Summary for lay audience

Several types of circulating fluidized bed (CFB) systems are studied via computational fluid dynamics (CFD) approach in this work. CFB is a kind of chemical reactor to continuously handle granular materials. By introducing a fluid, such as gas, liquid, or even both gas and liquid, particles will be suspended, resulting in multiphase flows in a CFB. Except for the commonly seen gas-solid CFB systems, new types of CFBs, such as the inverse liquid-solid CFB and the bubble induced inverse gas-liquid-solid three-phase fluidized bed, have been developed recently by changing the flow directions or the particle properties.

CFD approach is a numerical method that solves a set of governing equations, which describe the velocity and pressure fields of the multiphase flows, to simulate the flow mechanisms in the CFB systems. Due to the fast development of the computer technology, CFD modelling has become an effective and economical tool to investigate the flow structures in various CFB systems. Different CFD models have been developed in this work for the gas-solid CFB riser and downer reactors, an inverse liquid-solid CFB, and a bubble-induced three-phase fluidized bed, respectively. The flow structures, such as profiles of solids concentration and velocity, flow development, and the interactions between particles and fluid are investigated. .A cluster-driven drag model for the simulation of gas-solid CFB risers is proposed, which includes the characteristics of particle clusters based on the data obtained from experiments.

The expansion of the fluidization technology relies on both experimental and numerical works. Experimental work can help improve the numerical theories by providing more accurate descriptions of the underlying physics with a comprehensive knowledge of the fluidized bed systems. CFD modelling can supplement to the experimental study by carrying out the simulations under a wider operating window and provide more information in the micro or meso scale. The fulfillment of the fluidization map can be achieved by the co-work from experimental studies and numerical simulations.

Co-Authorship Statement

Chapters 3-7: Zeneng Sun carried out the simulation work and the data analysis under the supervision of Prof. Jesse Zhu and Prof. Chao Zhang. Individual papers will be submitted for publications.

Chapter 8: Numerical study on liquid-solid flow characteristics in inverse circulating fluidized beds

Authors: Yangfan Song, Zeneng Sun, Chao Zhang, Jesse Zhu, Xiaofeng Lu

Zeneng Sun conducted the first-phase for the CFD simulations, including data and literature collections, CFD model sections, initial and boundary conditions, and preliminary validation of the CFD model. Yangfan Song carried out the simulation work under different operating conditions in consultation with Zeneng Sun, and under the supervision of Prof. Jesse Zhu and Prof. Chao Zhang. The draft paper was written by Yangfan Song and the data analysis was revised by Yangfan Song and Zeneng Sun under the supervision of Prof. Jesse Zhu and Prof. Chao Zhang. Prof. Xiaofeng Lu gave some comments on the manuscript. This article has been published in the journal of Advanced Powder Technology in Feb. 2019.

Chapter 9: Experimental and numerical studies on a bubble-induced inverse gas-liquid-solids fluidized bed

Authors: Yunfeng Liu, Zeneng Sun, Xiliang Sun, Jesse Zhu, Chao Zhang

The experimental work was carried out by Xiliang Sun and the data analysis of the experimental results was prepared by Xiliang Sun under the supervision of Prof. Jesse Zhu. The three-phase CFD model was selected by Zeneng Sun under the supervision of Prof. Jesse Zhu and Prof. Chao Zhang. The simulation work was carried out by Yunfeng Liu in consultation with Zeneng Sun. The data analysis of the simulation results was prepared by Yunfeng Liu and Zeneng Sun under the supervision of Prof. Jesse Zhu and Prof. Chao Zhang. The final version of the paper was completed by Zeneng Sun and modified by Prof. Jesse Zhu and Prof. Chao Zhang, which will be submitted for publications.

Acknowledgments

First of all, I would like to express my sincere gratitude to my main supervisor, Dr. Jesse Zhu, for his valuable guidance, continuous encouragement, and unfailing support not only to my research work, but also to my life. Many thanks to him for offering me an opportunity to come to Canada for a graduate study and for believing in me when I was just graduated from college. I always feel privileged and super grateful to have such an earnest, experienced, and enthusiastic supervisor during my stay in Canada. I still vividly remember the days we spent together on discussing on my research projects, revising papers, and travelling around in China to visit the academic institutions. I truly appreciate his professional and extraordinary dedication to my research work, which also inspires me to keep on an unending self-improvement. His willingness and devotion to motivate young students like me deserves my utmost respect.

My sincere thanks also go to my co-supervisor, Dr. Chao Zhang, for her kindness and patience to me. Her careful supervision is a great help to the completion of this thesis work as well as the preparation of my manuscripts. She always gives me valuable suggestions when I feel confused with my research work and provides instant assistance throughout all my consultations. Her elegance, composure, and wisdom impressed me deeply and will continuously lead me to keen on working hard during my future career.

I would also express my thanks to all my colleagues from the fluidization group, especially to Xiaoyang Wei, Tian Nan, and Zhijie Fu for the time we had weekly meetings and discussions together. Particularly, many special and sincere thanks go to Yangfan, Song, Yunfeng Liu, and Xiliang Sun, for their kind cooperation and enthusiastic support to my thesis work. It is my honor and privilege to work with these lovely, dedicated, imaginative, and open-minded people. Furthermore, I would also like to thank my colleagues from the modelling group including Huirui Han, Yunfeng Liu, and Hao Luo. I really enjoyed having hot-pot in the winter and BBQ in the summer with you all. Besides, I would like to thank Shan Gao, Qingliang Yang, Danni Bao, Long Sang, Xinping Zhu and Shuyu Liu for the weekends and holidays we gathering together and it is my pleasure to share many happy times with you all.

Last but not least, I would like to express my deepest gratefulness to my dearest parents. Dear dad and mum, you probably never know how lucky I feel to be a child of you and how important you two mean to me. It is you who not only gave birth to me but also show me what the life is and teach me how to love the people I cared. I'm so grateful that you never asked me to be outstanding or excellent at everything, and I know the only wish you have on me is to be happy with my life and I'm trying my best to. Thank you for pouring your hearts into my growth and providing me with the best education although the both of you didn't have chance to college. Love is a force that naturally comes from the deep bottom of our hearts and that sticks us together wherever I am. Without you I don't have the courage to task myself, to risk the uncertainties, to breakthrough my limitations. You have set yourselves as examples that shapes me to be an honest, persevering and resilient person. Although we don't understand each other sometimes, you are always being my inner strength for me to make through my hard times. I always love you, truly and deeply.

Finally, this work is especially dedicated to my dear grandma, who although no longer with me. So many times there has been a throwback to when I spent the whole summer with you in the country. It's a pity you couldn't see me graduate, but you never walked out of my heart.

Five years' study is a long journey, I cherish everyone who being a part of my life and appreciate all their help along the way. Let me finish my acknowledgement with this quote from Ralph Emerson, "The years teach much which the days never know.", and the people also teach me much which they never know.

Table of Contents

List of Tables

List of Figures

Chapter 1

1   Introduction

Hydrodynamics and the underlying flow mechanisms of multiphase flows including gas-solid, liquid-solid, and gas-liquid-solid systems in various types of circulating fluidized beds are studied via the computational fluid dynamic (CFD) approach in this work. Numerical studies done on the wide range of fluidization systems and the data exchange between the experimental and numerical studies provide more insight into the fundamental studies of fluidization technology on a high-level and big-picture view.

The research background, objectives, and the structure of this thesis are briefly presented in this chapter.

1.1   Background

Fluidization phenomenon is commonly seen in our daily life and has been applied in a wide range of fields in industries over nearly a century since the first fluidized bed reactor was developed for coal gasification in the 1920s (Kunii & Levenspiel, 1969). An efficient and easy operation of granular materials can be achieved in a fluidized bed by introducing fluids into the equipment at a certain velocity. Various types of fluidized bed reactors operated under different conditions are designed for applications in many areas such as oil refinery, coal combustion and gasification, particle coating, pharmaceutical processes, and wastewater treatment (Jahnig, et al., 1980; Fan, et al., 1982 and Zhu & Cheng, 2005).

Since the 1970s, computational fluid dynamic (CFD) approach has become an effective and more economic tool used for the research of fluidization phenomenon with the development of computer science (Berruti & Kalogerakis, 1989; Gidaspow & Ding, 1990; Sinclair & Jackson, 1989; and Tsuo & Gidaspow, 1990a). CFD modelling helps researchers better understand the flow mechanisms in different types of fluidized beds and provides more flow details when experimental measuring technology is limited. Nowadays, the fast growth of computational energy makes numerical simulations to play a more significant role in the fundamental studies of fluidization (Luo, et al., 2015; Stroh et al., 2019; Tsuji,

et al., 1993; Tsuo & Gidaspow, 1990b; Zhang, et al., 2015). In this work, CFD modelling is used as the main approach for studying the flow structures of various fluidized beds.

During the development of fluidization technology, the most successful commercial applications are found in the upward gas-solid fluidization process for gas-solid reactions such as coal combustion and gasification or catalytic gas-phase reactions such as FCC process (Horio, et al., 1992; Zhu & Cheng, 2005). As a result, the fundamental research has focused on the gas-solid fluidized bed reactors since the 1920s revealing more details in the hydrodynamics of the gas-solid flow in different types of fluidized beds and guiding the following expansion of fluidization.

Over the years, fluidization technology went through many developments, from low-velocity operation to high-velocity operation by increasing fluid velocity, and from low-density operations to high-density operations by increasing solids flux (Bi & Grace, 1999; Yerushalmi & Cankurt, 1979; Zhu & Bi, 1995). Furthermore, by changing the fluidizing agent, the flow regime map of fluidization has expanded from gas-solid to liquid-solid and gas-liquid-solid three-phase fluidizations (Li & Kwauk, 2003; Richardson & Zaki, 1997). In addition, when lighter particles were used, inverse liquid-solid or gas-liquid-solid three-phase fluidizations were developed by changing the particle or fluid properties (Fan, et al., 1982; Karamanev & Nikolov, 1992).

During the operation of the fluidization process, solid particles will be suspended by the pass-through fluid flow and will behave like a fluid after minimum fluidization, so that a conventional low-velocity fluidized bed can be constructed for the batch operation of fluidization. Further increasing the fluid velocity could lead to an entrainment of particles at some point and a circulating fluidized bed (CFB) with the recycling of the entrained particles was developed for high-velocity continuous fluidization operations in contrast to the conventional low-velocity batch operations. A circulating fluidized bed system usually consists of a riser and a downer where both the upward and downward fluidizations can be operated respectively.

For gas-solid fluidization, by increasing gas velocity, the gas-solid fluidized beds can be classified into bubbling fluidized bed, slugging fluidized bed, turbulent fluidized bed

corresponding to conventional low-velocity operations, and circulating fluidized bed corresponding to continuous high-velocity operations (Bai, et al., 1993; Grace, 1990; Horio, et al., 1992; Ishii & Horio, 1991; Yerushalmi & Cankurt, 1979). Both conventional fluidized beds and the circulating fluidized beds have been widely applied in industries including chemical, food and pharmaceutical, mineral and energy processes (Jahnig et al., 1980; Zhu & Cheng, 2005).

Under a high-velocity gas-solid fluidization operation, solids circulation rate (G_s) becomes another important parameter affecting the overall flow structures together with the superficial fluid velocity in a circulating fluidized bed. It has been pointed out that in a gas-solid CFB riser, a higher solids circulation rate results in a higher overall bed density and distinct gas-solid flow structures from the low-density CFB riser. The high-density CFB riser usually operates under a solids circulation rate higher than 400kg/m^{2}s for Group A particles has been distinguished as new type of fluidization operation from the low-density CFB riser in 1995 (Grace, et al., 1999; Wang, et al., 2014; Zhu & Bi, 1995). A high-density operation performed under higher gas velocity in a HDCFB riser makes it a very desirable reactor for catalytic gas-phase reactions accompanying with quick catalyst deactivation process such as the FCC process for its better gas-solid contacting and higher conversion. However, severe particle clustering phenomenon is observed in CFB riser reactors due to the hydrodynamic and cohesive effects. The existence of particle clusters aggravates the non-uniformity of the gas-solid flow structure in the CFB riser and hampers the gas-solid mass and heat transfers (Wang, et al., 2014a; 2014b).

With the disadvantages of the GSCFB riser reactor in mind, the GSCFB downer, which used to only act as the solids recycling apparatus, was employed as a new type of fluidized bed chemical reactor to provide a more uniform flow condition. In a gas-solid CFB downer reactor, both gas and particles travel downward with a short developing region because particles accelerate very fast due to gravity (Wang, et al., 2015). Less particle clusters are found in the GSCFB downer and the gas-solid flow structure is uniform both axially and radially with less back-mixing of gas and solids (Wang, et al., 2015). A short and uniform residence time distribution of gas and solids in the GSCFB downer makes it more suitable for chemical reactions as it requires short reaction time, for example, when intermediates

in the reaction are valuable. Although many of the fundamental research and experiments have been carried out in gas-solid fluidization, the flow mechanisms under high-density operations in CFB systems are still not fully studied due to the restriction of experimental and measuring techniques. CFD approach can extend the research of high-density CFB operations to some extremely dense conditions simply by simulation and provide better understanding of the flow mechanisms.

Although the gas-solid circulating fluidization technology has been well utilized, fluidization has expanded to liquid-solid circulating fluidization since the 1990s and shortly afterwards into gas-liquid-solid three-phase fluidization (Fan, 1985; Razzak, et al., 2009; 2010; Renganathan & Krishnaiah, 2004). By changing the fluidizing agent from gas to liquid, particles can uniformly disperse in the liquid flow and the above-mentioned particle clustering phenomenon becomes insignificant in (gas)-liquid-solid fluidized beds.

Similar to the gas-solid CFB system, high-velocity operations can be achieved in a circulating liquid-solid fluidized bed (LSCFB) and a circulating gas-liquid-solid three-phase fluidized bed (GLSCFB) (Razzak et al., 2009). Traditional industrial applications such as leaching and washing, adsorption and ion exchange, or some bioprocesses widely take place in the LSCFB or GLSCFB when heavier particles are used. By changing the particle density to be lower than the liquid density, the so-called inverse liquid-solid fluidized bed (ILSFB) is developed in which both the solids and liquid flow downward (Choi & Shin, 1999). In the inverse liquid-solid fluidized bed, light particles are initially packed in the top of the reactor and then are fluidized and move downward by the by downward flowing liquid. When the downward flowrate of the liquid is high enough, entrainment of the particles also occurs and an inverse circulating fluidized bed (ILSCFB) system is developed.

Gas bubbles also can be introduced in to the inverse liquid-solid fluidized bed reactor as a fluidizing agent other than the liquid, leading to the bubble induced inverse gas-liquid-solid three-phase fluidized bed reactor. Increasing interests from the biochemical fields especially the area of wastewater treatment are found in the bubble induced inverse fluidized bed (BIFB) in which a film of biomass can form and attach to the surface of

particles and react with the wastewater with the movements of particles. Compared to the upward gas-liquid-solid (GLS) three-phase fluidized bed reactor, the BIFB provides a more flexible oxygen supply, less clogging of the biomass, reduced shearing effects to the bio-film caused by liquid flow, and longer residence time of the liquid, with a lower or even negligible liquid velocity under a homogeneous flow condition.

Currently, less modelling work has focused on the LSCFB and bubble induced GLSFB most likely because of the lack of enough experimental data. However, the future applications of these two new types of fluidized beds are very promising and CFD approach is a helpful tool urgently needed in industrial design, optimization, and scale-up. Therefore, in this work, reliable CFD models studying the hydrodynamics in a LSCFB and bubble induced GLSFB needs to be developed respectively and validated with the experimental data collected in the same group.

Additionally, numerical studies on fluidized bed reactors can be generally classified into two approaches: the Eulerian-Lagrangian (EL) method and Eulerian-Eulerian (EE) method. The Eulerian-Lagrangian (EL) method tracks the movements of every particle and less assumptions are used, but costs more computational resources (Benyahia et al., 2000; Hartge, et al., 2009; Tsuji et al., 1993; Van Der Hoef, et al., 2004; Zhou, et al., 2002; Zhu, et al., 2008). The Eulerian-Eulerian (EE) method treats the particles as a secondary fluid phase by coupling the kinetic theory of granular flow model for the solids phase so that it is more desirable for simulations on large-scale fluidized bed equipment due to less computational costs.

The numerical theories of the multiphase flow in fluidized beds employed many simplifications and empirical correlations so that discrepancies are found between the experimental and simulation results. Especially in gas-solids CFB systems in which the existence of particle clusters cannot be ignored, the underlying physics in the gas-solids interactions are not fully understood both experimentally nor numerically due to its complexity. The particle clusters consists of a group of single particles with a denser solids concentration than the surrounding dilute gas-solid suspension due to the hydrodynamic or cohesive effects (Cocco, et al., 2010). The clustering phenomenon is one of the most

remarkable characteristics of a gas-solid CFB reactor, which results in the non-uniform distributions of the solids holdup and particle velocity. The effects of clusters are usually included in the drag calculation, which accounts for the gas-solids interactions in CFD models (Agrawal, et al., 2001; Li et al., 2002; Syamlal & O'Brien, 1994; Tsuo & Gidaspow, 1990). Since the clusters have different properties from freely moving single particles such as larger size and higher solids holdup, the ideal drag law for the dispersed particulate system is longer applicable in a GSCFB. Knowing the existence of particle clusters, various drag models are developed by researchers based on their own understanding of the clustering phenomenon. Most of the current drag models were developed in the 1990s when the experimental work on gas-solids fluidization hasn't expanded to the high-density operations. Therefore, the modified drag calculations which rely on the experimental results mainly in the low-density operations appear to be not very accurately predict the flow structures under high-density operations. Furthermore, with the development of measuring techniques, more characteristics of clusters can be extracted and analyzed by new approaches such as image processing by high-speed cameras and wavelet analysis of the optical probe data. Therefore, properties of clusters can be statistically characterized and were explicitly used into the calculation of the drag force in this work for the gas-solid CFB system.

1.2 Research objectives

The overall objective is to comprehensively study the hydrodynamics and the underlying flow mechanisms of the multiphase flows in various types of circulating fluidized bed (CFB) systems under a wide range of operating conditions via computational fluid dynamic (CFD) approach.

With the overall objective in mind, the following objectives are included:

- To investigate the gas-solid flow structures in both the riser and downer reactors of a gas-solid circulating fluidized bed system via a validated CFD model. (Chapters 3, 4 & 5)

- To study the effects of the entrance geometric structure of the CFB riser on the simulation results.

- To compare the solids holdup distributions, particle velocity profiles both axially and radially between the CFB riser and downer.

- To study the transition phenomenon in the CFB riser and downer reactors from dilute to dense flow conditions respectively.

- To investigate the combined effects of the superficial gas velocity and solids circulation rate on the overall bed density and local solids distribution between low-density fluidization operations and high-density fluidization operations.

- To develop a cluster-driven drag model, which directly employs the characteristics of particle clusters into the calculation of the drag force in a gas-solid CFB reactor with the help of the image and wavelet analysis from the experimental data. (Chapters 6&7)

  - To validate the proposed cluster-driven drag model with the experimental data.

  - To obtain a better understanding of the effects of the clustering phenomenon on gas-solids flows.

  - To give further parametric studies of the proposed cluster-driven drag model by studying the effects of cluster size and density.

- To develop a validated CFD model for an inverse liquid-solid circulating fluidized bed (ILSCFB). (Chapter 8)

  - To study the effects of different superficial liquid velocity, solids circulation rate, and particle types on the distributions of solids holdup and particle velocity in an ILSCFB.

  - To compare the flow structures between the binary-particle system and the single-particle system via CFD approach.

- To propose a three-phase Eulerain-Eulerian CFD model for the bubble-induced inverse gas-liquid-solid fluidized bed. (Chapter 9)

  - To study the flow regimes under different gas velocities and the transitions between the flow regimes in the bubble-induced inverse fluidized bed (BIFB) via both the experimental and numerical works.

  - To study the instantaneous distributions solids and liquid in the BIFB by CFD model.

  - To study the effects of different types of particles on the solids distribution and transition gas velocity between the flow regimes in the BIFB.

1.3 Thesis structure

Chapter 1 provides a general introduction of this research work.

Chapter 2 gives a detailed literature review on the experimental and numerical work of circulating fluidization systems, the clustering phenomenon in gas-solid circulating fluidized bed, and the CFD treatments on the clustering effects.

Chapter 3 investigates the effects of inlet boundary conditions in CFD modeling on flow structures inside circulating fluidized bed risers

Chapter 4 compares the hydrodynamics and flow structures between high-density and low-density operations in a gas-solid CFB riser via numerical simulations.

Chapter 5 numerically studies the hydrodynamics and flow structures of low-density conditions to high-density conditions in a gas-solid CFB downer. The scale-up effects in the gas-solid CFB downer are also investigated via CFD approach.

Chapter 6 proposes a cluster-driven drag model for gas-solids circulating fluidized bed riser by directly employing the properties of particle clusters into the calculation of the drag force.

Chapter 7 provides a detailed study of the clustering phenomenon in the gas-solid CFB riser via the proposed cluster-driven drag calculation. The clustering effects of cluster size, density, and slip velocity are discussed.

Chapter 8 numerically studies the hydrodynamics and flow structures in an inverse liquid-solid circulating fluidized bed.

Chapter 9 develops a validated CFD model for the bubble-induced inverse gas-liquid-solid three-phase model.

Chapter 10 presents the conclusions of this study and recommendations for the future work.

References

Agrawal, Loezos, Syamlal & Sundaresan (2001). The role of meso-scale structures in rapid gas–solid flows. Journal of Fluid Mechanics, 445, 151–185.

Bai, Jin, & Yu (1993). Flow regimes in circulating fluidized beds. Chemical Engineering & Technology: Industrial Chemistry-Plant Equipment-Process Engineering-Biotechnology, 16(5), 307–313.

Benyahia, Arastoopour, Knowlton, Ted & Massah. (2000) Simulation of particles and gas flow behavior in the riser section of a circulating fluidized bed using the kinetic theory approach for the particulate phase. Powder Technology, 112(1–2), 24–33.

Berruti & Kalogerakis. (1989). Modelling the internal flow structure of circulating fluidized beds. The Canadian Journal of Chemical Engineering, 67(6), 1010–1014.

Bi & Grace (1999). Flow patterns in high-velocity fluidized beds and pneumatic conveying. Canadian Journal of Chemical Engineering, 77(2), 223–230.

Choi & Shin (1999). Hydrodynamics study of two different inverse fluidized reactors for the application of wastewater treatment. Korean Journal of Chemical Engineering, 16(5), 670–676.

Cocco, Shaffer, Hays, Karri & Knowlton (2010). Particle clusters in and above fluidized beds. Powder Technology, 203(1), 3–11.

Fan, Muroyama & Chern (1982). Hydrodynamic characteristics of inverse fluidization in liquid-solid and gas-liquid-solid systems. The Chemical Engineering Journal, 24(2), 143–150.

Muroyama and Fan (1985), Fundamentals of gas-liquid-solid fluidization. AIChE J., 31: 1-34.

Gidaspow & Ding (1990). A bubbling fluidization model using kinetic theory of granular flow. AIChE Journal, 36(4), 523–538.

Grace (1990). High-velocity fluidized bed reactors. Chemical Engineering Science, 45(8), 1953–1966.

Grace, Issangya, Bai, Bi & Zhu (1999). Situating the high-density circulating fluidized bed. AIChE Journal, 45(10), 2108–2116.

Hartge, Ratschow, Wischnewski & Werther (2009). CFD-simulation of a circulating fluidized bed riser. Particuology, 7(4), 283–296.

Horio, Ishii & Nishimuro (1992). On the nature of turbulent and fast fluidized beds. Powder Technology, 70(3), 229–236.

Ishii & Horio (1991). The flow structures of a circulating fluidized bed. Advanced Powder Technology, 2(1), 25–36.

Jahnig, Campbell, Martin (1980) History of Fluidized Solids Development at Exxon. In: Grace J.R., Matsen J.M. (eds) Fluidization. Springer, Boston, MA

Karamanev and Nikolov (1992), Bed expansion of liquid-solid inverse fluidization. AIChE J., 38: 1916-1922.

Kunii & Levenspiel (2013). *Fluidization engineering*. Elsevier

Li, Cheng, Zhang, Yuan, Nemet & Fett (2002). The EMMS model — its application, development and updated concepts. Chemical Engineering Science, 54(22), 5409–5425.

Li & Kwauk (2003). Exploring complex systems in chemical engineering—the multi-scale methodology. Chemical Engineering Science, 58(3–6), 521–535.

Luo, Wu, Yang, Fang & Fan (2015). High-fidelity simulation of the 3-D full-loop gas-solid flow characteristics in the circulating fluidized bed. Chemical Engineering Science, 123, 22–38.

Razzak, Barghi & Zhu (2010). Axial hydrodynamic studies in a gas–liquid–solid circulating fluidized bed riser. Powder Technology, 199(1), 77–86.

Razzak, Barghi, Zhu & Mi (2009). Phase holdup measurement in a gas–liquid–solid circulating fluidized bed (GLSCFB) riser using electrical resistance tomography and optical fibre probe. Chemical Engineering Journal, 147(2–3), 210–218.

Renganathan & Krishnaiah (2004). Liquid phase mixing in 2-phase liquid–solid inverse fluidized bed. Chemical Engineering Journal, 98(3), 213–218.

Richardson & Zaki (1997). Sedimentation and fluidisation: Part I. Chemical Engineering Research and Design, 75(3), S82–S100.

Sinclair & Jackson (1989). Gas-particle flow in a vertical pipe with particle-particle interactions. AIChE Journal, 35(9), 1473–1486.

Stroh, Daikeler, Nikku, May, Alobaid, von Bohnstein, Epple (2019). Coarse grain 3D CFD-DEM simulation and validation with capacitance probe measurements in a circulating fluidized bed. Chemical Engineering Science, 196, 37–53.

Syamlal & O'Brien (1987). The derivation of a drag coefficient formula from velocity-voidage correlations. Technical Note, US Department of energy, Office of Fossil Energy, NETL, Morgantown, WV.

Tsuji, Kawagucchi & Tanaka (1993). Discrete particle simulation of a fluidized bed. Powder Technology, 77(1), 79–87.

Tsuo & Gidaspow (1990). Computation of flow patterns in circulating fluidized beds. AIChE Journal, 36(6), 885–896

Van Der Hoef, Van Sint Annaland, & Kuipers (2004). Computational fluid dynamics for dense gas-solid fluidized beds: A multi-scale modeling strategy. Chemical Engineering Science, 59(22–23), 5157–5165.

Wang & Zhu (2015). Axial solids flow structure in a high density gas–solids circulating fluidized bed downer. Powder Technology, 272, 153–164.

Wang, Li, Zhu, Wang, Barghi & Zhu (2015). A comparison of flow development in high density gas-solids circulating fluidized bed downer and riser reactors. AIChE Journal, 61(4), 1172–1183.

Wang, Zhu, Barghi & Li (2014a). Axial and radial development of solids holdup in a high flux/density gas-solids circulating fluidized bed. Chemical Engineering Science, 108, 233–243.

Wang, Zhu, Li & Barghi (2014b). Detailed measurements of particle velocity and solids flux in a high density circulating fluidized bed riser. Chemical Engineering Science, 114, 9–20.

Yerushalmi & Cankurt (1979). Further studies of the regimes of fluidization. Powder Technology, 24(2), 187–205.

Zhang, Lei, Wang, Xu & Xiao (2015). A numerical study of gas-solid flow hydrodynamics in a riser under dense suspension upflow regime. Powder Technology, 280, 227–238.

Zhou, Flamant, Gauthier & Lu (2002). Lagrangian approach for simulating the gas–particle flow structure in a circulating fluidized bed riser. Int. J. Multiphase Flow 28, 1801–1821. 28, 1801–1821.

Zhu, Zhou, Yang & Yu (2008). Discrete particle simulation of particulate systems: A review of major applications and findings. Chemical Engineering Science, 63(23), 5728–5770.

Zhu & Cheng (2005). Fluidized Bed Reactors and Applications. In Multiphase Flow Handbook (p. 5.55-5.93).

Zhu & Bi (1995). Distinctions between low density and high density circulating fluidized beds. The Canadian Journal of Chemical Engineering, 73(5), 644–649.

Chapter 2

2 Literature review

2.1 Introduction to fluidization systems

Fluidization process is widely applied not only in the industries but also in our daily life to easily handle granular materials. A fluidized bed is an equipment for stationary packed particles in a column to be blew-up or suspended and then can behave like liquid by introducing a flowing fluid such as gas or liquid.

Various fluidization systems have been developed with the expansion of the fluidization technology since the 1920s (Zhu & Cheng, 2005). By changing the fluid media, solid particles can be fluidized either by a liquid like water or a gas like air to form a liquid-solid or a gas-solid fluidization system, and even by both the gas and liquid to form a gas-liquid-solid three-phase fluidization system (Fan, 1985). By changing the fluid velocity, the fluidization system can be classified into a conventional low-velocity fluidized bed and a high-velocity continuous fluidized bed with the increase in fluid velocity (Yerushalmi, et al., 1976). Under the high-velocity operation, the entrainment of particles will occur because the fluid flow rate is high enough. A circulating fluidized bed is developed if the entrained particles are collected and recycled back to the column so that the continuous operation of particles is accomplished (Reh, 1995). By changing the particle density, inverse liquid-solid fluidized bed has been developed when lighter particles were used (Fan, et al., 1982). Further introducing gas bubbles into the liquid-solid fluidized bed, a bubble-induced inverse three-phase fluidized bed is developed (Fan, et al., 1982). By changing the flow directions, a fluidized bed downer reactor with both the fluid and particles flowing downward in the column is also developed for some quick reactions (Zhang, et al., 2001). With the development of the fluidization technology, the expansion of the fluidization map has provided various fluidized bed systems for different industrial uses and also more extensive fundamental researches are needed especially by numerical studies.

2.2　Gas-solids circulating fluidized bed systems

In upward gas-solids fluidization, the fluidized bed systems can be divided into the conventional fluidized beds including the bubbling bed, slugging bed, and turbulent bed corresponding to the low-velocity operations and the continuous high-velocity "fast" fluidized bed which stands for the circulating fluidized bed riser operating under a gas velocity beyond the transport velocity as shown in Figure 2-1 (Bi & Grace, 1995; Grace, 1990; Yerushalmi & Cankurt, 1979). Under the high-velocity operation, the circulating fluidized bed (CFB) system has been successfully applied into many chemical processes since the 1940s when the first CFB was constructed by Winkler because of its higher gas throughput and the continuous handling of the solid materials (Zhu & Cheng, 2005). Nowadays, the CFB system enjoys numerous applications in the industries including gas-solids reactions such as coal combustion and gasification, gas phase catalytic reactions such as fluid catalytic cracking (FCC) process, fine powder process such as pharmaceutical coating and drug delivery, and some physical processes such drying (Zhu & Cheng, 2005).
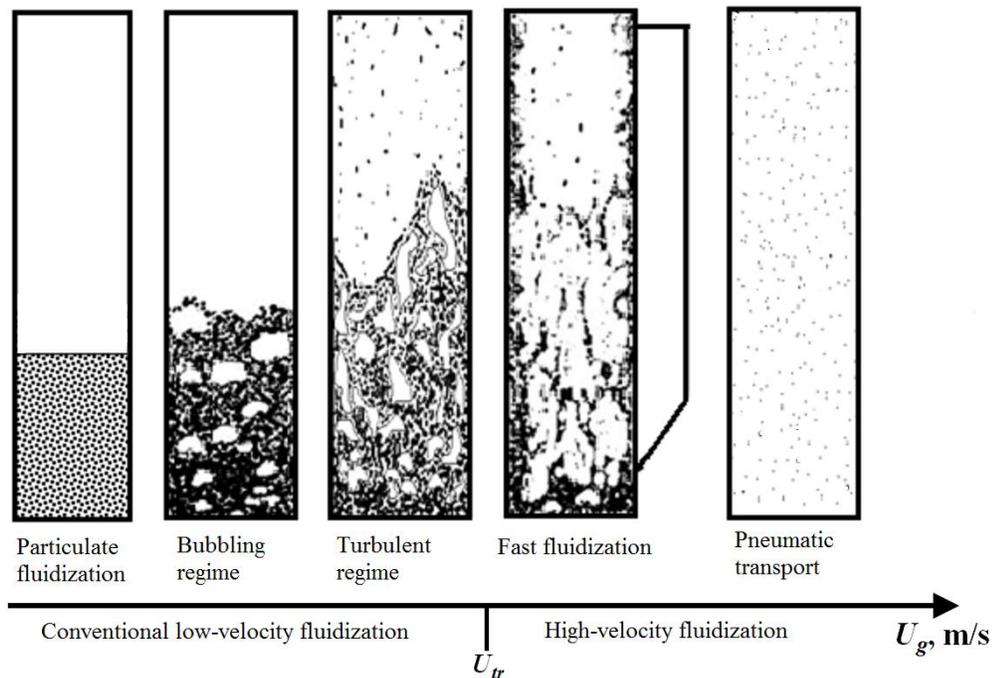
Figure 2-1 Upward gas-solid fluidized bed systems with increasing gas velocity

A circulating fluidized bed (CFB) system as shown in Figure 2-2 usually consists a riser column where most of the chemical reactions take place in and a downer column which used to be simply a returning pipe for the recycle of the particles and now becomes a reactor in some cases for quick chemical reactions.
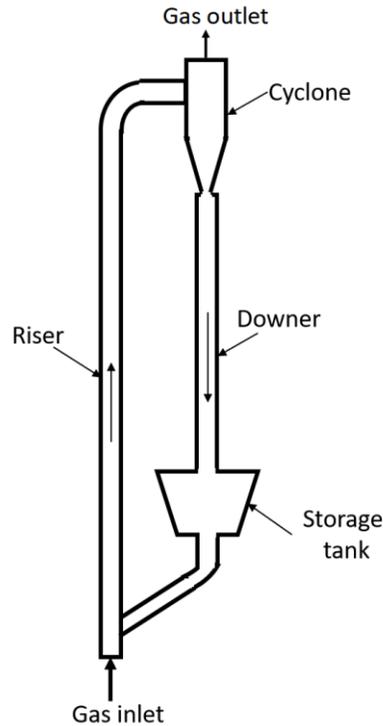
Figure 2-2 Typical sketch of a CFB system

2.2.1 General flow structure in CFB risers

In a CFB riser reactor, both the gas and solid particles flow upward under a high gas velocity so that less back-mixing of particles is achieved compared with the conventional fluidized beds. The dilute phase plays the dominant role in the CFB riser which results in a wide dilute core region of upward flowing solids suspension in the center of the riser (Wang, et al., 2014a). On the other hand, a denser annular layer with higher solids holdup exists in the wall region of the CFB riser due to the wall effects and more severe particle clustering phenomenon near the wall (Ishii & Horio, 1991). Traditionally, the above-mentioned radial gas-solid flow structure in a CFB riser is called a "core-annulus" flow structure as shown in Figure 2-3. Axially, the gas-solid flow in a CFB riser can be either

15

exponential or bottom-dense and upper-dilute as known as the "S shape" profile of the solids holdup depending on the solids circulation rate and inventory in the standpipe as shown in Figure 2-4. The non-uniform structures inside a CFB riser is due to the existence of particle clustering phenomenon (Horio, et al., 1992). Particle clusters are a group or a denser cloud of particles which are closely constrained and have an obviously higher local solids holdup than the surrounding dilute suspensions due to the hydrodynamic effects or cohesive effects (Cocco, et al., 2010). More details about the particle clusters inside a CFB riser will be discussed in the next section.

With increasing solids circulation rate, the CFB riser expands from low-density operation to high-density operation. The hydrodynamics inside a low-density CFB (LDCFB) riser and a high-density CFB (HDCFB) riser are quite different due to the increased overall solids holdup as shown in Figure 2-5 (Wang, et al., 2014b). As a result, the high-density CFB riser has been distinguished as a unique flow regime from the LDCFB riser since the 1995 (Zhu & Bi, 1995). In an HDCFB riser, the solid circulation rate is usually higher than $G_s = 400$ kg/m^{2}s leading to a higher overall bed density higher than $\varepsilon_s = 0.05$, which contributes to a higher mass and heat transfer efficiency and more intensive gas and solids contacting for a higher conversion (Wang, et al., 2014b). Fundamental studies revealed that the dilute core region shrinks to be less than r/R = 0.5 in an HDCFB riser, in the meantime, the wall layer of an HDCFB riser becomes wider and much denser, and even can reach a local solids holdup as high as ε_s=0.05 under some extremely high solids fluxes (Wang, et al., 2014b). Also, a longer bottom denser region with higher solids holdup is found in the HDCFB riser due to the high G_s, however, sometimes the axial profile of solids holdup could become exponential shape again with a much higher solids holdup from the entrance of the riser to the top under the extremely high solids circulation rate ($G_s \geq 800$ kg/m^{2}s) as shown in Figure 2-6 (Wang, et al., 2014b). The transition from LDCFB regime to HDCFB regime was comprehensively studied by the detailed measurement of solids flux, particle velocity, and radial and axial development of solids holdup in a macroscope view with the help of the optical fiber probe (Wang, et al., 2014a; 2015a). However, more detailed flow development from the microscope view and the effects of the underlying gas-solids interactions to the formation of the particle clusters and the corresponding transition from LDCFB to HDCFB still need more extensive studies.
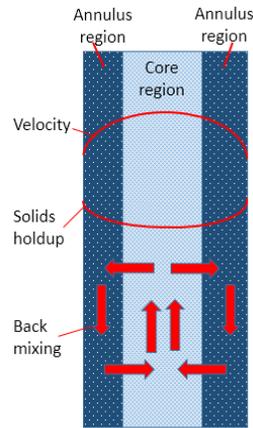
Figure 2-3 Typical radial flow structures in a CFB riser
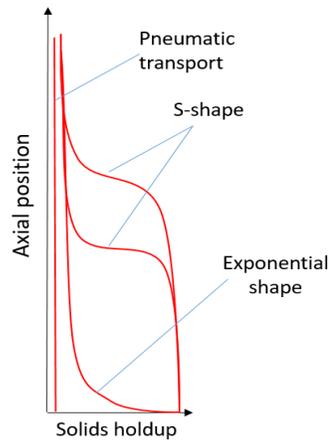
Figure 2-4 Typical axial flow structures in a CFB riser
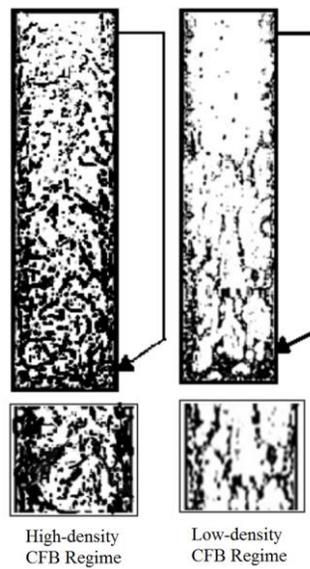
Figure 2-5 Flow structures in HDCFB riser and LDCFB riser
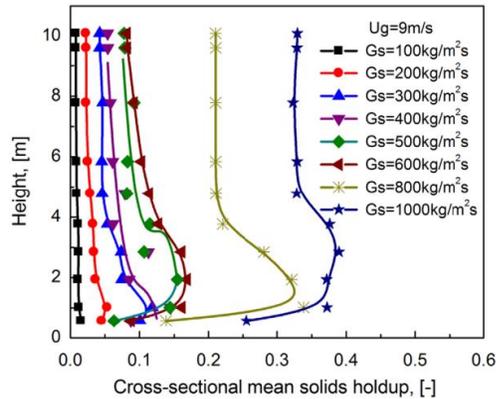
Figure 2-6 Typical axial solids holdup profiles in HDCFB risers and LDCFB risers (Wang, et al., 2014a)

2.2.2 General flow structure in CFB downers

In contrast to the CFB riser reactor where the gas-solids suspension flows upwardly, a CFB downer reactor in which both the gas and solids flow concurrently downward also shows promising potential in some quick chemical reactions due to its much shorter and uniform residence time distribution of gas and solids. The gas-solid flow structure becomes much uniform in a CFB downer since the gas and particles flow with the same direction of the gravity. Consequently, a much wider and more uniform dilute region which almost occupies the whole cross-sectional area of the CFB downer with a slightly higher solids holdup at the wall is found radially inside a downer as shown in Figure 2-7 (Wang, et al., 2016). Axially, a much shorter entrance denser region below the gas distributor followed by a uniform fully developed region along the downer is recognized in the downer reactor as shown in Figure 2-8 (Wang, et al., 2015b). Since the gas and solids flow with the same direction as the gravity, the acceleration of the gas and particles is very fast so that the slip velocity between the gas and particles becomes smaller and there is almost no back-mixing of the gas and solids in a downer comparing with the CFB riser.
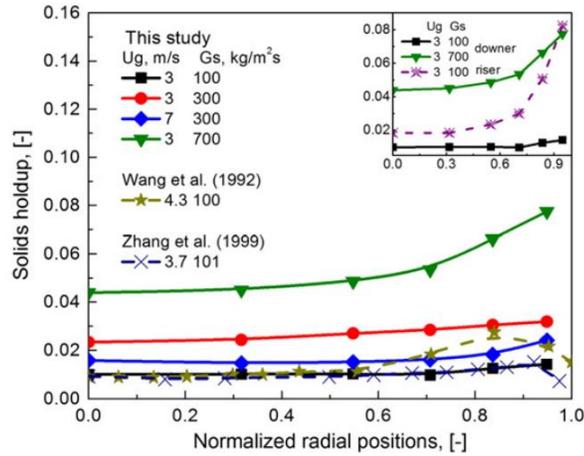
Figure 2-7 Typical radial distributions of solids holdup in a CFB downer (Wang et al., 2016)
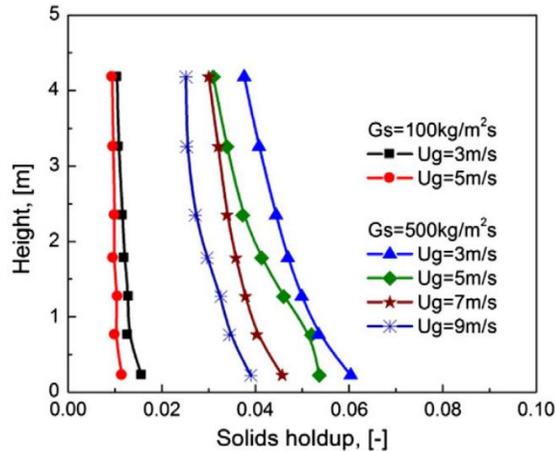
Figure 2-8 Typical axial distributions of solids holdup in a CFB downer (Wang et al., 2015b)

2.3 Inverse liquid-solid and gas-liquid-solid fluidized bed

Inverse fluidization usually can be achieved in liquid-solid and gas-liquid-solid fluidized bed systems where light particles with a density lower than liquid are used. Since the particles are lighter than liquid, a downward flow of liquid is required to overcome the net buoyancy of the particles and so that to fluidize them. Such type of fluidization operation is name as inverse liquid-solid fluidization (Fan, et al., 1982).

19

In the inverse liquid-solid fluidized bed (ILSFB), light particles are initially packed at the top of the fluidized bed and flow downward after being fluidized when gradually increasing the liquid velocity as shown in Figure 2-9. The local solids holdup distributions are much more uniform both axially and radially with less fluctuations in an inverse LSFB comparing with the gas-solid system (Renganathan & Krishnaiah, 2005). The uniform liquid-solid flow structures inside an ILSFB contributes to a narrower spread in residence time distribution (RTD) curve since relatively less dispersion or back-mixing of the liquid phase exists in the ILSFB. However, higher liquid velocity, larger Archimedes number, and a wider size distribution of particles are found to aggravate the liquid phase dispersion in a ILSFB (Renganathan & Krishnaiah, 2004). Fan et al. (1982) developed a correlation of the bed voidage in an inverse liquid-solid fluidized bed (ILSFB) based on the relationship of the velocity ratio (U_r) and the liquid phase holdup (ε_l). Karamanev and Nikolov (1992) developed a correlation of the bed expansion associating with the Richadson and Zaki equation (Richardson and Zaki, 1954) in an ILSFB based by the studies on twelve kinds of particles. They also found that the drag on a freely rising light particle is different from a falling heavy sphere and more intensive fluctuations of light particles will occur so that a less minimum fluidization velocity is needed in the ILSFB than the upward LSFB (Karamanev & Nikolov, 1992). The minimum fluidization velocity (U_{mf}) in an ILSFB is also found to be independent with the initial packed bed height while increase with increasing particle diameter and decreasing particle density (Lakshmi, et al., 2000).
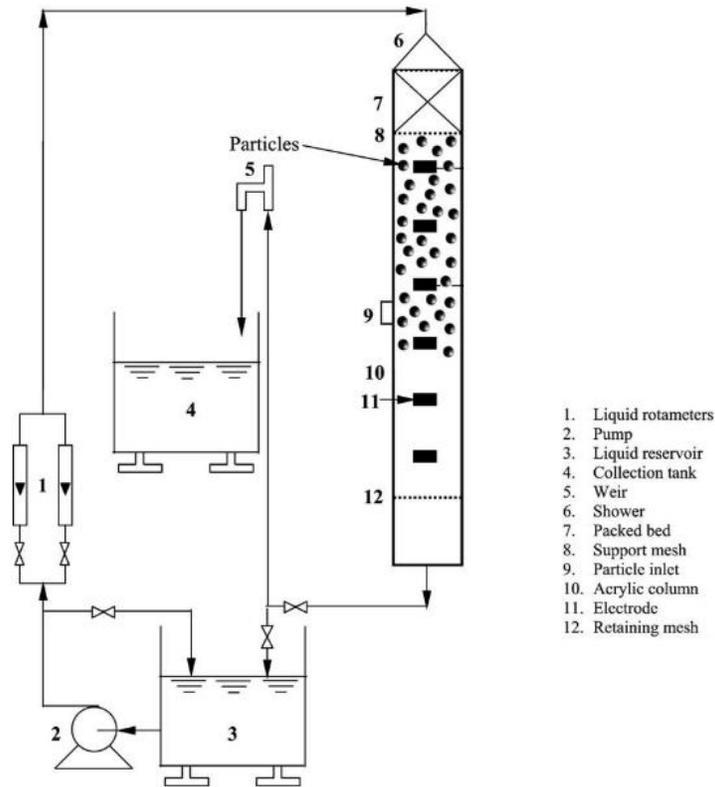
Figure 2-9 A typical schematic diagram of an inverse liquid-solid fluidized bed

(Renganathan & Krishnaiah, 2004)

Once the liquid velocity is high enough, the particles could reach the bottom of the fluidized bed and might accumulate above the retaining mesh, while the entrainment of particles actually will happen if the retaining mesh is removed. The circulation of particles can be easily realized by connecting a upcomer column with upward flowing solids suspension to the inverse fluidized bed so that an inverse liquid-solid circulating fluidized bed (ILSCFB) system is developed as shown in Figure 2-10. Not too much research work has been reported on ILSCFB until recently Sang (2013) conducted a comparison between conventional upward liquid-solid fluidization and inverse liquid-solid fluidization in an ILSCFB system. The hydrodynamics in the ILSCFB downer is very similar to the inverse LSFB where a uniform liquid-solid flow structure is found. Two different kinds of liquid can be operated separately in the downer and upcomer with the circulation of the particles so that industrial applications such as wastewater treatment or ion exchange process can be accomplished in an ILSCFB system. Since less work has been done on the ILSCFB system,

the detailed liquid-solid flow structures under a wide operating range with different types of particles still need a comprehensive study.
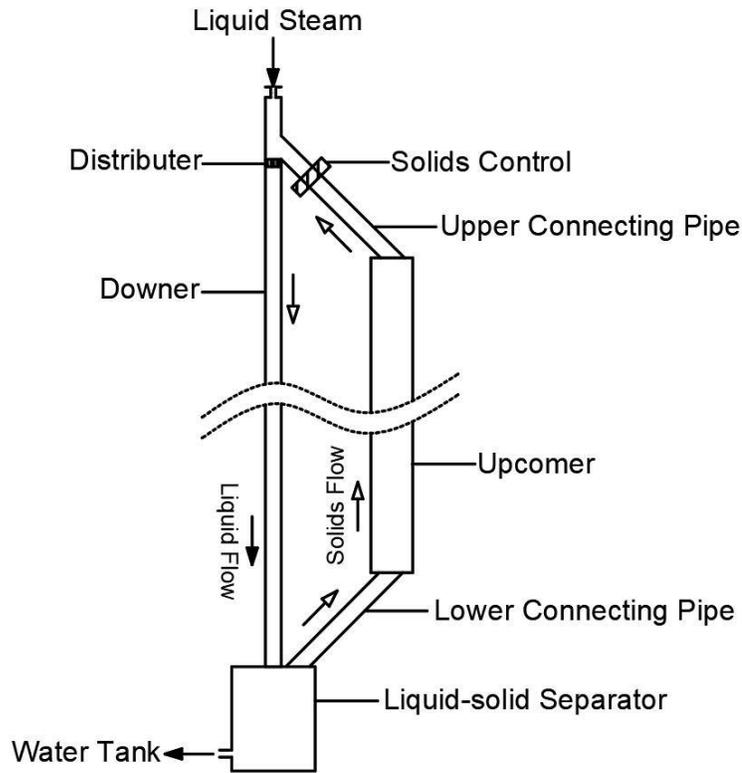
Figure 2-10 A typical sketch of an inverse liquid-solid circulating fluidized bed system

By introducing gas bubbles into the inverse liquid-solid fluidized bed form the bottom gas distributor, a bubble-induced inverse gas-liquid-solid three-phase fluidized bed is developed as shown in Figure 2-11 (Sun, 2017). A gas distributor was added to the bottom of the liquid-solid fluidized bed column which can continuously introduces gas bubbles into the column. During the operation of the bubble-induced inverse fluidized bed (BIFB), there can be a zero liquid velocity which stands for a batch mode of the liquid phase and the fluidization of the particles happens layer by layer once the gas bubble flow reaches and fluidize the bottom layer of the packed particles. The measurements of the bed pressure drop, phase holdups, and the onset gas velocities of every flow regime in the three-phase BIFB have recently been done by Sun (2017). With increasing gas velocity, the BIFB will

go through the fixed bed regime, bed expansion regime, transition regime, complete fluidization regime, and a freeboard regime as shown in Figure 2-12.

In the bed expansion regime and the transition flow regime of BIFB, the fluidized bed has a top-dense and bottom-dilute distribution of solid particles due to the incompletion of the particle fluidization under lower gas velocity. When the superficial gas velocity is beyond the complete fluidization velocity, the particles will uniformly distribute in the BIFB. Once the gas velocity increases too high to reach the freeboard regime, the entrainment of particles could happen if there is no restriction for particles at the bottom of the BIFB and a top only gas-liquid two-phase will occur. The transitional gas velocities to the flow regimes are found to increase by reducing the light particle density, and by decreasing the particle size or particle loading. Apparently, the average gas holdup increases with increasing gas velocity, while the liquid phase holdup decreases and the solids holdup remains constant. Currently, only preliminary experimental results on the BIFB are collected and the transitional gas velocities are mainly obtained by eye observation. The fluidization mechanism in the BIFB and the gas-liquid-solid three-phase flow structures still needs more investigation.
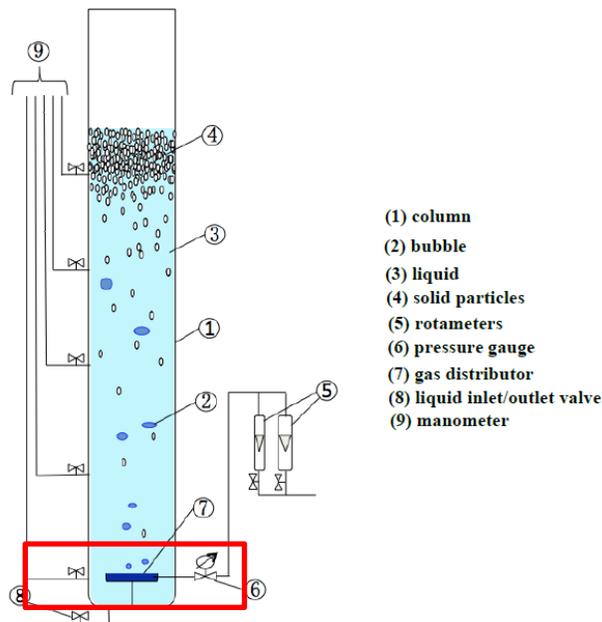
Figure 2-11 A typical sketch of a bubble-induced inverse gas-liquid-solid three-phase fluidized bed system (Sun, 2017)
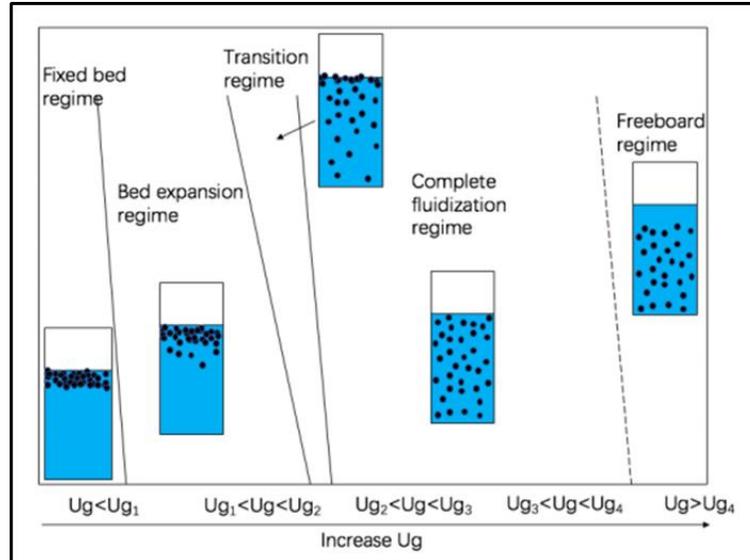
Figure 2-12 A flow regime diagram of bubble-induced inverse three-phase fluidization system (Sun, 2017)

2.4 Numerical work on fluidized bed systems

With the fast development of computer technology, numerical modelling has become an effective tool to study the flow mechanism in a fluidized bed since the 1980s (Sinclair & Jackson, 1989; Tsuo & Gidaspow, 1990). The Eulerian-Lagrangian (EL) and Eulerian-Eulerian (EE) methods are the two major numerical theories for the simulation of the flows in a fluidized bed system.

In the EL approach, the fluid phase is treated as continuum and the solids phase is regarded as a discrete phase. The so-called discrete element method (DEM) is applied to track each particle based on the Lagrangian force balance equation. Some researchers used EL method to simulate CFBs where solids-phase is very dilute and the equipment is not very large, such as Tsuji et al. (1993) and Hoomans et al. (1996). Although a clear and simple physical mechanism of solids-phase is obtained by the EL approach because less assumptions and empirical correlations are made, the high computational cost and time because every particle in the system has to be tracked become the biggest obstacle for this method. For large-scale CFB reactors, which always contains more than one million particles, EL method is not very suitable.

The Eulerian-Eulerian (EE) approach, which also simply referred to as the two-fluid model (TFM) approach, treats both the fluid and solids phases as interpenetrating continua. The conservation equations of mass, momentum and energy are applied as governing equations for all the phases. All the governing equations are closed either by providing constitutive relations obtained from empirical information, or, in the case of granular flows, by application of kinetic theory. Due to the assumption of continuum, the properties of solid phase such as phase pressure, shear viscosity, and bulk viscosity need to be defined explicitly. The EE method is widely used for simulations of two-phase flows in fluidized beds, for example, the works by Sinclair & Jackson (1989), Ding & Gidaspow (1990), Tsuo & Gidaspow (1990), Benyahia et al. (2000), Van Wachem et al. (2001). CFD-TFM approach occupies an important position in the design, optimization, and scale-up of the fluidized bed. Compared with the EL method, the EE approach costs less computational time and energy, which makes it more favorable for the simulation on large-scale fluidized bed. In addition, the flow structures in the pilot or industrial scale equipment are different from that in the lab-scale ones due to the scale-up effects of the chemical reactor, EE approach is selected in this work because the tested CFB systems are in pilot scale.

2.4.1 The kinetic theory of granular flow

The kinetic theory of granular flow (KTGF) was introduced to the CFD-TFM approach to predict the random motions of particles. Granular temperature is proportional to the kinetic energy of the particle random motions taking the analogy to the temperature of the gas (Ding and Gidaspow, 1990). This granular kinetic theory explains the mechanism of solids viscosity which is widely used in studies for fluid-solid two-phase flows (Hosseini et al, 2013). The EE approach with the kinetic theory of granular flow is the most acceptable method to simulate fluid−solid flows in a CFB. With an additional transport equation coupled in the CFD-TFM model, the granular temperature associating with the solids fluctuating energy is calculated and further the pressure and bulk viscosity of the solids phase are also obtained. Sinclair & Jackson (1989) first introduced kinetic theory to deal with the solids phase stress. Kinetic energy associated with the single particle velocity fluctuations is represented by a granular temperature, which is proportional to the mean square of the random velocity fluctuations of particles.

$$\frac{3}{2}\Theta = \frac{1}{2} < v'_{s\tau}v'_{s\tau} >$$ (2-1)

where Θ is granular temperature, $v'_{s\tau}$ denotes the random component of the particle velocity. By solving the granular temperature, solids viscosity and solids pressure can be calculated as the functions of granular temperature.

2.4.2 Turbulence model

In EE approach, conservation equations are solved for both the gas and solids phases. While dealing with the momentum equations, the Reynolds averaging method is employed to separate the instantaneous velocity into the mean and fluctuating components. The Reynolds-averaged Navier-Stokes (RANS) equation is shown as below.

$$\rho \left[\frac{\partial U_i}{\partial t} + U_j \frac{\partial U_i}{\partial x_j}\right] = -\frac{\partial P}{\partial x_i} + \frac{\partial}{\partial x_j}[(\frac{\partial U_i}{\partial x_j} + \frac{\partial U_j}{\partial x_i}) - \rho(\overrightarrow{u_i u_j})]$$ (2-2)

where U_i, and P represent the mean motion and the phase pressure, and $\overrightarrow{u_i}$ and $\overrightarrow{u_j}$ are the fluctuating motions. It is too complicated to simulate the instantaneous motions. Therefore, a so-called Reynolds stress $\rho(\overrightarrow{u_i u_j})$ which is a re-worked version of the fluctuating contribution to the non-linear acceleration terms in the momentum equations for averaged motion is used.

To calculate the Reynolds stress, turbulence model is introduced in the CFD-TFM model. The turbulence model can be applied in both the fluid and solids phases or only in the fluid phase. Besides, a laminar model can also be used to each phase but is not suitable for the multiphase flows in a high-velocity fluidized bed. Two-equation turbulence models are one of the commonly used type of turbulence models based on Boussinesq eddy viscosity assumption (Pitsch, 2014). Models like the k-epsilon model and the k-omega model have become industrial standard models and are commonly used for most types of engineering problems. Two-equation turbulence models are an active area of research and new refined two-equation models are still being developed.

By definition, two-equation models include two extra transport equations to represent the turbulent properties of the flow. This allows a two-equation model to account for history

26

effects like convection and diffusion of turbulent energy. Most often one of the transported variables is the turbulent kinetic energy, k. The second transported variable varies depending on what type of two-equation model it is. Common choices are the turbulent dissipation, ε, or the specific dissipation, ω. The second variable can be thought of as the variable that determines the time and special scales of the turbulence, whereas the first variable, k, determines the energy in the turbulence.

Among all the turbulence models, the k-epsilon model is very popular for industrial applications due to its good convergence rate and relatively low memory requirements (Hartge, 2009). Although the turbulence model for each phase is much more complicated than other models, it has the better prediction ability. Thus, turbulence model for each phase cooperated with KTGF in the EE approach is the most effective method for simulations on multiphase flows in fluidized beds.

2.4.3 Drag model

The interphase force term from the momentum exchange represents the interactions between the fluid and solids phases, which mainly stands for the drag force associating with the clustering phenomenon in a fluidized bed.

There are several empirical or semi-empirical correlations for the drag force calculation either based on the experimental data of the pressure drop or relative velocity of the fluidized bed, or based on numerical theories such as the energy minimization multi-scale concept. However, how to validate the choice of drag model is the biggest problem we are facing because the drag model is strongly dependent on particle diameter and shape.

Comparing different drag models in CFD, the commonly used drag models such as Gidaspow model (Gidaspow, 1994), Syamlal-O'Brien model (Syamlal & O'Brien, 1994), and EMMS model (Li et al., 2002), can predict the solids holdup along the circulating fluidized bed systems well to some extent. But, they still lack validations and some of the parameters in the correlations have no specific physical meanings (Lundberg et al. 2008, Liu, 2014, Wang, 2010). More discussion related with the clustering phenomenon especially in the gas-solid fluidization system will be provided in the next section.

2.5 Clustering phenomenon in gas-solid CFB risers

In a gas-solid fluidization system, solid particles tend to form particle clusters which are a group of particles constrained in a dense cloud and have an obvious higher solids holdup than the surrounding dilute suspensions (Horio & Clift, 1992). The non-uniformity of the flow structures in a gas-solid CFB riser such as the bottom dense region and the "core-annulus" radial distribution of the solids can be attributed to the existence of clusters. The clustering phenomenon is of great importance in the operation of a gas-solids fluidized bed. On the one hand, the contacts between the gas and solids and the mass and heat transfers are hindered due to the clusters since the particles captured inside a cluster have less opportunities to contact with the gas phase. On the other hand, the existence of clusters on the contrast helps achieve a more throughput of the reaction products since more particles could be "preserved" in the CFB riser in forms of clusters.

Both the hydrodynamic effects and the cohesive effects can account for the formation of clusters in the gas-solid system (Cocco et al., 2010; Horio & Clift, 1992). With the help of the advanced experiment techniques, researchers are able to detect the clusters inside a CFB riser by many means such as the image processing through high-speed camera or a laser-sheet technique, and wavelet decomposition of the optical fiber probe data (Guenther & Breault, 2007; Horio & Kuroki, 1994; Li, et al., 1991). The size, density (solids holdup), shape or duration time of the clusters are identified under different operating conditions (Cahyadi et al., 2017; Mondal, et al., 2016; Yang & Zhu, 2014). However, for a long time until now, the characteristics of the clusters vary in a wide range due to the different identification and detection methods. The size of the clusters could vary in two orders-of-magnitude from a millimeter scale to a centimeter scale as shown in Figure 2-13 (Cahyadi et al., 2017). Even the axial and the radial trends of the cluster size could not find a unified description form different experiments results as shown in Figure 2-13. Similar variations are also found in the voidage of the clusters as shown in Figure 2-14. Factors such as the superficial gas velocity, the solids circulation rate and the properties of particles all have big impacts on the size and voidage distributions of the particle clusters.
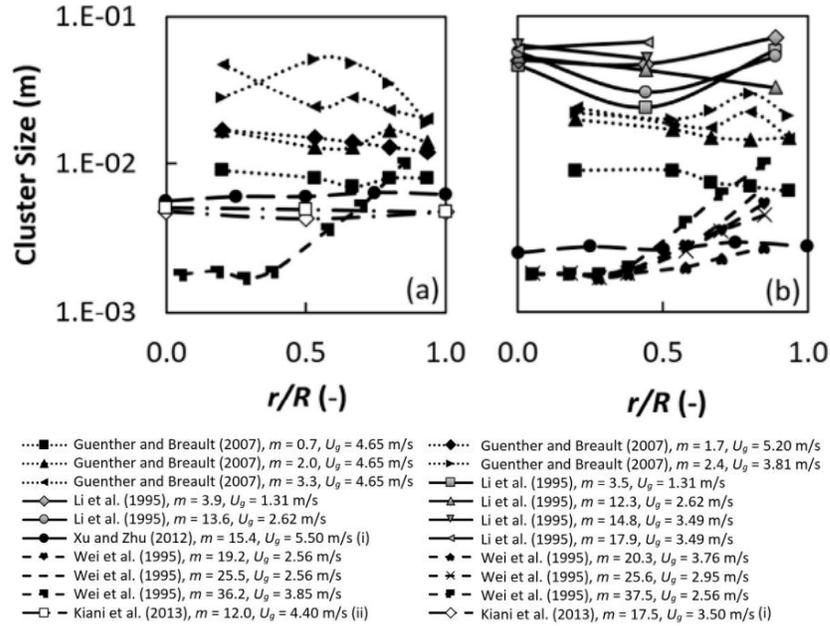
Figure 2-13 Radial trends of cluster size at (a) h/H≈0.2-0.3, (b) h/H≈0.5-0.6.

(Cahyadi et al., 2017)
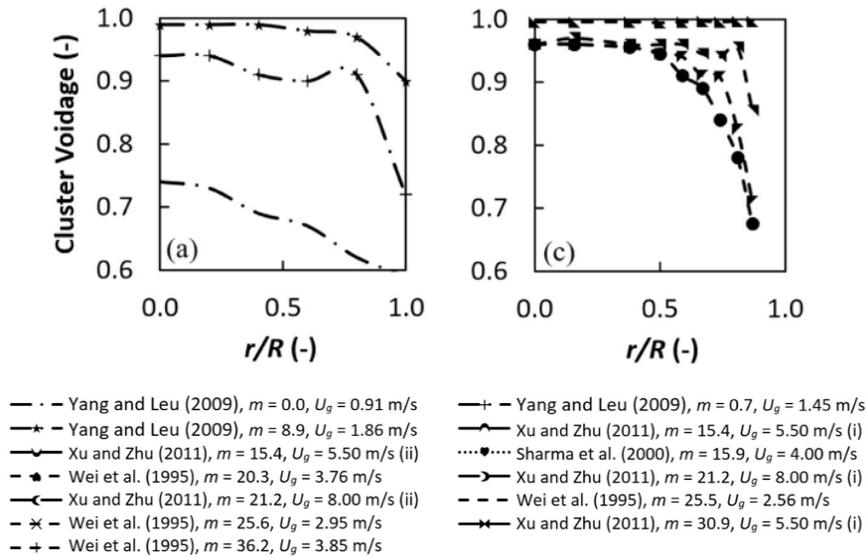
Figure 2-14 Radial trends of cluster voidage at (a) h/H≈0.1, (b) h/H≈0.6-0.7.

(Cahyadi et al., 2017)

With the help of both the image processing of the high-speed video and wavelet analysis of the optical fiber probe data, two types of the clusters are classified: The "core" clusters in which particles are tightly packed and the "cluster of clusters" which consists of a series

of core clusters (Xu & Zhu, 2012; Yang & Zhu, 2015). The "core" clusters can be considered as stably existed with constant size and shape while ring up in the gas-solid CFB riser. The "cluster of clusters" mainly stands for the loosely aligned "core" clusters with changeable shapes and sizes in the CFB riser. Statistical data through image processing and wavelet decomposition on the size, density, and distributions of the "core" clusters under various operating conditions in a gas-solid CFB system can be obtained (Wei, 2019).

2.6 Numerical treatments on clustering phenomenon in GSCFB riser

Hydrodynamic studies by experiments reveal many details of the gas-solid flow inside a CFB and therefore give rise to the fast development of computational fluid dynamic (CFD) models of CFBs (Sinclair & Jackson, 1989; Ding & Gidaspow, 1990; Tsuo & Gidaspow, 1990; Benyahia, et al., 2000; Deen, 2007; Hartge, et al., 2009; Wang, et al., 2010). However, the CFD models have suffered a lot of obstacles to predict the multiphase flow mechanisms at the very beginning and the agreement between experimental work and numerical results has not been fully achieved due to the inaccurate prediction on the non-uniform flow structures in the CFBs (Agrawal, et al, 2001; Ibsen, et al.,2004; Helland, et al.,2007). With the help of the innovative experimental techniques, the clustering phenomenon has been observed and carefully investigated since the 1990s (Horio & Clift, 1992; Li, et al., 1991; Zou, et al., 1994). Modelling people also take the clustering phenomenon into account when refining the numerical models.
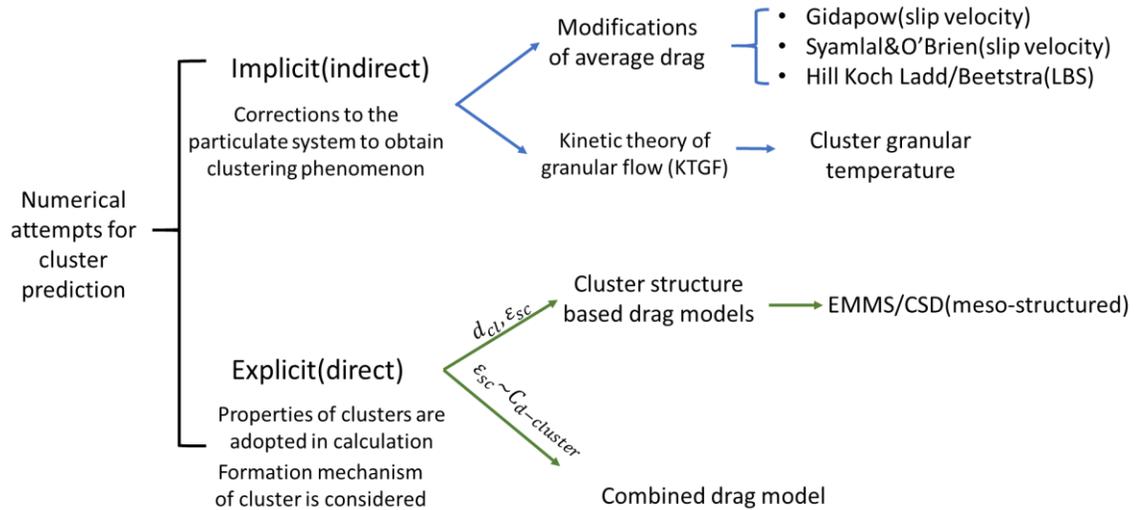
Figure 2-15: An overview of numerical attempts for cluster prediction

The dynamic nature and unclear physics of clusters in a CFB riser give rise to a variety of modified CFD models taking clusters into account based on different understandings of the clustering phenomenon. Both the EL and EE methods treat the fluid-particle interactions by the calculation of the drag force. Modifications to the drag models are made to differ the cluster behavior from single particles (Lu et al., 2014). Also in EE approach, the granular temperature model sometimes were also modified to include a cluster's granular temperature (Ding & Gidaspow, 1990; Benyahia et al., 2000). The current CFD models can be classified based on how the features of clusters are implemented in the simulations as shown in Figure 2-15: one is the explicit way that modifies the CFD models by adding the formation mechanism of clusters numerically, the other one is the implicit way that only modifies the properties of the mean flow by experimental work of clusters aiming to obtain more accurate results (Crowe, et al.,2011; Deen, et al.,2007; Tsuji et al., 1998; 2008; Helland et al, 2000; 2005; 2007; Wassen et al., 2001; Zhou et al., 2002; Ibsen et al., 2004; Shuyan et al., 2005; Zou et al., 2008; Liu and Lu, 2009; Mehrabadi et al., 2016; Carlos Varas et al., 2017).

2.6.1 Implicit ways of drag model modifications

The implicit way takes the ideal particulate system as the benchmark and makes corrections to the numerical equations to present the clustering phenomenon indirectly. The effects of

clusters are added into the modifications on the macro-scale level so that it seems like a correction of the overall gas-solid system but no particular properties of clusters such as the cluster size, cluster velocity, and cluster density are used. Because of the lack of the experimental conclusion of the clusters, modelling people have to add a correction factor into the calculation of the uniform particulate system based on their own understanding of the formation mechanism of clusters. These correction factors are usually some empirical correlations to solve the discrepancy between the realistic system and the ideal particulate system. Many traditional drag modifications dealing with the correction on the particle slip velocity can be categorized into this group. And the modifications on particle granular temperature are also considered as implicit ways because none of the cluster properties are used in the correction.

The averaged drag force of the gas-solid system can be presented as following:

$$\beta = \frac{3}{4} C_{Ds} \frac{\rho_g \alpha_s \alpha_g |v_g - v_s|}{d_p} \alpha_g^{-n} \tag{2-3}$$

where C_{Ds} is the drag coefficient, ρ_g is the gas density, α_s and α_g are the volume fraction of the solids phase and gas phase respectively, v_g and v_s are the gas and particle velocities respectively, and d_p is the particle diameter. The value of C_{Ds} is different from the drag coefficient of a single particle due to the existence of clusters. Corrections to the drag coefficient imply the different understandings of the clustering effects on the uniformity of the multiphase flow. Three types of the modifications on the drag models are concluded as following:

(1) Drag modifications from Ergun equation

If the pressure drop difference is considered as the main consequence from the clusters, the correlation of pressure drop will be applied to correct the drag coefficient. For example, Gidaspow (1990) combined the Ergun equation and Wen and Yu correlation to calculate the overall drag in a gas-solid system.

(2) Drag modifications from R-Z equation

The slip velocity is also considered as the main difference between homogeneous particulate system and the non-uniform system. More residence is for gas when penetrating a denser suspension of particles so that the terminal velocity of particles changes with the voidage as the Richardson-Zaki correlation (Richardson and Zaki, 1954) shows. Syamlal and O'Brien (1994) and Gibilaro et al. (1985) have correlated the multiparticle drag coefficient as functions of particle terminal velocity and voidage inspired by the RZ equation. The concept of the relative velocity is introduced which expresses the ratio of the terminal settling velocity of a multiparticle system to that of an isolated particle as a function of the void fraction:

$$v_r = \alpha_g^{n-1} \qquad \text{(2-4)}$$

The correlated drag coefficient is not only a function of Reynolds number and voidage, but also depends on the relative velocity which accounts for the effects of slip velocity.

(3) The Lattice-Boltzmann method (LBM)

Lattice-Boltzmann method (LBM) is adopted by Hill et al. (2001) to calculate the exact drag in the gas-solid flow. Particles are fixed and randomly dispersed in the system and a range of Reynolds numbers (Re) and solids volume fraction, ϕ, are selected to calculate the drag force exerted by the surrounding fluid (Benyahia et al., 2006). Precisely fitting equations of the dimensionless drag factor, F, are derived from the LBM and the drag coefficient C_{Ds} is a function of F as Eq (2-6) shows:

$$C_{Ds} = 12 \frac{\alpha_g^2}{Re_r} F \qquad \text{(2-5)}$$

Generally, the modified drag models are in good agreement with the experimental findings for the upper dilute region of the riser of CFBs. However, in most cases, the simulations fail to describe the lower part of the riser.

By examining Eq (2-4) again, the implicit corrections to the drag usually focus on the drag coefficient, C_{Ds}, and the voidage function, α_g^{-n}. The non-uniformity of the gas-solid flow is concluded into these two terms because in the early time researchers attributed the effects

of clusters to the concentration difference based on macro-scale level. So the C_{Ds} and α_g^{-n} are widely studied to correct the deviation of the macro-scale profiles of velocity and volume fractions from the particulate system. However, these corrections haven't separate the properties of clusters from single particles, which is a big limitation of these drag models.

2.6.2 Explicit ways of drag model modifications

Unlike the implicit way, the explicit way intends to adopt the characteristics of clusters into calculation directly and present the numerical generation of clusters by calculations, such as the mesoscale structure drag models and the combined drag model (Harris, 2002; Cahyadi, et al., 2017).

Clusters are considered as a mesoscale structured particle clouds and the gas flow can hardly penetrate a cluster. Unlike the averaged drag models, concepts such as cluster diameter, d_{cl}, cluster density, α_{sc}, are introduced into the drag calculations and the drag force of the system is the sum of single particles and dense suspensions which mainly denotes to the clusters.

This type of drag models divides the gas-solid flow inside a CFB riser into a dense phase which contains clusters and a dilute phase which only has single particles in it. Li et al. (1999) came up with the concept that the interactions between the gas and solids have three scales: micro-scale which denotes for individual single particles, mesoscale which represents the cluster size with the interactions between the dilute and dense phases, and macro-scale which is the global gas-solid suspension system. The behavior of particles is complex due to the multi-scale of gas-solid interactions. Eight parameters are used to describe this multi-scale flow structure as shown in Figure 2-16. Clusters are detected when the energy dissipation by the overall drag is minimum which means the desirable clusters only occur at the steady state of the whole system. Two commonly used mesostructured drag models are developed from this theory: the energy minimization multiscale model (EMMS) (Li, et al., 1999) and the cluster structure dependent model (CSD) (Lu, et al., 2005).

Dense phase: $U_{pc}, U_c, \varepsilon_c, f, d_{cl}$ **+** $U_f, U_{pf}, \varepsilon_f$ **for** **Dilute phase = 8 variables**

Micro-scale

slip velocity between particle and fluid in dense cluster:

$$U_{sc} = U_c - \frac{U_{pc}\varepsilon_c}{1-\varepsilon_c}$$

Meso-scale

slip velocity between dilute broth and dense cluster:

$$U_{si} = \left(U_f - \frac{U_{pc}\varepsilon_f}{1-\varepsilon_c} \right)(1-f)$$

Micro-scale

slip velocity between particle and fluid in dilute broth:

$$U_{sf} = U_f - \frac{U_{pf}\varepsilon_f}{1-\varepsilon_f}$$

Macro-scale

Global average slip velocity within equipment boundaries:

$$U_s = U_g - \frac{U_p\varepsilon}{1-\varepsilon}$$

$$U_g \qquad U_p = \frac{G_s}{\rho_p}$$

Figure 2-16: Eight parameters and three scales of interaction in heterogeneous flow structure of CFB. (Li et al., 1999)

Yang et al. (2003) further developed the EMMS model coupled in the two-fluid approach to calculate the drag coefficient from structure parameters and later the EMMS model is adopted in EL models. Li, et al. (2011) developed their own drag models based on the EMMS model and the local particle force balance was revised by introducing particle acceleration. Wang, et al. (2008) employed a revised EMMS model in Eulerian approach and predicted the cluster size as a function of solids concentration and the mean solids holdup plus 2 times of its standard deviation is selected to define the concentration inside a cluster which has a good agreement with the correlations by Zou et al. (2008). The EMMS model and CSD model define the diameter of clusters to be infinite at minimum fluidization which is still questionable and some uncertainties about the accuracy of EMMS models to predict the cluster size and porosity remain (Chen et al., 2016). Some assumptions remain

unclear and unconvinced and are questioned by many researchers, for example, the EMMS model assumed that the solids concentration in the clusters is close to the maximum packing and the particles are homogeneously dispersed in a cluster which is unrealistic (Helland, et al., 2007; Hartge, et al., 2009; Goldschmid,t et al., 2004).

Helland et al. developed a combined drag model calculating the drag of dilute clusters (lp/dp>2) and dense clusters (lp/dp<2) respectively. Two combined drag models taking the clustering effects into account are examined with experimental results and a solid concentration value (0.9, 0.95) is set as a switch from a dilute cluster to a dense cluster. The U-shaped clusters are recognized and cluster rising velocity is compared with the experimental data from Van Den Moortel and the same trends are achieved but the quantitive agreement is unsatisfied (Helland, et al., 2000a; Helland, et al., 2005).

Zou et al. proposed a new cluster-based drag model based on DSMC method which calculates the Reynolds number of clusters from an equivalent diameter of clusters correlated by Xu and Kato (1999):

$$d_{cl} = d_p \frac{A\rho_p}{\rho_{sus}} \tag{2-6}$$

where A is a correction parameter and ρ_{sus} is the suspension density of clusters both derived from the EMMS model. They correlated the cluster diameter and cluster drag coefficient with the local solid concentration in a CFB riser. The improvement of the cluster-based drag model is obvious when comparing with the traditional drag model but the agreement with the experimental data is not very good.

Noymer et al. (2000) proposed a drag model which neglects the particle-wall interactions and only considers the descent velocity of clusters and the drag is calculated based on the flow passing through and around the clusters. Although a good agreement of cluster velocity between simulation and experiments is obtained, many details are lost due to too many simplifications are used and none of the CFD models uses this simplified drag model until now.

Table 2-1 EE models for cluster prediction

Models by EE approach	Height, m	Width, m	d_p, m	Density, kg/m³	U_g, m/s	Drag model	Identification/Detection
Gidaspow&Tsuo, 1990	5.5	0.0762	5.20E-04	2620	4.9	Gidaspow	NA
S. BENYAHIA et al., 2001	14.2	0.2	7.60E-05	1712	5.2	Arastoopour	Arastoopour et al. (1990)
N. Yang et al., 2003	10.5	0.09	5.40E-05	930	1.52	EMMS	EMMS
L. Cabezas-Go'mez et al.,2003	5.5	0.076	5.20E-04	2620	5		Sharma et al., (2000)
C.H. Ibsen et al., 2004	1	0.032	1.64E-04	2400	1	Gidaspow	
L. Huilin et al., 2005	10	0.076	6.70E-05	1500	8	CSD	CSD
L. Cabezas-Go'mez et al., 2008	5.5	0.0762	5.20E-04	2620	5	Gidaspow	Sharma et al.
J. Wang et al.,2008	10.5	0.09	5.40E-04	930	1.52	EMMS	EMMS/Sharma et al. (2000) and Liu (2005)
	16.5	0.3	1.80E-04	1420	3.22, 4.78		EMMS
	7.2	0.09	1.00E-04	2560	4		EMMS
W. Shuai et al., 2012	10	0.076	6.70E-05	1500	3.5	modified CSD	equivalent cluster diameter (Gu&Chen,1998)
C. Chen et al.,2016	10.5	0.09	5.40E-05	930	1.52	QL-EMMS	QL-EMMS
S. Wang et al., 2016	8.5	0.4	3.00E-04	2500	7.76	CSD	CSD

Table 2-2: EL models for cluster prediction

Models by EL approach	Height/ Width/ Depth, m	d_p,m	Density, kg/m³	U_g, m/s	Number of particles	Drag model	Identification/Detection
Y. Tsuji et al., 1998	4 0.0762	5.20E-04	2620	4,5,6			porosity function, n=2.7
E. Helland et al, 2000	1 0.1	1.26E-04	2400	1	250000	Schiller and Naumann	porosity function, n=4.7
E. Wassen et al., 2001	0.8 0.03	1.00E-04	2620	25.5		Morsi and Alexander (1972)	particle to gas mass loading ratios n>5
H. Zhou et al., 2002	0.38 0.07	7E-04/ 1.2E-03	2650/1350	6.5/7.2	>7000	Wen&Yu	porosity function, n=4.7 ,2.3
C.H. Ibsen et al., 2004	1 0.032	1.64E-04	2400	1	40500	Schiller and Naumann	potosity function, n=4.7
W. Shuyan et al., 2005	1 0.08	1.00E-03	1700	4.9	1000000	Schiller and Naumann with porosity function	Soong et al, 1995
E. Helland et al., 2005	0.5 0.05	1.33E-04	2400	1	7.2E+04	combined drag model	Sharma et al., (2000)
E. Helland et al., 2007	2 0.2	1.26E-04	2400	0.9/1.1		combined drag model	

L.M. Zou et al., 2008	3 0.15	7.40E-05	1770	4		Cluster-based drag coefficient model	hydrodynamic equivalent cluster diameter by Xu and Kato (1999)
T. Tsuji et al.,2008	periodic,0.128 0.256 0.256	1.28E-04	2470		16,127,388	Schiller and Nauman	SVF spectrums wave number
H. Liu, H. Lu, 2009	1 0.08	1.26E-04	2600	1.5		Schiller and Naumann with porosity function	Sharma et al.
T. Wang et al.,2015	0.3 0.032 0.0012	1.2e-04/1.85e-04	2400	1	201,000	Beetstra et al./Gidaspow	Cluster granular temp.
M. Mehrabadi et al., 2016	L/Dp=10				191/515/668	drag comparison	Cocco et al.(2010)
A.E.Carlos Varas et al., 2017	1.57 0.07 0.0006	8.50E-04	2500	5.55-6.74		N/A	dense core>0.4, local solids holdup>0.2

Table 2-1 and Table 2-2 list out the CFD models regarding the clustering phenomenon either by the EE or EL approach. The particles selected in EL models are larger than the ones in EE approach and superficial gas velocity in EL method is also relatively lower which means the solid suspension in EL models are usually denser. Since the cluster properties vary from the operating conditions, particle properties, and equipment size, the cluster behavior in large scale and high-density CFBs by EL simulations are still lacking. Whilst, the EE models take many attempts on large equipment and smaller particles because they are less restricted by the computational energy. But most of the modifications in EE approach are implicit and the validation is still questionable.

Many correlations of cluster size and velocity have been claimed by different CFD models but the detection methods of clusters used in the calculation vary from different criteria so the comparability and the consistency of the correlations of cluster size, velocity, shape, and concentration remain further validations.

2.7 Conclusions

For gas-solid CFB systems, the flow structures and the flow developments differ a lot between high-density operation and low-density operation. The general flow structure in a GSCFB riser is less uniform than that in the GSCFB downer. Both the superficial gas

velocity and solids circulation rate have significant impacts on the transition from dilute condition to dense condition. CFD approach can provide more details when comparing the high-density and low-density operations in the GSCFB riser and downer.

Two new types of the fluidized beds, the inverse liquid-solid CFB and the bubble induced fluidized bed were experimentally studied. Uniform flow structures are found in these two fluidized bed systems. However, less information on the detailed hydrodynamics in these two new fluidized beds is provided by experimental studies. Currently, numerical studies are lacking on these two new fluidized bed systems.

The clusters in the gas-solid CFB riser results in the non-uniform flow structure. The dynamic nature and unclear physics of clusters in a CFB riser give rise to a variety of CFD models taking clusters into account based on different understandings of the clustering phenomenon.

However, the fidelity of the models is still questionable. It seems that experimental works on particle clusters are an empirical process from macro-scale to micro-scale, and the identification of clusters in numerical calculations is usually a process from micro-scale to macro-scale to the contrary. The two opposite ways dealing with the cluster phenomenon by experiments and modelling also resulted in the discrepancy on cluster predictions between CFD and experiments.

Nomenclature

C_{Ds}	Drag coefficient of the gas-solid system
d_{cl}	Equivalent diameter of clusters, m
d_p	Particle diameter, m
G_s	Solids circulation rate, kg/m^{2}s
h/H	Relative axial position
k	Turbulent kinetic energy, m^2/s^2
r/R	Relative radial position

Re_r	Relative particle Reynolds number, $= \frac{\rho_g v_r d_p}{\mu_g}$
$\overrightarrow{u_{\iota,J}}$	Fluctuating velocity of the flow, m/s
U_g	Superficial gas velocity, m/s
$U_{i,j}$	Mean velocity of the flow, m/s
U_l	Superficial liquid velocity, m/s
U_{mf}	Minimum fluidization velocity, m/s
U_{tr}	Transport superficial gas velocity to fast fluidization, m/s
v_g	Gas phase velocity, m/s
v_r (U_r)	Relative velocity: the ratio of the terminal settling velocity of a multiparticle system to that of an isolated particle
v_s	Solid phase velocity, m/s
$v'_{s\tau}$	Random component of the particle velocity, m/s
α_g	Gas phase volume fraction
α_s	Solid phase volume fraction
β	Momentum exchange coefficient
ε	Dissipation rate of the turbulent kinetic energy
ε_l	Liquid holdup in fluidized bed
ε_s	Solids holdup in fluidized bed
ρ_g	Gas density, kg/m^3
ρ_p	Particle density, kg/m^3
ρ_{sus}	Suspension density of clusters in EMMS model, kg/m^3
Θ	Granular temperature of particles, m^2/s^2
ω	Specific rate of dissipation turbulent kinetic energy

References

Agrawal, Loezos, Syamlal & Sundaresan (2001). The role of meso-scale structures in rapid gas–solid flows. Journal of Fluid Mechanics, 445, 151-185.

Baharanchi, Ahmadreza Abbasi, Seckin Gokaltun, and George Dulikravich. Performance improvement of existing drag models in two-fluid modeling of gas–solid flows using a PR-DNS based drag model. Powder Technology 286 (2015): 257-268.

Beetstra, Van der Hoef, and Kuipers. Drag force of intermediate Reynolds number flow past mono- and bidisperse arrays of spheres. AIChE Journal 53.2 (2007): 489-501.

Benyahia, Arastoopour, Knowlton, & Massah. (2000). Simulation of particles and gas flow behavior in the riser section of a circulating fluidized bed using the kinetic theory approach for the particulate phase. Powder Technology, 112(1–2), 24–33.

Benyahia, Arastoopour, and Knowlton. (2002). Two-dimensional transient numerical simulation of solids and gas flow in the riser section of a circulating fluidized bed. Chemical Engineering Communications 189.4: 510-527.

Benyahia, Sofiane, Madhava Syamlal, and O'Brien. (2006). Extension of Hill-Koch-Ladd drag correlation over all ranges of Reynolds number and solids volume fraction. Powder Technology 162.2: 166-174.

Bi & Grace (1995). Flow regime diagrams for gas-solid fluidization and upward transport. International Journal of Multiphase Flow, 21(6), 1229–1236.

Bolio, Yasuna & Sinclair (1995). Dilute turbulent gas-solid flow in risers with particle-particle interactions. AIChE Journal, 41(6), 1375–1388.

Breault, Ronald, Ludlow & Yue. (2005). Cluster particle number and granular temperature for cork particles at the wall in the riser of a CFB. Powder Technology 149.2: 68-77.

Cabezas-Gomez, da Silva, Navarro & Milioli (2008). Cluster identification and characterization in the riser of a circulating fluidized bed from numerical simulation results. Applied Mathematical Modelling, 32(3), 327-340.

Cahyadi, Anantharaman, Yang, Karri, Findlay, Cocco, & Chew (2017). Review of cluster characteristics in circulating fluidized bed (CFB) risers. Chemical Engineering Science, 158, 70–95.

Carlos Varas, Peters & Kuipers (2017). CFD-DEM simulations and experimental validation of clustering phenomena and riser hydrodynamics. Chemical Engineering Science, 169, 246–258.

Chapman. & Cowling (1970). The Mathematical Theory of Non-Uniform Gases, 3rd edn. Cambridge University Press.

Chen, Cheng, Dai & Qi. (2016). Improvement of EMMS drag model for heterogeneous gas–solid flows based on cluster modeling. Chemical Engineering Science 141: 8-16.

Cocco, Shaffer, Hays, Reddy Karri & Knowlton (2010). Particle clusters in and above fluidized beds. Powder Technology, 203(1), 3–11.

Schwarzkopf, Sommerfeld, Crowe & Tsuji (2011). Multiphase flows with droplets and particles. CRC press.

Deen, van Sint Annaland, van der Hoef & Kuipers (2007). Review of discrete particle modeling of fluidized beds. Chemical Engineering Science, 62, 28–44.

Ding and Gidaspow. (1990). A bubbling fluidization model using kinetic theory of granular flow. AIChE journal 36.4: 523-538.

Dong, Yang, Zou & Yu (2006). Role of interparticle forces in the formation of random loose packing. Physical review letters, 96(14), 145505.

Enwald, Hans, Peirano & Almstedt. (1996). Eulerian two-phase flow theory applied to fluidization. International Journal of Multiphase Flow 22: 21-66.

Muroyama & Fan. (1985). Fundamentals of gas-liquid-solid fluidization. AIChE J., 31: 1-34.

Fan, Muroyama & Chern (1982). Hydrodynamic characteristics of inverse fluidization in liquid-solid and gas-liquid-solid systems. The Chemical Engineering Journal, 24(2), 143–150.

Gibilaro, Di Felice, Waldram & Foscolo (1985). Generalized friction factor and drag coefficient correlations for fluid-particle interactions. Chemical Engineering Science, 40(10), 1817–1823.

Gidaspow (1994). One-dimensional steady gas-solid flow. Multiphase Flow and Fluidization, 31–60.

Gokaltun, Munroe & Subramaniam (2014). Development of a two-fluid drag law for clustered particles using direct numerical simulation and validation through experiments. Florida International University, Miami, FL (United States).

Goldschmidt, Beetstra & Kuipers. (2004). Hydrodynamic modelling of dense gas-fluidised beds: comparison and validation of 3D discrete particle and continuum models. Powder Technology 142.1: 23-47.

Cabeza & Milioli. (2003). Numerical study on the influence of various physical parameters over the gas–solid two-phase flow in the 2D riser of a circulating fluidized bed. Powder Technology 132.2: 216-225.

Grace (1990). High-velocity fluidized bed reactors. Chemical Engineering Science, 45(8), 1953–1966.

Guenther & Breault (2007). Wavelet analysis to characterize cluster dynamics in a circulating fluidized bed. Powder Technology, 173(3), 163–173.

Harris, Davidson & Thorpe. (2002). The prediction of particle cluster properties in the near wall region of a vertical riser. Powder Technology 127.2: 128-143.

Hartge, Ratschow, Wischnewski, & Werther (2009). CFD-simulation of a circulating fluidized bed riser. Particuology, 7(4), 283–296.

Hartge, Ernst-Ulrich, Wischnewski & Werther. (2009). CFD-simulation of a circulating fluidized bed riser. Particuology, no. 4: 283-296.

Helland, Bournot, Occelli & Tadrist (2007). Drag reduction and cluster formation in a circulating fluidised bed. Chemical Engineering Science, 62(1-2), 148-158.

Helland, Occelli & Tadrist (2005) Numerical study of cluster and particle rebound effects in a circulating fluidised bed. Chemical engineering science 60.1: 27-40.

Helland, Eivind, Occelli & Tadrist (2000) Numerical study of cluster formation in a gas–particle circulating fluidized bed. Powder Technology 110.3: 210-221.

Hoomans, Kuipers, Briels & Swaaij (1996). Discrete particle simulation of bubble and slug formation in a 2d gas-fluidised bed: a hard-sphere approach. Science, 51(1), 99–118.

Horio & Clift (1992). A note on terminology: 'clusters' and 'agglomerates.' Powder Technology, 70(3), 196.

Horio & Kuroki (1994). Three-dimensional flow visualization of dilutely dispersed solids in bubbling and circulating fluidized beds. Chemical Engineering Science, 49(15), 2413–2421.

Horio, Ishii & Nishimuro (1992). On the nature of turbulent and fast fluidized beds. Powder Technology, 70(3), 229–236.

Hosseini, Hossein, Ahmadi & Olazar. (2013). CFD simulation of cylindrical spouted beds by the kinetic theory of granular flow. Powder Technology 246: 303-316.

Huilin, Qiaoqun, Yurong, Yongli, Ding & Xiang (2005). Numerical study of particle cluster flow in risers with cluster-based approach. Chemical Engineering Science, 60(23), 6757-6767.

Ibsen, Helland, Hjertager, Solberg, Tadrist & Occelli (2004). Comparison of multifluid and discrete particle modelling in numerical predictions of gas particle flow in circulating fluidised beds. Powder Technology, 149(1), 29-41.

Ishii & Horio (1991). The flow structures of a circulating fluidized bed. Advanced Powder Technology, 2(1), 25–36.

Karamanev & Nikolov (1992), Bed expansion of liquid-solid inverse fluidization. AIChE J., 38: 1916-1922.

Kohyama & Tamotsu. Cluster growth in particle-conserving cellular automata. Journal of statistical physics 63.3-4 (1991): 637-651.

Li, Chen, Wang & Qi (2011). QL-EMMS drag model & its revision for fluidized dense gas-solid two-phase flow. Journal of Engineering Thermophysics, 1.

Li, Xia, Tung & Kwauk (1991). Micro-visualization of clusters in a fast fluidized bed. Powder Technology, 66(3), 231–235.

Li, Cheng, Zhang, Yuan, Nemet, & Fett (2002). The EMMS model — its application, development and updated concepts. Chemical Engineering Science, 54(22), 5409–5425.

Li, Dietiker & Shahnam (2012). MFIX simulation of NETL/PSRI challenge problem of circulating fluidized bed. Chemical engineering science, 84, 746-760.

Liu & Lu. (2009) Numerical study on the cluster flow behavior in the riser of circulating fluidized beds. Chemical Engineering Journal 150.2: 374-384.

Liu & Xu. (2009) Modelling of dense gas-particle flow in a circulating fluidized bed by distinct cluster method (DCM). Powder Technology 195.3: 235-244.

Lu, Xu, Ge, Yue, Liu & Li (2014). EMMS-based discrete particle method (EMMS–DPM) for simulation of gas–solid flows. Chemical Engineering Science, 120, 67-87.

Lundberg, Joachim & Halvorsen. (2008). A review of some exsisting drag models describing the interaction between phases in a bubbling fluidized bed. In Proc. 49th Scand. Conf. Simulation and Modeling, Oslo University College, Oslo, Norway, pp. 7-8.

Mehrabadi, Mohammad, Murphy & Subramaniam. (2016). Development of a gas–solid drag law for clustered particles using particle-resolved direct numerical simulation. Chemical Engineering Science 152: 199-212.

Mondal, Kallio, Saxén & Hassel (2016). Experimental study of cluster properties in a two-dimensional fluidized bed of Geldart B particles. Powder Technology, 291, 420–436.

Moran, James & Glicksman. (2003). Experimental and numerical studies on the gas flow surrounding a single cluster applied to a circulating fluidized bed. Chemical Engineering Science 58.9: 1879-1886.

Niven & Robert (2000). Physical insight into the Ergun and Wen & Yu equations for fluid flow in packed and fluidised beds. Chemical Engineering Science 57.3: 527-534.

Noymer, Peter & Glicksman. (2000). Descent velocities of particle clusters at the wall of a circulating fluidized bed. Chemical engineering science 55.22: 5283-5289.

Reh (1995). New and efficient high-temperature processes with circulating fluid bed reactors. Chemical Engineering & Technology, 18(2), 75‑89.

Renganathan & Krishnaiah (2004). Liquid phase mixing in 2-phase liquid–solid inverse fluidized bed. Chemical Engineering Journal, 98(3), 213–218.

Renganathan & Krishnaiah (2005). Voidage characteristics and prediction of bed expansion in liquid–solid inverse fluidized bed. Chemical Engineering Science, 60(10), 2545–2555.

Richardson & Zaki (1954). Fluidization and sedimentation–Part I. Trans. Inst. Chem. Eng., 32, 38

Sang (2013). Particle fluidization in upward and inverse liquid-solid circulating fluidized bed. Ph. D thesis. University of Western Ontario.

Sinclair & Jackson (1989). Gas-particle flow in a vertical pipe with particle-particle interactions. AIChE Journal, 35(9), 1473–1486.

Soong, Tuzla & Chen. (1995). Experimental determination of cluster size and velocity in circulating fluidized bed. Fluidization VIII, Engineering Foundation, New York: 219-227.

Sun (2017). Bubble-induced inverse gas-liquid-solid fluidized bed. M.Sc thesis, University of Western Ontario.

Sundaresan & Sankaran. (2013). Role of hydrodynamics on chemical reactor performance. Current Opinion in Chemical Engineering 2.3: 325-330.

Syamlal & O'Brien (1987). The derivation of a drag coefficient formula from velocity-voidage correlations. Technical Note, US Department of energy, Office of Fossil Energy, NETL, Morgantown, WV.

Tsuji, Takuya, Ito & Tanaka. (2008). Multi-scale structure of clustering particles. Powder Technology 179.3: 115-125.

Tsuji, Kawagucchi & Tanaka (1993). Discrete particle simulation of a fluidized bed. Powder Technology, 77(1), 79-87.

Tsuji, Morikawa, & Shiomi, (1984). LDV measurements of an air-solid two-phase flow in a vertical pipe. Journal of Fluid Mechanics, 139, 417-434.

Tsuji, Tanaka & Yonemura. (1998). Cluster patterns in circulating fluidized beds predicted by numerical simulation (discrete particle model versus two-fluid model). Powder Technology 95.3: 254-264.

Tsuji, Yutaka, Tanaka & Ishida. (1992). Lagrangian numerical simulation of plug flow of cohesionless particles in a horizontal pipe. Powder technology 71.3: 239-250.

Tsuo & Gidaspow (1990). Computation of flow patterns in circulating fluidized beds. AIChE Journal, 36(6), 885-896.

Van Wachem, Schouten, JVan den Bleek, Krishna & Sinclair (2001). Comparative analysis of CFD models of dense gas-solid systems. AIChE Journal, 47(5), 1035-1051.

Lakshmi, Balamurugan, Sivakumar, Samuel & Velan (2000). Minimum fluidization velocity and friction factor in a liquid-solid inverse fluidized bed reactor. Bioprocess Engineering, 22(5), 461–466.

Wang, Liu, Lu, Xu, Yang & Gidaspow (2012). A cluster structure-dependent drag coefficient model applied to risers. Powder technology, 225, 176-189.

Wang, Liu, Lu, Liu, Ding & Li. (2005). Flow behavior of clusters in a riser simulated by direct simulation Monte Carlo method. Chemical Engineering Journal, 106(3), 197-211.

Wang, Zhu, Barghi & Li (2014a). Axial and radial development of solids holdup in a high flux/density gas-solids circulating fluidized bed. Chemical Engineering Science, 108, 233–243.

Wang, Zhu, Li & Barghi (2014b). Detailed measurements of particle velocity and solids flux in a high density circulating fluidized bed riser. Chemical Engineering Science, 114, 9-20.

Wang, Li & Zhu (2015). Axial solids flow structure in a high density gas–solids circulating fluidized bed downer. Powder Technology, 272, 153–164.

Wang, Zhu, Lan, Gao & Barghi (2016). Radial solids flow structure in high flux gas-solids circulating fluidized bed downers. Powder Technology, 301, 848–857.

Wang, Ge & Li (2008). Eulerian simulation of heterogeneous gas–solid flows in CFB risers: EMMS-based sub-grid scale model with a revised cluster description. Chemical Engineering Science 63.6: 1553-1571.

Wang, Wang, Chen, Liu, Lu & Sun (2016). Extension of cluster-structure dependent drag model to simulation of riser with Geldart B particles. Advanced Powder Technology 27.1: 57-63.

Wang, Yang, Lu, Yu, Wang & Ding (2009). CFD studies on mass transfer of gas-to-particle cluster in a circulating fluidized bed. Computers & Chemical Engineering 33.2: 393-401.

Wang, He, Yan, Tang & Schlabergb. (2015). Cluster granular temperature and rotational characteristic analysis of a binary mixture of particles in a gas-solid riser by mutative Smagorinsky constant SGS model. Powder Technology 286: 73-83.

Wang, Wei, Lu, Zhang, Shi & Li. (2010). A review of multiscale CFD for gas-solid CFB modeling. International Journal of Multiphase Flow 36.2: 109-118.

Wassen & Frank. (2001). Simulation of cluster formation in gas–solid flow induced by particle–particle collisions. International Journal of Multiphase Flow 27.3: 437-458.

Wei (2019). Experimental Investigations on the Instantaneous Flow Structure in Circulating Fluidized Beds. Ph.D. thesis. University of Western Ontario.

Xu & Zhu (2012). A new method for the determination of cluster velocity and size in a circulating fluidized bed. Industrial & Engineering Chemistry Research, 51(4), 2143-2151.

Xu, Ying & Subramaniam. (2010). Effect of particle clusters on carrier flow turbulence: A direct numerical simulation study. Flow, Turbulence and Combustion 85.3: 735-761.

Yang & Zhu (2014). A novel method based on image processing to visualize clusters in a rectangular circulating fluidized bed riser. Powder Technology, 254, 407-415.

Yang & Zhu (2015). Cluster identification using image processing. Particuology, 23, 16-24.

Yang, Wang, Ge & Li (2003). CFD simulation of concurrent-up gas–solid flow in circulating fluidized beds with structure-dependent drag coefficient. Chemical Engineering Journal, 96(1-3), 71-80.

Yerushalmi & Cankurt (1979). Further studies of the regimes of fluidization. Powder Technology, 24(2), 187–205.

Yerushalmi, Turner & Squires (1976). The fast fluidized bed. Industrial and Engineering Chemistry Process Design and Development, 15(1), 47–53.

Zhang, Huang & Zhu (2001). Gas-solids flow behavior: CFB riser vs. downer. AIChE Journal, 47(9), 2000–2011.

Zhang, Chu, Wei & Yu. (2008). A CFD–DEM study of the cluster behavior in riser and downer reactors. Powder Technology, 184(2), 151-165.

Zhou, Flamant, Gauthie, & Lu. (2002). Lagrangian approach for simulating the gas-particle flow structure in a circulating fluidized bed riser. International journal of multiphase flow, 28(11), 1801-1821.

Zhu, Zhou, Yang & Yu (2007). Discrete particle simulation of particulate systems: theoretical developments. Chemical Engineering Science, 62(13), 3378-3396.

Zhu & Bi (1995). Distinctions between low density and high density circulating fluidized beds. He Canadian Journal of Chemical Engineering, 73(5), 644–649.

Zhu & Cheng (2005). Fluidized Bed Reactors and Applications. in Multiphase flow handbook (p. 5.55-5.93).

Zou, Guo & Chan. (2008). Cluster-based drag coefficient model for simulating gas-solid flow in a fast-fluidized bed. Chemical Engineering Science 63.4: 1052-1061.

Chapter 3

3 Numerical study of the effects of inlet boundary conditions on gas-solid flows in a circulating fluidized bed riser

3.1 Introduction

Fluidization is a process that static granular materials become flowable and behave like a liquid when a fluid is introduced into the column and passes through the packed solid particles. One application of fluidization is the gas-solid fluidized bed, which is commonly used in modern chemical processes like conveying particles, performing continuous reactions (Kunii & Levenspiel, 1969). By gradually increasing the gas flow rate, a conventional gas-solid fluidized bed goes through the following flow regimes: bubbling fluidization, slugging fluidization and turbulent fluidization (Grace, 1986). Further increasing the superficial gas velocity leads to the fast fluidization where the solids will be entrained out of the column once the gas velocity exceeds the terminal velocity of particles (Bi & Grace, 1995; Lim et al., 1995). If the entrained particles are collected and recycled back into the bed, a circulating fluidized bed reactor will be developed, which can handle the particles continuously. A typical circulating fluidized bed usually consists of two parts: the riser where chemical reactions take place and the downer where particles are recycled to the riser (Grace & Bi, 1997; Berruti, 1995; Zhang et al., 2001).

The applications of circulating fluidized bed (CFB) reactors have widely spread out across the chemical industries since the 1940s including fluid catalytic cracking (FCC), biomass gasification and coal combustion due to its numerous benefits (Grace et al., 2003). Comparing with the conventional fluidized beds, CFB reactors can operate with higher gas velocities resulting in better gas and solids contacting efficiency, more intensive and uniform solids mixing and effective gas-solid mass and heat transfer (Wang et al., 2014; 2015). Comprehensive studies on the hydrodynamics inside a CFB riser by experiments can be dated back to the early 1940s. Axial profiles of solids concentration show that a typical CFB riser has a bottom-dense and upper-dilute profile which is known as the S-Shape profile (Wang et al., 2014; 2015). Other profiles like C-shape and exponential shape

mainly come from the effects of entrance and exit (Pugsley et al., 1997; Cheng, 1998). The radial profile of solids concentration is known as the core-annulus structure which describes a center dilute and dense layer of solids suspension near the wall. The dimension of the center uniform region of solids holdup also depends on the operating conditions (Wang et al., 2014; 2015; Huang et al., 2006; Qi, et al., 2003).

Recently, computational fluid dynamics (CFD) modeling has become an effective tool to investigate the hydrodynamics inside a CFB riser with the fast development of computer science and multiphase flow models (Wang et al., 2010; Hartge et al., 2009). The advantage of CFD modeling is that it allows observation of flow properties at locations which may not be accessible to (or harmful for) measuring instruments without disturbing the flow itself. Moreover, CFD can be used as a qualitative tool for narrowing down the choices between various designs. Designers and analysts can study prototypes numerically, and then test the designs by experiments only for those which show promise.

Various models have been implemented in CFD simulations to better understand the flow structure in the riser reactors since the 1980s (Ding & Gidaspow, 1990; Tsuo et al., 1990). Also, more specified inlet boundary conditions of both the gas and solids phases are needed since many researchers have observed the influences of the entrance and exit geometry of CFB risers by experiments (Grace, 1996; Cheng et al., 1998; Zhu & Zhu, 2008; Zhu et al., 2010). However, from the modeling aspect, the effects of the geometry of the entrance of a riser are rarely reported and only a few researchers pay attention to specifying a more realistic geometry structure and inlet boundary conditions (Li & Guenther, 2012). Uniform velocity inlet boundary conditions of both the gas and solids phases are often applied to the CFD models for easier convergence and faster solutions (De Wilde et al., 2005; Peng et al., 2011). Many studies have showed that the solids holdup distributions along the radial and axial directions of the risers depend on the geometric structure of the entrance (Breault et al., 2017; Cheng et al., 1998; Zhu & Zhu, 2008; Zhu et al., 2010). Therefore, a more realistic inlet boundary conditions based on the entrance structure of a CFB riser reactor is critical to obtain a more accurate gas-solid flow structure.

3.2 Configuration of the CFB riser
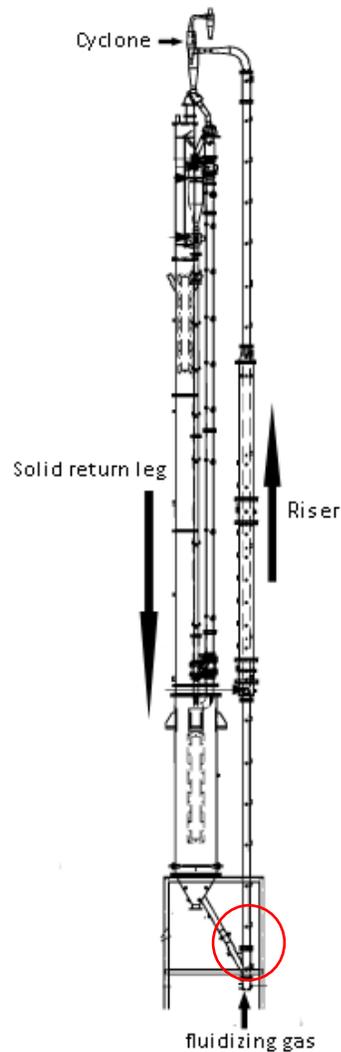
Figure 3-1 Configuration of the CFB riser (Li, 2010)
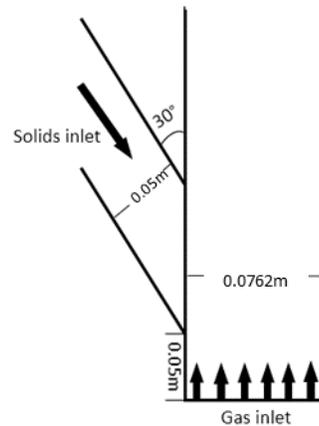
Figure 3-2 Geometric structure at the inlet of the riser
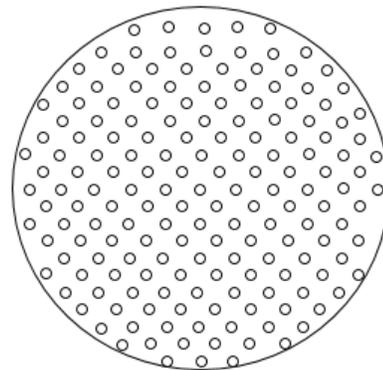
Figure 3-3 Gas distributor of the riser

Based on the hydrodynamic experiments from Li (2010), the circulating fluidized bed riser tested via CFD model is of 10 m high with a diameter of 7.62 cm (3in) as shown in Figure 3-1. Figure 3-2 shows a zoomed in schematic diagram of the red-circled part in Figure 3-1 of the geometric structure at the entrance region of the riser. During the operation, gas enters the riser through a perforated gas distributor as shown in Figure 3-3 from the bottom to provide better gas-solid mixing and avoid the defluidized zones. The distributor arranges

272 nozzles with a diameter of 2mm opening area of 18%, which helps form a uniform gas inlet distribution. The circulated particles return to the riser through the side pipe which connects the riser and the storage tank. This side feeding pipe is 5.08 mm (2 in) in diameter with an angle of 30° to the riser. During the operation, the air enters the riser from every nozzle of the gas distributor and accelerates the solids from the returning pipe with a high velocity.

3.3 CFD model descriptions

A set of basic governing equations consisting of the mass and momentum conservation equations of both phases are used to solve the gas-solid flows (ANASYS, 2013).

3.3.1 Governing equations

Continuity equation of gas phase:

$$\frac{\partial}{\partial t}(\alpha_g \rho_g) + \nabla \cdot (\alpha_g \rho_g \overrightarrow{v_g}) = 0 \tag{3-1}$$

where α_g is the volume fraction of gas phase, $\overrightarrow{v_g}$ is the velocity vector and ρ_g is the density of the gas phase.

Continuity equation of solids phase:

$$\frac{\partial}{\partial t}(\alpha_s \rho_s) + \nabla \cdot (\alpha_s \rho_s \overrightarrow{v_s}) = 0 \tag{3-2}$$

where $$\alpha_g + \alpha_s = 1 \tag{3-3}$$

and α_s is the volume fraction of solid phase, $\overrightarrow{v_s}$ is the velocity vector and ρ_s is the density of the solid phase.

Momentum equation of gas phase:

$$\frac{\partial}{\partial t}(\alpha_g \rho_g \overrightarrow{v_g}) + \nabla \cdot (\alpha_g \rho_g \overrightarrow{v_g} \overrightarrow{v_g}) = -\alpha_g \nabla P + \nabla \cdot \overline{\overline{\tau_g}} + \alpha_g \rho_g \vec{g} + K_{sg}(\overrightarrow{v_s} - \overrightarrow{v_g}) \tag{3-4}$$

where $\overline{\overline{\tau_g}}$ is the gas phase stress-strain tensor, P is the phase pressure.

$$\overline{\overline{\tau_g}} = \alpha_g \mu_g \left(\nabla \cdot \overrightarrow{v_g} + \nabla \cdot \overrightarrow{v_g}^T \right) + \alpha_g \left(\lambda_g - \frac{2}{3} \mu_g \right) \nabla \cdot \overrightarrow{v_g} \overline{\overline{I}} \qquad (3\text{-}5)$$

where $\overrightarrow{v_g}$ and $\overrightarrow{v_s}$ are the velocities of the gas phase and solid phase, μ_g and λ_g are the shear and the bulk viscosity of gas phase, and $K_{sg}(= K_{sg})$ is the interphase momentum exchange coefficient.

Momentum equation of solids phase:

$$\frac{\partial}{\partial t} (\alpha_s \rho_s \overrightarrow{v_s}) + \nabla \cdot (\alpha_s \rho_s \overrightarrow{v_s} \overrightarrow{v_s}) = -\alpha_s \nabla P - \nabla P_s + \nabla \cdot \overline{\overline{\tau_s}} + \alpha_s \rho_s \vec{g} + K_{sg} \left(\overrightarrow{v_g} - \overrightarrow{v_s} \right) \quad (3\text{-}6)$$

where $\overline{\overline{\tau_s}}$ is the solid phase stress-strain tensor

$$\overline{\overline{\tau_s}} = \alpha_s \mu_s \left(\nabla \cdot \overrightarrow{v_s} + \nabla \cdot \overrightarrow{v_s}^T \right) + \alpha_s \left(\lambda_s - \frac{2}{3} \mu_s \right) \nabla \cdot \overrightarrow{v_s} \overline{\overline{I}} \qquad (3\text{-}7)$$

To calculate the solid phase pressure, P_s, solids shear viscosity, μ_s, and bulk viscosity, λs in the solids phase momentum equation, the kinetic theory of granular flow is used (Sinclair and Jackson, 1989).

3.3.2 Granular temperature model

The granular temperature of solid phase associates with the kinetic energy of the random movements of the particles, which can be expressed as:

$$\Theta s = \frac{1}{3} v'_{s\tau} v'_{s\tau} \qquad (3\text{-}8)$$

where $v'_{s\tau}$ is the fluctuation velocity of particles which associates with the collisions between the particles.

Granular temperature equation (Ding & Gidaspow, 1990):

$$\frac{3}{2} \left[\frac{\partial}{\partial t} (\rho_s \alpha_s \Theta s) + \nabla \cdot (\alpha_s \rho_s \overrightarrow{v_s} \Theta s) \right] = \left(-P_s \overline{\overline{I}} + \overline{\overline{\tau_s}} \right) : \nabla \overrightarrow{v_s} + \nabla \cdot (k_{\Theta s} \nabla \Theta) - \gamma_{\Theta s} + \varnothing_{gs} \quad (3\text{-}9)$$

where $\left(-P_s\overline{\overline{I}} + \overline{\overline{\tau_s}}\right)$ is the generation of energy by the solid stress tensor, $k_{\Theta s}\nabla\Theta$ stands for the diffusion energy, $\gamma_{\Theta s}$ is the collisional dissipation of energy, and $\emptyset_{gs} = -3k_{gs}\Theta s$ is the energy exchange between the gas phase and the solid phase.

The collisional energy can be obtained by Lun et al. (1984):

$$\gamma_{\Theta s} = \frac{12(1-e_{ss}^2)g_{0,ss}}{d_p\sqrt{\pi}}\rho_s\alpha_s^2\Theta_s^{3/2} \tag{3-10}$$

where d_p is the particle diameter, e_{ss} is particle-particle restitution coefficient, $g_{o,ss}$ is the radial distribution function of particles.

3.3.3 Turbulence model

The gas-solid two-phase flows are very complicated due to the vigorous interactions between the gas and solids. The motions of the particles are affected by the mean solids velocity, single particle fluctuations and the particle-particle collisions. Therefore, a turbulence model for per phase which is more accurate than the mixture turbulence model should be used in the simulation.

The standard k-**ε** turbulence model is applied into both the gas and solid phases (Launder & Spalding, 1974).

k equation of gas phase:

$$\frac{\partial}{\partial t}\left(\alpha_g\rho_g k_g\right) + \nabla\cdot\left(\alpha_g\rho_g\overrightarrow{v_g}k_g\right) = \nabla\cdot\left(\alpha_g\frac{\mu_{g,t}}{\sigma_k}\nabla k_g\right) + \left(\alpha_g G_{g,k} - \alpha_g\rho_g\varepsilon_g\right) + K_{sg}\left(C_{sg}k_s - \right.$$
$$\left. C_{gs}k_g\right) - K_{sg}\left(\overrightarrow{v_s} - \overrightarrow{v_g}\right)\cdot\frac{\mu_{s,t}}{\alpha_s\sigma_s}\nabla\alpha_s + K_{sg}\left(\overrightarrow{v_s} - \overrightarrow{v_g}\right)\cdot\frac{\mu_{g,t}}{\alpha_g\sigma_g}\nabla\alpha_g \tag{3-11}$$

ε equation of gas phase:

$$\frac{\partial}{\partial t}\left(\alpha_g\rho_g\varepsilon_g\right) + \nabla\cdot\left(\alpha_g\rho_g\overrightarrow{v_g}\varepsilon_g\right) = \nabla\cdot\left(\alpha_g\frac{\mu_{g,t}}{\sigma_k}\nabla\varepsilon_g\right) + \frac{\varepsilon_g}{k_g}(C_{1\varepsilon}\alpha_g G_{g,k} - C_{2\varepsilon}\alpha_g\rho_g\varepsilon_g +$$
$$C_{3\varepsilon}(K_{sg}\left(C_{sg}k_s - C_{gs}k_g\right) - K_{sg}(\overrightarrow{v_s} - \overrightarrow{v_g})\cdot\frac{\mu_{s,t}}{\alpha_s\sigma_s}\nabla\alpha_s + K_{sg}(\overrightarrow{v_s} - \overrightarrow{v_s})\cdot\frac{\mu_{g,t}}{\alpha_g\sigma_g}\nabla\alpha_g)) \tag{3-12}$$

where the turbulent viscosity, $\mu_{g,t} = \rho_g C_\mu \frac{k_g^2}{\varepsilon_g}$

k equation of solids phase:

$$\frac{\partial}{\partial t}(\alpha_s \rho_s k_s) + \nabla \cdot (\alpha_s \rho_s \overrightarrow{v_s} k_s) = \nabla \cdot \left(\alpha_s \frac{\mu_{s,t}}{\sigma_k} \nabla k_s\right) + (\alpha_s G_{s,k} - \alpha_s \rho_s \varepsilon_s) +$$

$$K_{gs}(C_{gs} k_g - C_{sg} k_s) - K_{gs}(\overrightarrow{v_g} - \overrightarrow{v_s}) \cdot \frac{\mu_{g,t}}{\alpha_g \sigma_g} \nabla \alpha_g + K_{gs}(\overrightarrow{v_g} - \overrightarrow{v_s}) \cdot \frac{\mu_{s,t}}{\alpha_s \sigma_s} \nabla \alpha_s \qquad (3\text{-}13)$$

ε equation of solids phase:

$$\frac{\partial}{\partial t}(\alpha_s \rho_s \varepsilon_s) + \nabla \cdot (\alpha_s \rho_s \overrightarrow{v_s} \varepsilon_s) = \nabla \cdot \left(\alpha_s \frac{\mu_{s,t}}{\sigma_k} \nabla \varepsilon_s\right) + \frac{\varepsilon_s}{k_s}(C_{l\varepsilon} \alpha_s G_{s,k} - C_{2\varepsilon} \alpha_s \rho_s \varepsilon_s +$$

$$C_{3\varepsilon}\left(K_{gs}(C_{gs} k_g - C_{sg} k_s) - K_{gs}(\overrightarrow{v_g} - \overrightarrow{v_s}) \cdot \frac{\mu_{g,t}}{\alpha_g \sigma_g} \nabla \alpha_g + K_{gs}(\overrightarrow{v_g} - \overrightarrow{v_s}) \cdot \frac{\mu_{s,t}}{\alpha_s \sigma_s} \nabla \alpha_s\right) \qquad (3\text{-}14)$$

where the turbulent viscosity, $\mu_{s,t} = \rho_s C_\mu \frac{k_s^2}{\varepsilon_s}$.

3.3.4 Drag model

The interactions between the gas and solids can be included into a drag model. In the two-fluid CFD model, the momentum exchange, K_{gs} (=K_{sg}) is calculated by the drag model. The drag force of the gas-solid flow is related to the particle properties, flow regimes, and the Reynolds number. For FCC process in the riser, the Syamlal and O'Brien (SO) drag model (Syamlal & O'Brien, 1987) is found to simulate the drag coefficient more accurately. The SO drag model is derived from the measurements of the terminal velocity of the particles and the momentum exchange coefficient can be expressed as:

$$K_{gs} = \frac{3\alpha_s \alpha_g \rho_g}{4 v_{r,s}^2 d_p}\left(0.63 + \frac{4.8}{\sqrt{\frac{Re_r}{v_r}}}\right)^2 \left(\frac{Re_r}{v_r}\right)|\overrightarrow{v_s} - \overrightarrow{v_g}| \qquad (3\text{-}15)$$

where Re_s is the relative Reynolds number: $Re_r = \frac{\rho_g d_p |\overrightarrow{v_s} - \overrightarrow{v_g}|}{\mu_g} \qquad (3\text{-}16)$

and $v_{r,s}$ is the velocity ratio of the terminal velocity of a multiparticle system to that of a single particle in the fluid, which is a correlation of the volume fraction and the terminal velocity of the particles:

$$v_r = 0.5(A - 0.06Re_s + \sqrt{(0.06Re_s)^2 + 0.12Re_s(2B - A) + A^2} \qquad (3\text{-}17)$$

with

$$A = \alpha_g{}^{4.14} \qquad (3\text{-}18)$$

and

$$B = 0.8\alpha_g{}^{1.28} \qquad (3\text{-}19)$$

for $\alpha_g \leq 0.85$, and

$$B = \alpha_g{}^{2.65} \qquad (3\text{-}20)$$

for $\alpha_g > 0.85$.

3.4 Mesh and solver information

Both the two-dimensional and three- dimensional CFD models were found to have good agreement with the experimental data for the general flow structure as reported from the comparison work done by Ekambara, et al. (2005). Therefore, the 2D CFD model is selected for the simulation of the CFB riser reactor for saving the computational cost. The two-dimensional quad grid system with finer mesh near the wall and the inlet as shown in Figure 3-4 is constructed because the parameters of a CFB riser change more greatly near those regions. For the original CFD case, the mesh was constructed based on the axisymmetric domain of the CFB riser and consists of 120000 cells with 60 nodes in the radial direction and 2000 nodes in the axial direction as shown in Figure 3-4 (a). The gas and solids inlets located at the bottom of the CFB riser and the outlet is located at the top. For the modified CFD case, the mesh was constructed based on the central domain of the CFB riser and consists of 320000 cells with 80 nodes in the radial direction and 4000 nodes in the axial direction. The gas inlet was located at the bottom of the CFB riser while the

solids inlets were moved to the sides of the CFB riser as shown in Figure 3-4 (b). The outlets for both the gas and solids phases were located at the top of the CFB riser.

The commercial software Fluent V14.5 is used for the simulation. Solid particles used in the simulation are FCC type particles with a density of 1500 kg/m^3 and diameter of 67 µm. The turbulent kinetic energy and turbulent dissipation rate and other convection terms are discretized by the second order upwind scheme, and the momentum equation is discretized by the QUICK scheme. The convergence criterion for each scaled residual component is specified of 5x10^{-4}. The simulation is carried out as a transient case which calculated for over 40s of the real time with a time step size of 0.0001s. The time averaged results are processed after the CFD case reaches a steady state when the mass flow rate at the outlet equals to the inlet.

(a) Mesh for the original case   (b) Mesh for the modified case
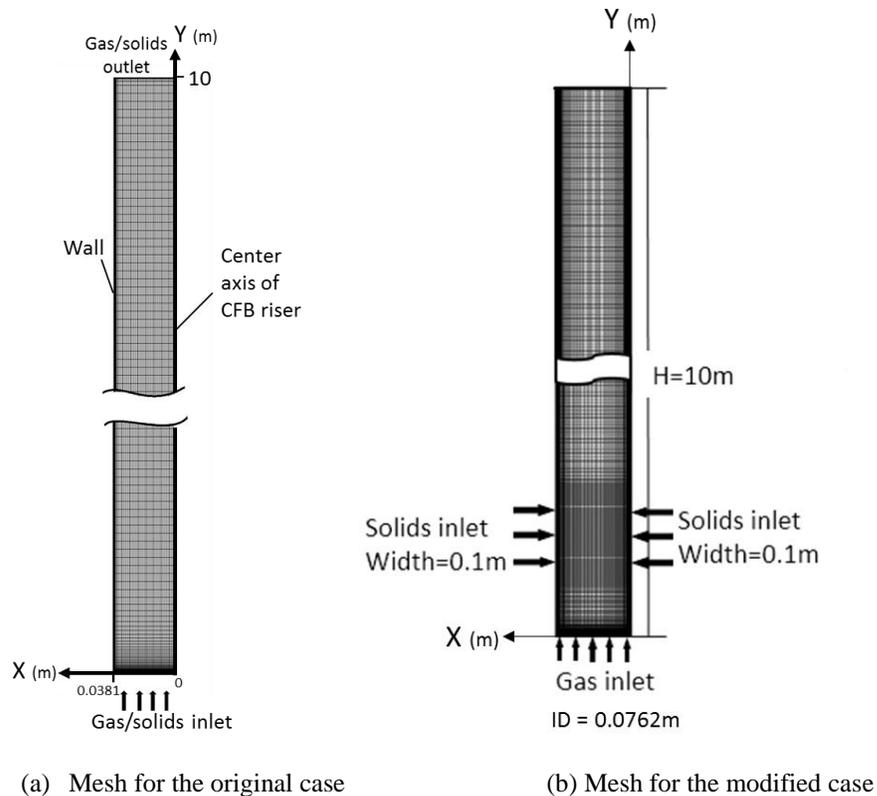
Figure 3-4: Meshes for the calculation domain in the testing riser

3.5 Boundary conditions and operating conditions

Gas is introduced into the riser from the bottom of the riser through the perforated gas distributor which form many small air jets with a very high gas velocity through the holes of the distributor. Therefore, a jet region is found to exist at the entrance part of the CFB riser. A jet inlet profile of the gas velocity is used for the gas phase to account for the jet effects and the number of jets is defined by the most jets which can be seen from the radial direction (Peng et al., 2010). The inlet gas velocity for the jet profile inlet boundary condition can be derived from the superficial gas velocity:

$$V_{g,in} = U_g/\phi \qquad\qquad (3\text{-}21)$$

where ϕ is the ratio of the opening area in the gas distributor.

For the solids phase, two different inlet boundary conditions are compared in this work as Figure 3-5 shows. The original solids inlet is at the bottom of the riser with uniform velocity. The modified solids inlet located on the side of the riser, two symmetric inlets are applied in the 2-D simulation referring to the solids returning pipe of the 3-D experimental equipment. The width and the location of the side solids inlets are defined by the real geometric structure of the returning pipe which has a diameter of 5 mm (2in) as Figure 3-2 shows. The inlet solids velocity is calculated from the constant solids circulation rate.

For the original inlet boundary conditions, the inlet velocity of the solid phase can be expressed as:

$$V_{s,in\_o} = \frac{G_s \cdot A_{out}}{\rho_p \cdot \varepsilon_{s,in} \cdot A_{in,btm}} \qquad\qquad (3\text{-}22)$$

where G_s is the solids circulation rate, A_{out} is the cross-sectional area of the riser outlet, $\varepsilon_{s,in}$ is the solid phase volume fraction at the inlet which is defined as 0.30, and $A_{in,btm}$ is the cross-sectional area of the riser inlet. For the original boundary condition which sets the solid phase inlet at the bottom of the riser, $A_{in,btm}=A_{out}$.

For the modified solids inlet boundary condition, the inlet velocity of the solid phase can be derived from the following:

$$V_{s,in\_m} = \frac{G_s \cdot A_{out}}{\rho_p \cdot \varepsilon_{s,in} \cdot A_{in,side}} \qquad (3\text{-}23)$$

where $A_{in,side}$ stands for the total area of the two symmetric solids inlets at the sides of the 2D computational domain.

(a)   (b)
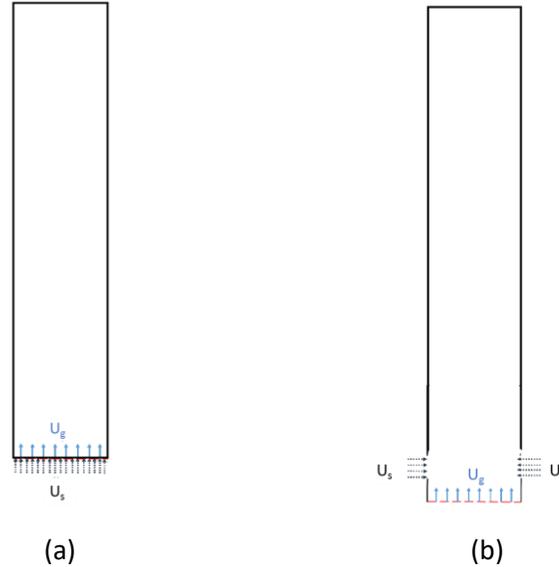
Figure 3-5 Inlet structure: (a): original inlet structure; (b): modified inlet structure

Table 3-1 Boundary conditions of the CFD model

Inlet of gas phase	
Position	The bottom of the riser
Type	Profile of velocity inlet
	Gas velocity=U_g/opening ratio of the gas distributor
Inlet of solids phase	
Position	Original: the bottom of the riser
	Modified: at the side of the riser
Type	Uniform velocity inlet
	Solids velocity=G_s/ ($\varepsilon_s \times \rho_S \times A_{,in}$)
	where ε_s is the solid phase volume fraction at the inlet
Wall	
Gas phase	No-slip velocity
Solids phase	Partial slip
	Specularity coefficient: 0.0001
	Particle-wall restitution coefficient: 0.9
Outlet	
Gas phase	Outflow
Solids phase	Outflow

Table 3-1 shows the specified boundary conditions of the gas and solids phase in the CFD model. The operating conditions and simulation parameters are shown in Table 3-2. The gas-solid CFB riser operated under a superficial gas velocity of 4, 5, 7 m/s, and a solids circulation rate of 100, 500 kg/m²s are selected in the simulation.

Table 3-2 Summaries of operating conditions

Gas density (kg∕m³)	1.225
Particle density (kg∕m³)	1500
Particle diameter (μm)	67
Superficial gas velocity (m∕s)	4,5,7
Particle circulation rate (kg/m²· s)	100,500
Particle-particle restitution coefficient	0.95
Specularity coefficient	0.0001

3.6 Results and discussion

3.6.1 Results from the original boundary conditions

The contours of the solid phase volume fraction at the entrance region and the outlet region of the CFB riser from the simulations with original inlet boundary conditions are plotted in Figure 3-6. The structure of the inlet gas distributor has a significant impact on the gas-solid flow structure and a jet region forms at the entrance region of the CFB riser due to the distributor effects as shown in Figure 3-6. When the gas entering the riser through the small holes of the distributor, the absolute gas velocity in every hole is far greater than the superficial gas velocity which is commonly used as the value of the uniform velocity inlet boundary condition of the gas phase. Therefore, the jet region cannot be predicted by using the uniform inlet velocity boundary condition and result in less lateral interactions between the gas and solids at the entrance region of the riser. In order to obtain the jet effects, profiles of velocity for the gas phase at the inlet are implemented in this work. The profile inlets do help achieve a more distinct core-annulus flow structure and a greater lateral dispersion of solids comparing with the simulation results from uniform velocity inlet. The velocity vector profiles of the gas and solids phase at the entrance region of the CFB riser also reveal the impacts from the jet profile as shown in Figure 3-7. The gas velocity is much higher in the air jets which results in a low-velocity area between the two adjacent air jets as shown in Figure 3-7 (a). For the solid phase, since the inlet solids velocity is

much smaller than the inlet gas velocity, the development of the solids flow depends greatly on the gas flow. Although the inlet velocity is uniform, the particles also present a higher velocity in the air jets due to the faster acceleration of the high-velocity gas and a much smaller particle velocity is found in the area between the adjacent jets as shown in Figure 3-7 (b). Correspondingly, denser solids suspensions can be found between two adjacent jets as shown in Figure 3-6 with the formation of the so-called jet region because the particles are pushed away from this region by the lateral gas flow.

However, those denser solids suspension regions which can be considered as the squeeze effects caused by air jets exist along the entire riser from the entrance to the exit as Figure 3-6 shows. This phenomenon has no physical significances because the gas-solid mixing and interactions are usually very vigorous in the riser and the jet region should disappear since the flow becomes fully developed after about 2m from the entrance. The reason why the numerical jet effects exists in the entire riser lies in the inaccurate solids phase inlet boundary condition which uses the same inlet velocity profile as the gas phase, but a much lower particle velocity in the jets than gas velocity. Gas and solids come into the riser at the same position, but obviously gas has more momentum due to its higher velocity. The velocity profiles of both gas and solids phase at the inlet region shown in Figure 3-7 prove that the gas velocity can be as high as about 30m/s in the hole of the distributor. However, the uniform solids inlet velocity of the original model is calculated by $G_s / (\varepsilon_s \times \rho_s)$, which is much lower. For instance, when $G_s = 100$ kg/m^{2}s, the inlet solids velocity is only 0.222m/s if the solids volume fraction at the inlet is set as 0.3. In this way, solids are easily guided by the gas flow and less lateral gas-solid interactions take place. Therefore, more realistic inlet boundary conditions are needed to better investigate the flow structure inside a riser reactor.
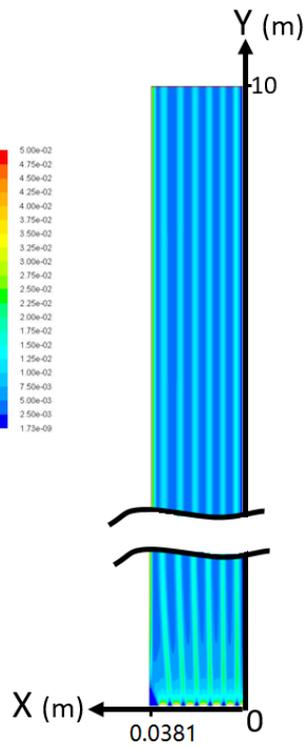
Figure 3-6 Contours of solids phase volume fraction, $U_g= 5$ m/s, $G_s=100$ kg/m^{2}s

(a) Gas phase
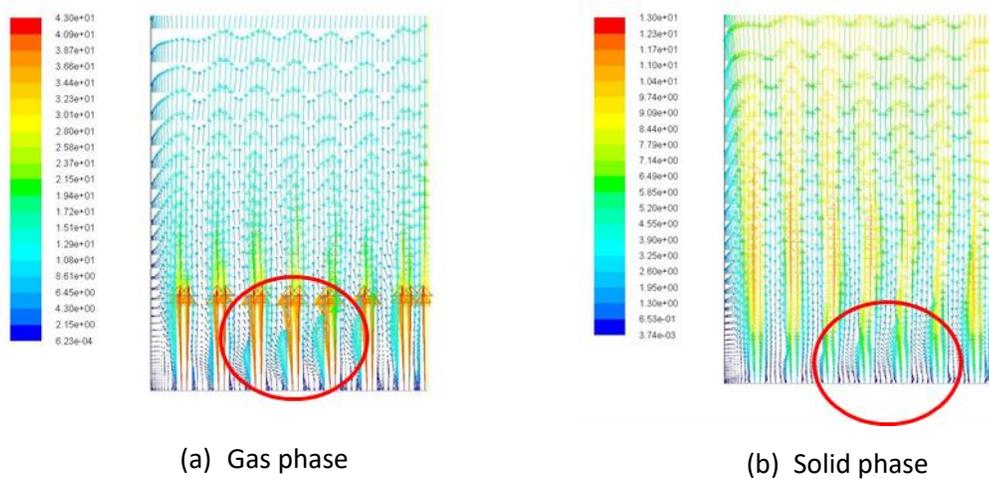
(b) Solid phase

Figure 3-7 Velocity vectors of the gas and solids at the entrance region of the CFB riser, $U_g= 5$ m/s, $G_s=100$ kg/m^{2}s

3.6.2 Results from the modified boundary conditions

(a) Gas phase
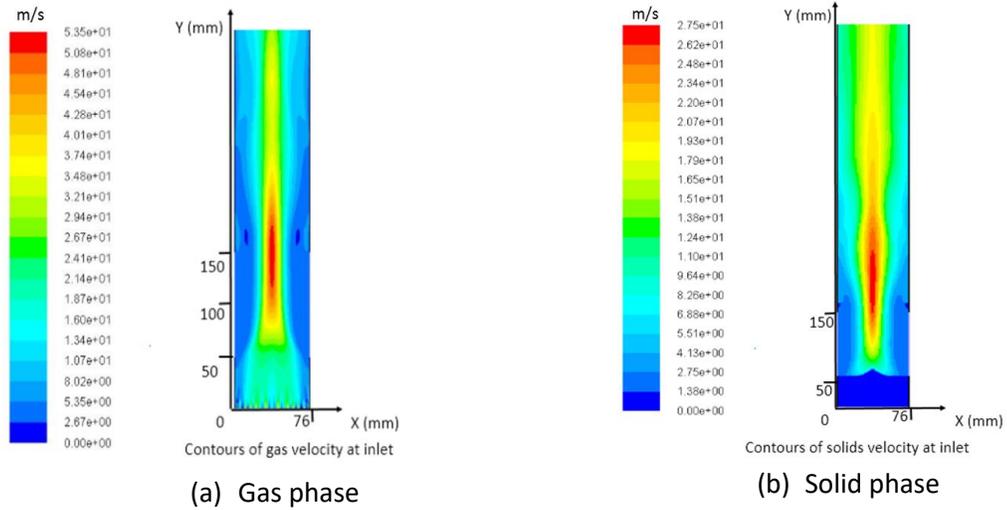
(b) Solid phase

Figure 3-8 Contours of velocity of gas and solid phases at inlet, $U_g = 7$ m/s, $G_s = 500$ kg/(m²s)
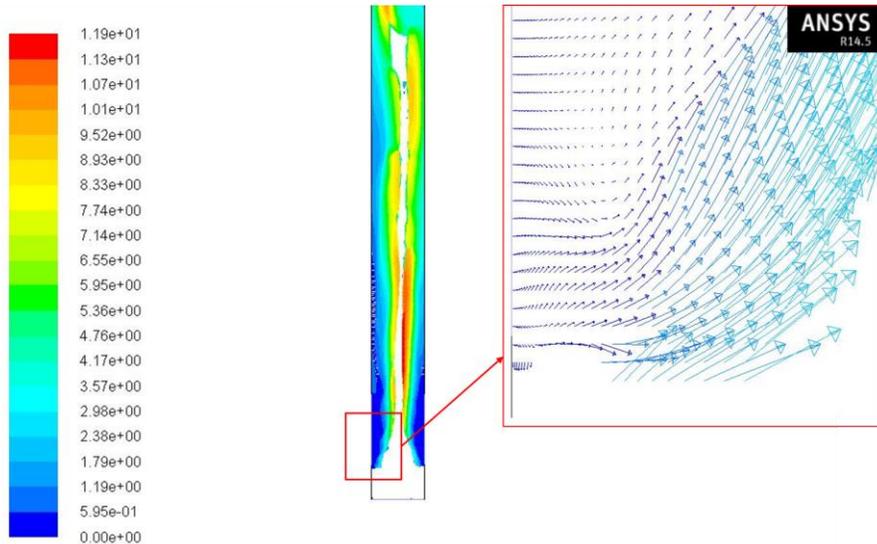
Figure 3-9 Velocity vector profile of solid phase with the modified inlet boundary conditions at the entrance region of the CFB riser $U_g= 7$ m/s, $G_s=500$ kg/m²s

A modification to the inlet boundary conditions is shown in Figure 3-5 (b), which keeps the profile inlet for the gas velocity at the bottom unchanged and moves the solids inlet to the sides of the riser. This modification is based on the actual geometric structure of the solids returning pipe of the CFB riser as Figure 3-2 shows. Analogous to the 3-D cylindrical

experimental equipment with solids entering from one side only, two symmetric inlets of solids which are at the same height with the position of the returning pipe are implemented by the 2-D simulation.

Figure 3-8 shows the velocity contours of both gas and solids phases by the modified inlet boundary conditions. The velocity contours indicate that the squeeze effects can be eliminated when the solids enter the riser form the side. It can be found from the contours of gas velocity that the air jets effect still works and gas accelerates quickly from every jet at the bottom and form a main gas flow with higher velocity in the center before the side solids inlets. The modified solids inlets allow particles coming into the riser with a radial velocity at a higher position than the gas inlet as shown in Figure 3-8 (a) (b), so that the particles can be pushed up directly by the gas main flow and are not influenced by air jets.

The velocity vector profile of the particles at the inlet further reveals a more realistic flow development of the solid flow with the modified model as shown in Figure 3-9. After the particles enter the CFB riser from the sides, the particle velocity is very small at the wall initially and increases quickly once the solid flow encounters the main gas flow. The vector profile shows that the particles obtained a large amount of the momentum form the upward flowing gas main flow so that the particles not only accelerate fast but also turn into the upward velocity direction with the gas in a very short time as shown in Figure 3-9.

The contours of solids volume fraction at the entrance region shown as Figure 3-10 further prove the improvements of the modified inlet boundary conditions which shows a better lateral gas-solid mixing and a clear core-annulus flow structure. The profile velocity inlet for the gas phase still works comparing with a uniform inlet since all the small gas jets converge together through the bottom of the riser to form a main gas flow with a clear power-law velocity profile of gas. It can be found that only a very short length of the riser is occupied for the formation of the main gas flow. No squeeze effects can be seen by the modified inlet boundary conditions because the main gas flow has already formed before the solids inlets. Thus, unlike the original inlet settings which the air jets dominate the trend of solids flow, solids have no chances to directly contact the gas jets and interact with the

converged gas flow instead. On the other hand, more lateral momentum carried by the solids contributes significantly to the gas-solid mixing when the modifications are applied.

Contours of solids volume fraction at inlet
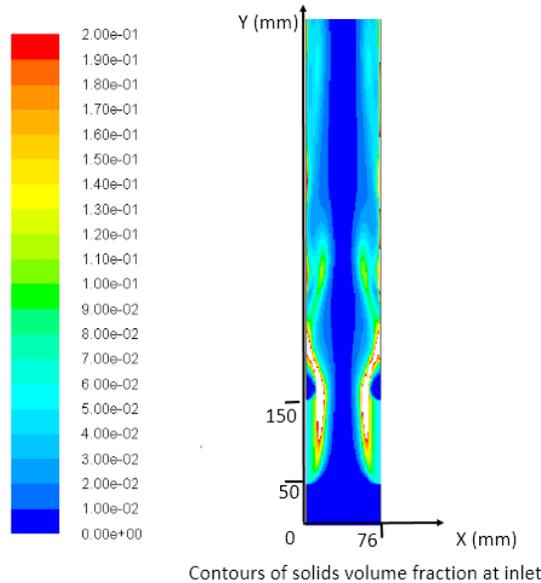
Figure 3-10 Contours of solids volume fraction at inlet, U_g = 7 m/s, G_s = 500 kg/m^{2}s

More details are revealed in Figure 3-11 where the radial velocity profiles of gas and solids phases at different heights near the inlets are presented. From the velocity profiles of gas, it can be seen that the air jets converged before h=0.05 m of the riser which is lower than the side solids inlets. The velocity profiles of solids phase clearly show the enhancement of lateral gas-solid mixing along the riser at the inlet. The symmetric solids inlets located from h=0.05 m to h=0.15 m, Figure 3-11 (b) indicates that initially most of the particles move near the wall region, and accelerate upward and gradually move to the center of the riser with the increasing of lateral momentum transfer. And a main solid flow also forms after h=1.0 m which proves a good lateral mixing between gas and solids phases and agrees with the experimental descriptions of the jet region in the riser as well.

The simulation results of the solids holdup profiles between the original and modified inlet boundary conditions at the height as 4.81 m and 7.35 m of the riser are presented in Figure 3-12. Although both the original and the modified CFD results don't agree with the experimental data very well which means more efforts need to be done in the future, the results from modified boundary conditions show a same trend with the experimental data.

The modified CFD model shows a much higher solid holdup than the original case near the wall region which means more lateral dispersions of solids are obtained. The results from the modified case agree with the experimental results better than the original case because the inlet boundary conditions are more realistic and can present the actual gas-solid flow structure at the entrance of the riser.

U_g = 7 m/s, G_s = 500 kg/(m²·s)

U_g = 7 m/s, G_s = 500 kg/(m²·s)

U_g = 4 m/s, G_s = 100 kg/(m²·s)

U_g = 4 m/s, G_s = 100 kg/(m²·s)

U_g = 5 m/s, G_s = 100 kg/(m²·s)

U_g = 5 m/s, G_s = 100 kg/(m²·s)

(a) Radial profile of gas velocity

(b) Radial profile of particle velocity

Figure 3-11 Velocity profiles of gas and solids phases at different heights
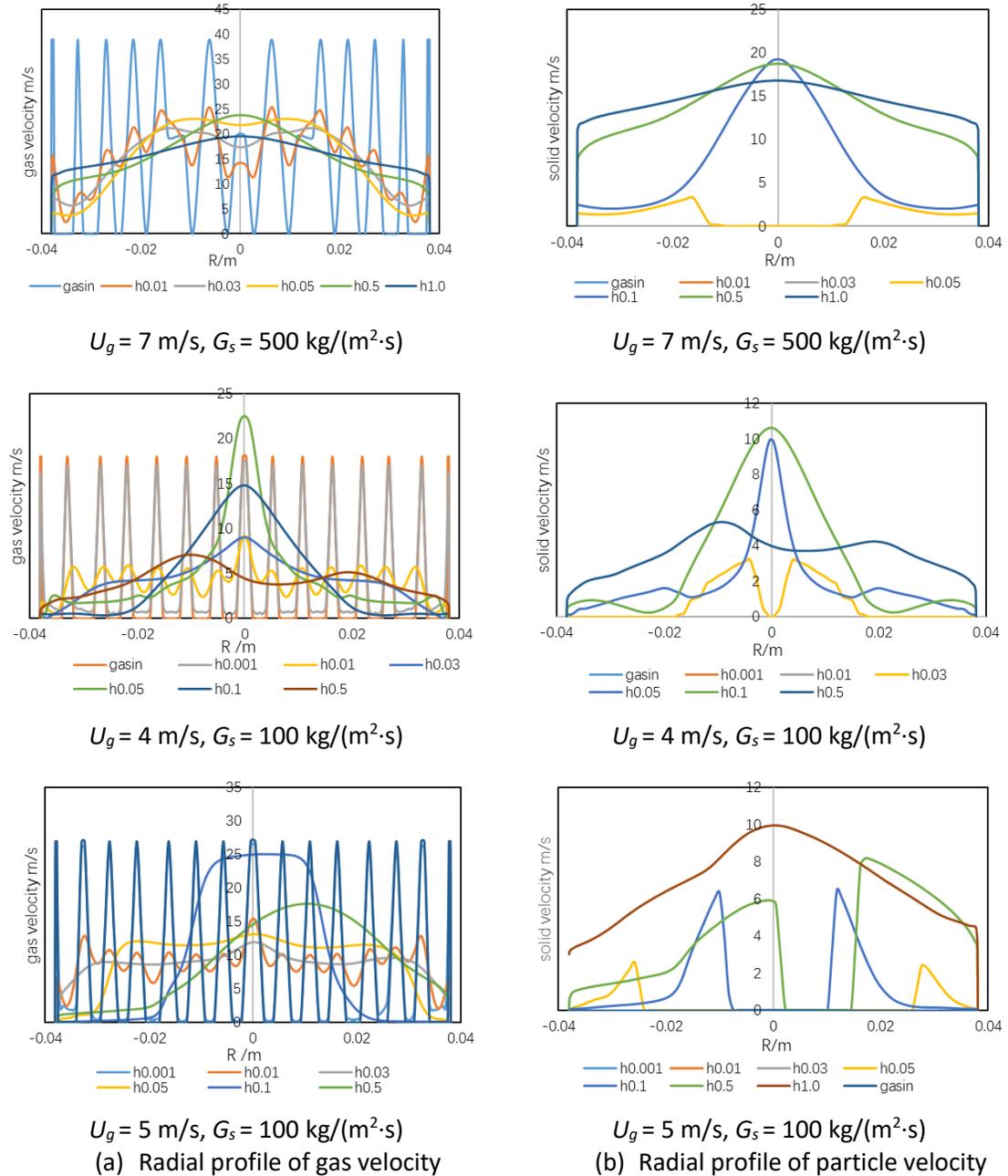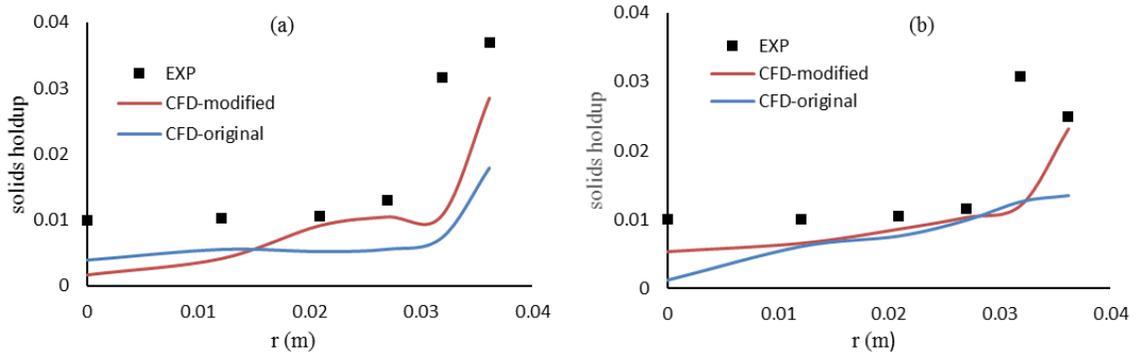
Figure 3-12 Comparison of the solids holdup profiles at (a): h=4.81m; (b): h=7.35m
(U_g = 5 m/s, G_s = 100 kg/m²s)

3.7 Conclusion

The effects of the inlet boundary conditions on the gas-solid flow structure in a circulating fluidized bed riser are investigated by numerical simulations. The position and the structure of the inlets are critical to the gas and solids flow structures in a circulating fluidized bed riser. A more realistic modification to both the gas and solids inlet boundary conditions based on the configuration of the experimental equipment is proposed and a more realistic flow structure is achieved. Instead of the velocity profile inlet boundary conditions of both the gas and solids phases, the modified inlet boundary conditions take geometry effects of the solids returning pipe into account and make the connect port between the riser and the solids returning pipe as the inlet of the solids in the numerical simulations. The CFD results show that a main gas flow forms due to the effects of the gas distributor and the unrealistic squeeze effect is eliminated with the help of the modified solids inlet boundary conditions. The interactions between the gas and particles are improved and the lateral dispersion of solids is enhanced as well. The CFD model with modified inlet boundary conditions also achieves a better agreement with the experimental results on the local solids holdup distribution.

Nomenclature

A_{out} Cross-sectional area of the riser outlet, m²

$A_{in,btm}$	Cross-sectional area of the riser inlet for gas phase, m^2
$A_{in,side}$	Total area of the two solids inlets at the sides of the riser, m^2
d_p	Particle diameter, m
e_{ss}	Coefficient of particle-particle restitution
$g_{o,ss}$	Radial distribution function of particles
G_s	Solids circulation rate, kg/m^{2}s
$\bar{\bar{I}}$	unit tensor
h	Axial distance from the gas distributor, m
H	Total height of the CFB riser, m
k	Turbulent kinetic energy, m^2/s^2
P	Fluid phase pressure, Pa
P_s	Solids phase pressure, Pa
r	Radial position of the CFB riser, m
R	Radius of the CFB riser, m
Re_r	Relative particle Reynolds number, $= \frac{\rho_g d_p |\vec{v_s}-\vec{v_g}|}{\mu_g}$
U_g	Superficial gas velocity, m/s
v_g	Gas phase velocity, m/s
v_r (U_r)	Relative velocity: the ratio of the terminal settling velocity of a multiparticle system to that of an isolated particle
v_s	Solid phase velocity, m/s
$v'_{s\tau}$	Random component of the particle velocity, m/s
$V_{g,in}$	Inlet gas velocity, m/s
V_{s,in_o}	Original inlet velocity of the solid phase, m/s
V_{s,in_m}	Modified inlet velocity of the solid phase, m/s
α_g	Gas phase volume fraction
α_s	Solid phase volume fraction
$\gamma_{\Theta s}$	Collisional dissipation of energy
$K_{sg}=K_{gs}$	Interphase momentum exchange coefficient
ε	Dissipation rate of the turbulent kinetic energy

λ_g	Gas phase bulk viscosity, kg/ms
λ_s	Solids phase bulk viscosity, kg/ms
μ_g	Gas shear viscosity, kg/ms
$\mu_{g,t}$	Gas phase turbulent viscosity, kg/ms
μ_s	Solids shear viscosity, kg/ms
$\mu_{s,t}$	Solids phase turbulent viscosity, kg/ms
ρ_g	Gas density, kg/m^3
ρ_s	Particle density, kg/m^3
Θ	Granular temperature of particles, m^2/s^2
$\overline{\overline{\tau_g}}$	Gas phase stress-strain tensor, kg/s^2
$\overline{\overline{\tau_s}}$	Solid phase stress-strain tensor, kg/s^2
ϕ	Ratio of the opening area in the gas distributor

Subscripts

g	Gas phase
s	Solids phase

References

ANSYS, Inc. (2013). Chapter 17. Multiphase Flows. ANSYS Fluent Theory Guide. Pp. 527-586.

Benyahia, Arastoopour, Knowlton & Massah. (2000). Simulation of particles and gas flow behavior in the riser section of a circulating fluidized bed using the kinetic theory approach for the particulate phase. Powder Technology, 112(1–2), 24–33.

Berruti, Pugsley, Godfroy, Chaouki & Patience (1995). Hydrodynamics of circulating fluidized bed risers: a review. The Canadian Journal of Chemical Engineering, 73(5), 579-602.

Bi & Grace (1995). Flow regime diagrams for gas-solid fluidization and upward transport. International Journal of Multiphase Flow, 21(6), 1229–1236.

Boemer & Renz. (1997). Eulerian simulation of bubble formation at a jet in a two-dimensional fluidized bed. International Journal of Multiphase Flow 23.5: 927-944.

Breault, Monazam, Shadle, Rowan & Macfarlan (2017). The effect of riser end geometry on gas-solid hydrodynamics in a CFB riser operating in the core annular and dilute homogeneous flow regimes. Powder technology, 316, 181-189.

Cheng, Wei, Yang & Jin (1998). Inlet and outlet effects on flow patterns in gas-solid risers. Powder Technology, 98(2), 151-156.

De Wilde, Van Engelandt, Heynderickx & Marin (2005). Gas–solids mixing in the inlet zone of a dilute circulating fluidized bed. Powder Technology, 151(1-3), 96-116.

Ding & Gidaspow. (1990). A bubbling fluidization model using kinetic theory of granular flow." AIChE journal 36.4: 523-538.

Ekambara, Dhotre & Joshi. (2005). CFD simulations of bubble column reactors: 1D, 2D and 3D approach. Chemical Engineering Science, 60(23), 6733-6746.

Grace (1996). Riser geometry influence on CFB particle and fluid dynamics." Proceedings of Circulating Fluidized Bed Technology V. PL2-1.

Grace (1986). Contacting modes and behaviour classification of gas—solid and other two-phase suspensions. The Canadian Journal of Chemical Engineering, 64(3), 353–363.

Grace, Bi & Golriz (2003). Circulating fluidized beds. In M. D. Wen-Ching Yang (Ed.), Handbook of fluidization and fluid-particle systems (pp. 485–498). New York: CRC press.

Grace & Bi (1997). Introduction to circulating fluidized beds." Circulating fluidized beds. Springer Netherlands. 1-20.

Hartge, Ratschow, Wischnewski & Werther (2009). CFD-simulation of a circulating fluidized bed riser. Particuology, 7(4), 283-296.

Huang, Zhu & Pärssinen (2006). Comprehensive study on the solids acceleration length in a long CFB riser. Chemical Engineering & Technology: Industrial Chemistry-Plant Equipment-Process Engineering-Biotechnology, 29(10), 1197-1204.

Kunii & Levenspiel (2013). Fluidization engineering. Elsevier.

Launder & Spalding (1974). The numerical computation of turbulent flows. Computer Methods in Applied Mechanics and Engineering. 3 (2): 269–289.

Li (2010). Investigation of circulating fluidized bed riser and downer reactor performance for catalytic ozone decomposition. . Ph.D thesis, University of Western Ontario.

Li & Guenther. (2012). A CFD study of gas–solid jet in a CFB riser flow. AIChE Journal 58.3: 756-769.

Lim, Zhu & Grace. (1995). Hydrodynamics of gas-solid fluidization. International journal of multiphase flow 21: 141-193.

Lun, Savage, Jeffrey & Chepurniy. (1984). Kinetic theories for granular flow: inelastic particles in Couette flow and slightly inelastic particles in a general flowfield. Journal of fluid mechanics, 140, 223-256.

Patankar & Suhas "A calculation procedure for two-dimensional elliptic situations." Numerical heat transfer 4.4 (1981): 409-425.

Peng, Zhu & Zhang. (2011). A new approach to specify the inlet boundary conditions for computational fluid dynamics (CFD) modeling of hydrodynamic behavior of a circulating fluidized bed (CFB) riser. Industrial & Engineering Chemistry Research, 51(4), 2152-2165.

Peng, Zhu & Zhang. (2010). Numerical Study on the Effect of the Air Jets at the Inlet Distributor in the Gas-Solids Circulating Fluidized-Bed Risers. Industrial & Engineering Chemistry Research 49.11: 5310-5322.

Pugsley, Lapointe, Hirschberg & Werther (1997). Exit effects in circulating fluidized bed risers. The Canadian Journal of Chemical Engineering, 75(6), 1001-1010.

Sinclair & Jackson. (1989). Gas-particle flow in a vertical pipe with particle‐particle interactions. AIChE Journal 35.9: 1473-1486.

Syamlal & O'Brien (1987). The derivation of a drag coefficient formula from velocity-voidage correlations. Technical Note, US Department of energy, Office of Fossil Energy, NETL, Morgantown, WV.

Tsuo, Yuan & Gidaspow. (1990). Computation of flow patterns in circulating fluidized beds. AIChE Journal 36.6: 885-896.

Wang, Li, Zhu & Barghi (2015). A comparison of flow development in high density gas-solids circulating fluidized bed downer and riser reactors. AIChE Journal, 61(4), 1172-1183.

Wang, Zhu, Barghi & Li (2014). Axial and radial development of solids holdup in a high flux/density gas–solids circulating fluidized bed. Chemical Engineering Science, 108, 233-243.

Wang, Lu, Zhang, Shi & Li (2010). A review of multiscale CFD for gas–solid CFB modeling. International Journal of Multiphase Flow, 36(2), 109-118.

Zhang, Huang & Zhu. (2001). Gas-solids flow behavior: CFB riser vs. downer. AIChE journal 47.9: 2000-2011.

Zhu & Zhu. (2008). Characterization of fluidization behavior in the bottom region of CFB risers. Chemical Engineering Journal 141.1: 169-179.

Chapter 4

4   Comparisons of HDCFB and LDCFB risers via numerical simulations

4.1   Introduction

Gas-solids fluidization processes under high-velocity conditions are commonly applied in industries for its advantages of better gas-solids contacting, effective gas-solids mass and heat transfer, and higher gas throughput and so on (Grace, 1990). Under a high superficial gas velocity, the solids will be entrained out of the column once the gas velocity exceeds the terminal velocity of particles and the fluidized bed reactor becomes a circulating fluidized bed (CFB) if the entrained particles are collected and recycled back into the fluidized bed (Kunii & Levenspiel, 1997). CFB reactors, as the major application in the high-velocity fluidization regimes, are more favorable than conventional fluidized beds for many gas-phase catalytic reactions with quick deactivation of catalysts and continuously handling of the particles (Jahnig, et al., 1980). A typical CFB usually consists of two parts: the riser where chemical reactions take place and the downer where particles are recycled to the riser.

Gas-solids CFB systems have been studied extensively over the past decades with some new flow regimes such as the high-density CFB (HDCFB) being paid more attention to (Zou et al. 1994; Wang et al. 2014; 2015). The HDCFB was first academically distinguished from the low-density CFB (LDCFB) by the different profiles of the solids holdup in 1995 (Zhu & Bi 1995). After that, more comprehensive studies on the hydrodynamics in both HDCFB and LDCFB risers by experiments revealed different characteristics between low-density and high-density conditions (Bai & Kato 1999; Wang, et al. 2014a; 2014b; 2015). A LDCFB riser reactor for typical FCC particles operates usually under a solids circulation rate lower than 400 kg/m^{2}s, which has a dilute gas-solids suspension in the riser. On the contrast, an HDCFB operates under a higher solid circulation rate ($G_s \geq 400$ kg/m^{2}s), so that the overall bed density can achieve over 0.10 (Wang, et al. 2014a). A bottom-dense and upper-dilute distribution of the solids holdup in the axial direction is commonly seen in an HDCFB riser due to the higher G_s, however, an

exponential shape of the solids distribution is more likely to be found in a LDCFB at a less G_s (Wang, et al., 2015). A typical core-annulus flow structure in the radial direction which describes a center dilute and denser annular layer of solids suspension near the wall of the riser exists in both the HDCFB and LDCFB. However, the HDCFB has a shrinking core region compared with a LDCFB because of the higher G_s in the HDCFB as well (Bi & Grace, 1995).

Although the general flow structures between the LDCFB and HDCFB have been carefully investigated with the help of experimental studies during the past two decades, some flow details such as the velocity profiles of gas phase and the local slip velocity between the gas and particles still need further studies but are limited by the measuring techniques (Hensler et al. 2016; Horio 2010; Ullah, et al., 2013; Wang, et al. 2014; Zhang et al. 2015). With the development of computational fluid dynamic (CFD), more details on the flow structures in CFB riser can be revealed as well as the gas-solids interactions, mass and momentum transfers (Carlos, et al., 2017; Shah et al. 2016; Upadhyay & Park 2015). On the other hand, since the high-velocity fluidization system has expanded to high-density operations, a wider operating range of CFB risers under higher G_s and U_g is expected. The transition between the HDCFB riser and LDCFB riser was rarely studied and more detailed information on the hydrodynamics in CFB risers is needed to better distinguish the differences between the HDCFB and LDCFB instead of merely general flow structures. Furthermore, it is easy to compare the flow conditions in a CFB riser under the same superficial gas velocity or the same solids circulation rate. However, the prediction of the overall bed density in CFB risers under different operating conditions with various G_s-U_g pairs is also critical for industrial uses, but there are not enough experimental data available. Although some numerical work has been carried out on the HDCFB recently, detailed comparison between the HDCFB and the LDCFB is still rare in the reported literature (Armellini et al. 2015; Bakshi et al. 2015; Zhang et al. 2015). Therefore, the comparison of the gas and solids flow structures between the HDCFB and LDCFB risers and the relationship of the bed density under various conditions are investigated numerically in this work.

4.2   CFD model descriptions

A transient Eulerian-Eulerian approach of two-fluid model coupled with the kinetic theory of granular flow is employed to conduct the numerical study of the CFB riser. The basic governing equations of the mass and momentum conservations for both the gas and solids phases are shown as following (ANSYS 2013):

Continuity equation of the gas phase:

$$\frac{\partial}{\partial t}\left(\alpha_g \rho_g\right) + \nabla \cdot \left(\alpha_g \rho_g \overline{v_g}\right) = 0 \tag{4-1}$$

Continuity equation of the solids phase:

$$\frac{\partial}{\partial t}\left(\alpha_s \rho_s\right) + \nabla \cdot \left(\alpha_s \rho_s \overline{v_s}\right) = 0 \tag{4-2}$$

where $\alpha_g + \alpha_s = 1$ \hfill (4-3)

Momentum equation of the gas phase:

$$\frac{\partial}{\partial t}\left(\alpha_g \rho_g \overrightarrow{v_g}\right) + \nabla \cdot \left(\alpha_g \rho_g \overrightarrow{v_g}\overrightarrow{v_g}\right) = -\alpha_g \nabla P + \nabla \cdot \left(\alpha_g \left(\overline{\overline{\tau_g^m}} + \overline{\overline{\tau_g^{Re}}}\right)\right) + \alpha_g \rho_g \vec{g} + K_{sg}\left(\overrightarrow{v_s} - \right.$$

$$\left.\overrightarrow{v_g}\right) \tag{4-4}$$

where

$$\overline{\overline{\tau_g^m}} = -\frac{2}{3}\mu_{g.m}\nabla \cdot \overrightarrow{v_g}\overline{\overline{I}} + \mu_{g.m}\left(\nabla \overrightarrow{v_g} + \nabla \overrightarrow{v_g}^T\right) \tag{4-5}$$

$$\overline{\overline{\tau_g^{Re}}} = -\frac{2}{3}\left(\rho k_g + \mu_{g,t}\nabla \cdot \overrightarrow{v_g}\right)\overline{\overline{I}} + \mu_{g.t}\left(\nabla \overrightarrow{v_g} + \nabla \overrightarrow{v_g}^T\right) \tag{4-6}$$

Momentum equation of the solids phase:

$$\frac{\partial}{\partial t}\left(\alpha_s \rho_s \overrightarrow{v_s}\right) + \nabla \cdot \left(\alpha_s \rho_s \overrightarrow{v_s}\overrightarrow{v_s}\right) = -\alpha_s \nabla P - \nabla P_s + \nabla \cdot \left(\alpha_s \left(\overline{\overline{\tau_s^m}} + \overline{\overline{\tau_s^{Re}}}\right)\right) + \alpha_s \rho_s \vec{g} +$$

$$K_{sg}\left(\overrightarrow{v_g} - \overrightarrow{v_s}\right) \tag{4-7}$$

where

$$\overline{\overline{\tau_s^m}} = (\lambda s - \frac{2}{3}\mu_s)\nabla \cdot \overrightarrow{v_s}\overline{\overline{I}} + \mu_s(\nabla\overrightarrow{v_s} + \nabla\overrightarrow{v_s}^T) \tag{4-8}$$

$$\overline{\overline{\tau_s^{Re}}} = -\frac{2}{3}(\rho k_s + \mu_{s,t}\nabla \cdot \overrightarrow{v_s})\overline{\overline{I}} + \mu_{s.t}(\nabla\overrightarrow{v_s} + \nabla\overrightarrow{v_s}^T) \tag{4-9}$$

where P_s, is the solids phase pressure, $,\mu_s$ is the shear viscosity and λ_s is the bulk viscosity in the solids phase momentum equation. The fluctuation velocity of particles can be calculated by the granular temperature model.

Granular temperature equation (Gidaspow & Ding 1990):

$$\frac{3}{2}\left[\frac{\partial}{\partial t}(\rho_s\alpha_s\Theta s) + \nabla \cdot (\alpha_s\rho_s\overrightarrow{v_s}\Theta s)\right] = \left(-P_s\overline{\overline{I}} + \overline{\overline{\tau_s}}\right)\nabla\overrightarrow{v_s} + \nabla \cdot (k_{\Theta s}\nabla\Theta) - \gamma_{\Theta s} + \varnothing_{gs} \tag{4-10}$$

where

$$\varnothing_{gs} = -3k_{gs}\Theta s \tag{4-11}$$

The collisional energy can be obtained by:

$$\gamma_{\Theta s} = \frac{12(1-e_{ss}^2)g_{0,ss}}{d_p\sqrt{\pi}}\rho_s\alpha_s^2\Theta_s^{3/2} \tag{4-12}$$

The gas-solids two-phase flows are very complicated due to the vigorous interactions between the gas and solids. The motions of the particles are affected by the mean solids velocity, single particle fluctuations and the particle-particle collisions. Therefore, a turbulence model for each phase which is more accurate, is used in the simulation.

The standard k-**ε** turbulence model is applied into both the gas and solid phases.

k equation of the gas phase:

$$\frac{\partial}{\partial t}(\alpha_g\rho_g k_g) + \nabla \cdot (\alpha_g\rho_g\overrightarrow{v_g}k_g) = \nabla \cdot \left(\alpha_g\frac{\mu_{g,t}}{\sigma_k}\nabla k_g\right) + (\alpha_g G_{g,k} - \alpha_g\rho_g\varepsilon_g) + K_{sg}(C_{sg}k_s - $$
$$C_{gs}k_g) - K_{sg}(\overrightarrow{v_s} - \overrightarrow{v_g}) \cdot \frac{\mu_{s,t}}{\alpha_s\sigma_s}\nabla\alpha_s + K_{sg}(\overrightarrow{v_s} - \overrightarrow{v_g}) \cdot \frac{\mu_{g,t}}{\alpha_g\sigma_g}\nabla\alpha_g \tag{4-13}$$

ε equation of the gas phase:

$$\frac{\partial}{\partial t}\left(\alpha_g \rho_g \varepsilon_g\right) + \nabla \cdot \left(\alpha_g \rho_g \overrightarrow{v_g} \varepsilon_g\right) = \nabla \cdot \left(\alpha_g \frac{\mu_{g,t}}{\sigma_k} \nabla \varepsilon_g\right) + \frac{\varepsilon_g}{k_g}\left(C_{l\varepsilon}\alpha_g G_{g,k} - C_{2\varepsilon}\alpha_g \rho_g \varepsilon_g + \right.$$

$$\left. C_{3\varepsilon}(K_{sg}(C_{sg}k_s - C_{gs}k_g) - K_{sg}(\overrightarrow{v_s} - \overrightarrow{v_g}) \cdot \frac{\mu_{s,t}}{\alpha_s \sigma_s}\nabla \alpha_s + K_{sg}(\overrightarrow{v_s} - \overrightarrow{v_g}) \cdot \frac{\mu_{g,t}}{\alpha_g \sigma_g}\nabla \alpha_g)\right) \quad (4\text{-}14)$$

where the turbulent viscosity for the gas phase, $\mu_{g,t} = \rho_g C_\mu \frac{k_g^2}{\varepsilon_g}$

k equation of the solids phase

$$\frac{\partial}{\partial t}\left(\alpha_s \rho_s k_s\right) + \nabla \cdot \left(\alpha_s \rho_s \overrightarrow{v_s} k_s\right) = \nabla \cdot \left(\alpha_s \frac{\mu_{s,t}}{\sigma_k} \nabla k_s\right) + \left(\alpha_s G_{s,k} - \alpha_s \rho_s \varepsilon_s\right) + K_{gs}(C_{gs}k_g - $$

$$C_{sg}k_s) - K_{gs}(\overrightarrow{v_g} - \overrightarrow{v_s}) \cdot \frac{\mu_{g,t}}{\alpha_g \sigma_g}\nabla \alpha_g + K_{gs}(\overrightarrow{v_g} - \overrightarrow{v_s}) \cdot \frac{\mu_{s,t}}{\alpha_s \sigma_s}\nabla \alpha_s \quad (4\text{-}15)$$

ε equation of the solids phase

$$\frac{\partial}{\partial t}\left(\alpha_s \rho_s \varepsilon_s\right) + \nabla \cdot \left(\alpha_s \rho_s \overrightarrow{v_s} \varepsilon_s\right) = \nabla \cdot \left(\alpha_s \frac{\mu_{s,t}}{\sigma_k} \nabla \varepsilon_s\right) + \frac{\varepsilon_s}{k_s}\left(C_{l\varepsilon}\alpha_s G_{s,k} - C_{2\varepsilon}\alpha_s \rho_s \varepsilon_s + \right.$$

$$\left. C_{3\varepsilon}\left(K_{gs}(C_{gs}k_g - C_{sg}k_s) - K_{gs}(\overrightarrow{v_g} - \overrightarrow{v_s}) \cdot \frac{\mu_{g,t}}{\alpha_g \sigma_g}\nabla \alpha_g + K_{gs}(\overrightarrow{v_s} - \overrightarrow{v_g}) \cdot \frac{\mu_{s,t}}{\alpha_s \sigma_s}\nabla \alpha_s\right)\right) \quad (4\text{-}16)$$

where the turbulent viscosity for the solids phase, $\mu_{s,t} = \rho_s C_\mu \frac{k_s^2}{\varepsilon_s}$.

The interactions between the gas and solids is included into a drag model. In the two-fluid CFD model, the momentum exchange, K_{gs}, is calculated by a drag model. The drag force of the gas-solids flow is related to the particle properties, flow regimes, and the Reynolds number. For FCC process in risers, the Syamlal and O'Brien drag model (Syamlal & O'Brien 1989) is found to give a more accurate drag coefficient than other drag models and is used in this work.

$$K_{gs} = \frac{3\alpha_s \alpha_g \rho_g}{4 v_{r,s}^2 d_s}\left(0.63 + \frac{4.8}{\sqrt{\frac{Re_s}{v_{r,s}}}}\right)^2 \left(\frac{Re_s}{v_{r,s}}\right)|\overrightarrow{v_s} - \overrightarrow{v_g}| \quad (4\text{-}17)$$

4.3 Configuration of the CFB riser and the mesh setup
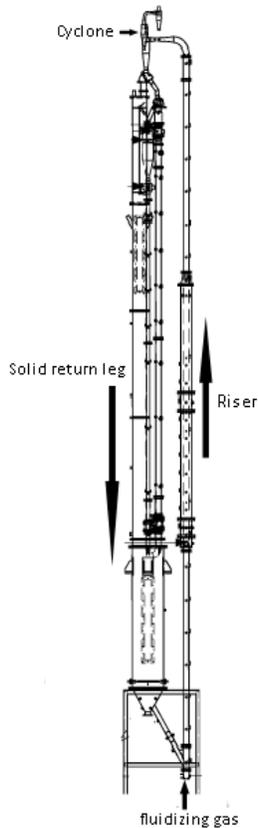
Figure 4-1: Configuration of the CFB riser (Li 2010)
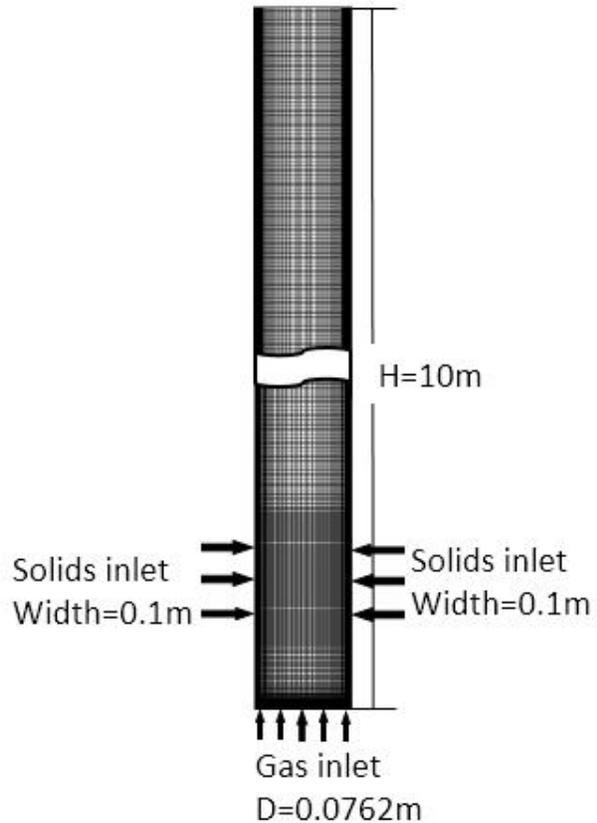
Figure 4-2: Mesh for the computational domain of the CFB riser

The CFB riser used in this study is of 10 m high with a diameter of 7.62 cm (3 in) as shown in Figure 4-1. A quad grid system with finer mesh near the wall and the inlet as shown in Figure 4-2 is used. The commercial software Fluent V16.5 is used for the simulation. Solids particles used in the simulation are FCC particles with a density of 1500 kg/m^3 and diameter of 67 µm (Li 2010; Wang 2013). The second-order discretization scheme is used for turbulent kinetic energy and turbulent dissipation rate and other convection terms with QUICK for momentum equation. A convergence criterion of 5×10^{-4} for each scaled residual component and the time step size of 0.0001s are specified.

4.4 Boundary and operating conditions

The boundary conditions used in the CFD simulations are listed in Table 4-1 based on the geometric structure and the operating conditions of the CFB riser system. A jet inlet profile is used to account for the jet effects and the number of jets is defined by the most jets which can be seen from the radial direction. For the solids phase, two symmetric solids inlets are applied on the two sides of the riser in the 2D simulation to represent the solids returning pipe of the 3D experimental equipment. The width and the location of the side solids inlets are defined by the actual geometric structure of the returning pipe used in the experiments, which has a diameter of 2in (5 mm). The inlet solids velocity is calculated based on the solids circulation rate. The operating conditions and simulation parameters are shown in Table 4-2.

Table 4-1: Boundary conditions

Inlet of the gas phase	
Position	The bottom of the riser
Type	Velocity profile
	Gas velocity=U_g/ opening ratio of the gas distributor
Inlet of the solids phase	
Position	The sides of the riser
Type	Uniform velocity
	Solids velocity=G_s/ ($\varepsilon_s \times \rho_s$)
	where ε_s is the solids volume fraction.
Wall	
Gas phase	No-slip velocity
Solids phase	Partial slip
	Specularity coefficient: 0.0001
	Particle-wall restitution coefficient: 0.9
Outlet	
Gas phase	Outflow
Solids phase	Outflow

Table 4-2: Operating conditions

Gas density (kg∕m³)	1.225
Particle density (kg∕m³)	1500
Particle diameter (μm)	67
Superficial gas velocity (m∕s)	3, 5, 7, 9
Particle circulation rate (kg∕m² s)	100, 300, 400, 500, 700
Particle-particle restitution coefficient	0.95
Specularity coefficient	0.0001

4.5 Grid independent test and data processing

Three sizes of 2D meshes from coarse to fine are used for the grid independent test and the comparison results are listed in **Error! Reference source not found.**. The time-averaged mass flow rate, superficial velocity, and pressure for both the gas and solids phases at the riser outlet from these three meshes are compared and the results show that all of the differences between the coarse and fine meshes are less than 3%. Therefore, the medium mesh and the fine mesh can provide the grid independent results and are applied in CFD simulations in this work.

Table 4-3 Grid information and results of independent test

Mesh #	Nodes	Mass flow rate of solids at outlet, kg/s	Mass flow rate of gas at outlet, kg/s	Absolute pressure, Pa	Average U_g at outlet, m/s	Average U_s at outlet, m/s	Average volume fraction of solids phase
1	60×1600	7.722675	0.473682	98504.23	5.150485	4.928585	0.015731
2	80×2500	7.758255	0.473103	98467.92	5.144864	4.946518	0.015762
3	120×4000	7.880415	0.475582	98376.93	5.18047	4.937413	0.016146
1 vs. 2	Difference	0.46%	0.12%	0.04%	0.11%	0.36%	0.19%
2 vs. 3	Difference	1.55%	0.52%	0.09%	0.69%	0.18%	2.38%

The variations of the bed static pressure drop and solids mass flow rate at the riser outlet with time are shown as Figure 4-3. The transient data show strong fluctuations at the beginning. Then, the results reach a quasi-steady state where the mean values are almost constant. The numerical results presented in this work are taken from the time averaged data after the simulation reaches a quasi-steady state as shown in Figure 4-3.
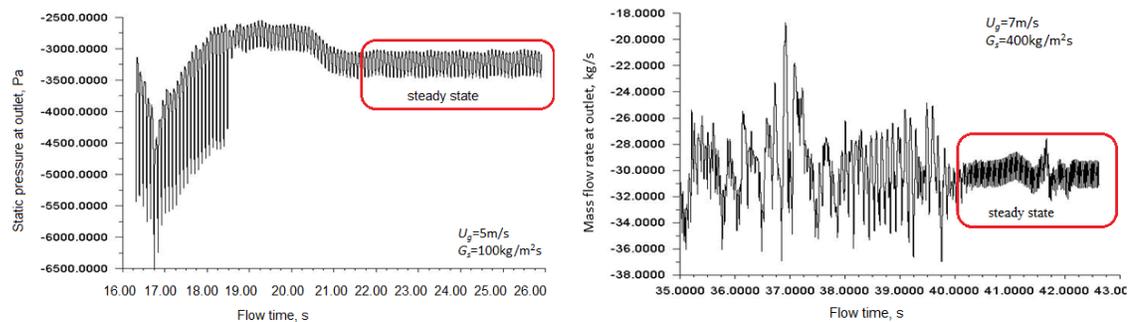
(a) Bed pressure drop   (b) Solids mass flow rate of at the outlet

Figure 4-3 Variations of the predicted bed pressure drop and solids mass flow rate at the outlet with time

4.6 Results and discussion

4.6.1 Radial and axial profiles of the solids holdup

The numerical results of the radial profiles of the solids holdup under low-density and high-density conditions at the height of 7.35m from the bottom of the riser are compared with the experimental data from Li (2010) and Wang (2013) as shown in Figure 4-4. A typical core-annulus the solids distribution structure with a dilute center and a dense wall layer of solids suspension can be observed in both the LDCFB and HDCFB risers, which agrees with the experimental observations well. Figure 4-4 (a) shows that the LDCFB has a more dilute gas-solids suspension and a wider and flatter core region (r/R = o to 0.7) in the riser due to the lower solids circulation rate. However, a much higher solids concentration is achieved in the HDCFB and the core region shrinks to r/R = 0 to 0.5 with a higher solids holdup as well. Comparing with the LDCFB, the HDCFB has a less uniform radial flow structure with a thicker region near the wall where the solids holdup rises dramatically to the wall, and even exceeds ε_s =0.20 under some much denser conditions. The radial uniformity can be improved but the local bed density is reduced by a higher gas velocity under the same G_s or a lower solids circulation rate under the same U_g, which is consistent with the experimental results. At the same superficial gas velocity, when increasing solids circulation rate to the high-density conditions of the CFB riser, the G_s has a greater impact on the wall region than the center of the riser so that an extremely high solid concentration can be found near the wall in the HDCFB.
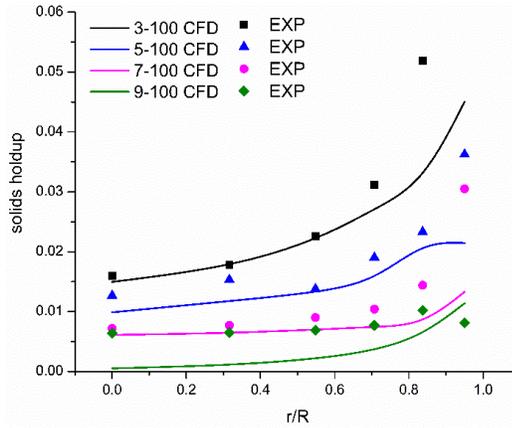
(a) LDCFBs (U_g = 3, 5, 7, and 9 m/s, G_s = 100 kg/m²s)
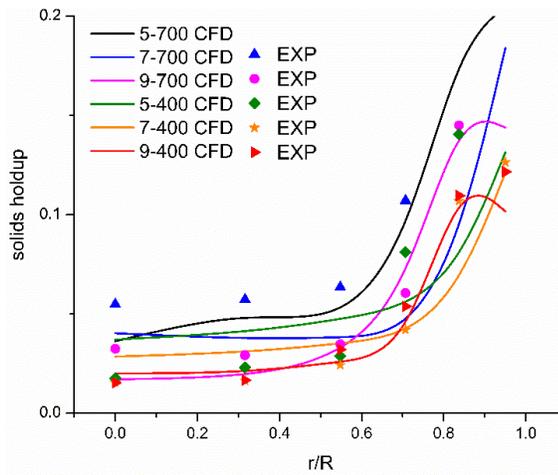
(b) HDCFBs (U_g = 5, 7, and 9 m/s, G_s = 400, 700 kg/m²s)

Figure 4-4: comparison of the radial solids holdup profiles in the LDCFB and HDCFB at height = 7.35 m
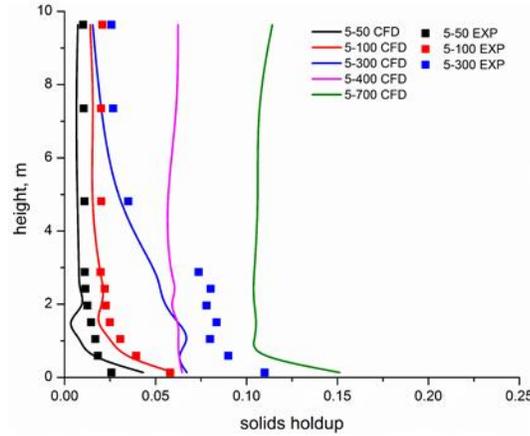
Figure 4-5: Axial solids holdup profiles under different solids circulation rates
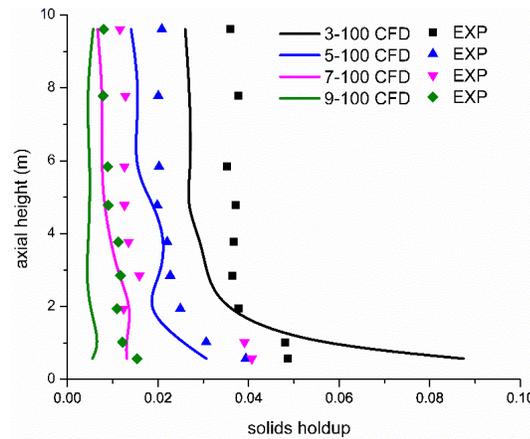
Figure 4-6: Axial solids holdup profiles under different superficial gas velocities

The axial profiles of the solids holdup under the same U_g or the same G_s are compared in Figure 4-5 and Figure 4-6, respectively. A more distinct dense bottom region can be found under dense conditions indicating that increasing G_s will let more solids accumulated at the bottom of the riser, which increases the overall bed density and results in a higher gas-solids contacting. The fully developed flow is achieved at h=3 m, both the LDCFB and HDCFB risers, ie. the solids distribution is uniform in the axial direction after h = 3 m.

Compared with the numerical results of the radial profiles, although the same tendency with the experimental data is achieved by the numerical simulations, deviations are found especially under dense conditions. For example, the cross-sectional solids holdup at the lower part of the riser under $U_g = 5$m/s and $G_s = 300$ kg/m^{2}s from the CFD results is around

84

0.07, which is lower than the cross-sectional solids holdup ($\varepsilon_{s,EXP} = 0.08$) measured in experiments as shown in Figure 4-5. Such a deviation of 12.5% between the simulation results and the experimental data is acceptable for the prediction of the overall tendency of the axial and radial distribution of the solids phase. A more accurate model is still needed and the reason of the discrepancy between the simulation results and the experimental data needs to be discovered. The lower solids holdup predicted by the CFD model might be due to the underestimation of the clustering effects by the current drag model in the CFB riser. On the other hand, the current drag model used in the simulations was developed based on the experimental data for LDCFB since most of the HDCFB experiments were conducted in the lately 20 years. The prediction of the solids holdup in the HDCFB riser in which more severe clustering effects are found is more likely to be underestimated. More discussion on the reason of the deviations of the simulation results from the experimental data will be stated in Chapter 6. Future work on the drag model modifications for a wider range of operating conditions will be performed in Chapters 6 and 7.

4.6.2 Transition from the LDCFB to HDCFB

4.6.2.1 Axial uniformity of the solids holdup distribution

Studies on the transition from low-density to high-density operating conditions in high velocity fluidization systems can be dated back to the 1990s, high bed density is the most remarkable characteristic under a high-density condition so that generally an overall bed density of $\varepsilon_s = 0.1$ is considered as the boundary to separate the LDCFB and HDCFB operations (Wang, et al., 2015). However, the flow details in an HDCFB have not been compared with the ones in LDCFB, and the transition between the LDCFB and HDCFB has not been specified.

Merely an overall bed density is not enough to distinguish the HDCFB from the LDCFB, Bai and Kato (1999) pointed out a saturation carrying capacity of gas, G_s^*, which describes the flow conditions by the shape of the axial solids holdup profile in the riser quantitatively. The saturated carrying solids circulation rate, G_s^*, is determined when the solids holdup at the bottom of the riser becomes constant and more solids accumulate at the bottom of the riser. Based on Bai and Kato's statement, the proposed saturation carrying solids

circulation rate, G_s^*, where the axial profile of solids distribution turns from an exponential shape to a S-shape marks the maximum achievable solids concentration in the dense region of the CFB riser. However, most of the experiments from Bai and Kato's study operated at $G_s \leq 200$kg/m^{2}s, which nowadays can only be considered as an intermediate dense condition between LDCFB and actual HDCFB and the so-called saturation solids concentration can be bridged, so that more studies on the axial profiles are needed.

Numerical results of the axial profiles of the solids distributions under the same gas velocity and different solids circulation rates are compared as shown in Figure 4-7, in which a low-density condition ($G_s = 100$ kg/m^{2}s), a high-density condition ($G_s = 700$ kg/m^{2}s), and an intermediate condition ($G_s = 300$ or 400 kg/m^{2}s) are selected for the comparison purpose. A typical exponential axial structure of solids holdup is found in a LDCFB as shown in Fig. 4-6 (G_s=100 kg/m^{2}s), the solids suspension is dilute and uniformly distributed along the riser except for a very short entrance region under the low G_s. Under the intermediate G_s around the saturated carrying G_s^*, both the exponential profile ($U_g = 7$ m/s, $G_s = 300$ kg/m^{2}s) and the S-shape profile ($U_g = 9$ m/s, $G_s = 400$ kg/m^{2}s) of the solids holdup can be found. The solids tend to accumulate at the bottom of the riser when G_s exceeds G_s^* and the denser bottom zone enlarges with the increase in G_s to form a typical S-shape axial profile of solids under a relatively high-density condition, which is consistent as the descriptions from Bai and Kato (1999). However, in an HDCFB when G_s reaches 700 kg/m^{2}s, the entire riser is occupied by the denser and relatively more uniform solids suspension flow and the exponential shape of the axial profile reoccurs instead of the S-shape profile with a much higher solids holdup as shown in Figure 4-7. With the increase in solids circulation rate, both the LDCFB and HDCFB show a relatively more uniform exponential axial profile of solids holdup but the solids holdup is much higher in the HDCFB, however, a less uniform S-shape profile with a denser bottom zone in the riser is often found under intermediate conditions. With the transition from the LDCFB to HDCFB, the accumulation of solids at the bottom of the riser occurs beyond the saturated carrying G_s^*, which increases the nonuniformity of the gas-solids flow when increasing G_s. However, further increasing G_s to a typical HDCFB, the inflection of the upper dilute and bottom dense zones disappears because the denser solids suspension occupies the entire riser and the gas-solids flow becomes homogeneous again with a much higher density.
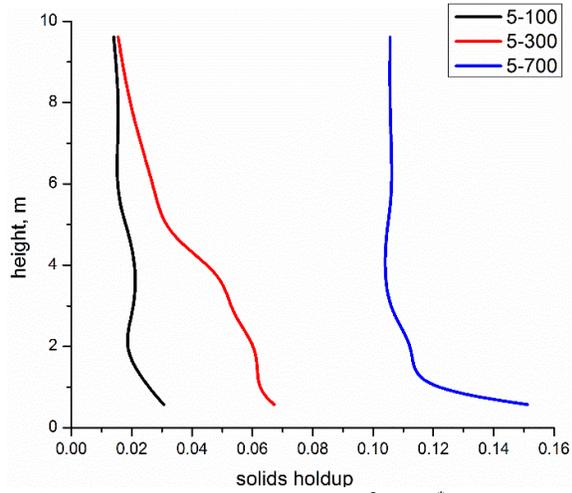
(a) U_g = 5m/s, G_s = 100, 300, 700 kg/m^{2}s (G_s^* = 150 kg/m^{2}s)
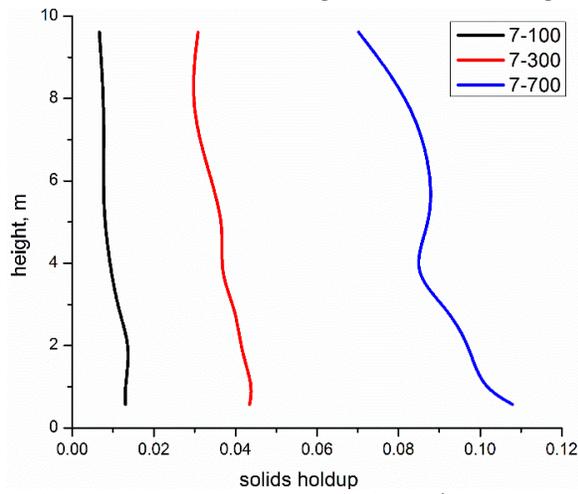
(b) U_g= 7 m/s, G_s = 100, 300, 700 kg/m^{2}s (G_s^* = 278 kg/m^{2}s)
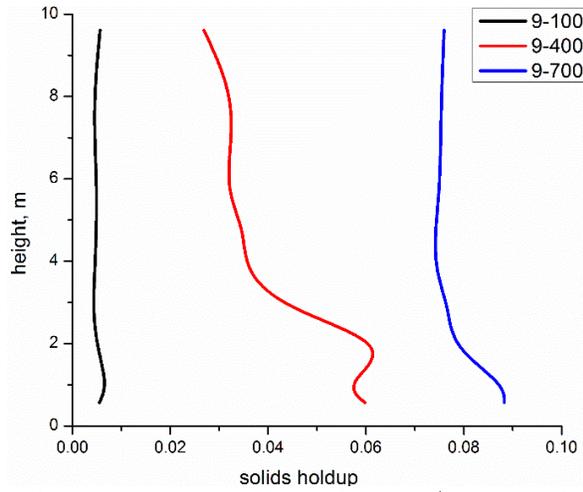
(c) U_g = 9m/s, G_s = 100, 400, 700 kg/m^{2}s (G_s^* = 442 kg/m^{2}s)

Figure 4-7: Axial distributions of the solids holdup under different operating conditions

87

4.6.2.2 Radial uniformity of the solids holdup distribution

In the LDCFB, the solids holdup at wall decreases obviously from nearly 0.10 to 0.01 and increases gradually in the center region along the riser from the bottom to the upper zone as shown in Figure 4-8(a). Correspondingly, the center dilute region has a low solids concentration expands from r/R = 0 - 0.58 to r/R = 0 - 0.85, indicating a more uniform local solids distribution in the radial direction from the entrance region to the fully developed region of the LDCFB riser. However, such an obvious decrease in the solids holdup at the wall does not happen in the HDCFB as shown in Figure 4-8 (b). A denser and thicker wall region was developed at the entrance region of the HDCFB riser and the solids holdup only drops slightly along the riser, i.e. the denser wall layer due to the high G_s exists along the entire HDCFB riser. Unlike the LDCFB where the center dilute region becomes wider in the upper zone of the riser, the dilute core region in the HDCFB even shrinks from the bottom to the exit of the riser as shown in Figure 4-8 (b). Except for a dilute core region with a flat solids holdup distribution and a wall region with dramatically increased solids holdup, a transition region between the core and the wall layer is from r/R = 0.4 to r/R = 0.6 in the HDCFB where the solids holdup gradually increases form the center to the wall.

(a)

(b)
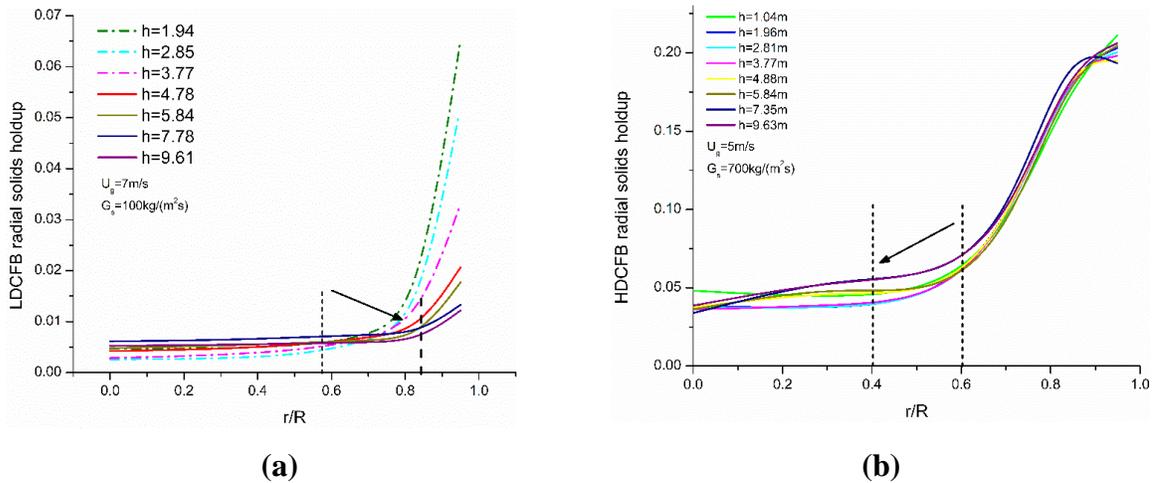
Figure 4-8: Local profiles of solids holdup at different heights (a) LDCFB (U_g = 7 m/s, G_s = 100 kg/m²s); (b) HDCFB (U_g = 7 m/s, G_s = 700 kg/m²s)
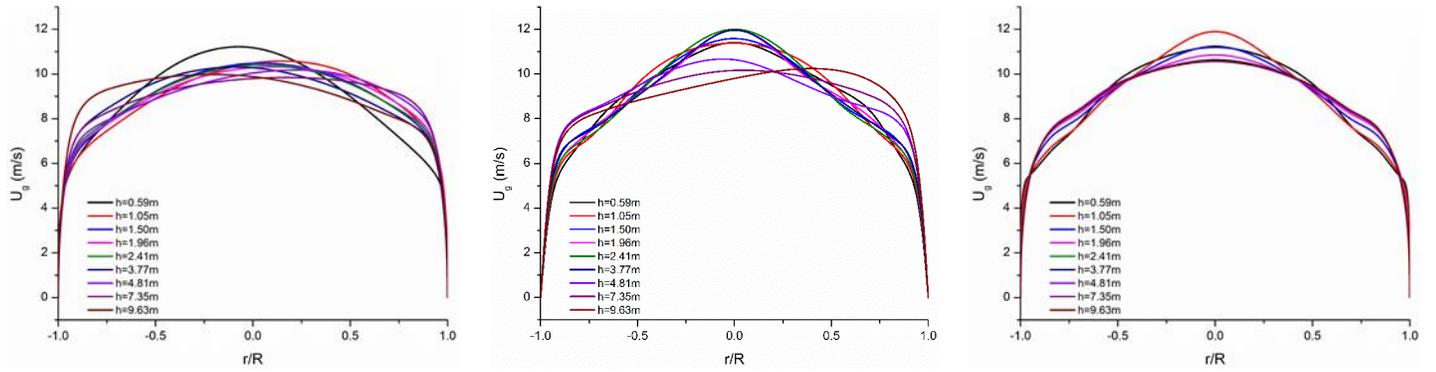
Radial profiles of gas velocity at different heights under U_g = 9m/s, G_s = 100, 400, 700kg/(m²s)
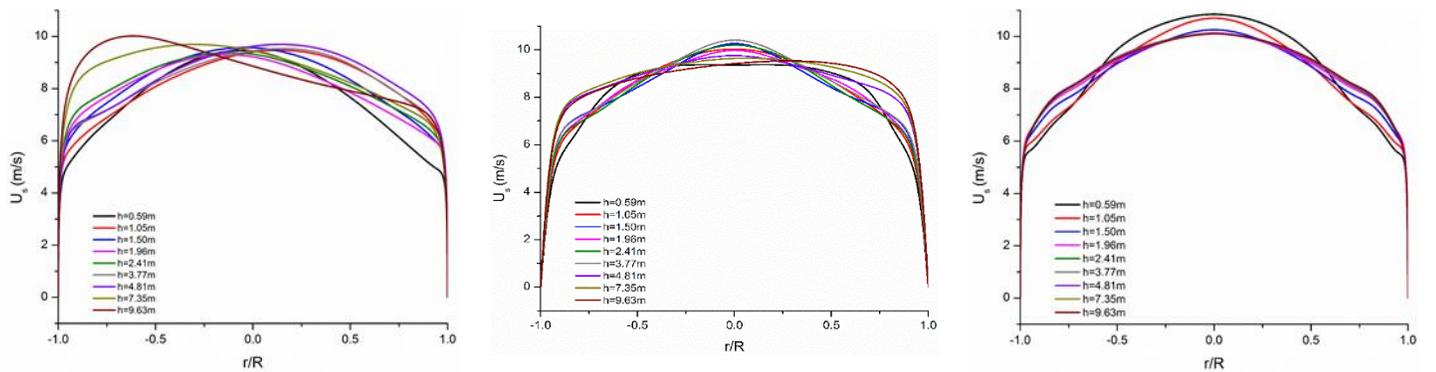
Radial profiles of particle velocity at different heights under U_g = 9m/s, G_s = 100, 400, 700 kg/(m²s)
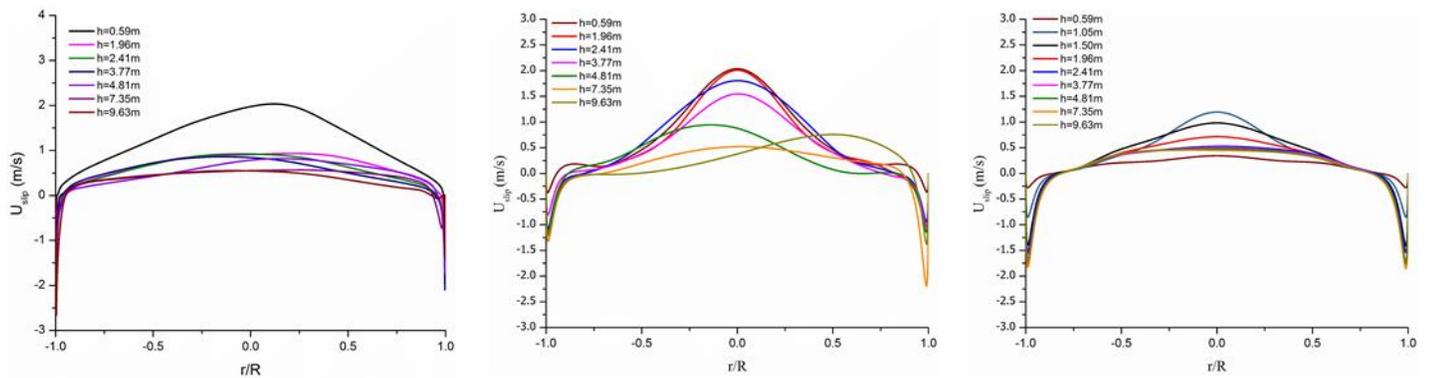
Radial profiles of slip velocity at different heights under U_g = 9m/s, G_s = 100, 400, 700 kg/(m²s)
(a) LDCFB   (b) Intermediate condition   (c) HDCFB

Figure 4-9: Profiles of the axial velocities for gas and solids phases, and slip velocities between the gas and particles in the LDCFB and HDCFB (a) LDCFB; (b) Intermediate condition; (c) HDCFB

Although sharing some similar characteristics of the local flow structures such as the typical core-annulus distribution of solids, higher solids circulation rates display impacts

not only on the bed density but also on the uniformity of the velocity profiles as shown in Figure 4-9. The axial velocity profiles of the gas and solids phases, and the slip velocity between the gas and particles also reveal the transitions of the flow structure from low-density operations to high-density operations as shown in Figure 4-9.

Generally, both the axial velocity profiles of gas and particles show a power-law profile with a higher velocity in the center and lower velocity at wall as shown in Figure 4-9. Both the gas and particle velocity profiles along the radial direction are more uniform in the entire riser in the LDCFB than those in the HDCFB, where a higher axial velocity in the center of the riser and a lower axial velocity near the wall region can be found. Therefore, in the HDCFB, more solids particles flow through the wider annulus layer which contributes a thicker and denser wall region of the solids distribution as shown in Figure 4-8 (b). The development process of the flow uniformity from LDCFB to HDCFB can be illustrated by the diagram for the intermediate condition (U_g = 9m/s, G_s = 400 kg/m^{2}s) as shown in Figure 4-9 (b), under a moderate solids circulation rate, the axial velocity profile is less flatter at the bottom of the riser while becomes flatter at the upper zone which echoes the s-shape axial profile of the solids holdup in Figure 4-7 (c).

The slip velocities which are the difference from the axial velocities between gas and particles from the low-density conditions to the high-density conditions are also plotted in Figure 4-9. The slip velocity becomes lower and more uniform along the axial direction in the riser, which is reasonable since the gas-solids flow gradually develops to a fully developed state after the entrance region. However, the slip velocity under the intermediate condition has the least uniform distribution and a much higher slip velocity in the center region at the bottom dense zone of the riser, which indicates a more active gas-solids interactions and a transition state from the LDCFB to HDCFB in that region of the riser.

Besides, the axial solids velocity is found to be larger than the axial gas velocity close to the wall of the CFB riser under some cases, which results in the slip velocities to be negative near the wall region. In fact, it should be noted that the velocity magnitude of the gas phase is still larger than the one of the solids phase near the wall region, while the lateral velocity of the gas phase is much larger than the lateral particle velocity, leading to

a smaller axial gas velocity than the axial particle velocity there. Future study should be carried out on the more accurate wall boundary conditions for the gas-solids CFB riser.

4.6.2.3 Flow development of the solids phase

With the help of numerical results, the gradients of particle velocity ($\Delta V_p = \frac{\left|V_{p_{x,y+1}} - V_{p_{x,y}}\right|}{V_{p_{x,y}}} \times 100\%$) can be derived based on the solids velocity difference between the two axial neighboring grids. The solids flow with the gradients less than 2% is defined as the fully developed state. The lowest positions with the time averaged results of $\Delta V_p < 2\%$ along the CFB riser are marked as shown in Figure 4-10 which indicate the positions for the solid flow firstly becomes fully developed. Three operating conditions (U_g = 5m/s, G_s = 100, 400, 700 kg/m^{2}s) from the low-density operating condition to the high-density operating condition in the CFB riser are compared in Figure 4-10. The trendlines of scattered positions of the fully developed flow are also fitted as shown in Figure 4-10.
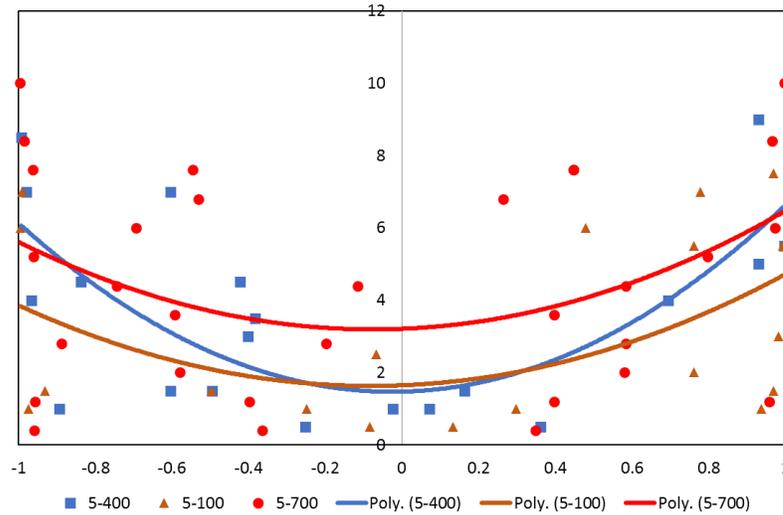
Figure 4-10 Local positions of $\Delta V_p < 2\%$ in the CFB riser for the fully developed solids flow

Generally, the developing region of the solids flow in the CFB riser is less than a half of the length of the CFB riser due to the high-velocity conditions. The increase in the solids velocity is faster in the center region of the riser and gradually become slower towards the

wall due to the wall effects, and the effect of clusters near the wall since more clusters exist in the near wall region. So the solids holdup in the fully developed region is lower in the center and higher near the wall of the riser as shown in Figure 4-10. From a low-density operating condition to a high-density operating condition, the solids flow takes a longer development region in the CFB riser since more particles need to be accelerated under a higher solids circulation rate. As shown in Figure 4-10, the trendline of the marked fully developed positions in the LDCFB (G_s=100 kg/m^{2}s) seems to be parallel with the trendline in the HDCFB (G_s=700 kg/m^{2}s) but with different entrance lengths, indicating that the developments of the solids flow are similar in the radial direction between the dilute and dense flow conditions. However, when the CFB riser is operated under the intermediate condition (G_s = 400 kg/m^{2}s), the profile of the marked fully developed positions for the solids flow is less flatter than the cases for LDCFB and HDCFB as shown in Figure 4-10. Under the intermediate condition (G_s = 400 kg/m^{2}s), the solids flow in the center region of the CFB riser is closer to the LDCFB while the flow in the wall region is closer to the HDCFB, which also indicates that the impacts of the high-density operation act in the wall region at first and then intrude to the center region of the CFB riser.

4.6.3 Prediction of the overall bed density

The numerical simulations for a wide operating range of CFB risers from dilute to dense conditions are conducted in this work and Figure 4-11 and Figure 4-12 show the numerical results of the axial solids holdup distribution and overall bed density under different operating conditions. It can be found that the solids holdup tends to have a greater increase when increasing G_s while less increase is caused by increasing U_g, which indicates that the solids circulation rate has a greater impact on the transition of the overall bed density than the superficial gas velocity. Higher G_s in a HDCFB results in more particle clusters, so that a higher bed density is achieved since the denser clusters move slower than single particles in the riser.

As discussed before, the general gas-solids flow structure and the overall bed density of a CFB riser under the same superficial gas velocity or the same solids circulation rate are similar. However, the relationship between the flow conditions operated under different G_s-U_g pairs is unclear due to lacking enough experimental data. Although several

correlations of the overall bed density have been proposed before (Issangya et al. 1999), none of them covered the high-density conditions ($G_s > 400$ kg/m^{2}s) in a CFB riser. Therefore, the combined effects of U_g and G_s on the overall bed density of the CFB riser is investigated in this study. Since different flow structures between the HDCFB and LDCFB have been revealed in literatures due to the much higher solids circulation rate in the HDCFB, a more accurate correlation to predict the overall bed density covering both the LDCFB and HDCFB regimes is needed.
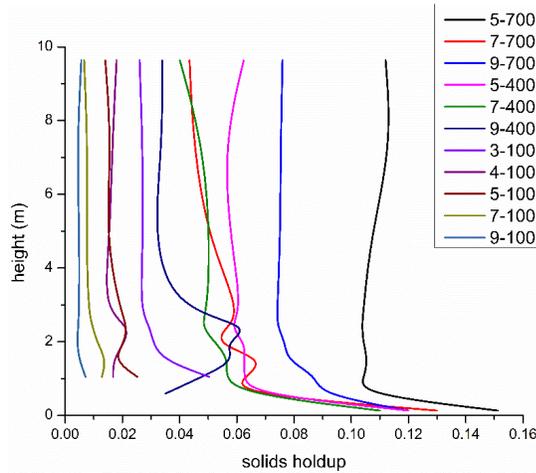
Figure 4-11: Axial solids holdup distribution in LDCFBs and HDCFBs
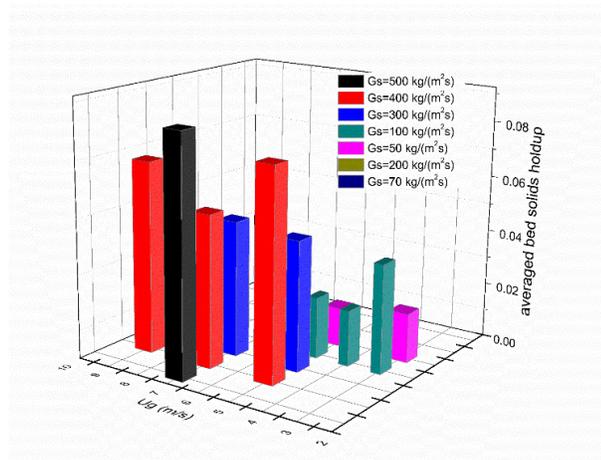
Figure 4-12: Overall bed density of LDCFBs and HDCFBs

The CFD results of the overall bed density, which are obtained by the averaged volume fraction of the solids phase in the whole computational domain, agree with the

experimental data within a deviation of 30% for most of the cases as shown in **Error! R eference source not found.** although there are some small deviations for the overall bed density in several cases since the particle clustering phenomenon is underestimated under extremely higher G_s conditions. The overall bed densities under different U_g-G_s conditions are listed in Table 4-4.

The overall bed density can be considered as a function of the superficial gas velocity and solids circulation rate. Under ideal homogeneous flow condition in which particles are uniformly dispersed, the overall solids holdup in the dispersed gas-solids system without including the clustering effects can be derived as:

$$\varepsilon_s' = \frac{G_s}{\rho_p \cdot V_p} \tag{4-18}$$

where ε_s' is the overall bed density in the homogeneous gas-solids system, V_p is absolute particle velocity. In the gas-solids CFB riser where particle clusters exist causing a larger slip velocity between gas and particles, the particle velocity is assumed as a function of the superficial gas velocity. Thus, the overall solids holdup in a gas-solids CFB riser can be roughly estimated as:

$$\varepsilon_s = (\frac{G_s}{\rho_p \cdot U_g})^m \tag{4-19}$$

where ε_s represents the overall bed density in the heterogeneous gas-solids system in the CFB riser. However, under extremely dense conditions, the clustering phenomenon is much more severe which results in the accumulation of solids inside the CFB riser as known as the saturation of particles described by Bai and Kato (1995). Under high-density conditions, G_s has a greater impact on the overall bed density than U_g especially when G_s is much greater than G_s^* as discussed before, so a correction factor based on the exceeded G_s of the saturation carrying capacity is needed in the calculation. The correction factor related to the saturation capacity and the Froude number (Fr $=\frac{U_g}{\sqrt{g d_p}}$) is included to adjust the overall solids holdup under high-density conditions and can be expressed as:

$$(\frac{G_s - G_s^*}{G_s \cdot Fr})^n \tag{4-20}$$

By fitting with the experimental data, the two exponents are selected as: m=0.9, and n is decided by the ratio of the excess solids circulation rate and the Stokes number of the gas-solids flow. Froude number and Stoke number are taken into consideration because they both present the impacts from the external flow field on the particles.

Therefore, an index for predicting the average bed solids holdups under different operating conditions is developed based on the numerical results as shown in the following:

$$I = (\frac{G_s}{\rho_p \cdot U_g})^{0.9} + (\frac{G_s - G_s^*}{G_s \cdot F_r})^n, \qquad n = \begin{cases} 2, & \frac{G_s - G_s^*}{S_{tr}} < 0; \\ 0.45, & 0 < \frac{G_s - G_s^*}{S_{tr}} < 1.5; \\ 0.85, & \frac{G_s - G_s^*}{S_{tr}} \geq 1.5 \end{cases} \qquad (4\text{-}21)$$

where Fr is Froude number: $Fr = \frac{U_g}{\sqrt{g d_p}}$, G_s^* is the saturation carrying capacity from Bai and Kato (1995). The index consists of a general correlation of the overall bed density $(\frac{G_s}{\rho_p \cdot U_g})^{0.9}$ in a CFB riser and a correction factor $(\frac{G_s - G_s^*}{G_s \cdot F_r})^n$ due to the high-density condition.

Table 4-4: Overall bed densities of different G_s-U_g pairs

U_g, m/s	G_s, kg/m²s	CFD-ε_S	EXP-ε_S	I
5	50	0.0140	0.0120	0.010791
7	70	0.0150	0.0100	0.010807
10	100	0.0097	NA	0.010815
9	100	0.0102	NA	0.011845
3	50	0.0180	0.0180	0.016921
7	100	0.0186	0.0150	0.014771
5	100	0.0220	0.0230	0.019942
4	100	0.0200	0.0260	0.024588
9	200	NA	0.0320	0.021931
7	200	0.0390	0.0400	0.027484
9	300	0.0690	0.0600	0.031571
7	300	0.0480	0.0630	0.064592
10	400	0.0500	NA	0.037202
9	400	0.0490	0.0700	0.040901
5	300	0.0460	0.0880	0.122671
7	400	0.0540	0.0960	0.098711

9	500	NA	0.1010	0.077316
5	400	0.0750	0.1040	0.077169
7	500	0.0850	0.1070	0.118841
9	600	NA	0.1170	0.098503
9	700	0.0884	0.1340	0.113758
7	600	NA	0.1280	0.135016
5	700	NA	0.1130	0.124271
10	1400	NA	0.1198	0.119107

Figure 4-13 compared the overall bed densities from the volume-weighted CFD results of the solids phase volume faction and from the experimental data with the proposed index (*I*), respectively. It can be seen that most of the results from CFD and experiment agree well with that from the proposed index (*I*) within a deviation of 30%, indicating the promising practicability of the proposed index for comparing the overall bed density under different operating conditions.
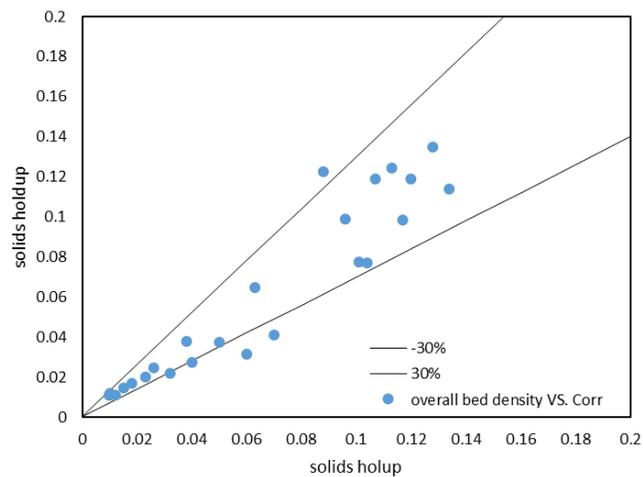
Figure 4-13 Comparisons of the proposed index (*I*), experimental data, and CFD results

It should be noted that the index (*I*) has little deviations from the experimental data of the overall bed density under very dilute or extremely dense flow conditions because the saturation capacity (G_s^*) from Bai and Kato (1995) was correlated based on the experiments operated under a $G_s \leq 120$ kg/m²s, which needs further correction for high-density operating conditions. However, the index (*I*) still can be used to indicate the rank

of the overall bed density in the CFB riser under different U_g-G_s pairs because it shows a good consistence with the experimental results of the overall bed density as shown in Table 4-5. A 3D map of the predicted overall bed density by Eq. (4-21) under different U_g-G_s pairs is plotted as Figure 4-14. A plane of ε_s=0.10 almost evenly divides the 3D map into a low-density regime and a high-density regime as shown in Figure 4-14. Obviously, the greater curvature of the 3D map takes place in the HDCFB regime indicating that the high-density operations have a significant impact on the increase in the overall bed density in a CFB riser. More details are provided in Figure 4-15 where a 2D map with a series of overall solids holdup lines (ε_s=0.05, 0.10, 0.15, 0.20) is plotted according to the top view of the 3D map (Figure 4-14).
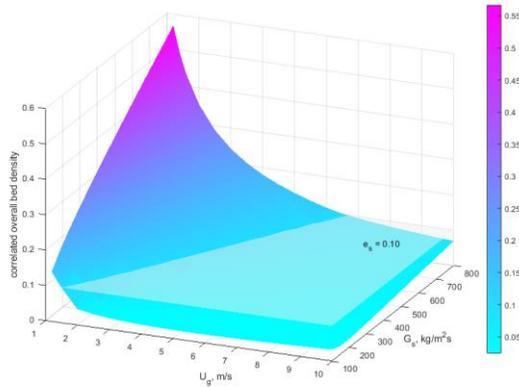
Figure 4-14: 3D map of the predicted overall bed density
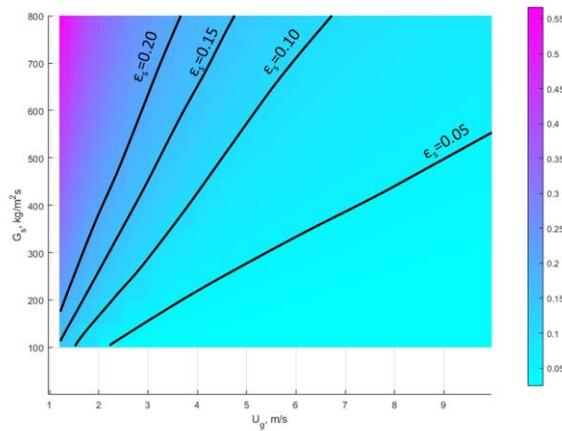
Figure 4-15: 2D map of the predicted overall bed density

97

4.7 Conclusion

The comparisons between LDCFBs and HDCFBs are discussed based on the CFD results. The high-density conditions in a CFB riser show many different distinct characteristics from the low-density conditions. The typical core-annulus radial flow structure appears in both LDCFBs and HDCFBs, however, a HDCFB has a much denser and wider annulus layer. Both the LDCFB and HDCFB have an exponential shape of the axial solids holdup profile while the S-shape profile can be found under intermediate conditions, indicating the transition between the LDCFB and HDCFB. Velocity profiles of gas, particles, and slip velocity also show the transition between the LDCFB and HDCFB in which both the LDCFB and HDCFB have a relatively higher uniformity of the gas-solids flow and the one under intermediate condition shows the worst uniformity. An index is developed as a function of the superficial gas velocity and solids circulation rate to predict the overall bed density under different U_g-G_s operating conditions.

Nomenclature

d_p	Particle diameter, m
e_{ss}	Coefficient of particle-particle restitution
Fr	Froude number, $=\dfrac{U_g}{\sqrt{g d_p}}$
$g_{o,ss}$	Radial distribution function of particles
G_s	Solids circulation rate, kg/m^{2}s
G_s^*	Saturation carrying capacity of gas, kg/m^{2}s
$\bar{\bar{I}}$	unit tensor
h	Axial distance from the gas distributor, m
H	Total height of the CFB riser, m
k	Turbulent kinetic energy, m^2/s^2
P	Fluid phase pressure, Pa
P_s	Solids phase pressure, Pa
r	Radial position of the CFB riser, m

R	Radius of the CFB riser, m
Re_r	Relative particle Reynolds number, $= \dfrac{\rho_g d_p |\overrightarrow{v_s} - \overrightarrow{v_g}|}{\mu_g}$
U_g	Superficial gas velocity, m/s
v_g	Gas phase velocity, m/s
v_r (U_r)	Relative velocity: the ratio of the terminal settling velocity of a multiparticle system to that of an isolated particle
v_s	Solid phase velocity, m/s
$v'_{s\tau}$	Random component of the particle velocity, m/s
ΔV_p	Gradients of particle velocity,
V_p	Absolute particle velocity, m/s
$V_{p_{x,y}}$	Particle velocity in every grid, m/s
$V_{g,in}$	Inlet gas velocity, m/s
$V_{s,in}$	Inlet velocity of the solid phase, m/s
α_g	Gas phase volume fraction
α_s	Solid phase volume fraction
$\gamma_{\Theta s}$	Collisional dissipation of energy
$K_{sg}=K_{gs}$	Interphase momentum exchange coefficient
ε	Dissipation rate of the turbulent kinetic energy
ε'_s	Overall solids holdup in the dispersed gas-solids system
ε_s	Overall solids holdup in a gas-solids CFB riser
λ	Phase bulk viscosity, kg/ms
μ	Phase shear viscosity, kg/ms
$\mu_{g,t}$	Gas phase turbulent viscosity, kg/ms
$\mu_{s,t}$	Solids phase turbulent viscosity, kg/ms
ρ_g	Gas density, kg/m^3
ρ_s	Particle density, kg/m^3
$\emptyset_{gs}$	Granular temperature of particles, m^2/s^2
$\overline{\overline{\tau}}$	Phase stress-strain tensor, kg/s^2
φ	Ratio of the opening area in the gas distributor

Subscripts:

g	Gas phase
s	Solids phase
x	x axis
y	y axis
p	Particles

References

ANSYS, Inc. (2013). Chapter 17. Multiphase Flows. ANSYS Fluent Theory Guide. Pp. 527-586

Armellini, Costanzob, Castroa, Vergela & Martignonic (2015). Effect of different gas-solid drag models in a high-flux circulating fluidized bed riser. Chemical Engineering, 43: 1627-32.

Bai & Kato. (1995). Saturation Carrying Capacity of Gas and Flow Regimes in CFB. Journal of Chemical Engineering of Japan 28(2): 179-85.

Bai & Kato. (1999). Quantitative Estimation of Solids Holdups at Dense and Dilute Regions of Circulating Fluidized Beds. Powder Technology 101(3): 183-90.

Bakshi, Altantzis, Bates & Ghoniem. (2015). Eulerian–Eulerian simulation of dense solid-gas cylindrical fluidized beds: impact of wall boundary condition and drag model on fluidization. Powder Technology 277: 47–62.

Bi & Grace. (1995). Flow regime diagrams for gas-solid fluidization and upward transport. International Journal of Multiphase Flow 21(6): 1229–36.

Carlos Varas, Peters & Kuipers (2017). CFD-DEM simulations and experimental validation of clustering phenomena and riser hydrodynamics. Chemical Engineering Science, 169, 246–258.

Ding & Gidaspow. (1990). A bubbling fluidization model using kinetic theory of granular flow. AIChE journal 36.4: 523-538.

Grace. (1986). Contacting Modes and Behaviour Classification of Gas-solid and Other Two‐phase Suspensions. The Canadian Journal of Chemical Engineering 64(3): 353‐63.

Grace (1990). High-velocity fluidized bed reactors. Chemical Engineering Science, 45(8), 1953–1966.

Hensler, Firsching, Bonilla, Wörlein, Uhlmann & Wirth (2016). Non-invasive investigation of the cross-sectional solids distribution in CFB risers by X-ray computed tomography. Powder technology, 297, 247-258.

Horio. (2010). Fluidization Science, Its Development and Future. Particuology 8(6): 514-24.

Issangya, Bai, Bi, Lim, Zhu & Grace. (1999). Suspension densities in a high-density circulating fluidized bed riser. Chemical Engineering Science, 54(22), 5451-5460.

Jahnig, Campbell & Martin (1980) History of Fluidized Solids Development at Exxon. In: Grace J.R., Matsen J.M. (eds) Fluidization. Springer, Boston, MA

Kunii, Daizo & Levenspiel. (1997). Circulating Fluidized-Bed Reactors. Chemical Engineering Science 52(15): 2471–82.

Li (2010.) Investigation of circulating fluidized bed riser and downer reactor performance for catalytic ozone decomposition. Ph.D thesis, University of Western Ontario.

Shah, Utikar, Pareek, Evans & Joshi. (2016). Computational fluid dynamic modelling of FCC riser: A review. chemical engineering research and design, 111, 403-448.

Syamlal & O'Brien. (1989). Computer Simulation of Bubbles in a Fluidized Bed. AIChE Symposium Series. 85 (1989) 22-31.

Ullah, Atta, Wang & Li. (2013). 'Generalized Fluidization' Revisited. Industrial and Engineering Chemistry Research 52(33): 11319–32.

Upadhyay, Mukesh & Park. (2015). CFD Simulation via Conventional Two-Fluid Model of a Circulating Fluidized Bed Riser: Influence of Models and Model Parameters on Hydrodynamic Behavior. Powder Technology 272: 260–68.

Wang (2013). High-Density Gas-Solids Circulating Fluidized Bed Riser and Downer Reactors. Ph.D thesis, University of Western Ontario.

Wang, Wang, Li, Barghi & Zhu (2014). Catalytic ozone decomposition in a high density circulating fluidized bed riser. Industrial & Engineering Chemistry Research, 53(16), 6613-6623.

Wang, Li & Zhu (2015). Axial solids flow structure in a high density gas–solids circulating fluidized bed downer. Powder Technology, 272, 153–164.

Wang, Zhu, Barghi & Li (2014a). Axial and radial development of solids holdup in a high flux/density gas-solids circulating fluidized bed. Chemical Engineering Science, 108, 233–243.

Wang, Zhu, Li & Barghi (2014b). Detailed measurements of particle velocity and solids flux in a high density circulating fluidized bed riser. Chemical Engineering Science, 114, 9-20.

Zhang, Degrève, Dewil & Baeyens. (2015). Operation Diagram of Circulating Fluidized Beds (CFBs). Procedia Engineering 102: 1092–1103.

Zhang, Lei, Wang, Xu & Xiao (2015). A numerical study of gas–solid flow hydrodynamics in a riser under dense suspension upflow regime. Powder technology, 280, 227-238.

Zhu & Bi. (1995). Distinctions between Low Density and High Density Circulating Fluidized Beds. The Canadian Journal of Chemical Engineering 73(5): 644–49.

Zou, Bin, Li, Xia & Ma. (1994). Cluster Structure in a Circulating Fluidized Bed. Powder Technology 78(2): 173–78.

Chapter 5

5 Numerical study on a gas–solid circulating fluidized bed downer reactor

5.1 Introduction

With the increasing demand for petroleum products, chemical industry has seen more applications of high-velocity gas-solid circulating fluidized bed (CFB) reactors in the fast fluidization regime since the 1990s (Lehner & Wirth, 1999; Zhang, et al., 2001; Zhu, et al., 1995). A CFB system consists of a riser where chemical reactions take place and a downer that is usually used to recycle particles. However, the CFB downer reactor has attracted much more attention for chemical reactions in recent years due to its advantages compared with CFB risers such as more uniform flow structures, shorter residence time, and less back mixing (Zhu et al., 1995). Both the gas and solids flow downward concurrently in the CFB downer reactor in which the gravity also helps promote the relatively homogeneous flow development of the gas-solid suspension (Zhu et al., 1995). A remarkable fully developed region with nearly plug-flow condition was characterized and correlations on in the downer reactor, which is welcomed for gas phase catalytic reactions due to the less back-mixing (Lehner & Wirth, 1999; Li, et al., 2011; and Qi, et al., 2008). The hydrodynamic characteristics including axial and radial flow structures, mass and heat transfers, and reaction performances inside CFB downer have been comprehensively studied and compared with the CFB riser experimentally (Li et al., 2011; Lu et al., 2005; Ma & Zhu, 1999; Tuzla et al., 1998; Vaishali, et al., 2008; Wei, et al., 1994 and Zhang et al., 2001).

On the other hand, the gas-solid fluidization has reached a high-density operating condition in the CFB downer experimentally resulting in a more promising future application of downer reactor (Chen, et al., 2005; Guan et al., 2011; and Wang, et al., 2015). Compared to the low-density downer rector in which the solids holdup is too low to a high throughput, the high-density downer reactor under denser flow conditions is able to achieve a higher solids holdup with the help of the large solids circulation rate (Guan et al., 2011; Wang, et al., 2015). The hydrodynamics are found to be affected by the operating conditions in the downer reactor, which results in that both the radial and axial profiles of the solids holdup

and the particle velocity in the high-density downer are quite different from that in the low-density downer (Wang, et al., 2015a; 2015b and 2016). However, less numerical work has been conducted on CFB downers and only a few papers published with low solids circulation rate (Bolkan, et al., 2003; Cheng et al., 2014; Khongprom, et al., 2012; Liu, et al., 2017; Samruamphianskun, et al., 2012). Although both Eulerian-Eulerian two-fluid approach and Eulerian-Lagrangian discrete element method have been used for simulations of CFB downer reactor, the majority of them were focused on parametric studies on the numerical models by comparing different turbulence models, drag models, or the granular temperature models (Chalermsinsuwan, et al., 2012; Cheng, et al., 1999; Shu et al., 2014). Very few numerical studies on the gas-solid flow mechanism in downer reactors for gas phase catalytic reactions requiring smaller particles such as FCC have been carried out. Also, the CFD approach is considered as an effective tool for design and scale-up of chemical reactors with less cost and pollution. Most of the current experimental work on downer rectors were in lab-scale and better understanding of the scale-up effects in the downer is needed for industrial uses. Thus, a CFD model on a downer reactor for FCC particles is developed in this work and the scale-up effects are studied numerically as well.

5.2 Configuration of the CFB downer

5.2.1 Experimental CFB systems

The downer reactor simulated in this work is a part of a multifunctional circulating fluidized bed (MCFB) system as the red circled part shown in Figure 5-1 (Wang, 2013). The downer rector is 5.8 m high with a diameter of 7.62cm (3in), which is connected with a riser to complete the solids circulation. Figure 5-2 shows a zoomed in schematic diagram of the gas distributor and solids feeding tubes at the entrance region of the CFB downer. A premixing for the particles to reach a minimum fluidization stage happens above the gas distributor as shown in Figure 5-2. The main gas distributor located at the top of the downer reactor with multiple holes which has an opening area of 50% to provide uniform gas inlet distribution. Several solids feed tubes introduce particles into the downer from the top at the same height of the gas distributor as shown in Figure 5-2. A high solids inventory of FCC particles up to 450 kg is equipped in the CFB system to provide enough pressure for high-density CFB operations with large solids circulation rate (Wang, 2013). Particles are

entrained out of the riser under a high superficial gas velocity, following with a pre-fluidization process by the auxiliary gas supply to achieve a smooth gas-solid suspension, and then enter into the downer reactor through the solids feed tubes with inlet gas through the main gas distributor simultaneously at the top. Solids particles used in the experiment are FCC particles with a density of 1500 kg/m^3 and diameter of 67 µm (Wang, 2013).

5.2.2 Mesh of the CFB downer

Figure 5-1 Configuration of the CFB system (Wang, 2013)

Figure 5-2 Schematic diagram of the gas distributor and solids inlet of the downer (Wang, 2013)

Figure 5-3 Mesh of the computational domain
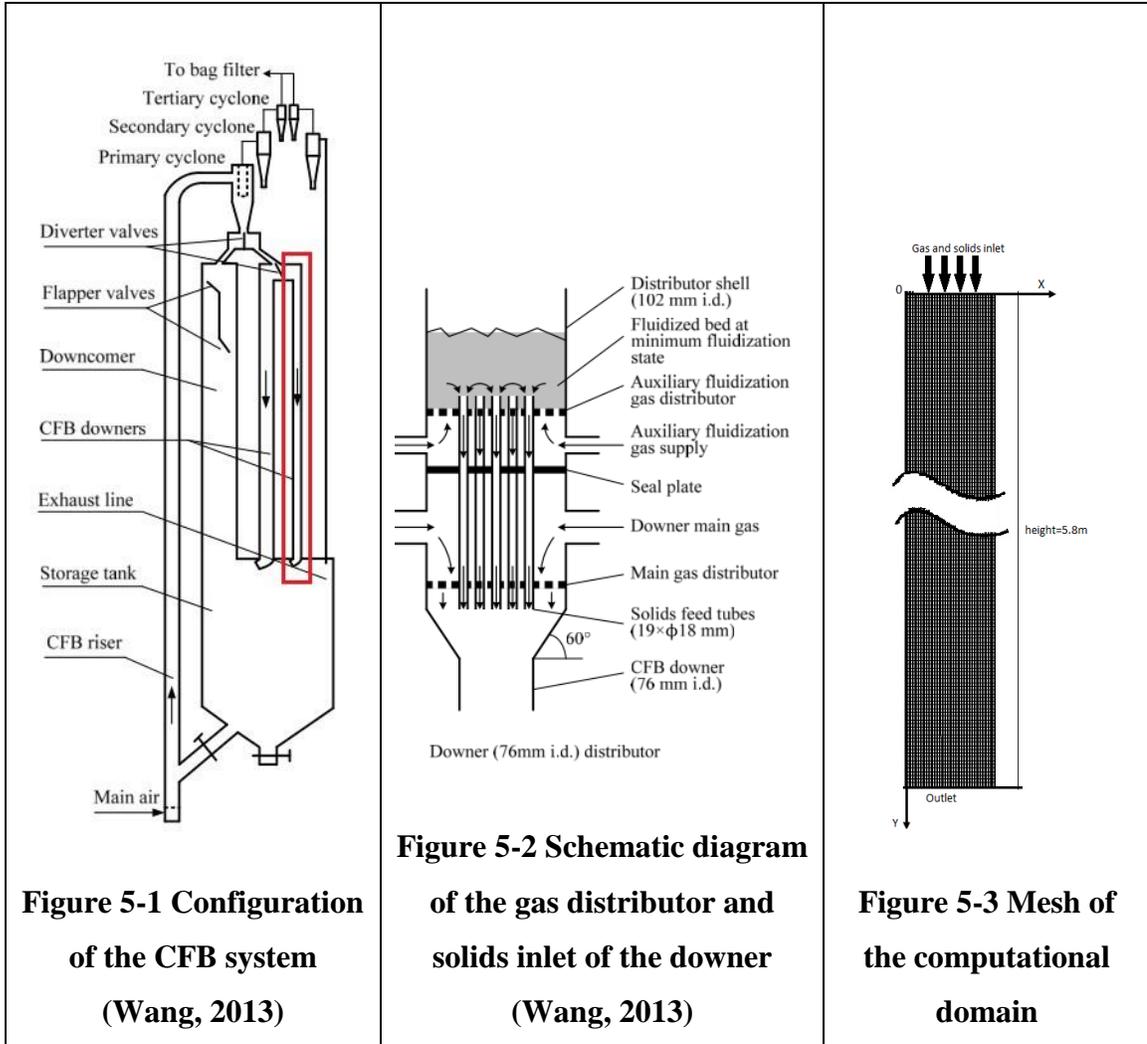
A quad grid system with finer mesh near the wall and the inlet as shown in Figure 5-3 is applied because the flow parameters in a CFB change greatly near those regions. Two sizes of meshes for the experimental downer and a scaled-up downer are setup in this work. The scaled-up downer has an inner diameter of 0.2m (8in) and the same height (5.8m) as the experimental downer. The mesh consists of 160000 cells with 80 nodes in the radial

direction and 2000 nodes in the axial direction. The minimum orthogonal quality of the mesh is 1.00 and the maximum aspect ratio is 3.8052, which indicate a good quality of the mesh. Because the grid systems are very similar between the CFB riser and downer reactors, detailed information of the grid independent test results can be found in Chapter 4.

5.3 Numerical method

5.3.1 Governing equations

A set of basic governing equations consisting of the mass and momentum conservation equations of both phases are used to solve the gas-solid flows (ANSYS, 2013).

Continuity equation for the gas phase:

$$\frac{\partial}{\partial t}\left(\alpha_g \rho_g\right) + \nabla \cdot \left(\alpha_g \rho_g \overline{v_g}\right) = 0 \tag{5-1}$$

Continuity equation for the solids phase:

$$\frac{\partial}{\partial t}\left(\alpha_s \rho_s\right) + \nabla \cdot \left(\alpha_s \rho_s \overline{v_s}\right) = 0 \tag{5-2}$$

where $\alpha_g + \alpha_s = 1$ \hfill (5-3)

Momentum equation for the gas phase:

$$\frac{\partial}{\partial t}\left(\alpha_g \rho_g \overrightarrow{v_g}\right) + \nabla \cdot \left(\alpha_g \rho_g \overrightarrow{v_g}\overrightarrow{v_g}\right) = -\alpha_g \nabla P + \nabla \cdot \left(\alpha_g \left(\overline{\overline{\tau_g^m}} + \overline{\overline{\tau_g^{Re}}}\right)\right) + \alpha_g \rho_g \vec{g} + K_{sg}\left(\overrightarrow{v_s} - \overrightarrow{v_g}\right) \tag{5-4}$$

where

$$\overline{\overline{\tau_g^m}} = -\frac{2}{3}\mu_{g.m}\nabla \cdot \overrightarrow{v_g}\overline{\overline{I}} + \mu_{g.m}\left(\nabla\overrightarrow{v_g} + \nabla\overrightarrow{v_g}^T\right)$$

$$\overline{\overline{\tau_g^{Re}}} = -\frac{2}{3}\left(\rho k_g + \mu_{g.t}\nabla \cdot \overrightarrow{v_g}\right)\overline{\overline{I}} + \mu_{g.t}\left(\nabla\overrightarrow{v_g} + \nabla\overrightarrow{v_g}^T\right)$$

Momentum equation for the solids phase:

$$\frac{\partial}{\partial t}(\alpha_s \rho_s \overrightarrow{v_s}) + \nabla \cdot (\alpha_s \rho_s \overrightarrow{v_s}\overrightarrow{v_s}) = -\alpha_s \nabla P - \nabla P_s + \nabla \cdot \left(\alpha_s \left(\overline{\overline{\tau_s^m}} + \overline{\overline{\tau_s^{Re}}}\right)\right) + \alpha_s \rho_s \vec{g} +$$

$$K_{sg}\left(\overrightarrow{v_g} - \overrightarrow{v_s}\right) \tag{5-5}$$

where

$$\overline{\overline{\tau_s^m}} = (\lambda s - \frac{2}{3}\mu_s)\nabla \cdot \overrightarrow{v_s}\overline{\overline{I}} + \mu_s(\nabla \overrightarrow{v_s} + \nabla \overrightarrow{v_s}^T)$$

$$\overline{\overline{\tau_s^{Re}}} = -\frac{2}{3}(\rho k_s + \mu_{s,t}\nabla \cdot \overrightarrow{v_s})\overline{\overline{I}} + \mu_{s.t}(\nabla \overrightarrow{v_s} + \nabla \overrightarrow{v_s}^T)$$

where the solid phase pressure (Ps), the solids shear viscosity (μ_s), and the solids bulk viscosity (λs) in the momentum equation are derived from the kinetic theory of granular flow model (Gidaspow & Ding, 1990). The fluctuation velocity of particles, which comes from the collisions between the particles, also can be calculated by the granular temperature.

Transport equation for the granular temperature (Gidaspow & Ding, 1990):

$$\frac{3}{2}\left[\frac{\partial}{\partial t}(\rho_s \alpha_s \Theta s) + \nabla \cdot (\alpha_s \rho_s \overrightarrow{v_s}\Theta s)\right] = \left(-P_s\overline{\overline{I}} + \overline{\overline{\tau_s}}\right):\nabla \overrightarrow{v_s} + \nabla \cdot (k_{\Theta s}\nabla\Theta) - \gamma_{\Theta s} + \emptyset_{gs} \tag{5-6}$$

where

$$\emptyset_{gs} = -3k_{gs}\Theta s$$

The collisional energy can be obtained by:

$$\gamma_{\Theta s} = \frac{12(1 - e_{ss}^2)g_{o,ss}}{d_s\sqrt{\pi}}\rho_s\alpha_s^2\Theta_s^{3/2}$$

The gas-solid two-phase flows are very complicated due to the vigorous interactions between the gas and solids. The motions of the particles are affected by the mean solids

velocity, single particle fluctuations and the particle-particle collisions. Therefore, a turbulence model for per phase, which is more accurate, is used in the simulation.

The standard k-ε turbulence model is applied into both the gas and solid phases.

k equation of the gas phase:

$$\frac{\partial}{\partial t}(\alpha_g \rho_g k_g) + \nabla \cdot (\alpha_g \rho_g \vec{v_g} k_g) = \nabla \cdot \left(\alpha_g \frac{\mu_{g,t}}{\sigma_k} \nabla k_g\right) + (\alpha_g G_{g,k} - \alpha_g \rho_g \varepsilon_g) + K_{sg}(C_{sg}k_s -$$

$$C_{gs}k_g) - K_{sg}(\vec{v_s} - \vec{v_g}) \cdot \frac{\mu_{s,t}}{\alpha_s \sigma_s} \nabla \alpha_s + K_{sg}(\vec{v_s} - \vec{v_g}) \cdot \frac{\mu_{g,t}}{\alpha_g \sigma_g} \nabla \alpha_g \qquad (5\text{-}7)$$

ε equation of the gas phase:

$$\frac{\partial}{\partial t}(\alpha_g \rho_g \varepsilon_g) + \nabla \cdot (\alpha_g \rho_g \vec{v_g} \varepsilon_g) = \nabla \cdot \left(\alpha_g \frac{\mu_{g,t}}{\sigma_k} \nabla \varepsilon_g\right) + \frac{\varepsilon_g}{k_g}(C_{1\varepsilon} \alpha_g G_{g,k} - C_{2\varepsilon} \alpha_g \rho_g \varepsilon_g +$$

$$C_{3\varepsilon}(K_{sg}(C_{sg}k_s - C_{gs}k_g) - K_{sg}(\vec{v_s} - \vec{v_g}) \cdot \frac{\mu_{s,t}}{\alpha_s \sigma_s} \nabla \alpha_s + K_{sg}(\vec{v_s} - \vec{v_g}) \cdot \frac{\mu_{g,t}}{\alpha_g \sigma_g} \nabla \alpha_g)) \quad (5\text{-}8)$$

where the turbulent viscosity, $\mu_{g,t} = \rho_g C_\mu \frac{k_g^2}{\varepsilon_g}$

k equation of the solids phase:

$$\frac{\partial}{\partial t}(\alpha_s \rho_s k_s) + \nabla \cdot (\alpha_s \rho_s \vec{v_s} k_s) = \nabla \cdot \left(\alpha_s \frac{\mu_{s,t}}{\sigma_k} \nabla k_s\right) + (\alpha_s G_{s,k} - \alpha_s \rho_s \varepsilon_s) + K_{gs}(C_{gs}k_g -$$

$$C_{sg}k_s) - K_{gs}(\vec{v_g} - \vec{v_s}) \cdot \frac{\mu_{g,t}}{\alpha_g \sigma_g} \nabla \alpha_g + K_{gs}(\vec{v_g} - \vec{v_s}) \cdot \frac{\mu_{s,t}}{\alpha_s \sigma_s} \nabla \alpha_s \qquad (5\text{-}9)$$

ε equation of the solids phase:

$$\frac{\partial}{\partial t}(\alpha_s \rho_s \varepsilon_s) + \nabla \cdot (\alpha_s \rho_s \vec{v_s} \varepsilon_s) = \nabla \cdot \left(\alpha_s \frac{\mu_{s,t}}{\sigma_k} \nabla \varepsilon_s\right) + \frac{\varepsilon_s}{k_s}(C_{1\varepsilon} \alpha_s G_{s,k} - C_{2\varepsilon} \alpha_s \rho_s \varepsilon_s +$$

$$C_{3\varepsilon}\left(K_{gs}(C_{gs}k_g - C_{sg}k_s) - K_{gs}(\vec{v_g} - \vec{v_s}) \cdot \frac{\mu_{g,t}}{\alpha_g \sigma_g} \nabla \alpha_g + K_{gs}(\vec{v_g} - \vec{v_s}) \cdot \frac{\mu_{s,t}}{\alpha_s \sigma_s} \nabla \alpha_s\right) \quad (5\text{-}10)$$

where the turbulent viscosity, $\mu_{s,t} = \rho_s C_\mu \frac{k_s^2}{\varepsilon_s}$.

The interactions between the gas and solids is included into a drag model. In the two-fluid CFD model, the momentum exchange, K_{gs} is calculated by the drag model. The drag force

of the gas-solid flow is related to the particle properties, flow regimes, and the Reynolds number. For FCC process in the riser, the Syamlal and O'Brien drag model (Syamlal & O'Brien, 1994) was found to calculate the drag coefficient more accurately and is used in this work.

$$K_{gs} = \frac{3\alpha_s \alpha_g \rho_g}{4v_r^2 d_s} \left(0.63 + \frac{4.8}{\sqrt{\frac{Re_r}{v_r}}} \right)^2 \left(\frac{Re_r}{v_r} \right) | \overrightarrow{v_s} - \overrightarrow{v_g} | \tag{5-11}$$

5.3.2 Boundary conditions

A profile velocity inlet boundary condition is used to both gas and solid phases at the top of the downer according to configurations of the gas distributor and solid feed tubes as shown in Fig. 7-3. For the solids phase, the actual solid inlet velocity in the feed tubes can be calculated based on the solids circulation rate, G_s, which is

$$V_{s,in} = G_s / (\varepsilon_{mf} \times \rho_s) \tag{5-12}$$

where $\varepsilon_{mf} = 0.58$, is the overall solids holdup under the minimum fluidization condition. The gas phase is assumed to have the same inlet velocity in the solid feed tubes. The gas inlet velocity at the jets of the gas distributor can be obtained from the superficial gas velocity, U_g, which is

$$V_{g,in} = (U_g \times A_T) - (V_s \times A_T \times (1\text{-}\varphi)) / (A_T \times \varphi) \tag{5-13}$$

where A_T is the cross-sectional area of the downer, and φ is the opening ratio of the gas distributor. No slip wall boundary condition is applied to the gas phase and partial slip wall boundary condition with a specularity coefficient of 0.0001 and a particle-wall restitution coefficient of 0.95 is applied to the solid phase in the simulation. The outflow boundary condition is used for both the gas and solids outlets located at the bottom of the downer.

5.3.3 Operating conditions

CFD simulations for a total of 13 cases are conducted under a superficial gas velocity from 3 to 7 m/s and a solids circulation rate from 100 to 700 kg/m²s in both the experimental and the scaled-up downers as shown in Table 5-1. Time averaged data was collected after

the simulation reaches a steady condition and the numerical results are compared with the available experimental data to validation the CFD model used in this work.

Table 5-1. CFD cases under different operating conditions

Cases #	Superficial gas velocity, U_g, m/s	Solids circulation rate, G_s, kg/m^{2}s	Downer ID, m
1	3	100	0.762
2, 3	5	100	0.0762, 0.2
4, 5	5	200	0.0762, 0.2
6, 7	5	300	0.0762, 0.2
8	5	500	0.0762
9, 10	5	700	0.0762, 0.2
11, 12	7	100	0.0762, 0.2
13, 14	7	200	0.0762, 0.2
15, 16	7	300	0.0762, 0.2
17	7	500	0.0762
18, 19	7	700	0.0762, 0.2

5.4   Results and discussion

5.4.1 Axial distribution of solids holdup

The general axial profiles of the solids holdup in the downer are shown in Fig. 5-4 under different superficial gas velocities at a same solids circulation rate. Figs. 5-5 and 5-6 show the axial solids holdup profiles from dilute to dense conditions under the superficial gas velocities of 5 m/s and 7m/s, respectively. A good agreement between the numerical results and the experimental data is achieved as shown in Figs. 5-4 to 5-6. It is clear that the overall solids concentration in a downer increases with the increase in the solids circulation rate and decrease in the gas velocity as shown in Figs. 5-4 to 5-6. The gas-solid suspension in the downer is very dilute, which usually has a solids holdup less than 0.05, because the particles move downward in the same direction of the gravity, so that they are accelerated to a high velocity quickly.
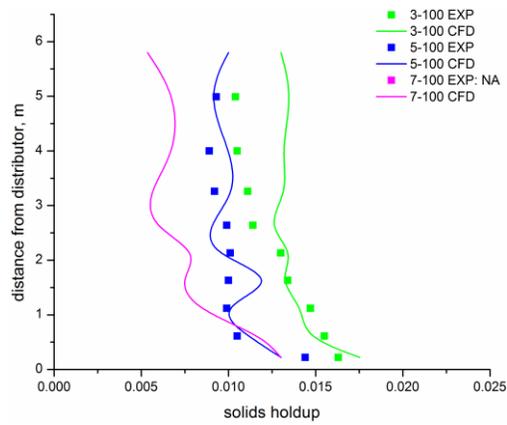
Figure 5-4 Axial profiles of the solids holdup under G_s = 100 kg/m²s
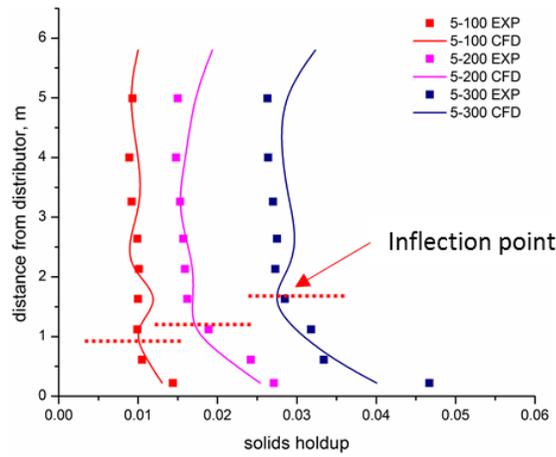
Figure 5-5 Axial profiles of the solid holdup in the 3 in downer under U_g = 5 m/s
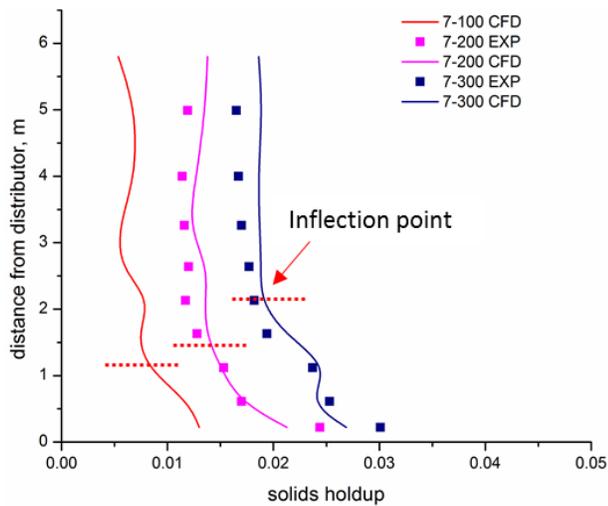
Figure 5-6 Axial profiles of the solid holdup in downer (ID = 3 in) under U_g = 7 m/s

Generally, the axial solids holdup prolife in the downer has an exponential profile with a distinct inflection point dividing the dense region and dilute region along the downer as shown in Figs. 5-4 and 5-5. A short dense entrance region forms near the gas distributor because the particles are under acceleration and then the solids holdup gradually decreases and reaches a uniform and much more dilute distribution to the outlet at the bottom of the downer indicating the formation of the fully developed solids flow. With the increase in the solids circulation rate or decrease in the superficial gas velocity, a longer dense region is found in the downer suggesting a longer flow development stage.
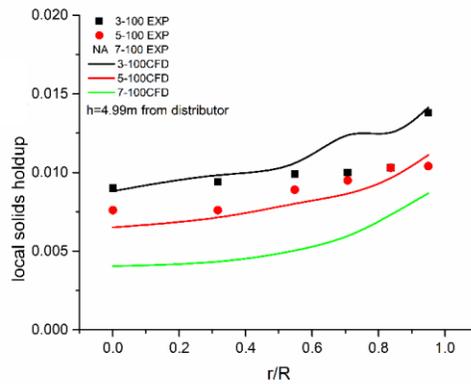
Figure 5-7 Radial profiles of the solid concentration in the 3 in downer at different superficial gas velocities under $G_s = 100$ kg/m²s
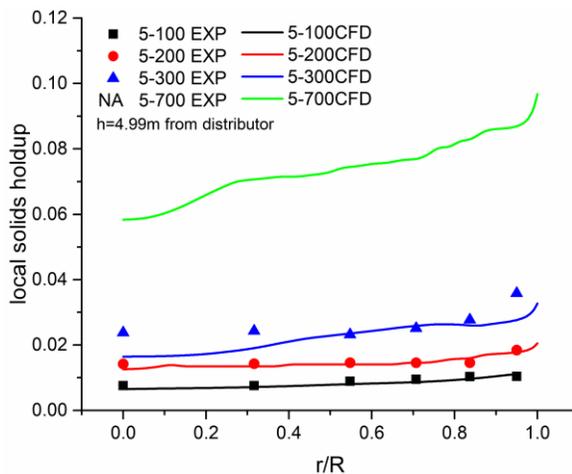
Figure 5-8 Radial profiles of the solid concentration in the 3 in downer at different solids circulation rates under $U_g = 5$ m/s

Since the experimental data were collected only at six radial positions (r/R = 0, 0.316, 0.548, 0.707, 0.837, 0.950) across the downer, more detailed flow information can be obtained from the numerical results as shown in Fig. 5-7. Generally, the solids distribution in the radial direction is uniform with a wide and flat core (r/R = 0 - 0.9) and there is a thin but dense annular region near the wall with a much higher solids concentration due to the wall friction and possibly some clustering effects in that region. Comparing with the typical core-annulus radial flow structure in a CFB riser, which has a thick and much denser wall region with a solids concentration up to 0.4 (Wang, et al., 2015), the gas-solid suspension in the downer is much more uniform in the CFB downer. By increasing the solids circulation rate or decreasing the superficial gas velocity, the radial flow structure still exhibits a uniform profile in the downer. In contrast to the CFB riser reactor in which the flow structures differ a lot when increasing G_s, both the axial and radial flow structures in the downer from the numerical results are similar when G_s increases while only the overall solids holdup increases as shown in Figs. 5-5 to 5-8. As reported in the literature, one of the factors caused the non-uniformity of the gas-solid flow structure in a CFB system is due to the clustering phenomenon. The relatively uniform radial profile in the downer indicates a more homogeneous gas-solid flow existing with less significant gas-solid interactions and less particle agglomerations.

5.4.2 Prediction of the overall bed density

Numerical results for the axial profiles of the solids holdup in the downer covering a wide range of the operating conditions have a good agreement with the experimental data as shown in Fig. 5-9. Therefore, the CFD model is believed to be reliable enough to predict the overall bed density inside a downer. The overall bed densities sorted in an ascending order under different operating conditions in the downer are obtained from the CFD simulations as shown in Tab. 5-2. Under different U_g-G_s pairs, the gas-solid suspension goes through very dilute conditions to some dense conditions with the overall bed density ranging from ε_s = 0.005 to 0.08. Also, an average superficial solids velocity along the downer reactor can be obtained from numerical calculation as listed in Tab. 5-2. A systematic slip factor (F_{slip}) indicating the excess of the solids velocity compared with the

superficial gas velocity due to the acceleration of the particles inside the downer is found to be:

$$F_{slip} = \frac{1}{n}\sum_{i=0}^{n}\frac{\overline{U_s}}{U_g} \approx 1.45 \qquad (5\text{-}14)$$
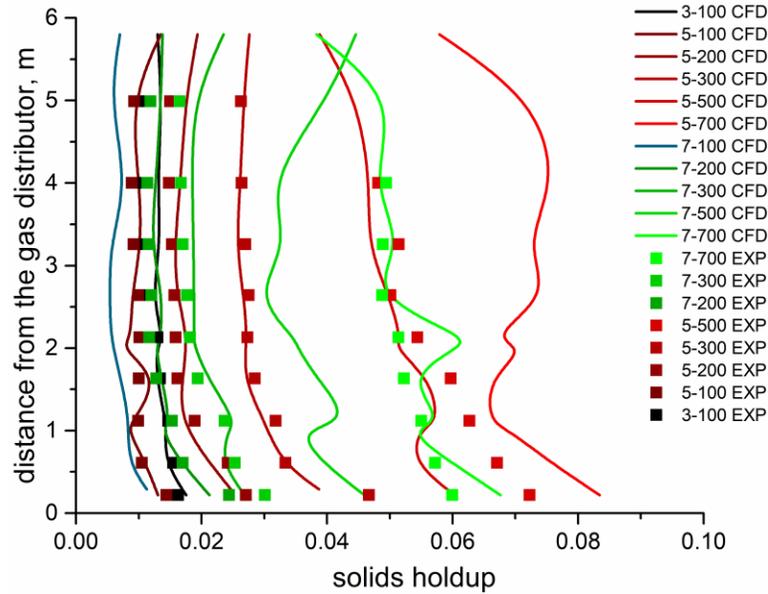
Figure 5-9 Comparison of the axial solids holdup distributions between the CFD results and experimental data

The overall bed density is one of the most important parameters when determining the operation conditions for a downer reactor. The prediction of the overall bed density under different U_g-G_s pairs plays a significant role in the industries, however, it is difficult to derive the relationship of the overall bed densities under different operating conditions simply by experiments. A correlation to predict the overall bed density in the downer reactor is developed based on the numerical results from the overall bed density and the average slip factor as the following:

$$\bar{\varepsilon}_s = G_s/(\rho_s \cdot U_g \cdot F_{slip}) \qquad (5\text{-}15)$$

where $U_g \geq 1\text{m/s}$. The comparison between the numerical results and the results from the proposed correlation for the overall bed density is plotted in Fig. 5-10. The differences between the numerical results and the results from the correlation under various operating

conditions are within ±15% indicating the validation of the proposed correlation for the overall bed density in the downer with a slip factor of 1.45.

Table 5-2 Comparison of the overall bed densities between the CFD results and the results from the propose correlation in ascending order

ranking	Overall bed density (CFD results)	Overall bed density (Correlation) $\overline{\varepsilon_s}$	U_g (m/s)	G_s (kg/m²s)	$\overline{U_s}$ (m/s) (CFD results)	G_s/U_g (kg/m³)
1	0.0066	0.0066	7	100	10.1040	14
2	0.0097	0.0092	5	100	6.8729	20
3	0.0130	0.0153	3	100	5.1277	33
4	0.0133	0.0131	7	200	10.0246	29
5	0.0170	0.0184	5	200	7.8431	40
6	0.0193	0.0197	7	300	10.3634	43
7	0.0268	0.0276	5	300	7.4627	60
8	0.0344	0.0328	7	500	9.6901	71
9	0.0485	0.0460	5	500	7.0175	100
10	0.0497	0.0460	7	700	9.3147	100
11	0.0689	0.0644	5	700	6.7731	140
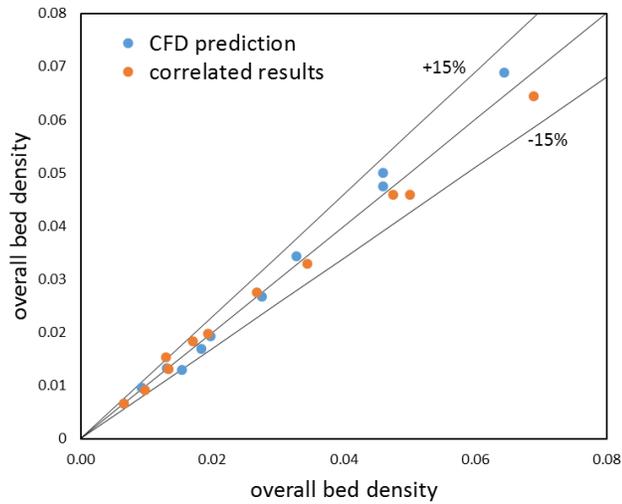
Figure 5-10 Comparison of the overall bed density between the CFD results and the results from the proposed correlation
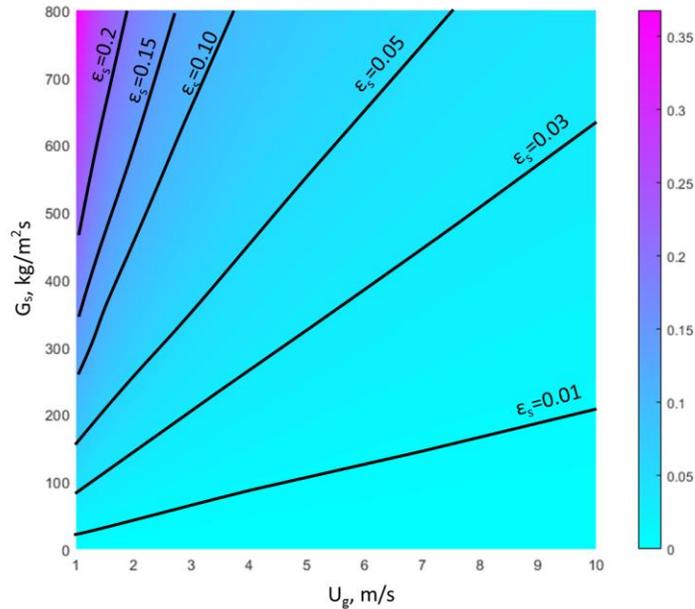
Figure 5-11 2D map of the predicted overall bed density in the downer reactor

A two-dimensional map of the overall bed density in the downer obtained by the proposed correlation, which covers the superficial gas velocities of 1-10 m/s and the solids circulation rates of 0-800 kg/m^{2}s, is generated as shown in Fig. 5-11. A series of iso-potential lines presenting the same overall bed density under the operations from a low-density condition to a high-density condition with different U_g-G_s pairs are also marked on the 2D map. In addition to the correlation for the overall bed density, the ratio of the solids circulation rates (G_s) to the superficial gas velocities (U_g) is actually more important in the industrial applications to predict the actual flow condition in the downer since U_g and G_s are the two operating parameters that can be directly obtained from measurements. For downer reactors operated with a same overall bed density under different U_g-G_s pairs, the G_s/U_g ratio should be a constant since these iso-potential lines of the overall bed density are nearly linear as shown in the 2D map. However, as the overall bed density increases, the slope (G_s/U_g) of the iso-potential overall bed density lines increases rapidly from a low-density operations to a high-density operations in the downer indicating that decreasing U_g has a greater affect than increasing G_s to promote the gas-solid flow transitions from a dilute condition to a dense condition in the downer. The overall bed density of 0.03 with a G_s/U_g ratio around 65kg/m^3 can be considered as the boundary between the low-density

downer and the high-density downer because the iso-potential line for the overall bed density of 0.03 almost divides the 2D map into two operating windows with the same area.
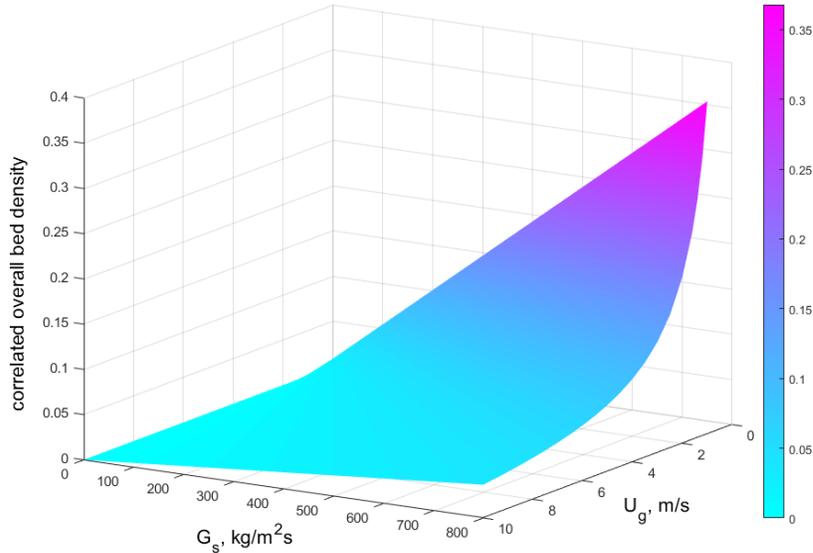
Figure 5-12 3D map of the predicted overall bed density in the downer reactor

A three-dimensional map of the overall bed density in the downer reactor also can be generated as shown in Fig. 5-12. The impacts from G_s and U_g on the bed density can be further discussed separately by the 3D map. Under low-velocity operations where U_g is less than 4m/s, the superficial gas velocity has a greater impact than the solids circulation rate on the overall bed density so that a small decrease of U_g can result in a significant increase of the overall bed density. However, under high-velocity operations with U_g greater than 4m/s, the superficial gas velocity and the solids circulation rate tend to have similar affects on the increase of the bed density. Also, the transition in the downer from low-density condition to the high-density condition becomes more gradual under the high-velocity operation. Therefore, gas-solid reactions requiring large throughput of gas or solids such as coal combustion are more suitable to be operated under high-velocity operations, while catalytic reactions requiring a higher contacting efficiency are more suitable to be operated under relatively low-velocity operations.

5.4.3 Solids phase flow development
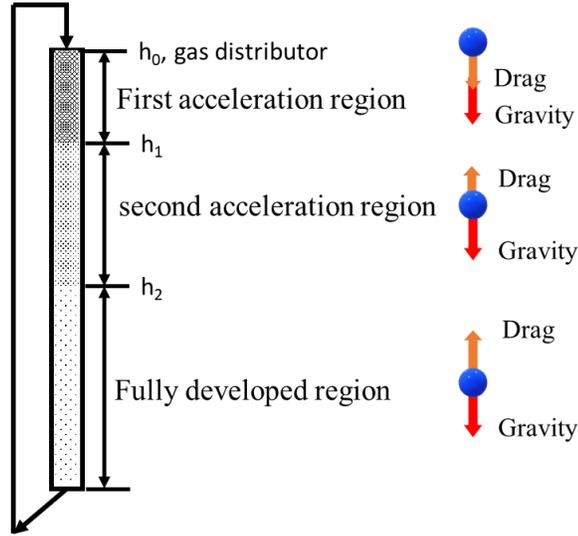
Figure 5-13 Sketch of the development of the solids flow

The solids flow development in a downer reactor can be divided into three stages based on the relationship between the drag force and gravity acting on the particle as sketched in Fig. 5-13. Generally, the solids enter the downer at a low velocity and can be quickly accelerated through two acceleration stages to reach a constant velocity in the fully developed zone. The acceleration of the particles in the downer can be illustrated by the profiles of the cross-sectional particle velocity and the slip velocity between particles and gas under different operating conditions as shown in Figs. 5-14 and 5-15.

The solids flow goes through a first acceleration region at the entrance region of the downer where the gas velocity is greater than the particle velocity, so that both the drag force and the gravity force are downward as shown in Fig. 5-13. The inlet velocity of the solids flow at the top of the downer decreases with the increase in the solids circulation rate as shown in Fig. 5-14. The reason might because that the agglomeration of particles becomes more severe at the entrance region of the downer under a higher solids circulation rate, resulting a lager slip velocity as shown in Fig. 5-15. The particles accelerate quickly in the first acceleration stage due to the large downward acceleration from the combined effects of the drag force and the gravity. Once the particle velocity increases to the same value as the superficial gas velocity, there is no slip velocity between the particles and gas as shown in

Fig. 5-15, resulting in a zero drag force which is the boundary between the first and the second acceleration stages in the downer. In the second acceleration stage, the drag force changes to the upward direction because particles will have greater velocity than the gas phase, so that a positive slip velocity along the downer is obtained and it increases along the downer as shown in Fig. 5-15. The upward drag force gradually increases with the increase in the slip velocity, but it still less than the gravity in the second stage, resulting in a smaller acceleration than the one in the first stage. Correspondingly, the increase in the particle velocity becomes more gradual in the second acceleration stage as shown in Fig. 5-13. Once the upward drag force increases to balances the gravity of the particles, the gas-solid flow reaches the fully developed region where the particle velocity and the slip velocity are almost constant since there is no acceleration as shown in Figs. 5-14 and 5-15. However, under some extremely high-density operation conditions, the velocities still vary significantly due to more severe agglomeration effects in the downer, which might have a significant impact on the force balance on the particles.

Therefore, the zero slip velocity is marked as the boundary between the first and the second acceleration regions in the downer as the dotted arrows shown in Fig. 5-15. The onset of the fully developed region is at the point when the gradient of the positive slip velocity firstly becomes less than 0.01 as the solid arrows shown in Fig. 5-15.

(a)   (b)
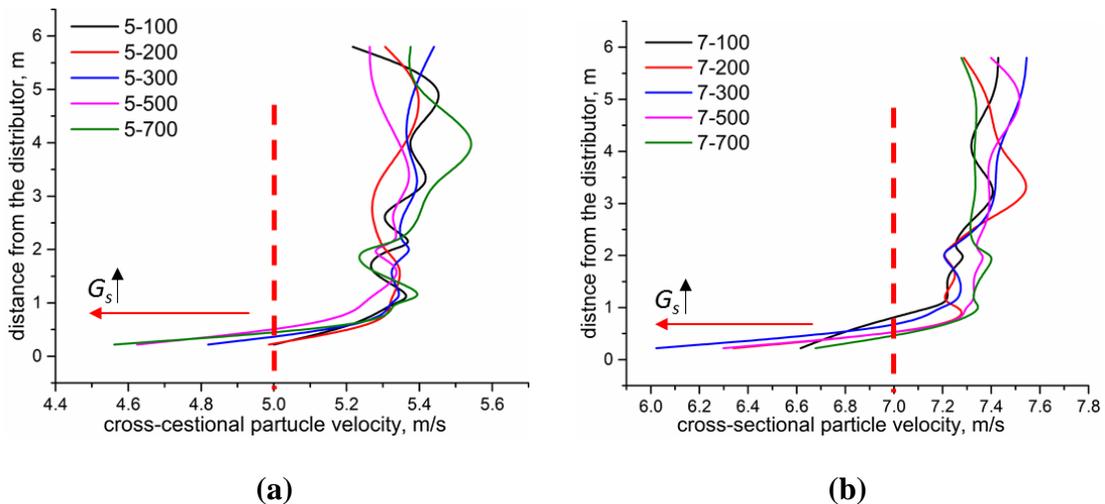
Figure 5-14 Cross-sectional particle velocity along the downer (a) $U_g = 5$ m/s and (b) $U_g = 7$ m/s

(a)   (b)
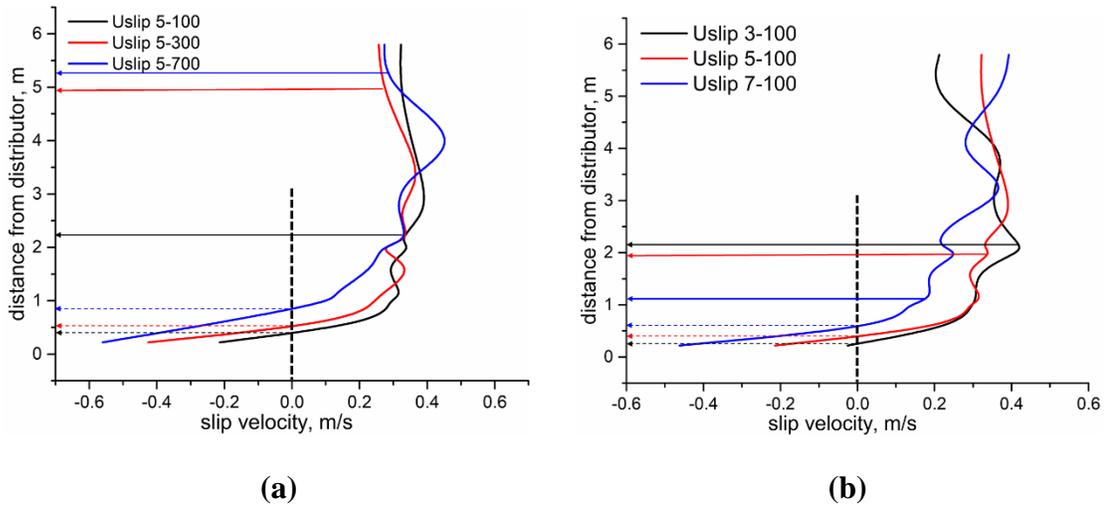
Figure 5-15 Cross-sectional slip velocity along the downer (a) U_g **= 5 m/s (b)** G_s **= 100 kg/m²s**
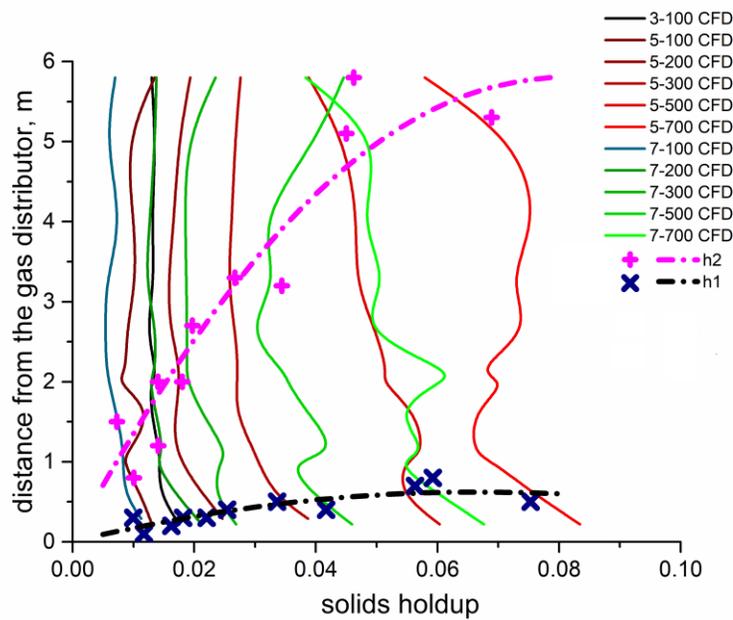
Figure 5-16 Tendency of the lengths of the three stages in the downer under different operating conditions

More detailed data on the boundaries of the three regions in the downer under various operating conditions are marked as shown in Fig. 5-16. It can be seen from Fig. 5-16 that

from a low density to a high density operation condition, both lengths of the first and second acceleration regions increase.

After entering the downer from the top inlet, the solids suspension undergoes a very quick first acceleration stage, resulting in a dense and short entrance region that is always less than 1m (h_1-h_0 < 1m) from the gas distributor. The length of the second acceleration region increases significantly with the increase in the overall bed density from a low-density operation condition to a high-density operation condition. Under dilute conditions ($G_s \leq 30$ 0kg/m^{2}s), the total length of the two acceleration regions is less than half of the length of the entire downer, which means that the fully developed region occupies the major part of the downer. Such a low-density downer reactor is more favorable for reactions in which the mass transport or diffusion is the control step of the kinetics in the chemical reaction. Under dense conditions (G_s > 300 kg/m^{2}s), more fluctuations in the solids holdup and particle velocity are noticed from Figs. 5-16 and 5-14 due to the more severe agglomeration effects. When the solids circulation rate is extremely high (G_s = 700 kg/m^{2}s), the fluctuations of the flow are stronger, which results in a longer second acceleration region that even occupies almost the entire downer. Although the fluctuations increase in a high-density downer, the solids holdup distribution is still more uniform than the one in a CFB riser, so that reactions in which the intermediate product is more valuable and requiring higher throughput are more suitable to be conducted in a high-density downer.

5.4.4 Scale-up effects

The scale-up effects are studied in this work by comparing the numerical results from a downer of 0.0762 m (3 in) ID and a wider downer of 0.2 m (8 in) ID. The general flow structures and radial solids distributions at different axial locations from the distributor are compared in Fig. 5-17. Generally, the overall axial gas-solid flow structures are close between the 3 in downer and 8 in downer as shown in Fig. 5-17. However, by increasing the downer diameter, the axial non-uniformity is increased, especially in the fully developed region where slight fluctuations of the cross-sectional solids holdup are found.
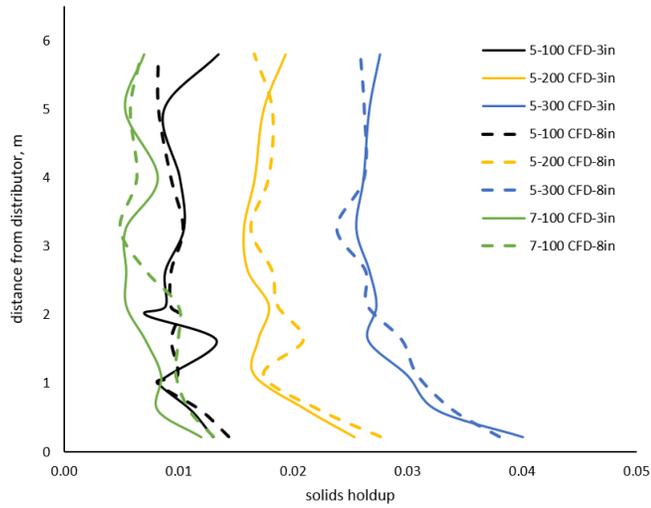
Figure 5-17. Comparison of the axial solids holdup profiles between the 3 in and 8 in downers
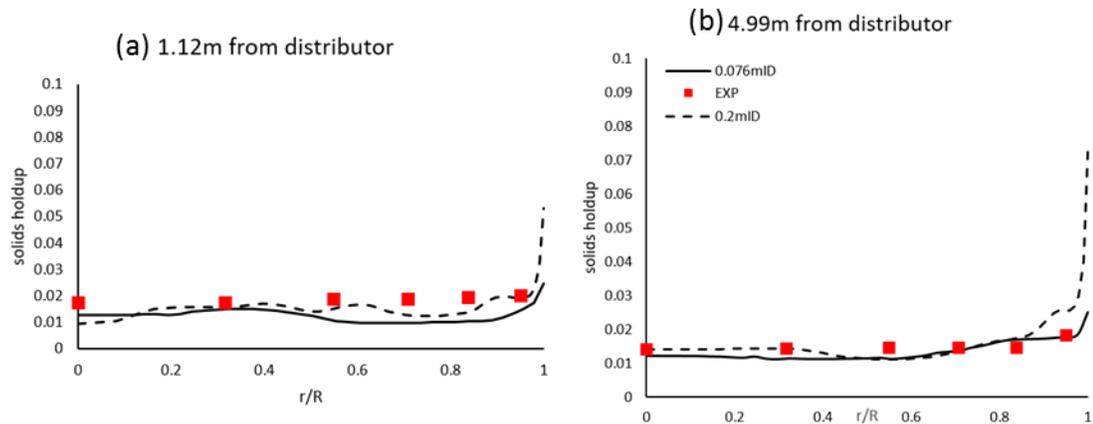
Figure 5-18. Comparison of the radial solids holdup profiles between the 3 in and 8 in downers under dilute conditions (U_g = 5 m/s and G_s = 200 kg/m²s)
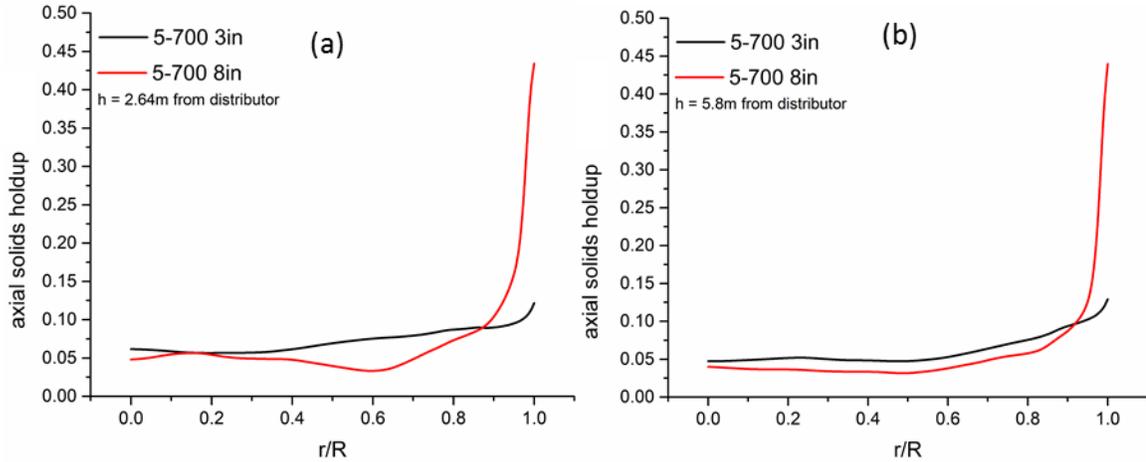
Figure 5-19 Comparison of the radial solids holdup profiles between the 3 in and 8 in downers under high-density conditions (U_g = 5m/s and G_s = 700kg/m²s)

The radial solids holdup profiles show that the dilute and uniform core region of the downer shrinks with the increase in the diameter of the downer under both the dilute and dense operation conditions as shown in Figs. 5-18 and 5-19. The solids holdups in the center region are still close between the 3in downer and the scaled-up downer under dilute flow condition as shown in Fig. 5-18. However, a lower solids holdup in the center region is found in the scaled-up downer under the high-density condition since the solids holdup near the wall is much higher than that under the low-density condition as shown in Fig. 5-19. Slight fluctuations of the radial solids holdup distribution are found in the developing region near the solids entrance of the scaled-up downer as shown in Fig. 5-18 (a) and Fig. 5-19 (a), indicating that the distributor effect are promoted in the scale-up downer.

The wall effects also promoted in the scale-up downer, which is consistent with the experimental observations (Yan & Zhu, 2004). The scaled-up downer reactor has a wider and denser wall region with a solids holdup greater than 0.05 near the wall which is about three times of the one in the smaller downer. The wall effects are more severe in the fully developed region than the entrance region of the downer where a much higher solids concentration up to 0.08 can be seen in Fig. 5-18 (b).

Similar scale-up effects are found in both CFB risers and downers experimentally and numerically, which reveal that the wall effects become more important in scale-up

downers. Particles in the scaled-up downer tend to lose more momentum due to the wall friction and particle-wall interactions, resulting in a lower velocity and more intensive gas-solid interactions. Consequently, more particle clusters are formed in the scaled-up downer, which move upward slower, so that solids holdup is higher. However, comparing with the severe clustering phenomenon in the CFB riser, the clusters effects in the scaled-up downer are relatively insignificant since the bulk of the scaled-up downer is still under uniform distribution for good mass and heat transfer. Moreover, with more particles retained in the scaled-up downer due to the clustering phenomenon, more total gas-solid contacting area is obtained, which is favorable for gas-phase catalytic reactions.

5.5 Conclusion

The axially and radially flow structures are uniform in a CFB downer reactor, which is desirable for gas phase catalytic reactions requiring shorter reaction time and less back-mixing. The radial uniformity of the solids holdup in the downer reactor also suggests a less significant clustering phenomenon in the CFB downer.

The development of the gas-solid flow along the downer reactor can be divided into three stages including the first and second acceleration regions and the fully developed region based on the relationship between the drag force and the gravity on the particles. Under low-density operation conditions, the fully developed region occupies the major part of the downer. Under high-density operation conditions, the length of the second acceleration region increases with the increase in the overall bed density and gradually occupies the major part of the downer.

A correlation to predict the overall bed density in the downer is developed based on the numerical results. A 2D map and 3D map of the overall bed density are generated based on the proposed correlation. An overall bed density of 0.03 corresponding to a ratio of solids circulation rate to the superficial gas velocity, G_s/U_g, around 65 kg/m^3 can be considered as the boundary of the low-density operation and high-density operation of the downer.

The scale-up effects on the CFB downer are studied numerically and similar conclusions to the scale-up effects on the CFB riser are found. The wall effects are promoted in the scale-up downer reactor. A wider and denser annulus region is found in the scaled-up downer. However, comparing with the CFB downer, the enhanced non-uniformity by scale-up effects on the downer reactor is negligible. Higher gas throughput can be obtained in the scaled-up downer, which indicates a promising future for the industrial use of the CFB downer reactors.

Nomenclature

A_T	Cross-sectional area of the downer, m^2
d_p	Particle diameter, m
e_{ss}	Coefficient of particle-particle restitution
F_{slip}	Slip factor
$g_{o,ss}$	Radial distribution function of particles
G_s	Solids circulation rate, kg/m^2s
$\bar{\bar{I}}$	unit tensor
h	Axial distance from the gas distributor, m
H	Total height of the CFB downer, m
k	Turbulent kinetic energy, m^2/s^2
P	Fluid phase pressure, Pa
P_s	Solids phase pressure, Pa
r	Radial position of the CFB downer, m
R	Radius of the CFB downer, m
Re_r	Relative particle Reynolds number, $= \dfrac{\rho_g d_p |\overrightarrow{v_s} - \overrightarrow{v_g}|}{\mu_g}$
U_g	Superficial gas velocity, m/s
$\overline{U_s}$	Superficial solids velocity, m/s
v_g	Gas phase velocity, m/s

v_r (U_r)	Relative velocity: the ratio of the terminal settling velocity of a multiparticle system to that of an isolated particle
v_s	Solid phase velocity, m/s
$v'_{s\tau}$	Random component of the particle velocity, m/s
$V_{g,in}$	Inlet gas velocity, m/s
$V_{s,in}$	Inlet velocity of the solid phase, m/s
α_g	Gas phase volume fraction
α_s	Solid phase volume fraction
$\gamma_{\Theta s}$	Collisional dissipation of energy
$K_{sg}=K_{gs}$	Interphase momentum exchange coefficient
ε	Dissipation rate of the turbulent kinetic energy
ε_s	Overall solids holdup in a gas-solids CFB riser
$\overline{\varepsilon_s}$	Correlated overall bed density
λ	Phase bulk viscosity, kg/ms
μ	Phase shear viscosity, kg/ms
$\mu_{g,t}$	Gas phase turbulent viscosity, kg/ms
$\mu_{s,t}$	Solids phase turbulent viscosity, kg/ms
ρ_g	Gas density, kg/m^3
ρ_s	Particle density, kg/m^3
$\emptyset_{gs}$	Granular temperature of particles, m^2/s^2
$\overline{\overline{\tau}}$	Phase stress-strain tensor, kg/s^2
Φ	Ratio of the opening area in the gas distributor

Subscripts:

g	Gas phase
s	Solids phase
x	x axis
y	y axis
p	Particles

References

ANSYS, Inc. (2013). Chapter 17. Multiphase Flows. ANSYS Fluent Theory Guide. Pp. 527-586

Bolkan, Berruti, Zhu & Milne (2003). Modeling circulating fluidized bed downers. Powder Technology, 132(2-3), 85-100.

Chalermsinsuwan, Chanchuey, Buakhao, Gidaspow & Piumsomboon (2012). Computational fluid dynamics of circulating fluidized bed downer: Study of modeling parameters and system hydrodynamic characteristics. Chemical Engineering Journal, 189–190, 314–335.

Chen, Li & Kwauk (2005). Two-phase structure in a high-density downer. Powder Technology, 158(1–3), 115–123.

Cheng, Guo, Wei, Jin & Lin (1999). Modeling the hydrodynamics of downer reactors based on kinetic theory. Chemical Engineering Science, 54(13–14), 2019–2027.

Cheng, Zhang, Fushimi, Tsutsumi & Wang (2014). Numerical studies of solid–solid mixing behaviors in a downer reactor for coal pyrolysis. Powder Technology, 253, 722-732.

Gidaspow & Ding (1990). A bubbling fluidization model using kinetic theory of granular flow. AIChE Journal, 36(4), 523–538.

Guan, Fushimi, Ishizuka, Nakamura, Tsutsumi, Matsuda & Wang (2011). Flow behaviors in the downer of a large-scale triple-bed combined circulating fluidized bed system with high solids mass fluxes. Chemical Engineering Science, 66(18), 4212–4220.

Khongprom, Aimdilokwong, Limtrakul, Vatanatham & Ramachandran (2012). Axial gas and solids mixing in a down flow circulating fluidized bed reactor based on CFD simulation. Chemical Engineering Science, 73, 8-19.

Lehner & Wirth (1999). Characterization of the flow pattern in a downer reactor. Chemical Engineering Science, 54(22), 5471–5483.

Li, Zhu, Ray & Ray (2011). Catalytic reaction in a circulating fluidized bed downer: Ozone decomposition. Chemical Engineering Science, 66(20), 4615–4623.

Liu, Li & Zhu (2017). Modeling the hydrodynamics of downer reactors based on the meso-scale structure. Powder Technology, 314, 367–376.

Lu, Li, Du, Yao, Lin & Li (2005). Flow structures in the downer circulating fluidized bed. Chemical Engineering Journal, 112(1-3), 23-31.

Ma & Zhu (1999). Experimental study of heat transfer in a co-current downflow fluidized bed (downer). Chemical Engineering Science, 54(1), 41–50.

Qi, Zhang & Zhu (2008). Solids concentration in the fully developed region of circulating fluidized bed downers. Powder Technology, 183(3), 417-425.

Samruamphianskun, Piumsomboon & Chalermsinsuwan (2012). Computation of system turbulences and dispersion coefficients in circulating fluidized bed downer using CFD simulation. Chemical Engineering Research and Design, 90(12), 2164-2178.

Shu, Peng, Wang, Zhang, Li & Lin (2014). Comparative CFD Analysis of Heterogeneous Gas–Solid Flow in a Countercurrent Downer Reactor. Industrial & Engineering Chemistry Research, 53(8), 3378–3384.

Syamlal & O'Brien (1987). The derivation of a drag coefficient formula from velocity-voidage correlations. Technical Note, US Department of energy, Office of Fossil Energy, NETL, Morgantown, WV.

Tuzla, Sharma, Chen, Schiewe, Wirth & Molerus (1998). Transient dynamics of solid concentration in downer fluidized bed. Powder Technology, 100(2-3), 166-172.

Vaishali, Roy & Mills (2008). Hydrodynamic simulation of gas–solids downflow reactors. Chemical Engineering Science, 63(21), 5107–5119.

Wang. (2013). High-density gas-solids circulating fluidized bed riser and downer reactors. Ph.D thesis, University of Western Ontario.

Wang, Li & Zhu. (2015). Axial solids flow structure in a high density gas–solids circulating fluidized bed downer. Powder Technology, 272, 153–164.

Wang, Li, Zhu, Wang, Barghi & Zhu (2015). A comparison of flow development in high density gas-solids circulating fluidized bed downer and riser reactors. AIChE Journal, 61(4), 1172–1183.

Wang, Zhu, Lan, Gao & Barghi (2016). Radial solids flow structure in high flux gas-solids circulating fluidized bed downers. Powder Technology, 301, 848–857.

Wei, Wang, Jin, Yu & Chen (1994). Dispersion of lateral and axial solids in a cocurrent downflow circulating fluidized bed. Powder Technology, 81(1), 25–30.

Yan & Zhu. (2004). Scale-Up Effect of Riser Reactors (1): Axial and Radial Solids Concentration Distribution and Flow Development. Industrial & Engineering Chemistry Research, 43(18), 5810–5819.

Zhang, Huang & Zhu (2001). Gas-solids flow behavior: CFB riser vs. downer. AIChE Journal, 47(9), 2000–2011.

Zhu, Yu, Jin, Grace & Issangya, (1995). Cocurrent downflow circulating fluidized bed (downer) reactors — A state of the art review. The Canadian Journal of Chemical Engineering, 73(5), 662–677.

Chapter 6

6 A cluster-driven drag model for gas-solids two-phase flows in circulating fluidized bed risers

6.1 Introduction

A gas-solids circulating fluidized bed (CFB) riser reactor has a large number of applications in the industries including fluid catalytic cracking, combustion and gasification, pharmaceutical and food processes, and physical process such as drying (Grace, et al., 2003). A CFB riser usually operates under a high gas velocity, so that solids will be entrained out of the column and circulated through a downer. Consequently, the interactions between gas and particles are more intensive and the gas-solids flow structure is more complicated than the conventional low-velocity fluidized beds (Horio, et al., 1992; Takeuchi et al. 1986; Yerushalmi, et al., 1976).

Computational fluid dynamics (CFD) modeling has become an effective tool for researchers to design and study gas-solids CFB riser reactors since the 1970s when the Eulerian-Eulerian (EE) two-fluid model was developed by Lyczkowski et al. (1978). Unlike the Eulerian-Lagrangian (EL) method which tracks particles by a force balance equation, EE approach treats both the gas and solids phases as interpenetrating continua and the kinetic theory of granular flow has been introduced into the model to calculate the properties of solids phase. For the simulations of large-scale gas-solids CFB risers, the EE two-fluid method (TFM) is more widely used since it requires less computational time compared with EL method. In the past decades, numerical results have achieved good agreements with the experimental observations in the general trend of flow structure in a CFB riser such as the core-annulus radial structure of solids holdup and the power-law velocity distribution of particles (Almuttahar & Taghipour 2008; Benyahia et al. 2000; Samuelsberg & Hjertager 1996; Tsuji, et al., 1998). However, when it comes to the detailed local flow structures such as the radial solids holdup distribution, discrepancies between the numerical results and the experimental data are commonly seen because it is always difficult to accurately model the interactions between gas and particles, which is needed in CFD simulations. Based on experimental observations, individual particles tend to

agglomerate to clusters when moving in the riser resulting in the hydrodynamics of the gas-solids flow in a CFB riser too complicated to be numerically modelled.

6.1.1 Particle clustering phenomenon in CFB risers

Particle clustering phenomenon is a typical microscopic characteristics in gas-solids CFB riser due to strong hydrodynamic effects and cohesive forces (Cocco et al. 2010; Horio & Clift 1992). A cluster usually consists of a group of single particles with a higher solid concentration than the surrounding gas-solids suspension (Sharma et al. 2000). Parametric studies on cluster characteristics such as its size, shape, and solids concentration have been done experimentally with the development of the measuring techniques (Lackermeier et al. 2001; Manyele, et al., 2002; Mondal et al. 2016; Xu & Zhu 2012). The clusters are found to have irregular shapes including large pieces such as strands and smaller spheres at different positions of the riser (Zou et al. 1994). Various sizes of clusters ranging from 0.001m to 0.1m are detected in a FCC CFB depending on the operating conditions and the corresponding identification method (Cahyadi et al. 2017). Both upward and downward moving clusters are detected in CFB risers at different positions under either dilute or dense conditions (Cahyadi et al. 2017). The cluster velocity measured experimentally for FCC particles also varies a lot form 0.25m/s to 3m/s (Harris, et al., 2002). A higher solids holdup, which even reaches 0.40 under certain high-density operations indicates the existence of clusters in a CFB riser. The average solids concentration of a cluster usually decreases along the axial direction of the riser and increases radially from the center towards the wall (Liu, et al., 2005; Yang & Zhu 2015; Yang & Leu 2009).

Particle clusters in the fluidized bed have significant impacts on their surrounding flow field due to their higher concentration, lower rising velocity, and other dynamic behaviors such as the continuously changing shape and size. The intensive gas-solids interactions result in the continuous formation and breakup of particle clusters in the CFB riser. On the one hand, less gas can penetrate the clusters because of the large shear force at their boundaries resulting in a larger slip velocity than freely moving individual particles. A lower conversion of chemical reactions is expected due to less exchange of fresh gas and the reacting gas in the clusters. On the other hand, more particles can stay in the CFB riser under higher gas flowrate due to the existence of clusters, so that higher gas throughput is

achieved for gas-phase reactions. However, the complex gas-particle and inter-particle interactions contribute the difficulties in numerical simulations of CFB risers.

6.1.2 CFD modelling on clustering phenomenon

When it comes to numerical simulations on the gas-solids flow in the CFB riser by TFM, gas-solids interactions are usually included into the calculation of the momentum transfer which associates with the drag force in the gas-solids system. Therefore, many efforts have been put into the modification of the drag models to include the clustering effects in CFB risers.

Most of the current drag models that include the clustering effects can be generally classified into three groups based on different understandings on the formation of clusters. In the first group, the drag model was developed based on the pressure drop of the fluidized bed, such as Wen and Yu model (1966), Gidaspow model (1990), and Huilin-Gidaspow model (2003). In the second group, modified drag models were obtained based on the concept of the Richardson-Zaki equation which relates the bed voidage with the terminal velocity of particles in fluidized beds, using different correlations for the volume fraction and particle relative velocity, such as the commonly used Syamlal-O'Brien model (1989) and Gibilaro model (1985). In both the above-mentioned groups, although the drag models were developed to include the clustering effect for the gas-solid system, only the properties of single particle were used as the input parameters into the models resulting in the deviations from the experimental data especially under denser conditions where more and larger clusters exist. On the other hand, the above-mentioned drag models were developed with the help of the experimental data which were collected before 2000, with the expansion of the gas-solids fluidization system since the new century, those drag models become not capable enough for wider operating ranges. In the third group, the meso-scale heterogeneity theory for the gas-solids system was used in the modified drag model and the size and density of a "numerical" cluster can be calculated from the modified drag model, such as the EMMS model (Li & Kwauk 2003) and CSD model (Shuai et al. 2011). Although "numerical" clusters were calculated based on the minimum energy dissipation theory form EMMS/CSD model, it has not been validated that those "numerical" clusters have the same properties as the real "observed" clusters existing in a fluidized bed.

6.1.3 Research gap between numerical work and experimental work

For numerical simulations, proper data of the cluster properties are not readily available since the size, shape, and density of clusters vary not only with the positions in the riser but also with the operating conditions as mentioned above, let along that there is no unified cluster identification method until now. Although the effects of clustering phenomenon on the overall flow structures in the riser were well accepted, the understanding on the formation and the dynamic natures of clusters from the point view of the CFD modelling is quite different from the experimental studies. The clustering effects are included into the gas-solids interactions through the drag models or granular temperature in numerical simulations. Most of the modified drag models only tried to include the clustering effect by adding a factor to the drag models developed for the uniformly distributed particles because of lack of fully understanding of the experimental data on clusters. However, the properties of single particles were still used in those modified drag models. Some of those modified drag models work well under certain flow conditions in fluidized beds, but they are not suitable for general cases. On the other hand, the circulating gas-solids fluidization has expanded into a wider operating range with high-density conditions where larger and more frequent clusters have been seen, however, most of the current drag models developed before 2000 failed for the high-density CFB riser and often underestimate the solids holdup inside a riser.

With more details of particle clusters inside a gas-solids fluidized bed have been revealed by advanced measurement technologies such as the high-speed video camera, the actual size, density, frequency, and concentration of the clusters can be detected nowadays. Directly including the properties of clusters into the calculation of the overall gas-solids drag force is a more efficient and realistic method to accurately predict the gas-solids interactions. A cluster-driven drag model that includes the clustering effect in gas-solids fluidization systems is developed in this study based on the statistical data of the clusters with the help of image analytical experiments.

6.2 The concept of cluster-driven drag correlation

Although clusters in CFB risers are detected to have various structures such as U-shape, strand, stripe, and sphere, a stable "core" with particular higher solids concentration exists and keeps constant both in size and solids holdup surrounded by the instantaneously transforming denser layers of particles (Xu & Zhu 2012; Yang & Zhu 2015). Smaller clusters might be more sphere-like because the majority of them is the highly concentrated "core" and the surrounding denser layer is very thin. Larger floc-like clusters consisting of multiple "cores" are commonly seen since smaller clusters tend to adhere together while moving and transforming in the riser (Xu & Zhu 2012). Those larger pieces of clusters can be considered as "cluster of core clusters". Therefore, particle clusters inside a CFB riser can be generally classified into two types based on its structures and behaviors when moving in the riser. One is "core" cluster in which particles are tightly packed by fluid so that can hardly breakup during rising in the CFB riser. Another type is "cluster of core clusters" consisting of many loosely aligned "core" clusters which frequently form and breakup in the riser. The "core" clusters are relatively smaller and more stable with higher solids concentration than the loose large "cluster of core clusters". In a gas-solids fluidized bed, only a certain portion of particles can move in the form of free individual particles and the particles captured inside a "core" cluster have less opportunities to contact with the surrounding fluid. Correspondingly, higher solids holdup and more nonuniform flow structure are detected in the CFB riser due to the clustering effects.

The early experimental work has been done to quantify the stable "core" clusters in the riser and tried to provide the drag models with more properties of clusters such as the size, density, velocity, volume fraction. Li et al., (1991) reported a "core" cluster size of 1mm under a dilute low-velocity CFB condition ($U_g < 3.5$m/s, $G_s < 35$kg/m^{2}s) by an image approach (Li et al. 1991). Cocco et al. (2010) found the clusters have an average size of 21 ± 1.7 particles and occupies 41% of the solids phase in a fluidized system for FCC particles via a high-speed video (Cocco et al. 2010). With the development of the measurement technologies and more experimental data collected especially under high-density conditions, the statistical results of the equivalent diameter and density of the "core"

clusters, and the portion of the "core" clusters in the total solids phase can be obtained from an image analysis.
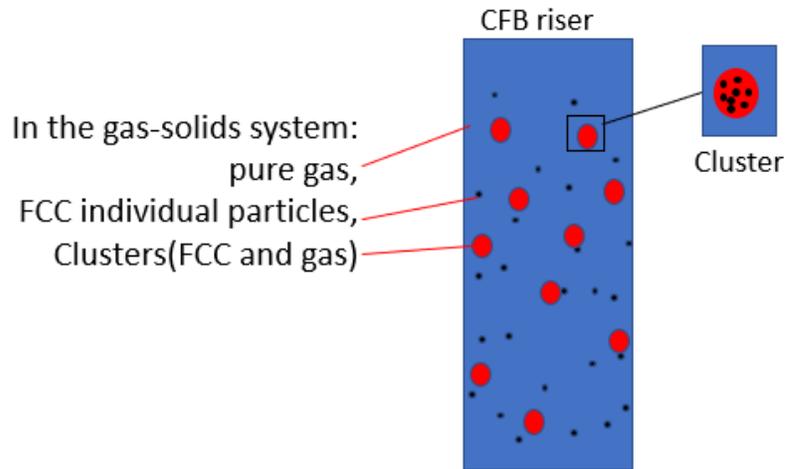
Figure 6-1: Sketch of a gas-solids fluidization system considering the existence of clusters

Several assumptions based on the experimental observations of clusters are made to construct the proposed cluster-driven drag model. Stable and spherical "core" clusters exist in the entire CFB riser and the mass and momentum transfers are negligible for the fluid and single particles captured inside a "core" cluster.

As shown in Figure 6-1, the gas-solids suspension in a CFB riser can be divided into a single particle phase (φ_p) which only contains freely moving individual particles, a cluster phase (φ_{cl}) which consists of stable "core" clusters, a pure gas phase which represents the gas bypassing the individual particles or clusters since part of the total gas is captured into the clusters (φ_g). Therefore, the gas-solids interactions inside a CFB riser can be divided into two classes based on the types of solid phase as shown in Figure 6-2. Class 1 considers the interaction between the clusters and the pure gas phase with the assumption that the clusters are stable spherical clouds of single particles existing in the fluidized bed ("core" clusters). Class 2 considers the interaction between the freely moving individual particles and the pure gas phase. The total drag force between gas and solids can be obtained from the summation of the drag forces from Class 1 and Class 2.
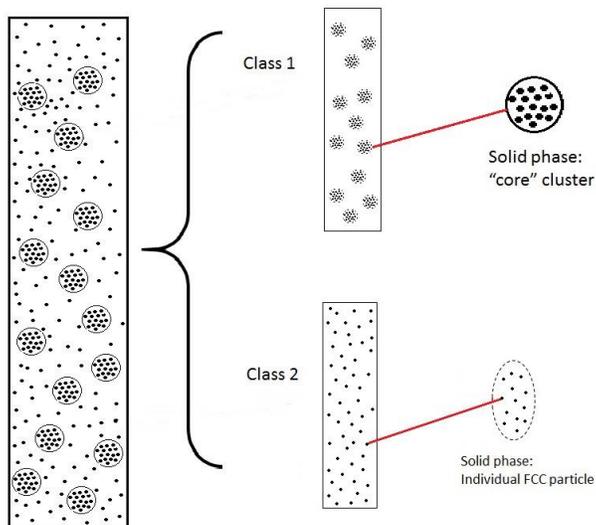
Figure 6-2: Schematic diagram of the cluster-driven drag model

6.2.1 Derivation of the correlation for the drag force
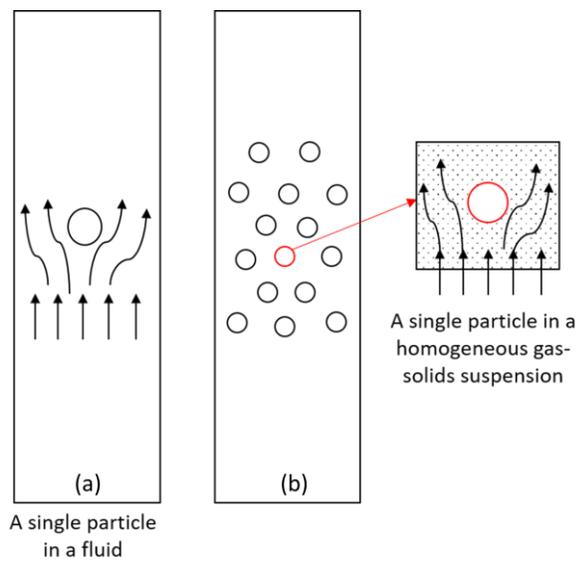
Figure 6-3: Drag force on a particle in ideal system and homogeneous dilute suspension

The derivation of the correlation for the drag force on a single particle in the ideal gas-solids system with a homogeneous dilute suspension is illustrated in Figure 6-3. Under the

most ideal condition where there is only one particle in the fluid as shown in Figure 6-3 (a), the drag force for a single particle can be determined based on the force balance:

$$F_d = V_{l\_p} \cdot g \cdot (\rho_s - \rho_g) \qquad (6\text{-}1)$$

where F_d is the drag force exerted on the particle in an ideal system, V_{l_p} is the volume of a particle, ρ_s and ρ_g represent the density of the particle and fluid respectively. Based on the definition of the drag force, which is in the direction of the flow velocity, the drag force on a particle also relates with the fluid velocity (Gidaspow, 1994):

$$F_d = \frac{1}{2} \cdot C_d \cdot \rho_g \cdot |U_{slip}| \cdot U_{slip} \cdot A_p \qquad (6\text{-}2)$$

where C_d is the drag coefficient for a single particle in a fluid, U_{slip} is the slip velocity between fluid and particle, and $A_p = \frac{\pi \cdot d_p^2}{4}$ is the reference area of a particle projecting to the fluid.

In a dilute homogeneous gas-solids system with multiple particles as shown in Figure 6-3 (b), particles are uniformly dispersed in the system so that the gas-solids suspension can be considered as mixture and the mixture density can be expressed as:

$$\rho_{sus} = \varepsilon_g \rho_g + (1 - \varepsilon_g)\rho_s \qquad (6\text{-}3)$$

where ε_g is the volume fraction of gas. For a single particle in the dilute homogeneous gas-solids suspension as shown in Figure 6-3 (b), solid particles are sparsely distributed so that the forces from other particles are negligible and the drag force exerted on a single particle is derived as:

$$F_d' = V_{l\_p} \cdot (\rho_s - \rho_{sus})g = V_{l\_p} \cdot \varepsilon_g \cdot (\rho_s - \rho_g)g = \varepsilon_g \cdot F_d \qquad (6\text{-}4)$$

Therefore, the total drag force per unit volume in the homogeneous gas-solids suspension can be calculated as:

$$F_D = n_p \cdot F_d'$$
(6-5)

where n_p is the number of the particles per unit volume in the system and $n_p = \frac{6(1-\varepsilon_g)}{\pi \cdot d_p^3}$.

The total drag per unit volume in the homogeneous gas-solids suspension can be written as:

$$F_D = \frac{3}{4} \cdot C_d' \cdot \frac{\varepsilon_g \cdot (1-\varepsilon_g) \cdot \rho_g \cdot |U_{slip}| \cdot U_{slip}}{d_p}$$
(6-6)

where C_d' is the drag coefficient in the homogeneous dilute gas-solids system, d_p is the diameter of the particles.

In Eulerian-Eulerian two-fluid approach, the drag force is included in the momentum transfer term in the conservation equation of momentum for each phase:

$$F_D = \beta \cdot (V_g - V_s)$$
(6-7)

where β is the momentum transfer coefficient. Since the slip velocity between gas and solids can be presented as $(V_g - V_s)$ locally, the momentum transfer coefficient can be derived based on Eq. (6-6):

$$\beta = \frac{3}{4} \cdot C_d' \cdot \frac{\varepsilon_g \cdot (1-\varepsilon_g) \cdot \rho_g \cdot |U_{slip}|}{d_p}$$
(6-8)

6.2.2 Cluster-driven drag model

Generally, in a gas-solids system, α_g is the volume fraction of the gas phase, and $\alpha_s = (1 - \alpha_g)$ is the volume fraction of the total solids phase which consists of the individual particles in Class 1 and the captured particles in the clusters of Class 2 as shown in Figure 6-2. To include the clustering effects in the drag model, the cluster size (d_{cl}), solid concentration in the cluster (d_{en_cl}), and the percentage of the total solids captured in the cluster phase (P_{cl}) are collected experimentally from the statistical data via clusters image analysis.

The portion of the freely moving individual particles in the total solids phase which is the volume fraction of the single particle phase inside the CFB riser is:

$$\varphi_p = (1 - P_{cl})(1 - \alpha_g) \tag{6-9}$$

The portion of the captured particles inside the clusters in the gas-solids system is:

$$\varepsilon_{cl} = \alpha_s - \varphi_p = P_{cl}(1 - \alpha_g) \tag{6-10}$$

Since the solids holdup in a cluster is d_{en_cl}, the volume fraction of the cluster phase is:

$$\varphi_{cl} = \frac{P_{cl}(1 - \alpha_g)}{d_{en\_cl}} \tag{6-11}$$

The portion of the captured gas inside the clusters is:

$$\varepsilon_{g\_cl} = \varphi_{cl} \cdot \left(1 - d_{en_{cl}}\right) = \frac{P_{cl}(1 - \alpha_g) \cdot \left(1 - d_{en_{cl}}\right)}{d_{en\_cl}} \tag{6-12}$$

The volume fraction of the pure gas phase outside of the clusters is:

$$\varphi_g = \alpha_g - \varepsilon_{g\_cl} \tag{6-13}$$

The correlation for sparsely distributed particles (Schiller & Naumann, 1935) is used for the calculation of the drag coefficients for both the cluster phase and single particle phase, but with different parameters for those two phases. When calculating the drag force for the cluster phase, the clusters are assumed as stable spheres ("core" clusters) with a constant diameter, d_{cl} and density, ε_{cl}, based on statistical data from the experiments. The volume fraction of the clusters phase is also obtained from the statistical experimental data by the image analysis. The slip velocity of the clusters is determined based on different operating conditions.

Drag model for Class 1:

The drag force in Class 1 comes from the interactions between the clusters (φ_{cl}) and the bypassing gas (φ_g). Numerically in two-fluid model, the momentum transfer coefficient between clusters and the bypassing gas is:

$$\beta_{cluster} = \frac{3}{4} \cdot C_{D\_cl} \cdot \frac{\varphi_g \cdot \varphi_{cl} \cdot \rho_g \cdot |U_{slip\_cl}|}{d_{cl}} \tag{6-14}$$

where C_{D_cl} is the drag coefficient of clusters in the gas-solid system, d_{cl} is the average diameter of the "core" clusters, and U_{slip_cl} is the slip velocity between clusters and surrounding fluid. Currently, the terminal velocity of clusters is assumed the same as its slip velocity associating with its size and the operating condition as shown in the following equation (Kunii and Levenspiel 1969):

$$U_{slip\_cl} = \sqrt{\frac{4}{3} \cdot \frac{d_{cl} \cdot g}{C_{D\_cl}} \cdot \frac{(\rho_{cl} - \rho_g)}{\rho_g}} \tag{6-15}$$

The drag coefficient of clusters (C_{D_cl}) is a function of cluster's Reynolds number since the clusters are treated as stable solid spheres in Class 1. According to Schiller & Naumann's correlation, for $1 < Re_{cl} < 1000$, the drag coefficient of the clusters is:

$$C_{D\_cl} = \frac{24}{Re_{cl}} (1 + 0.15 Re_{cl}^{0.687}) \tag{6-16}$$

For $Re_{cl} >= 1000$, the drag coefficient of the clusters is:

$$C_{D\_cl} = 0.44 \tag{6-17}$$

The cluster's Reynolds number is based on the properties of clusters and the fluid is:

$$Re_{cl} = \frac{\rho_g \cdot U_{slip\_cl} \cdot d_{cl}}{\mu_g} \tag{6-18}$$

The drag model for Class 2:

In Class 2, the drag force is due to the interaction between the pure gas (φ_g) and he freely moving single particles (φ_p). The momentum transfer coefficient between freely moving individual particles and pure gas is:

$$\beta_p = \frac{3}{4} \cdot C_{D\_p} \cdot \frac{\varphi_g \cdot \varphi_p \cdot \rho_g \cdot |U_{slip}|}{d_p} \tag{6-19}$$

where d_p is the diameter of single particles, the slip velocity in Class 2 is

$$U_{slip} = (V_g - V_s) = \sqrt{(U_{g_x} - U_{s_x})^2 + (U_{g_y} - U_{s_y})^2} \qquad \text{(6-20)}$$

C_{D_p} is the drag coefficient for freely moving particles based on the Reynold's number of single particles. For $Re_p < 1000$:

$$C_{D\_p} = \frac{24}{Re_p}\left(1 + 0.15Re_p^{0.687}\right) \qquad \text{(6-21)}$$

where $Re_p = \frac{\rho_g \cdot U_{slip} \cdot d_p}{\mu_g}$. For $Re_p \geqslant 1000$, the drag coefficient of the clusters is:

$$C_{D\_p} = 0.44 \qquad \text{(6-22)}$$

Therefore, the total momentum transfer coefficient for the gas-solid CFB riser is the summation of Class 1 and Class 2:

$$\beta_{gs} = \beta_p + \beta_{cl} \qquad \text{(6-23)}$$

The total drag for the gas-solids fluidization system in a CFB riser is:

$$F_D = (\beta_p + \beta_{cl}) \cdot (V_g - V_s) \qquad \text{(6-24)}$$

6.3 CFD model descriptions

6.3.1 Governing equations

The Eulerian-Eulerian two-fluid model coupling with the kinetic theory of granular flow is used for the simulation of the gas-solids flow in a CFB riser. A set of governing equations consisting of the mass and momentum conservation equations for both gas and solids phases are solved as listed in Table 6-1.

6.3.2 Configuration of the CFB riser and mesh description

The circulating fluidized bed riser is of 10 m high with a diameter of 7.62cm (3 in) as shown in Figure 6-4. Gas enters the riser through a perforated gas distributor from the bottom of the riser with an opening area ratio (γ) of 18%. The circulated particles return to the riser from the side pipe with an inner diameter of 5.08 mm (2 in). A quad grid system

with finer mesh near the wall and the inlet as shown in Figure 6-5 is used because the flow parameters in a CFB change greatly near those regions. The mesh information and gird independence test results were stated in Chapter 4. The commercial software Fluent V17 is used for the simulation.

Table 6-1: Governing equations

Continuity equation of gas and solids:	$\frac{\partial}{\partial t}(\alpha_g \rho_g) + \nabla \cdot (\alpha_g \rho_g \overline{v_g}) = 0$	(6-25)
Continuity equation of solids:	$\frac{\partial}{\partial t}(\alpha_s \rho_s) + \nabla \cdot (\alpha_s \rho_s \overline{v_s}) = 0$	(6-26)
Momentum equation of gas:	$\frac{\partial}{\partial t}(\alpha_g \rho_g \overrightarrow{v_g}) + \nabla \cdot (\alpha_g \rho_g \overrightarrow{v_g}\overrightarrow{v_g}) = -\alpha_g \nabla P + \nabla \cdot \left(\alpha_g \left(\overline{\overline{\tau_g^m}} + \overline{\overline{\tau_g^{Re}}}\right)\right) + \alpha_g \rho_g \vec{g} + \beta_{gs}(\overrightarrow{v_s} - \overrightarrow{v_g})$ where $\overline{\overline{\tau_g^m}} = -\frac{2}{3}\mu_{g.m}\nabla \cdot \overrightarrow{v_g}\overline{\overline{I}} + \mu_{g.m}(\nabla \overrightarrow{v_g} + \nabla \overrightarrow{v_g}^T)$, and $\overline{\overline{\tau_g^{Re}}} = -\frac{2}{3}(\rho k_g + \mu_{g.t}\nabla \cdot \overrightarrow{v_g})\overline{\overline{I}} + \mu_{g.t}(\nabla \overrightarrow{v_g} + \nabla \overrightarrow{v_g}^T)$.	(6-27)
Momentum equation of solids:	$\frac{\partial}{\partial t}(\alpha_s \rho_s \overrightarrow{v_s}) + \nabla \cdot (\alpha_s \rho_s \overrightarrow{v_s}\overrightarrow{v_s}) = -\alpha_s \nabla P - \nabla P_s + \nabla \cdot \left(\alpha_s \left(\overline{\overline{\tau_s^m}} + \overline{\overline{\tau_s^{Re}}}\right)\right) + \alpha_s \rho_s \vec{g} + \beta_{gs}(\overrightarrow{v_g} - \overrightarrow{v_s})$ where $\overline{\overline{\tau_s^m}} = (\lambda s - \frac{2}{3}\mu_s)\nabla \cdot \overrightarrow{v_s}\overline{\overline{I}} + \mu_s(\nabla \overrightarrow{v_s} + \nabla \overrightarrow{v_s}^T)$, and $\overline{\overline{\tau_s^{Re}}} = -\frac{2}{3}(\rho k_s + \mu_{s.t}\nabla \cdot \overrightarrow{v_s})\overline{\overline{I}} + \mu_{s.t}(\nabla \overrightarrow{v_s} + \nabla \overrightarrow{v_s}^T)$.	(6-28)
Granular temperature equation	$\frac{3}{2}\left[\frac{\partial}{\partial t}(\rho_s \alpha_s \Theta s) + \nabla \cdot (\alpha_s \rho_s \overrightarrow{v_s}\Theta s)\right] = \left(-P_s \overline{\overline{I}} + \overline{\overline{\tau_s}}\right):\nabla \overrightarrow{v_s} + \nabla \cdot (k_{\Theta s}\nabla \Theta) - \gamma_{\Theta s} + \emptyset_{gs}$ where $\emptyset_{gs} = -3k_{gs}\Theta s$. The collisional energy can be obtained by: $\gamma_{\Theta s} = \frac{12(1-e_{ss}^2)g_{o,ss}}{d_s\sqrt{\pi}}\rho_s\alpha_s^2\Theta_s^{3/2}$.	(6-29)
k equation for gas:	$\frac{\partial}{\partial t}(\alpha_g \rho_g k_g) + \nabla \cdot (\alpha_g \rho_g \overrightarrow{v_g}k_g) = \nabla \cdot \left(\alpha_g \frac{\mu_{g,t}}{\sigma_k}\nabla k_g\right) + (\alpha_g G_{g,k} - \alpha_g \rho_g \varepsilon_g) + \beta_{gs}(C_{gs}k_g - C_{sg}k_s) - \beta_{gs}(\overrightarrow{v_g} - \overrightarrow{v_s}) \cdot$ $\frac{\mu_{g,t}}{\alpha_g\sigma_g}\nabla\alpha_g + \beta_{gs}(\overrightarrow{v_g} - \overrightarrow{v_s}) \cdot \frac{\mu_{g,t}}{\alpha_g\sigma_g}\nabla\alpha_g$ where the turbulent viscosity, $\mu_{g,t} = \rho_g C_\mu \frac{k_g^2}{\varepsilon_g}$,	(6-30)
ε equation for gas:	$\frac{\partial}{\partial t}(\alpha_g \rho_g \varepsilon_g) + \nabla \cdot (\alpha_g \rho_g \overrightarrow{v_g}\varepsilon_g) = \nabla \cdot \left(\alpha_g \frac{\mu_{g,t}}{\sigma_k}\nabla\varepsilon_g\right) + \frac{\varepsilon_g}{k_g}(C_{1\varepsilon}\alpha_g G_{g,k} - C_{2\varepsilon}\alpha_g \rho_g \varepsilon_g + C_{3\varepsilon}(\beta_{gs}(C_{sg}k_s - C_{gs}k_g) - $ $\beta_{gs}(\overrightarrow{v_s} - \overrightarrow{v_g}) \cdot \frac{\mu_{s,t}}{\alpha_s\sigma_s}\nabla\alpha_s + \beta_{gs}(\overrightarrow{v_s} - \overrightarrow{v_g}) \cdot \frac{\mu_{g,t}}{\alpha_g\sigma_g}\nabla\alpha_g))$	(6-31)
k equation for solids:	$\frac{\partial}{\partial t}(\alpha_s \rho_s k_s) + \nabla \cdot (\alpha_s \rho_s \overrightarrow{v_s}k_s) = \nabla \cdot \left(\alpha_s \frac{\mu_{s,t}}{\sigma_k}\nabla k_s\right) + (\alpha_s G_{s,k} - \alpha_s \rho_s \varepsilon_s) + K_{gs}(C_{gs}k_g - C_{sg}k_s) - \beta_{gs}(\overrightarrow{v_g} - \overrightarrow{v_s}) \cdot$ $\frac{\mu_{g,t}}{\alpha_g\sigma_g}\nabla\alpha_g + \beta_{gs}(\overrightarrow{v_g} - \overrightarrow{v_s}) \cdot \frac{\mu_{s,t}}{\alpha_s\sigma_s}\nabla\alpha_s$ where the turbulent viscosity, $\mu_{s,t} = \rho_s C_\mu \frac{k_s^2}{\varepsilon_s}$	(6-32)
ε equation for solids:	$\frac{\partial}{\partial t}(\alpha_s \rho_s \varepsilon_s) + \nabla \cdot (\alpha_s \rho_s \overrightarrow{v_s}\varepsilon_s) = \nabla \cdot \left(\alpha_s \frac{\mu_{s,t}}{\sigma_k}\nabla\varepsilon_s\right) + \frac{\varepsilon_s}{k_s}(C_{1\varepsilon}\alpha_s G_{s,k} - C_{2\varepsilon}\alpha_s \rho_s \varepsilon_s + C_{3\varepsilon}(\beta_{sg}(C_{sg}k_g - C_{gs}k_s) - \beta_{gs}(\overrightarrow{v_s} - $ $\overrightarrow{v_g}) \cdot \frac{\mu_{s,t}}{\alpha_s\sigma_s}\nabla\alpha_s + \beta_{gs}(\overrightarrow{v_s} - \overrightarrow{v_g}) \cdot \frac{\mu_{s,t}}{\alpha_s\sigma_s}\nabla\alpha_s))$	(6-33)

| **Figure 6-4: Configuration of the CFB riser (Li 2010)** | **Figure 6-5: Mesh for the computational domain of the CFB riser** |

6.3.3 Boundary conditions and solver descriptions

Both the turbulent kinetic energy and turbulent dissipation rate term are discretized by the second order scheme and QUICK scheme is used for convection terms in the momentum equation. A time step size of 0.0001s and a convergence criterion of 5×10^{-4} for each scaled residual component are specified. The operating conditions of the fluidization system and properties of gas and solids phases are summarized in Table 6-2. A velocity profile based on the gas distributor of the CFB riser is employed as the inlet boundary condition for the gas phase, which is located at the bottom of the computational domain as shown in Figure 6-5. The inlet gas velocity profile is calculated as:

$$V_{g\_in} = U_g/\phi \qquad (6\text{-}34)$$

where ϕ is the opening ratio of the gas distributor. Two symmetric solid phase inlets are located at the same height on both sides of the computational domain which are analogous to the solids returning pipe of the 3D column as illustrated in Figure 6-5. The solid phase inlets have the same diameter as the solids returning pipe with a uniform inlet velocity:

$$V_{s\_in} = G_s/(\varepsilon_s \times \rho_s) \qquad\qquad (6\text{-}35)$$

where G_s is the solids circulation rate, ρ_s is particle density, and ε_s (=0.3) is the volume faction of solid phase at the inlet. No slip velocity boundary condition is applied at the wall for the gas phase and slip boundary condition with a specularity coefficient of 0.0001 and a restitution coefficient of 0.9 is employed for the solids phase at the wall. The outflow boundary condition is used for both the gas and solids phases at the outlet, which is at the top of the riser as shown in Figure 6-5.

Table 6-2: Operating conditions and properties of gas and solids

Gas density (kg/m^3)	1.225
Gas viscosity (kg/m·s)	1.7894x10^{-5}
Solids particles	FCC
Particle density (kg/m^3)	1550
Particle diameter (μm)	67
Particle-Particle restitution coefficient	0.9
Particle-Wall restitution coefficient	0.95
Specularity coefficient	0.0001

6.4 Results and discussion

6.4.1 CFD cases for simulations

Different cases as shown in Table 6-3 are used to validate the proposed cluster-driven drag model by comparing the results with experimental data as well as the numerical results from some commonly used drag models. The parameters of the "core" clusters such as cluster size, d_{cl}, cluster solids holdup, ε_{cl}, are obtained from the experimental data for a CFB riser operated under the same conditions (Yang & Zhu 2014, 2015; Wei, 2019). The ratio of the solids in the cluster phase to the total solids phase is set as 0.5 since many studies reported that about 40%-60% of the particles are captured in clusters in the gas-solids CFB riser for FCC particles (Cocco et al. 2010; Yang & Zhu 2015). A wide operating window from dilute to denser conditions with the solids circulation rate, G_s, ranging from 100 to 300 kg/m^{2}s under a high superficial gas velocity (U$_g$=5-7 m/s) is selected for the numerical study on the gas-solids CFB system as shown in Table 6-3. The experimental results are collected from Li (2010) and Wang (2013) conducted on the same gas-solids CFB riser as shown in Figure 6-4.

Table 6-3: Summary of CFD cases used in simulations

Case #	Ug, m/s	Gs, kg/m²s	Drag model	Cluster diameter, d_{cl}, m	Custer solids holdup, ε_{cl}	Solids ratio in clusters, p
1	5	100	Syamlal-O'Brien model (OS)	NA	NA	NA
2	5	100	Schiller&Naumann model	NA	NA	NA
3	5	100	Gidaspow model	NA	NA	NA
4	5	100	Cluster-driven model	0.006	0.052	0.5
5	5	300	Syamlal-O'Brien model (OS)	NA	NA	NA
6	5	300	Cluster-driven model	0.0052	0.185	0.5
7	7	300	Syamlal-O'Brien model (OS)	NA	NA	NA
8	7	300	Cluster-driven model	0.0051	0.1196	0.5

6.4.2 Evaluations of current commonly used drag models

Three commonly used drag models, the Gidaspow model that is from the combination of Wen & Yu correlation and Ergun equation (Tsuo & Gidaspow 1990), the Syamlal-O'Brien model that is based on the voidage correlation with particle terminal velocity (Syamlal & O'Brien 1994), and Schiller & Naumann model (ANSYS 2013) that is originated for a homogenous particulate system, are selected for the simulations of the gas-solids fluidization system. The results from those three drag models are compared with the experimental data for the radial profiles of solids holdup at different heights from the gas distributor as shown in Figure 6-6.

Among them, the Schiller & Naumann model is considered as a general form of the drag model for a system of sparsely distributed solid particles, which has a homogeneous gas-solids flow without particle agglomerations or clustering phenomenon. That is why the result from the Schiller & Naumann model has the worst agreement with the experimental data as shown in Figure 6-6, especially in the bottom zone or the wall region of the riser since more clusters are formed there. Both the Gidaspow model and the Syamlal-O'Brien model are found to agree with the experimental results well as shown in Figure 6-6. However, the Gidaspow model employs a correction factor ($\varepsilon_g^{-2.65}$) in the calculation of momentum transfer, which only associates with the voidage of the system and ignores the effects of slip velocity due to clusters. On the other hand, the Gidaspow model is discontinuous at ε_g=0.8 so that it is not applicable for high-density CFB riser which usually has a gas holdup less than 0.8 in the wall region. The numerical results from the Syamlal-

O'Brien model have the same tendency with the experimental data but underestimate the solids holdup in the center of the riser at the entrance region. By adjusting the drag model with the empirical correlation of both the voidage and velocity, the Syamlal-O'Brien model performs better than the Gidaspow model at the annulus region of the riser, but there are still little bit deviations with the experimental data near the wall.

Simulation results for the axial solids holdup profiles from the proposed cluster-driven drag model and the three typical drag models are compared with the experimental data as shown in Figure 6-7. A uniform axial solids distribution is predicted by the Schiller & Naumann model, which underestimates the solids holdup and does not agree with the exponential profile from the experimental data since this drag model was developed for a homogeneous particulate system. Both the Gidaspow model and the Syamlal-O'Brien model predicted an exponential shape of the axial solids holdup profile which have the same tendency as the experimental data. However, although the simulation results at the dense bottom region of the riser agree well with the experimental data, the solids holdup at the upper dilute zone of the riser was underestimated by both the Gidaspow model and the Syamlal-O'Brien model as shown in Figure 6-7. The reason lies in the underestimation of the radial solids holdup in the annulus region of the riser in the upper zone as shown in Figure 6-6 (d)-(f), so that the cross-sectional solids holdup is lower comparing with the experimental data. In conclusion, the simulation results of the solids holdup profiles show that all the three typical drag models can predict accurately in the upper fully developed region (above h=6m) of the CFB riser as shown in Figure 6-6 (e) and (f). However, the solids holdup is underestimated in the annulus region comparing with the one in the center of the riser using all the three typical drag models.

6.4.3 Validation of the cluster-driven drag model

The commonly drag models failed to directly include the effects of clusters from the drag model since the drag models for a homogeneous system are usually modified by adding a correction factor to the total drag of the system. However, those empirical factors were developed before 2000 when the operating range of gas-solids CFB risers was yet to expand into high-density conditions, and the experiments data collected were from small-scale equipment such as a CFB riser lower than 6 m high. When more and larger clusters

are formed in the CFB riser under denser conditions, such as in an HDCFB or in the wall region, larger deviations are detected since the effects of particle clusters in the CFB riser are still not correctly incorporated in those drag models. Therefore, although a reliable agreement can be achieved by those drag models for certain cases, the cluster-driven drag model covering a wider operating range from dilute to dense conditions of a CFB riser is proposed in this work.

The predicted axial solids holdup profile using the proposed drag model is compared with those from the three typical drag models as well as the experimental data as shown in Figure 6-7. It can be seen that an exponential profile of the axial solids holdup is also predicted by the proposed drag model. A better agreement with the experimental data is achieved than those from other commonly used drag models as shown in Figure 6-7.

(a) Height=1.96m

(d) Height=5.85m

(b) Height=2.88m

(e) Height=7.35m

(c) Height=3.77m   (f) Height=9.63m
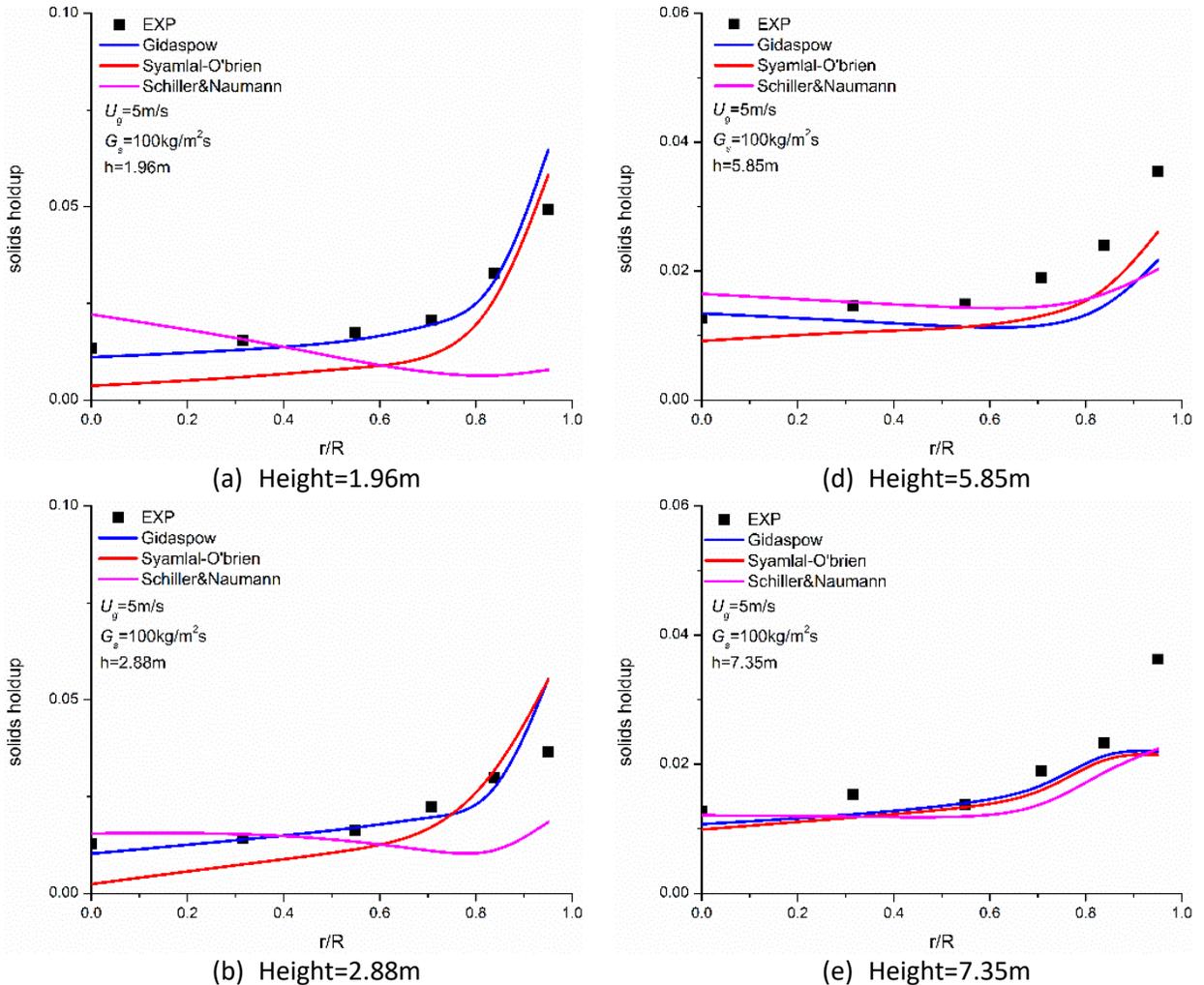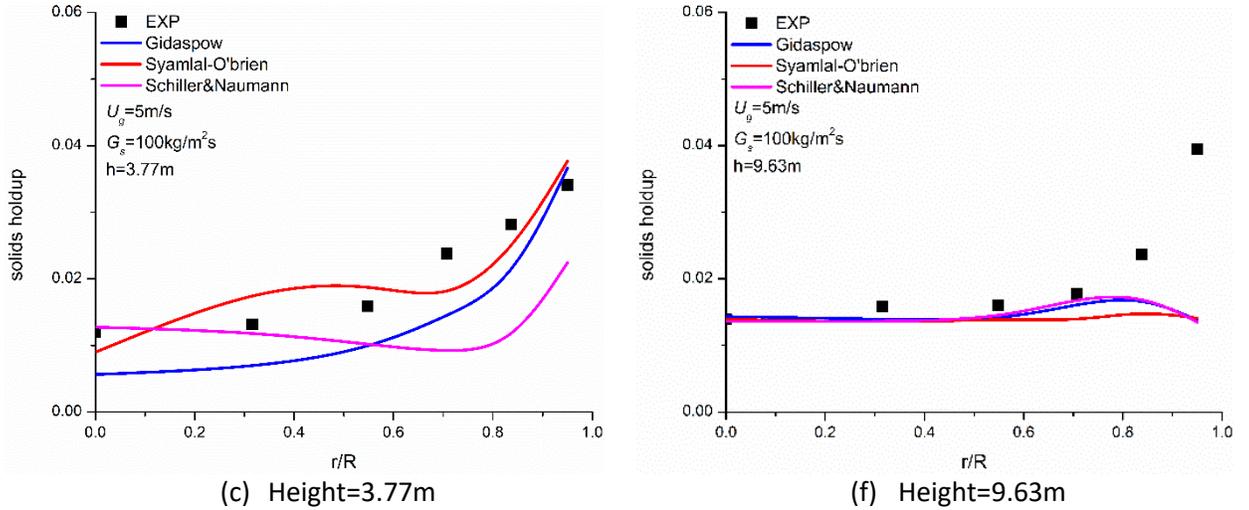
Figure 6-6: Comparison of the numerical results by commonly used drag models with the experimental data for the radial solids holdup profiles
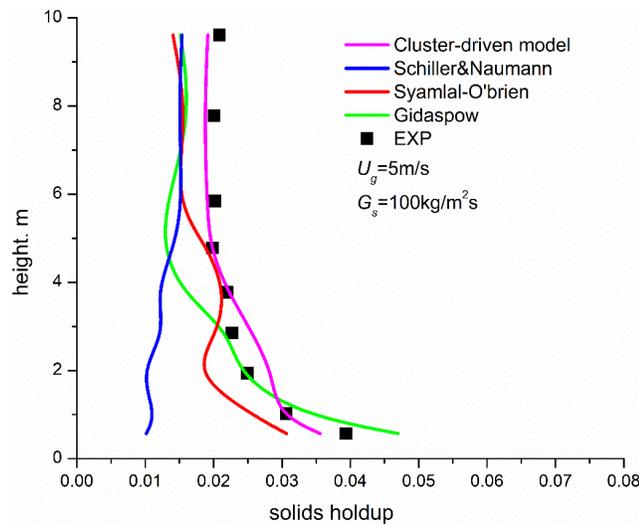
Figure 6-7: Comparison of numerical results by different drag models with the experimental data for the axial solids holdup profiles

6.4.4 Flow structures in the CFB riser

The results of the radial profiles of the solids holdup in the riser form the proposed cluster-driven drag model are compared with those from the Syamlal-O'Brien drag model as shown in Figure 6-8. The radial profiles of the solid phase velocity from the proposed drag model are plotted and achieved a good agreement with the experimental results as shown

in Figure 6-9. The clustering phenomenon is more severe in the wall region due to the lower particle velocity, so that a core-annulus profile of the solids distribution with a dilute suspension in the center and a dense layer near the wall is formed in the CFB riser. A better agreement with experimental results is achieved by the cluster-driven drag model than that from the Syamlal-O'Brien model, especially in the near wall region and the entrance region (Figure 6-8 (a)), where more clusters tend to form, and the local solids holdup is underestimated by the Syamlal-O'Brien model in those regions. In the upper fully developed zone of the riser, both the proposed cluster-driven model and the Syamlal-O'Brien drag model predict a dilute and flat core region in the riser, which agrees with the experimental results well. However, severe underestimation of the solids holdup near the wall region from the Syamlal-O'Brien drag model is found in the upper zone of the riser. It has been reported more and larger clusters are found near the wall of the riser (Manyele, Pärssinen, and Zhu 2002; Xu and Zhu 2012; Yang and Zhu 2015), the voidage and velocity correlation in the Syamlal-O'Brien drag model failed to predict the solids holdup under denser conditions with more severe clustering phenomenon near the wall region. The proposed cluster-driven drag model improves the prediction of the local solids holdup in the wall region as shown in Figure 6-8 (c) and (d).
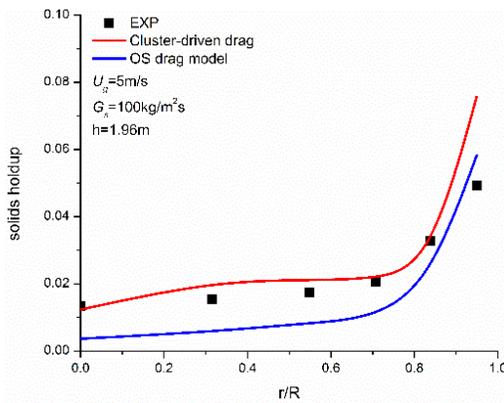
(a) H= 1.96m   (a) H = 1.96m
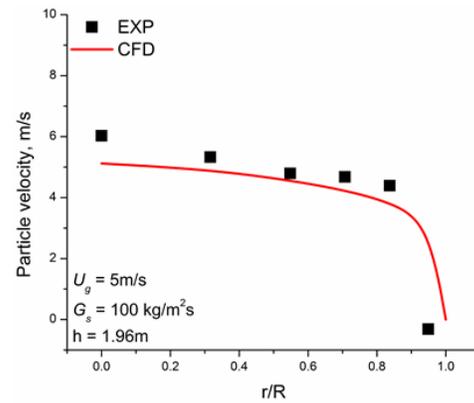
(b) H = 3.77m
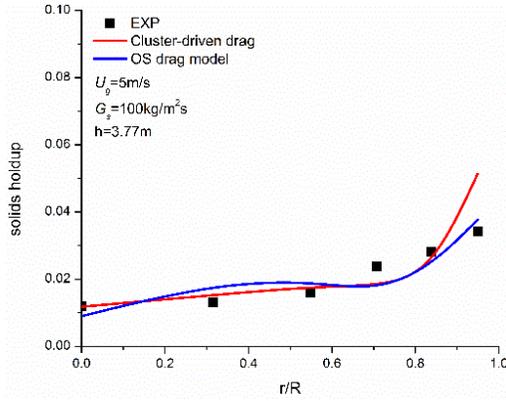
(b) H = 3.77m
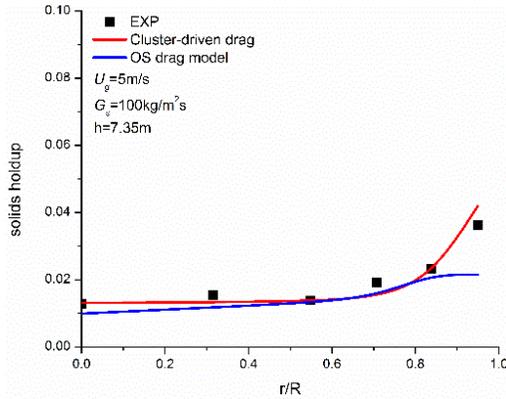
(c) H= 7.35m
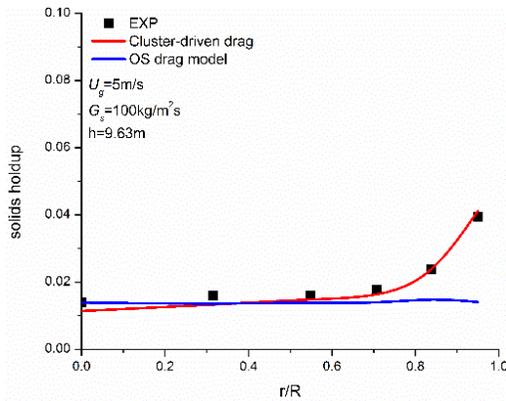
(c) H = 7.35m

(d) H= 9.63m

(d) H = 9.63m

Figure 6-8: Comparison of the Radial solids holdup profiles from the cluster-driven drag model and the Syamlal-O'Brien drag model
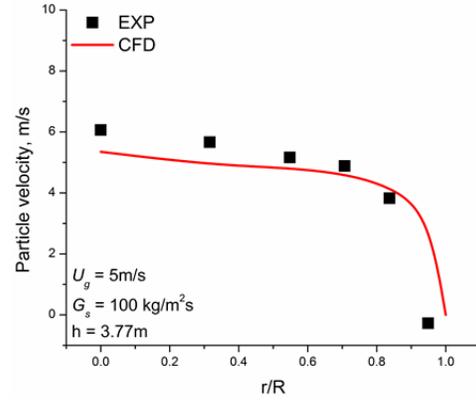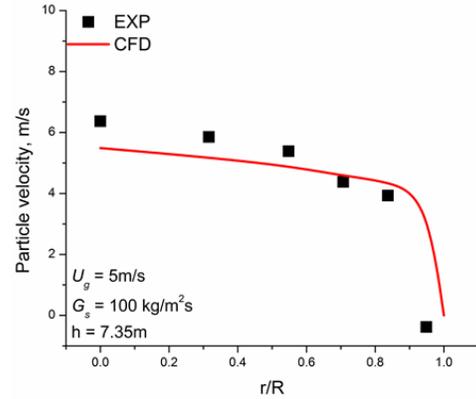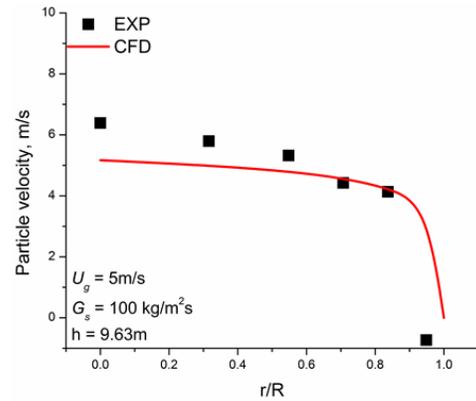
Figure 6-9 Radial profiles of solids holdup from cluster-driven drag model

Axial profiles of the solids holdup under different operating conditions are plotted in Figure 6-9. The overall bed density increases with the increase in the solids circulation rate or the decrease in the superficial gas velocity as shown in Figure 6-10. Generally, an exponential profile of the axial solids distribution with a denser bottom and a dilute upper zone is found in the riser. With the increase in the solids circulation rate, a clearer and relatively longer denser bottom region forms in the riser as shown in Figure 6-10, which also indicates that more severe clustering phenomenon takes place in the lower developing region of the riser. In the upper fully developed region of the riser, a good agreement with experimental data is achieved by the proposed cluster-driven model as shown in Figure 6-10. However, deviations are found in the bottom entrance region indicating that the clustering effect is still underestimated. Improvements including the axial cluster size distribution into the cluster-driven model will be made in the future.
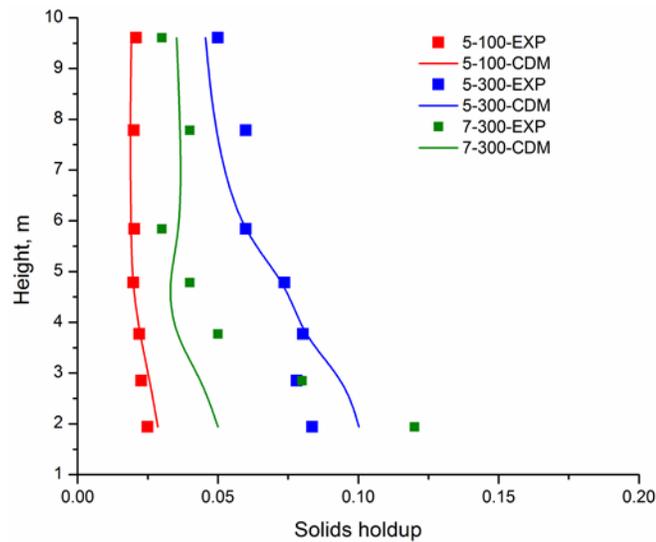
Figure 6-10: Axial profiles of the solids holdup under different operating conditions
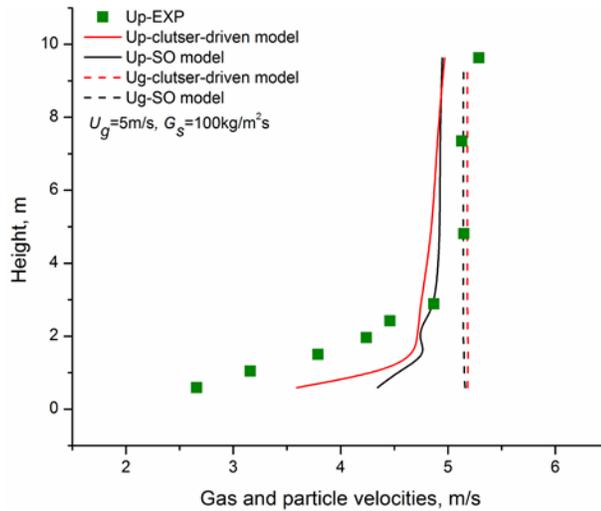
Figure 6-11: Axial profile of the gas phase and solid phase velocities

Further comparisons of gas and particle velocities and the slip velocity between the proposed cluster-driven model and the Syamlal-O'Brien model are illustrated in Figure 6-11 and Figure 6-12. The predicted velocity profiles of the gas and particles from the proposed cluster-driven model and the Syamlal-O'Brien are very close to each other as shown in Figure 6-11. For the solids velocity profile along the riser, although the predicted solids velocity slightly deviate from the experimental the data, same trend of the solids velocity acceleration along the CFB riser is achieved as shown in Figure 6-11. Both the proposed cluster-driven model and the Syamlal-O'Brien model predict an acceleration region which is around 2 m from the gas distributor. The proposed cluster-driven model predicts a lower solids velocity than the one obtained by the Syamlal-O'Brien model as shown in Figure 6-11 indicating greater momentum transfer is obtained by the cluster-driven drag model.

When it comes to the slip velocity between gas and solids, a larger slip velocity is predicted by the cluster-driven drag model than that from the Syamlal-O'Brien model, especially in the bottom developing zone and the middle part of the riser as shown in Figure 6-12. Generally, the gas velocity is greater than solids velocity in the CFB riser, which results in the upward drag force exerted on the particles. For particle clusters with larger size than the individual particles, the upward drag force on the clusters per unit volume reduces with the increase of the diameter since the drag force is proportional to the projected area of the

particles. Therefore, the slip velocity of the clusters becomes larger with the reduction of the drag force per unit volume. The larger slip velocity of the solid phase from the cluster-driven drag model indicates a more severe clustering effect in the CFB riser.

The same effect using the cluster-driven drag model also can be seen from the profile of the granular temperature of solids in Figure 6-13, where the from cluster-driven drag model is obviously greater than the one calculated by the Syamlal-O'Brien model.

From the view of clustering phenomenon in the CFB riser, the effect of the significant clustering phenomenon is captured by the cluster-driven model, so that a larger slip velocity is obtained since the clusters always move slower than single particles due to their larger size and higher concentration. Since the granular temperature associates with the particle fluctuations, a higher granular temperature of solids as shown in Figure 6-13 indicates more intensive fluctuations, and resulting in more intensive gas-particle and particle-particle interactions in the riser. On the other hand, continuously formation and breakup of clusters lead to more gas-particle or particle-particle interactions which enhance the momentum transfer between gas and solids, which results a higher granular temperature. Based on Figure 6-11 and Figure 6-12, it can be seen that more clusters tend to be formed in the acceleration region, which was also reported Pärssinen and Zhu (2001), Wang, et al. (2014), and Wang, et al. (2014). Therefore, both the slip velocity and granular temperature are higher at the bottom region due to the existence of clusters.
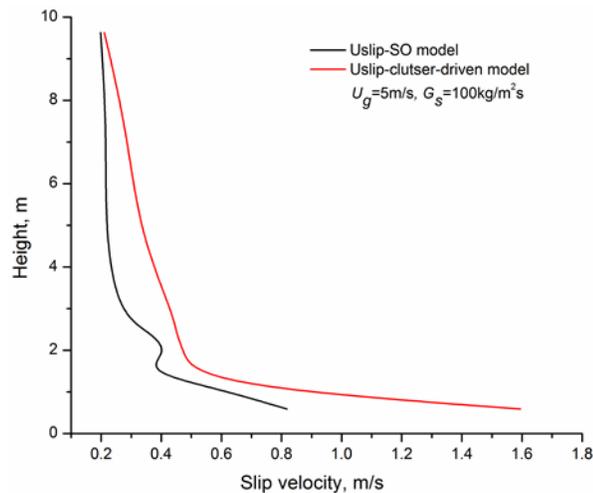
Figure 6-12: Comparison of the slip velocity from the Syamlal-O'Brien model and cluster-driven model
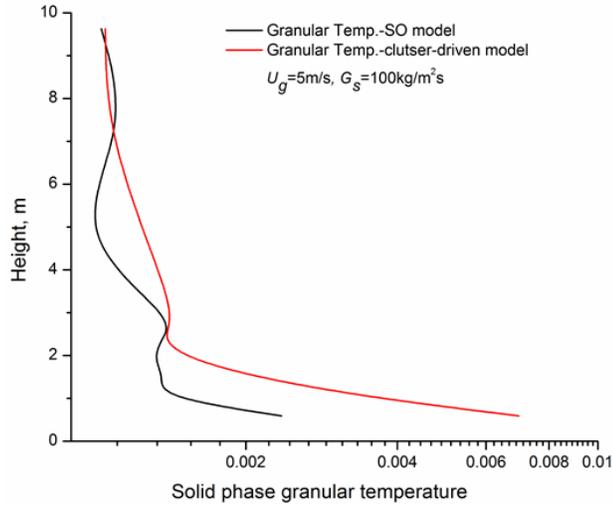
Figure 6-13: Comparison of the granular temperature from the Syamlal-O'Brien model and cluster-driven model

6.4.5 Effects of cluster size

The effects of the cluster size is the first factor numerically studied by the cluster-driven drag calculation as shown in Figure 6-14 and Figure 6-15. Three sizes of clusters are selected in the cluster-driven drag model: $d_{cl} = 0.0007$m which is the same diameter of an individual FCC particle, $d_{cl} = 0.0051$m which is the median size from the statistical data of a cluster from image analysis, and $d_{cl} = 0.01$m which is about 150 times of an individual particle and close to the maximum size from the statistical data. The numerical results of the local solids holdup profiles from these three cases at the bottom, middle, and upper parts of the CFB riser under a high-density operating condition (U_g=7m/s, G_s=300kg/m²s) are compared with the results from Syamlal-O'Brein drag model and experimental data plotted in Figure 6-14.

(a) H=2.88m

(b) H=5.85m
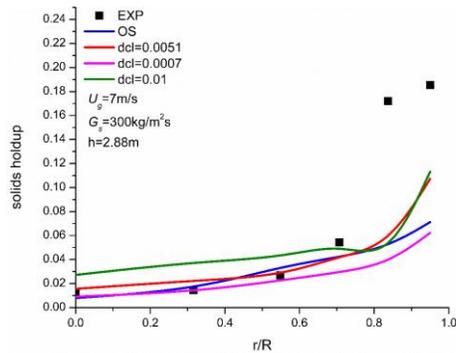
(c) H=9.63m
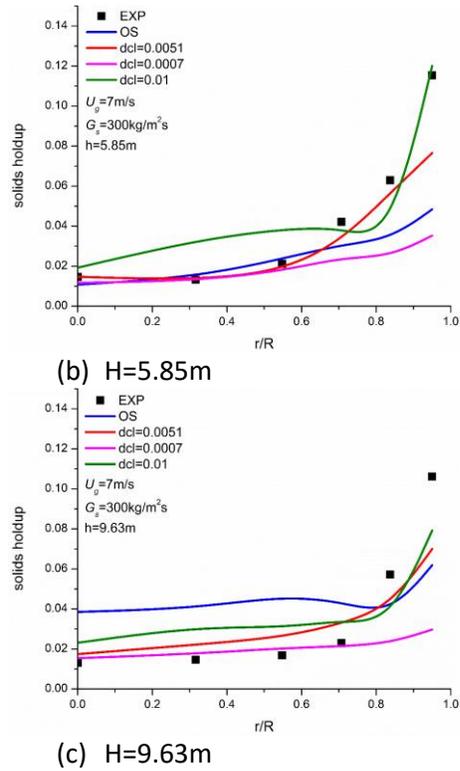
Figure 6-14: Numerical results from different cluster size by the proposed cluster-driven drag calculation
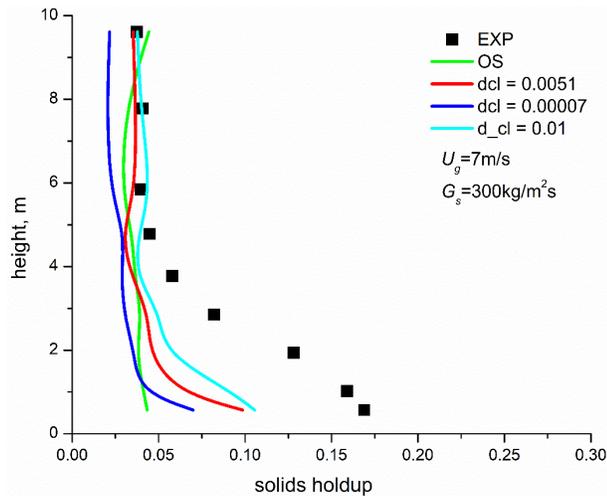
Figure 6-15: Results from simulations and experiments of overall solids holdup

Generally, all the drag calculations perform well in the numerical simulations with a well predicted core-annulus structure of local solids holdup in the riser which has the same tendency with the experimental data as shown in Figure 6-14. Certainly, a higher solids

holdup is obtained by the cluster-driven model with larger cluster size which is reasonable since the relative Reynolds number increases with the increasing size of the cluster and resulting in a reduction of drag per unit volume. In the center region of the riser, the effects of cluster size are less significant and only with the extremely large cluster ($d_{cl} = 0.01$m) the numerical results show a distinct deviation with the ones applying the statistical median cluster size or single particle diameter. Also, the effects of the cluster size are more distinct in the annulus layer than the center region of the riser, and the local solids holdup can be greatly enlarged for a better agreement with the experimental data by increasing the cluster size used in the calculation of drag. In the lower and middle parts of the riser, a good agreement in the center region is achieved by the drag calculations with smaller cluster size which is reasonable since smaller clusters tend to occur in the center dilute and high-velocity region of the riser. The cluster-driven drag model using single particle diameter as the cluster size and the Syamlal-O'Brien model work better in the center region of the riser, than the ones with large cluster diameter. However, an underestimation still happens in the wall region for all the drag calculations especially in the lower part of the riser but well improved by the drag calculation with extremely large clusters while an overestimation is detected in the center region in the meanwhile as shown in Figure 6-14 (a) and (b).

Near the top of the riser, all the drag models overestimate the local solids holdup in the center dilute region except for the cluster-driven drag model using the single particle diameter as cluster diameter indicating that less and smaller clusters occur in the center dilute region near the outlet since the flow is fully developed. Also, comparing with the well-established Syamlal-O'Brien drag model, an improvement in the wall region of the riser is achieved by increasing the cluster size in the cluster-driven model and the overestimation is much more severe by the Syamlal-O'Brien drag model than the other cluster-driven drag calculations in the center region at the top of the riser. In an HDCFB riser where the solids holdup increases dramatically in the wall region, the empirical voidage function used in Syamlal-O'Brien drag model might over-predict the uniformity of the flow structure in the dilute region resulting in an overestimation of the solids holdup in the center of the riser but an underestimation in the wall region as shown in Figure 6-14 (c).

Figure 6-15 shows comparison of the axial solids holdup profiles from all the drag models with the experimental data. In the upper dilute region of the riser (h>5m), increasing the size of clusters in the drag calculation has an insignificant impact on the overall solids holdup except for the one using dcl=0.00007m and a good agreement with the experimental data is achieved by all the drag models as shown in Figure 6-15. A much denser suspension in the lower region of the riser is one of the remarkable characteristics in an HDCFB riser as shown in Figure 6-15, however, the commonly used Syamlal-O'Brien drag model failed to predict such a denser condition since the major part of the data it collected for the empirical correlation came form low-density operations (Syamlal and O'Brien 1994). A higher overall solids holdup can be obtained by increasing the size of cluster in the cluster-driven model although an underestimation still exists comparing with the experimental data revealing the improvement achieved by including the cluster properties in the calculation of the drag as shown in Figure 6-15.

6.5 Conclusion

A cluster-driven drag model that directly employs the properties of particle clusters inside the CFB riser in the drag model is proposed for numerical simulations of the gas-solids circulating fluidized bed riser. With the help of statistical analysis of the clusters through image processing based on the experimental data, the characteristics of clusters including the size, density, and volume fraction of the clusters under different operating conditions in the CFB riser are used in the drag model. The drag force is obtained by the summation of the drag force from clusters and the drag from freely moving single particles in the CFB riser. Improvements in the prediction accuracy are achieved by employing more realistic properties of clusters in the cluster-driven drag model, such as a good agreement of the axial solids holdup profile with the experimental data and a better agreement of local solids distribution especially in the wall region of the riser. Larger slip velocity and higher granular temperature are predicted by the proposed cluster-driven model than that those from the commonly used drag model suggesting more intensive interactions between gas and particles due to the existence of clusters. Effects of the cluster size are discussed by the cluster-driven drag model, a larger cluster size results in a higher overall solids holdup, especially in the bottom part of the gas-solid CFB riser.

Nomenclature

$$A_p = \frac{\pi \cdot d_p^2}{4}$$ Reference area of a particle projecting to the fluid, m^2

C_{D_cl} Drag coefficient of clusters in the gas-solid system

C_{D_p} Drag coefficient of single particles in the gas-solid system

C_d Drag coefficient for a single particle in a fluid

C_d' Drag coefficient in the homogeneous dilute gas-solids system

F_D Total drag force per unit volume in the homogeneous gas-solids suspension

F_d Drag force for a single particle in the ideal gas-solids system

F_d' Drag force exerted on a single particle in multi-particle system

P_{cl} Percentage of the total solids captured in the cluster phase

Re_{cl} Reynolds number of clusters

Re_p Reynolds number of single particles

U_{slip} Slip velocity between fluid and particle, m/s

U_{slip_cl} Slip velocity between clusters and surrounding fluid, m/s

$V_{g,in}$ Inlet gas velocity, m/s

$V_{s,in}$ Inlet velocity of the solid phase, m/s

V_{s,in_m} Modified inlet velocity of the solid phase, m/s

d_{cl} Equivalent cluster diameter, m

d_{en_cl} Solid concentration in the cluster

d_p Particle diameter, m

$$n_p = \frac{6(1 - \varepsilon_g)}{\pi \cdot d_p^3}$$ Number of the particles per unit volume

α_g Gas phase volume fraction

α_s Solid phase volume fraction

$\beta_{cluster}$ Momentum transfer coefficient between clusters and the bypassing gas

β_{gs} Total momentum transfer coefficient between gas and solids

β_p	Momentum transfer coefficient between freely moving individual particles and pure gas
ε_{cl}	Portion of the captured particles inside the clusters in the gas-solids system
ε_g	Gas holdup
ε_{g_cl}	Portion of the captured gas inside the clusters
ε_s'	Solids holdup in a homogeneously dispersed gas-solids system
ρ_g	Gas density, kg/m^3
ρ_s	Particle density, kg/m^3
ρ_{sus}	Mixture density of the gas-solid suspension, kg/m^3
φ_{cl}	Volume fraction of cluster phase
φ_g	Volume fraction of pure gas phase bypassing the individual particles or clusters
φ_p	Volume fraction of single particle phase
g	Gravity acceleration, m/s^2
G_s	Solids circulation rate, kg/m^{2}s
h	Height from the gas distributor, m
h/H	Relative axial position
r/R	Relative radial position
U_g	Superficial gas velocity, m/s
V_{l_p}	Volume of a particle
ε	Gas voidage
ε$_s$	Solids holdup in the CFB riser
ф	Ratio of the opening area in the gas distributor

References

Almuttahar, Adnan & Taghipour. (2008). computational fluid dynamics of high density circulating fluidized bed riser: study of modeling parameters. Powder Technology 185(1): 11–23.

ANSYS, Inc. 2013. Chapter 17. Multiphase Flows. ANSYS Fluent Theory Guide. Pp. 527-586

Benyahia, Arastoopour, Knowlton & Massah. (2000). Simulation of particles and gas flow behavior in the riser section of a circulating fluidized bed using the kinetic theory approach for the particulate phase. Powder Technology 112(1–2): 24–33.

Cahyadi, Anantharaman, Yang, Karri, Findlay, Cocco & Chew (2017). Review of cluster characteristics in circulating fluidized bed (CFB) risers. Chemical Engineering Science, 158, 70-95.

Cocco, Shaffer, Hays, Karri & Knowlton (2010). Particle clusters in and above fluidized beds. Powder Technology, 203(1), 3-11.

Gibilaro, Di Felice, Waldram & Foscolo. (1985). generalized friction factor and drag coefficient correlations for fluid-particle interactions. Chemical Engineering Science 40(10): 1817–23.

Dimitri & Gidaspow. (1994). One-dimensional steady gas–solid flow." Multiphase Flow and Fluidization: 31–60.

Grace, Bi & Golriz. (2003). Circulating fluidized beds. in Handbook of Fluidization and Fluid-Particle Systems, ed. Marcel Dekker Wen-Ching Yang. New York: CRC press, 485-498.

Harris, Davidson & Thorpe. (2002). The prediction of particle cluster properties in the near wall region of a vertical riser. Powder Technology 127(2): 128–43.

Horio, Ishii & Nishimuro. (1992). On the nature of turbulent and fast fluidized beds. Powder Technology 70(3): 229–36.

Hori, & Clift. (1992). A note on terminology: 'Clusters' and 'Agglomerates.' Powder Technology 70(3): 196.

Lu & Gidaspow. (2003). Hydrodynamics of binary fluidization in a riser: CFD simulation using two granular temperatures. Chemical Engineering Science 58(16): 3777–92.

Kunii & Levenspiel (2013). Fluidization engineering. Elsevier.

Lackermeier, Rudnick, Werther, Bredebusch & Burkhardt (2001). Visualization of flow structures inside a circulating fluidized bed by means of laser sheet and image processing. Powder Technology, 114(1-3), 71-83.

Li, Xia, Tung & Kwauk. (1991). Micro-visualization of clusters in a fast fluidized bed. Powder Technology 66(3): 231–35.

Li & Kwauk. (2003). Exploring Complex Systems in Chemical Engineering—the Multi-Scale Methodology. Chemical Engineering Science 58(3–6): 521–35.

Li (2010). Investigation of circulating fluidized bed riser and downer reactor performance for catalytic ozone decomposition. Ph.D thesis, University of Western Ontario.

Liu, Gao & Li. (2005). Characterizing particle clustering behavior by PDPA measurement for dilute gas–solid flow. Chemical Engineering Journal 108(3): 193–202.

Lyczkowski, Robert, Gidaspow, Solbrig & Hughes. (1978). Characteristics and stability analyses of transient one-dimensional two-phase flow equations and their finite difference approximations. Nuclear Science and Engineering 66(3): 378–96.

Manyele, Pärssinen & Zhu. (2002). characterizing particle aggregates in a high-density and high-flux cfb riser. Chemical Engineering Journal 88(1–3): 151–61.

Mondal, Nandan, Kallio, Saxén & Hassel. (2016). Experimental study of cluster properties in a two-dimensional fluidized bed of geldart b particles. Powder Technology 291: 420–36.

Pärssine & Zhu. (2001). Particle velocity and flow development in a long and high-flux circulating fluidized bed riser. Chemical Engineering Science 56(18): 5295–5303.

Samuelsberg & Hjertager. (1996). An experimental and numerical study of flow patterns in a circulating fluidized bed reactor. International Journal of Multiphase Flow 22(3): 575–91.

Schiller & Naumann. 1935. A drag coefficient correlation. Z. Ver. Deutsch. Ing 77: 318–20.

Sharma, Arun, Tuzla, Matsen & Chen. (2000). Parametric effects of particle size and gas velocity on cluster characteristics in fast fluidized beds. Powder Technology 111(1–2): 114–22.

Syamlal & O'Brien (1987). The derivation of a drag coefficient formula from velocity-voidage correlations. Technical Note, US Department of energy, Office of Fossil Energy, NETL, Morgantown, WV.

Syamlal & O'Brien. (1989) Computer simulation of bubbles in a fluidized bed. AIChE Symposium Series. 85 (1989) 22-31.

Takeuchi, Hirama, Chiba, Biswas & Leung (1986). A quantitative definition and flow regime diagram for fast fluidization. Powder technology, 47(2), 195-199.

Tsuji, Tanaka & Yonemura. (1998). Cluster patterns in circulating fluidized beds predicted by numerical simulation (discrete particle model versus two-fluid model). Powder Technology 95(3): 254–64.

Tsuo, Yuan & Gidaspow. (1990). Computation of flow patterns in circulating fluidized beds. AIChE Journal 36(6): 885–96.

Wang, Liu, Lu, Xu, Yang & Gidaspow (2012). A cluster structure-dependent drag coefficient model applied to risers. Powder technology, 225, 176-189.

Wang, Zhu, Barghi & Li (2014a). Axial and radial development of solids holdup in a high flux/density gas-solids circulating fluidized bed. Chemical Engineering Science, 108, 233–243.

Wang, Zhu, Li & Barghi (2014b). Detailed measurements of particle velocity and solids flux in a high density circulating fluidized bed riser. Chemical Engineering Science, 114, 9-20.

Wang (2013). High-density gas-solids circulating fluidized bed riser and downer reactors. Ph.D thesis, University of Western Ontario.

Wen & Yu. (1966). A generalized method for predicting the minimum fluidization velocity. AIChE Journal 12(3): 610–12.

Xu & Zhu. (2012). A new method for the determination of cluster velocity and size in a circulating fluidized bed. Industrial & Engineering Chemistry Research 51(4): 2143–51.

Wei (2019). Experimental investigations on the instantaneous flow structure in circulating fluidized beds. Ph.D thesis, University of Western Ontario.

Yang & Zhu. (2014). A novel method based on image processing to visualize clusters in a rectangular circulating fluidized bed riser. Powder Technology 254: 407-15.

Yang & Zhu. (2015). Cluster identification using image processing. Particuology 23: 16–24.

Yang & Leu. (2009). Multiresolution analysis on identification and dynamics of clusters in a circulating fluidized bed. AIChE Journal 55(3): 612-29.

Yerushalmi, Turner & Squires. (1976). The fast fluidized bed. Industrial and Engineering Chemistry Process Design and Development 15(1): 47–53.

Zou, Li, Xia & Ma. (1994). Cluster structure in a circulating fluidized bed. Powder Technology 78(2): 173–78.

Chapter 7

7 Numerical study on particle clustering phenomenon in gas-solids circulating fluidized bed riser

7.1 Introduction

The past 100 years have witnessed the global blossom of the gas-solids fluidization technology in various fields including catalytic cracking of oil, coal combustion and gasification, calcination of mineral materials, and physical processes like drying (Grace, et al., 2003). A gas-solids fluidization process operates by continuously introducing gas flow through the granular materials at a certain velocity, so solids particles will be suspended and turn into a fluid-like state. With the expansion of fluidization technology, high-velocity gas-solids fluidized beds especially the circulating fluidized bed (CFB) has wide applications due to its advantages over the conventional low-velocity fluidized beds, such as the uniform temperature distribution, better gas-solids contacting, high mass and heat transfers (Grace 1990). A typical gas-solids CFB system consists of a riser where suspended particles flow upward and a downer where entrained particles flow downward. CFB risers are more commonly used as a chemical reactor, which attracted considerable fundamental studies on the flow structures inside it (Ommen & Ellis 2010, Yerushalmi & Cankurt 1979, Yerushalmi, et al., 1976). Radial and axial non-uniformity is one of the notable characteristics inside a CFB riser due to the existence of particle clusters (Grace 1986). In a gas-solids flow system, solids particles tend to agglomerate and form the so-called "clusters" inside a fluidized bed due to hydrodynamic or cohesive effects (Cocco et al., 2010).

Cluster is a group of particles which is highly concentrated than its surrounding dilute suspended particles in CFB risers (Horio & Clift, 1992). The shapes of clusters are characterized as sphere, U-shaped, and elongated strands or streams. Clusters are found to continuously form and breakup in the gas-solids CFB riser resulting in inevitable impacts on the flow structures. The dynamic behavior, irregular shapes, and higher concentration of clusters make the hydrodynamics in the CFB riser more complex. Therefore, studies on

clustering phenomenon have emerged rapidly in the past decades (Cocco et al. 2010; Sharma et al. 2000; Tsuji, et al., 1998).

Although different interpretations of data existed for years, the size, density, velocity, frequency, and axial and radial distributions of clusters are characterized with the help of some novel experimental techniques and analysis approaches (Lackermeier et al. 2001; Mondal et al. 2016; Xu & Zhu 2012). Cluster size is reported to vary from 0.001 m to 0.1 m and the cluster voidage is found to range from 0.4 under extremely dense conditions to over 0.9 in some dilute cases. Both increasing and decreasing trends of cluster size and voidage are observed axially and radially in CFB risers. Both upward and downward moving clusters are detected due to the local flow conditions and particle properties. Despite the dynamic nature of clustering phenomenon, "core" clusters with more spherical shape and relatively smaller size are detected to stably move in CFB riser (Yang & Zhu 2015). A series of small "core" clusters connected by denser wakes of particles usually form a larger piece of cluster whose shape transforms frequently since the "core" clusters are loosely aligned.

Being fully aware of the existence of particle clusters inside a gas-solids CFB riser, researchers have put lots efforts into better describing the clustering phenomenon in numerical models since the 1970s (Sinclair & Jackson 1989; Tsuo & Gidaspow 1990; Wen & Yu 1966). The clustering effects are included into the interactions between gas and particles in computational fluid dynamic (CFD) models. Comparing with the Eulerian-Lagrangian method, which requires higher computational time, the Eulerian-Eulerian (EE) approach is more applicable for simulations of large-scale CFB risers. The EE two-fluid model (TFM), which treats both the gas and solid phases as interpenetrating continua, has become an effective tool to simulate the gas-solids flow in a CFB riser. In the TFM, an accurate drag model is required to account for the clustering effects. Larger drag force is expected for a cluster due to its larger size and correspondingly lager slip velocity than a single particle. Unlike a homogeneous particulate system in which the drag force can be derived analytically, the drag force in a gas-solids CFB riser can be considered as a combination of the drag forces from freely moving single particles and the clusters. Current drag models used in gas-solids CFB riser simulations are mainly based on empirical

correlations in which a voidage function accounting for the clustering effects is commonly used, however, the underlying physics of those empirical correlations are still unclear. On the other hand, the operations of gas-solids CFB risers have expanded to high-density (HD) conditions with different flow structures as well as clustering phenomena from low-density (LD) conditions. Previous correlations used to account for the clustering phenomenon are not appropriate to describe the gas-solids interactions in a HDCFB because most of them were developed based on experimental data under more dilute conditions. Therefore, a more accurate drag model to include the clustering effect, which is named as cluster-driven drag model, is developed in this study with the help of image analysis in CFB risers based on the experimental date. In this cluster-driven drag model, the drag force is calculated by a summation of the drag force due to clusters and the drag force due to freely moving particles. The cluster size, voidage, and portion of particles captured in clusters, which are obtained from the statistical data via image analysis based on the experimental data, are employed in the proposed drag model. Numerical simulations using the proposed cluster-driven drag model for the gas-solids two-phase flows in a CFB riser from conditions to high-density conditions are carried out and the effects of clusters on the flow structures are investigated based on the numerical results.

7.2   CFD model descriptions

7.2.1 Governing equations and mesh setup

Experimental studies were conducted in a gas-solids CFB riser as shown in Figure 7-1 (Li, 2010; Wang, 2013). The CFB riser has an inner diameter of 0.0762 m (3 in) and is of 10 m in height (Li, 2010). The radial and axial data of solids holdups and particle velocities are obtained by optical fiber probes at different positions in the CFB riser. Since the experimental column is too large for a 3D simulation, two-dimensional CFD simulation is selected. A 2D mesh consisting of 120×4000 grids with finer grids near the wall and the inlets as shown in Figure 7-2 is used because the flow parameters in a CFB change greatly near those regions. The gird independent test was done in the previous work.

An Eulerian-Eulerian two-fluid model (TFM) is employed to simulate the gas-solids flows in a CFB riser. Both the gas and solids phases are treated as interpenetrating continua in

the TFM. The kinetic theory of granular flow (KTGF) is used in the TFM to obtain the pressure and bulk viscosity of the solids phase based on the granular temperature of the solids particles. The k-ε turbulence model is applied for both gas and solids phases. Table 7-1 lists the governing equations for the simulation of the gas-solids two-phase flow in a CFB riser. The commercial software ANSYS Fluent V17 is used for the simulations. The second order discretization scheme is selected for the turbulence equations and QUICK scheme is used for convection terms in the momentum equations. The convergence criterion is specified as 5×10^{-4} for each scaled residual component.
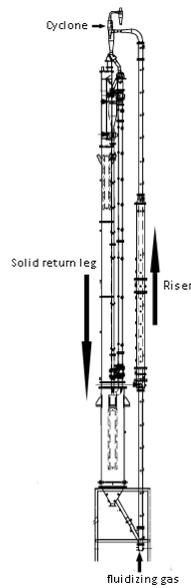
Figure 7-1: Configuration of the CFB riser (Li 2010)
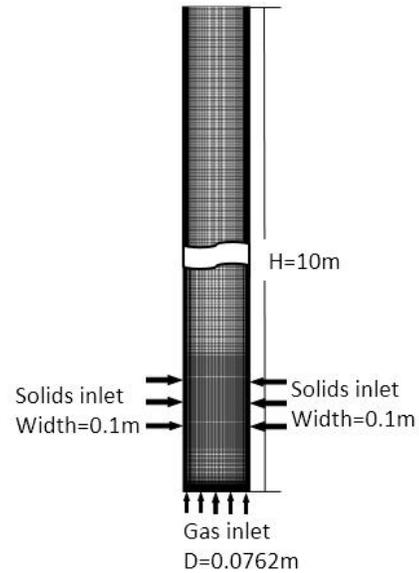
Figure 7-2: Mesh for the computational domain of the CFB riser

7.2.2 Boundary conditions

A velocity profile based on the gas distributor of the CFB riser is employed as the inlet boundary condition for the gas phase, which is located at the bottom of the computational domain as shown in Figure 7-2. Two symmetric solid phase inlets are located at the same height on both sides of the computational domain, which are analogous to the solids returning pipe of the 3D column as shown in Figure 7-1. The solid phase inlets have the same diameter as the solids returning pipe with a uniform inlet velocity. No slip velocity boundary condition is applied at the wall for the gas phase and partial slip boundary

condition with a specularity coefficient of 0.0001 and a restitution coefficient of 0.9 is employed for the solids phase at the wall. The outflow boundary condition is used for both the gas and solids phases at the outlet, which is at the top of the riser as shown in Figure 7-2.

7.2.3 Cluster-driven drag model

A cluster-driven model is proposed to include the clustering effect on the drag force in the gas-solids two-phase flow in the CFB riser. The gas-solids interactions inside a CFB riser can be divided into two classes based on the types of solid phase as shown in Figure 7-3, (1) the drag force between the single particles and the gas phase and (2) the drag force between the clusters and the gas phase with the assumption that the clusters are stable spherical clouds of single particles existing in the fluidized bed ("core" clusters). The total drag force between the gas and solids is the summation of those two drag forces. The detailed derivation of the cluster-driven drag model was given in the previous work. The drag coefficients for both the single particle and clusters are from the Schiller & Naumann's correlation (ANSYS 2013). Table 7-2 lists the equations and parameters used in the cluster-driven model.
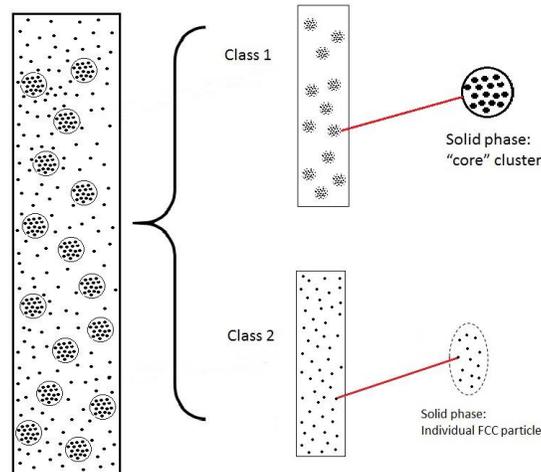
Figure 7-3: Schematic diagram of the cluster-driven drag model

Table 7-1: Governing equations

Continuity equation of gas and solids:	$\frac{\partial}{\partial t}(\alpha_g \rho_g) + \nabla \cdot (\alpha_g \rho_g \overrightarrow{v_g}) = 0$	(7-1)
Continuity equation of solids:	$\frac{\partial}{\partial t}(\alpha_s \rho_s) + \nabla \cdot (\alpha_s \rho_s \overrightarrow{v_s}) = 0$	(7-2)
Momentum equation of gas:	$\frac{\partial}{\partial t}(\alpha_g \rho_g \overrightarrow{v_g}) + \nabla \cdot (\alpha_g \rho_g \overrightarrow{v_g}\overrightarrow{v_g}) = -\alpha_g \nabla P + \nabla \cdot \left(\alpha_g \left(\overline{\overline{\tau_g^m}} + \overline{\overline{\tau_g^{Re}}}\right)\right) + \alpha_g \rho_g \vec{g} + \beta_{gs}(\overrightarrow{v_s} - \overrightarrow{v_g})$ where $\overline{\overline{\tau_g^m}} = -\frac{2}{3}\mu_{g.m}\nabla \cdot \overrightarrow{v_g}\overline{\overline{I}} + \mu_{g.m}\left(\nabla\overrightarrow{v_g} + \nabla\overrightarrow{v_g}^T\right)$, and $\overline{\overline{\tau_g^{Re}}} = -\frac{2}{3}(\rho k_g + \mu_{g.t}\nabla \cdot \overrightarrow{v_g})\overline{\overline{I}} + \mu_{g.t}(\nabla\overrightarrow{v_g} + \nabla\overrightarrow{v_g}^T)$.	(7-3)
Momentum equation of solids:	$\frac{\partial}{\partial t}(\alpha_s \rho_s \overrightarrow{v_s}) + \nabla \cdot (\alpha_s \rho_s \overrightarrow{v_s}\overrightarrow{v_s}) = -\alpha_s \nabla P - \nabla P_s + \nabla \cdot \left(\alpha_s \left(\overline{\overline{\tau_s^m}} + \overline{\overline{\tau_s^{Re}}}\right)\right) + \alpha_s \rho_s \vec{g} + \beta_{gs}(\overrightarrow{v_g} - \overrightarrow{v_s})$ where $\overline{\overline{\tau_s^m}} = (\lambda s - \frac{2}{3}\mu_s)\nabla \cdot \overrightarrow{v_s}\overline{\overline{I}} + \mu_s(\nabla\overrightarrow{v_s} + \nabla\overrightarrow{v_s}^T)$, and $\overline{\overline{\tau_s^{Re}}} = -\frac{2}{3}(\rho k_s + \mu_{s.t}\nabla \cdot \overrightarrow{v_s})\overline{\overline{I}} + \mu_{s.t}(\nabla\overrightarrow{v_s} + \nabla\overrightarrow{v_s}^T)$.	(7-4)
Granular temperature equation	$\frac{3}{2}\left[\frac{\partial}{\partial t}(\rho_s \alpha_s \Theta s) + \nabla \cdot (\alpha_s \rho_s \overrightarrow{v_s}\Theta s)\right] = \left(-P_s\overline{\overline{I}} + \overline{\overline{\tau_s}}\right):\nabla \overrightarrow{v_s} + \nabla \cdot (k_{\Theta s}\nabla\Theta) - \gamma_{\Theta s} + \emptyset_{gs}$ where $\emptyset_{gs} = -3k_{gs}\Theta s$. The collisional energy can be obtained by: $\gamma_{\Theta s} = \frac{12(1-e_{ss}^2)g_{0,ss}}{d_s\sqrt{\pi}}\rho_s\alpha_s^2\Theta_s^{3/2}$.	(7-5)
k equation for gas:	$\frac{\partial}{\partial t}(\alpha_g \rho_g k_g) + \nabla \cdot (\alpha_g \rho_g \overrightarrow{v_g} k_g) = \nabla \cdot \left(\alpha_g \frac{\mu_{g,t}}{\sigma_k}\nabla k_g\right) + (\alpha_g G_{g,k} - \alpha_g \rho_g \varepsilon_g) + \beta_{gs}(C_{gs}k_g - C_{sg}k_s) -$ $\beta_{gs}(\overrightarrow{v_g} - \overrightarrow{v_s}) \cdot \frac{\mu_{g,t}}{\alpha_g\sigma_g}\nabla\alpha_g + \beta_{gs}(\overrightarrow{v_g} - \overrightarrow{v_s}) \cdot \frac{\mu_{g,t}}{\alpha_g\sigma_g}\nabla\alpha_g$ where the turbulent viscosity, $\mu_{g,t} = \rho_g C_\mu \frac{k_g^2}{\varepsilon_g}$,	(7-6)
ε equation for gas:	$\frac{\partial}{\partial t}(\alpha_g \rho_g \varepsilon_g) + \nabla \cdot (\alpha_g \rho_g \overrightarrow{v_g}\varepsilon_g) = \nabla \cdot \left(\alpha_g \frac{\mu_{g,t}}{\sigma_k}\nabla\varepsilon_g\right) + \frac{\varepsilon_g}{k_g}(C_{1\varepsilon}\alpha_g G_{g,k} - C_{2\varepsilon}\alpha_g\rho_g\varepsilon_g + C_{3\varepsilon}(\beta_{gs}(C_{sg}k_s -$ $C_{gs}k_g) - \beta_{gs}(\overrightarrow{v_s} - \overrightarrow{v_g}) \cdot \frac{\mu_{s,t}}{\alpha_s\sigma_s}\nabla\alpha_s + \beta_{gs}(\overrightarrow{v_s} - \overrightarrow{v_g}) \cdot \frac{\mu_{g,t}}{\alpha_g\sigma_g}\nabla\alpha_g))$	(7-7)
k equation for solids:	$\frac{\partial}{\partial t}(\alpha_s \rho_s k_s) + \nabla \cdot (\alpha_s \rho_s \overrightarrow{v_s} k_s) = \nabla \cdot \left(\alpha_s \frac{\mu_{s,t}}{\sigma_k}\nabla k_s\right) + (\alpha_s G_{s,k} - \alpha_s \rho_s \varepsilon_s) + K_{gs}(C_{gs}k_g - C_{sg}k_s) -$ $\beta_{gs}(\overrightarrow{v_g} - \overrightarrow{v_s}) \cdot \frac{\mu_{g,t}}{\alpha_g\sigma_g}\nabla\alpha_g + \beta_{gs}(\overrightarrow{v_g} - \overrightarrow{v_s}) \cdot \frac{\mu_{s,t}}{\alpha_s\sigma_s}\nabla\alpha_s$ where the turbulent viscosity, $\mu_{s,t} = \rho_s C_\mu \frac{k_s^2}{\varepsilon_s}$	(7-8)
ε equation for solids:	$\frac{\partial}{\partial t}(\alpha_s \rho_s \varepsilon_s) + \nabla \cdot (\alpha_s \rho_s \overrightarrow{v_s}\varepsilon_s) = \nabla \cdot \left(\alpha_s \frac{\mu_{s,t}}{\sigma_k}\nabla\varepsilon_s\right) + \frac{\varepsilon_s}{k_s}(C_{1\varepsilon}\alpha_s G_{s,k} - C_{2\varepsilon}\alpha_s\rho_s\varepsilon_s + C_{3\varepsilon}(\beta_{sg}(C_{sg}k_g - C_{gs}k_s) -$ $\beta_{gs}(\overrightarrow{v_s} - \overrightarrow{v_g}) \cdot \frac{\mu_{s,t}}{\alpha_s\sigma_s}\nabla\alpha_s + \beta_{gs}(\overrightarrow{v_s} - \overrightarrow{v_g}) \cdot \frac{\mu_{s,t}}{\alpha_s\sigma_s}\nabla\alpha_s))$	(7-9)

Table 7-2: Cluster-driven drag model

Momentum transfer coefficient for clusters	$$\beta_{cl} = \frac{3}{4} \cdot C_{D\_cl} \cdot \frac{\varphi_g \cdot \varphi_{cl} \cdot \rho_g \cdot |U_{slip\_cl}|}{d_{cl}}$$	(7-10)
Slip velocity of clusters:	$$U_{slip\_cl} = \sqrt{\frac{4}{3} \cdot \frac{d_{cl} \cdot g}{C_{D\_cl}} \cdot \frac{(\rho_{cl} - g)}{\rho_g}}$$	(7-11)
Drag coefficient of clusters:	$C_{D\_cl} = \frac{24}{Re_{cl}}(1 + 0.15Re_{cl}{}^{0.687})$ for Re_{cl}<1000 $C_{D\_cl} = 0.44$ for $Re_{cl} \geq 1000$ where: $Re_{cl} = \frac{\rho_g \cdot U_{slip\_cl} \cdot d_{cl}}{\mu_g}$	(7-12)
Momentum transfer coefficient for single particles	$$\beta_p = \frac{3}{4} \cdot C_{D\_p} \cdot \frac{\varphi_g \cdot \varphi_p \cdot \rho_g \cdot |U_{slip}|}{d_p}$$	(7-13)
Drag coefficient of single particles:	$C_{D\_p} = \frac{24}{Re_p}\left(1 + 0.15Re_p{}^{0.687}\right)$ for Re_p<1000 $C_{D\_p} = 0.44$ for Re_p>=1000 where: $Re_p = \frac{\rho_g \cdot U_{slip} \cdot d_p}{\mu_g}$	(7-14)
Momentum transfer coefficient for gas-solids system:	$$\beta_{gs} = \beta_p + \beta_{cl}$$	(7-15)

7.3 Results and discussion

7.3.1 Flow development

7.3.1.1 Solids holdup profiles

(a) Ug=5m/s,
    Gs=100kg/m²s

(b) Ug=5m/s,
    Gs=300kg/m²s

(c) Ug=5m/s,
    Gs=400kg/m²s
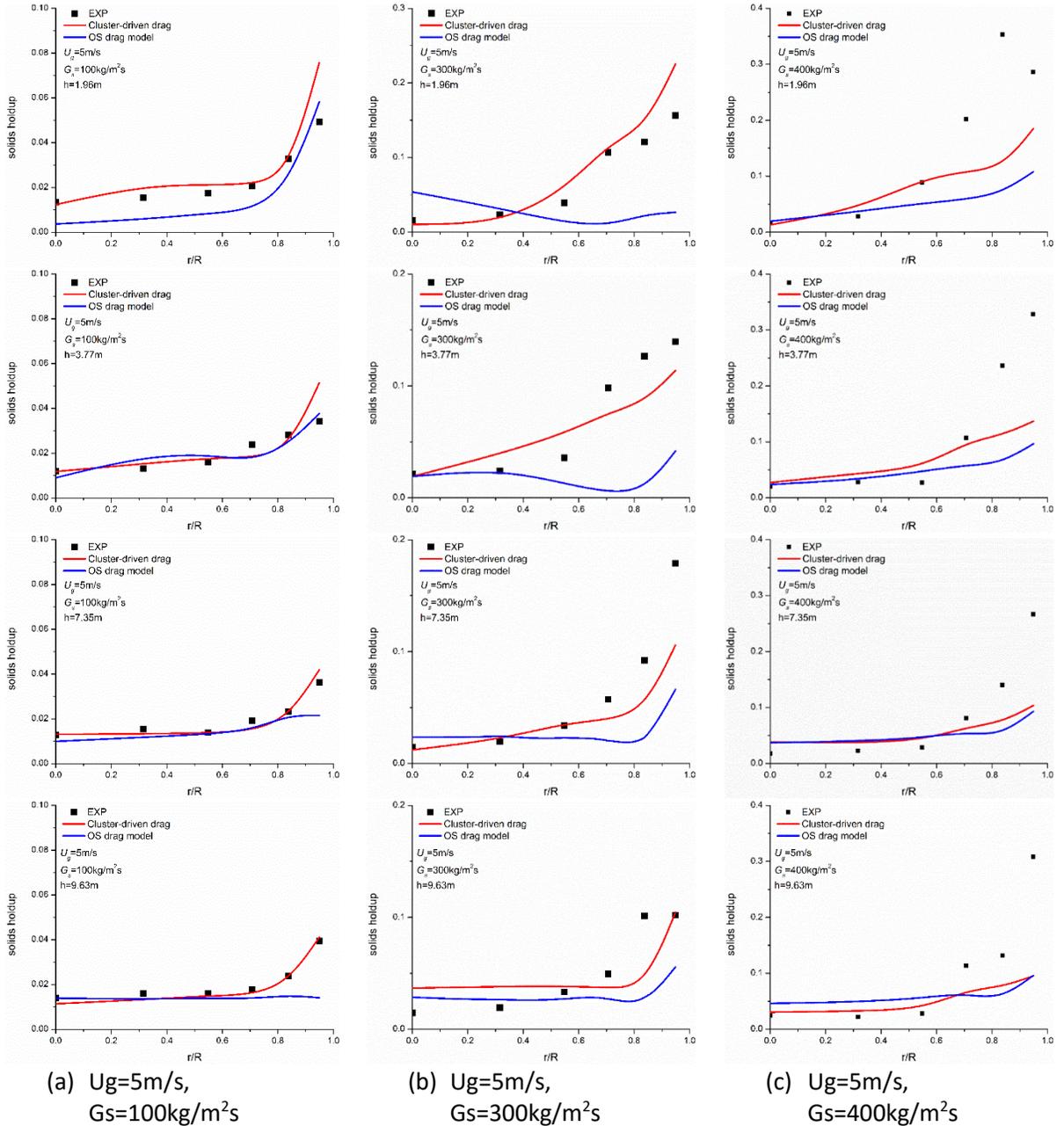
Figure 7-4: Solids holdup profiles in the radial direction at different heights of the CFB riser

Three cases of the gas-solids flows in the high-velocity CFB regime covering from dilute conditions to dense conditions under the same superficial gas velocity (U_g = 5 m/s, G_s = 100, 300, 400 kg/m^{2}s) are selected as shown in Figure 7-4. The numerical results of the radial solids holdup profiles at different heights along the CFB riser (h=1.96, 3.77, 7.35, and 9.63m from the gas distributor) using both the proposed cluster-driven drag model and the well-accepted Syamlal-O'brien drag model (1989) are plotted and compared with experimental data in Figure 7-4.

Generally, the gas-solids suspension is more dilute in the center of the riser and dense near the wall since the gas velocity is high in the center of the riser and low near the wall. Therefore, more severe clustering phenomena take place at the near wall region. In the axial direction, the dilute solids at the center of the riser with flat distribution in the radial direction expands along the riser due to the development of flow as shown in Figure 7-4. The dilute core region also shrinks with the increase in the solids circulation rate from r/R = 0-0.7 under a low-density condition as shown in Figure 7-4 (a) to r/R = 0-0.5 under high-density conditions as shown in Figure 7-4 (c). Both the cluster-driven model and Syamlal-O'brien drag model give a good agreement with the experimental data in the dilute center region of the riser, however, the Syamlal-O'brien drag model underestimates the solids holdup near the wall, especially in the upper zone of the riser (h > 6 m). Under a HDCFB condition ($G_s \geq$ 300 kg/m^{2}s), more solids tend to agglomerate together, which results in a less uniform gas-solids flow structure along the radial direction compared with the LDCFB. A thicker and much denser annulus layer is found in the riser where ε_s near the wall even reaches as high as 0.4 in some extremely dense cases although the solids holdups in the core region of the LDCFB and HDCFB are roughly the same as shown in Figure 7-4 (b) and (c).

7.3.1.2 Velocity profiles of gas and particles

(a) Solids holdup (b) Gas velocity, m/s (c) Particle velocity, m/s
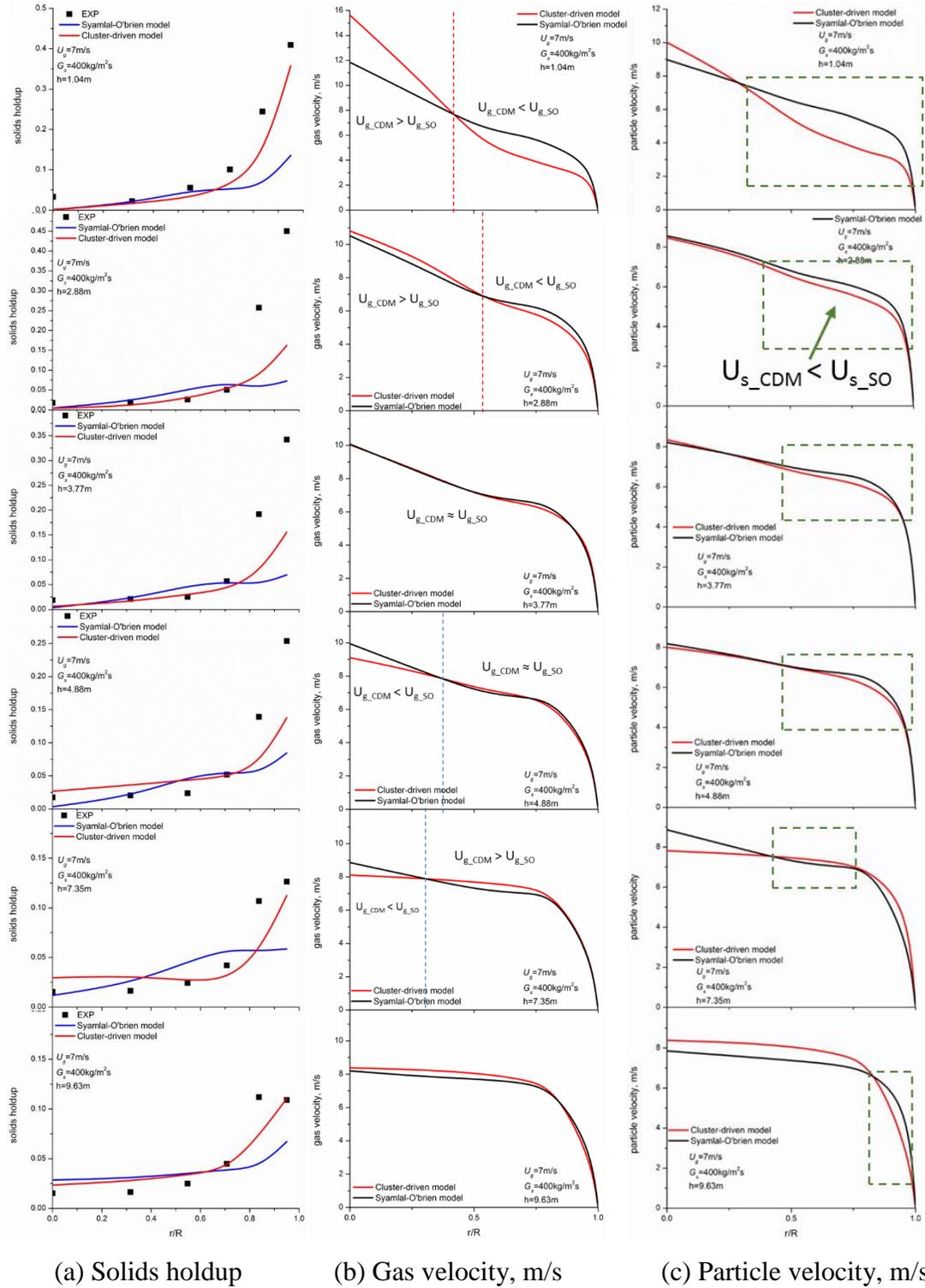
Figure 7-5: Velocity profiles of gas and particles in the radial direction at different heights of the CFB riser (U_g = 7 m/s, G_s = 400 kg/m²s)

More details on the flow structures can be revealed by the velocity profiles of both the gas and particles and the corresponding solids holdup profiles in the radial direction at different heights along the CFB riser, which are shown in Figure 7-5 under a high-density condition (U_g = 7 m/s, G_s = 400 kg/m²s). A typical downward power-law structure with higher velocity in the center of the riser and much lower velocity at the wall is found for both the gas and solids phases as shown in Figure 7-5 (b) and (c). Both the gas and particle velocity profiles become more uniform in the radial direction from the bottom to the top along the CFB riser. Also, the maximum velocity gradually reduces for both phases, and in the contrast, the boundary layer becomes thinner at the near wall region. Correspondingly, Figure 7-5 (a) shows more uniform solids holdup profiles in the upper dilute zone in the riser indicating that the flow structure becomes more uniform due to the less significant clustering effects.

Comparing with the gas velocity profile, the particle velocity profile is more uniform with a lower maximum velocity at the center of the riser. A larger slip velocity between the gas and solids can be found in the bottom zone of the riser (h < 5 m) as shown in Figure 7-5 (b) and (c), which means the gas-solid flow is under developing. The clustering effect could be more significant in the developing region due to the more intensive interactions between the gas and particles, so, the solids holdup is higher there as shown in Figure 7-5 (a). However, the gas and particle velocities becomes very close to each other with a nearly zero slip velocity in the upper zone of the riser, resulting in a fully developed region for the gas-solid flow with lower solids concentration. Due to the size of clusters, the rising velocities of clusters are lower compared with freely moving particles. Consequently, the local solids holdup will be higher due to a reduced particle velocity. Therefore, higher local solids holdup indicates more likely the formation of clusters, such as at the near wall region and the bottom region of the riser.

The major deviation between the numerical results and experimental data happens at the dense wall region of the riser where more clusters exist. The cluster-driven model predicts a narrower power-law profile of the gas velocity with a higher maximum velocity at the center of the riser and lower velocity at the near wall region than those from the Syamlal-O'Brien drag model in the entrance region of the riser (h = 1.04, 2.88 m). A better

agreement with the experimental data for the solids holdup at the near wall region is achieved using the cluster-driven model than that from the Syamlal-O'Brien drag model as shown in Figure 7-5 (a). The gas velocity profiles from the proposed cluster-driven model and Syamlal-O'Brien drag model are very close to each other in the upper part of the riser (h > 3.77 m), except for a lower maximum gas velocity in the center of the riser by the cluster-driven model. A distinct lower solids velocity is predicted by the cluster-driven model near the wall region along the entire riser, which results in a higher solids holdup there as shown in Figure 7-5 (a).

In summary, by including the average diameter of clusters and solid concentration of the clusters into the drag model, a better agreement with the experimental data was achieved for the solids holdup in the near wall region using the cluster-driven drag model, especially in a HDCFB. A slight underestimation in the wall region still happened because the actual size and density of the clusters in the annulus layer of the riser are usually higher than the average values, which are used in the cluster-driven model.

Table 7-3: Cluster properties under different operating conditions based on statistical data from experiments

U_g, m/s	G_s, kg/m²s	d_{cl}, m	V_{cl}, m³	ε_{cl}	d_p, m	V_{l_p}, m³	Number of particles
5	100	0.006	9.04779E-07	0.0520	0.000067	1.26E-12	37345
5	300	0.0052	5.88977E-07	0.1850	0.000067	1.26E-12	86488
5	400	0.0045	3.81704E-07	0.2450	0.000067	1.26E-12	74229
7	300	0.0051	5.55647E-07	0.1196	0.000067	1.26E-12	52749
7	400	0.0047	4.34893E-07	0.1550	0.000067	1.26E-12	53505

Table 7-3 lists the cluster properties under different operating conditions, such as the equivalent diameter (d_{cl}), the solid concentration (ε_{cl}), the volume of a cluster (V_{cl}), and the number of individual particles inside a cluster based on the data obtained from experiments.

With the increase in G_s under the same gas velocity, the size of cluster decreases slightly while its solid concentration (ε_{cl}) increases dramatically as shown in Table 7-3, which explains why the commonly used drag models such as Syamlal-O'Brien drag model do not perform well in the high-density case. The empirical correlations used in those drag models

are mainly based on the voidage function, which is related to the velocity ratio, not the cluster density. Although the Syamlal-O'Brien drag model used a voidage function in the near wall region the solid holdup under a much denser condition in a HDCFB is still underestimated. In the upper dilute zone of the riser, the non-uniformity of the radial solids distribution is under-predicted as well by the Syamlal-O'Brien drag model, which indicates that the use of the voidage function alone cannot correctly predict the drag force at the wall.

In the near wall region, the flow structures in the LDCFB and HDCFB differ a lot as shown in Figure 7-4. A much higher solids holdup and a wider wall layer are found in the HDCFB as shown in Figure 7-4 (b) and (c). From the point view of the clustering phenomenon, higher G_s results in smaller, but denser "core" clusters as shown in Table 7-3 and more "core" clusters tend to form in near the wall region, therefore, large "cluster of clusters" at the wall is formed.

7.3.2 Cluster distributions

7.3.2.1 Fidelity of the CFD models
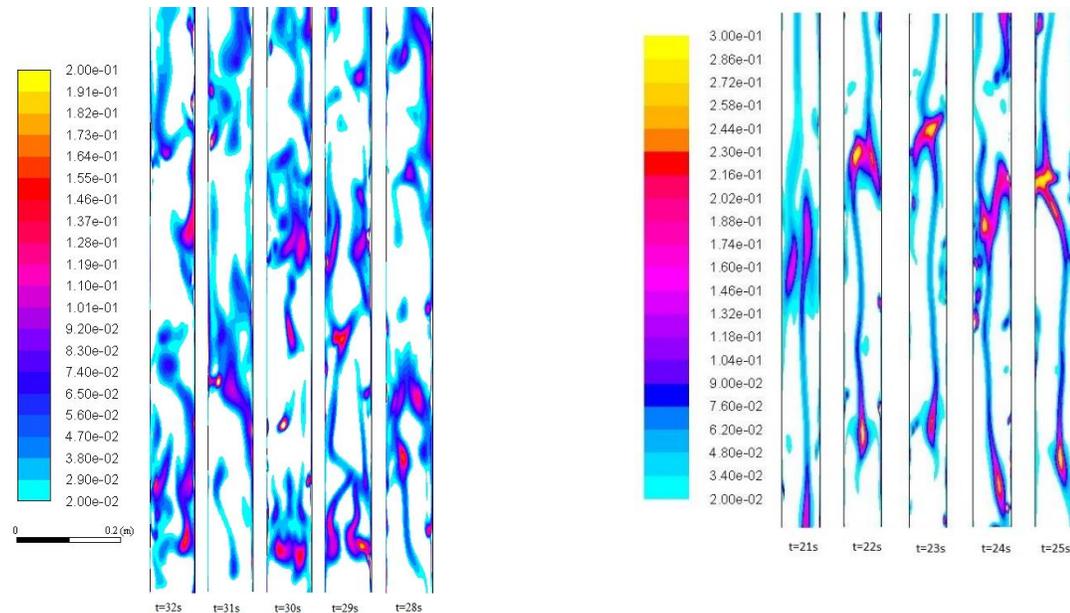
H=1-2m
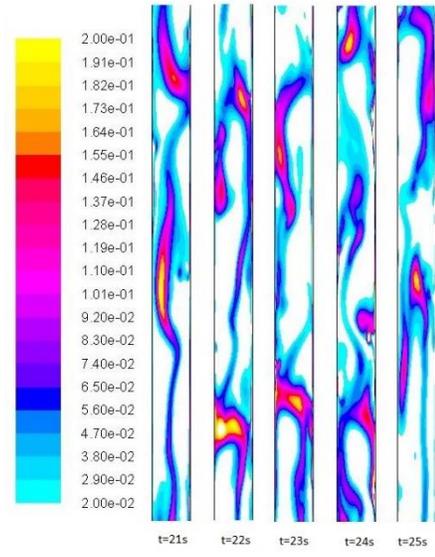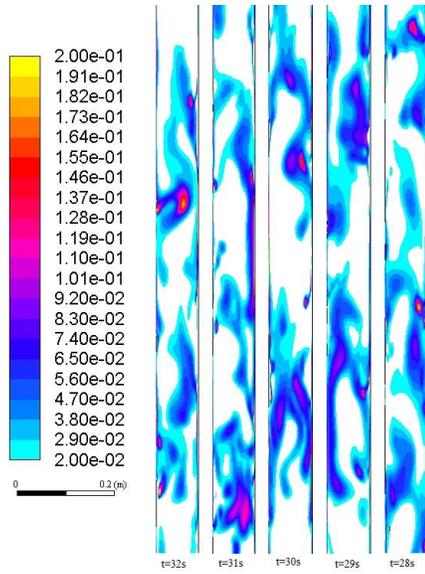
H=2-3m
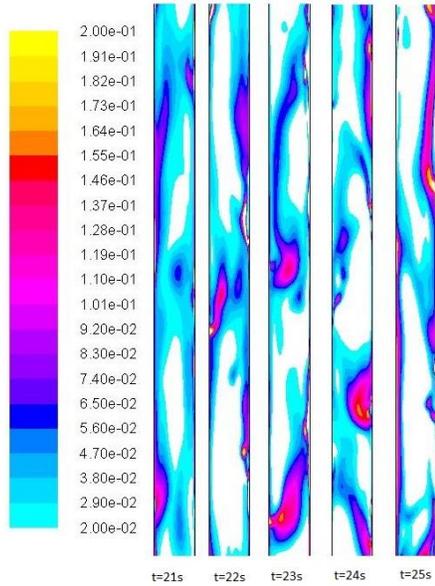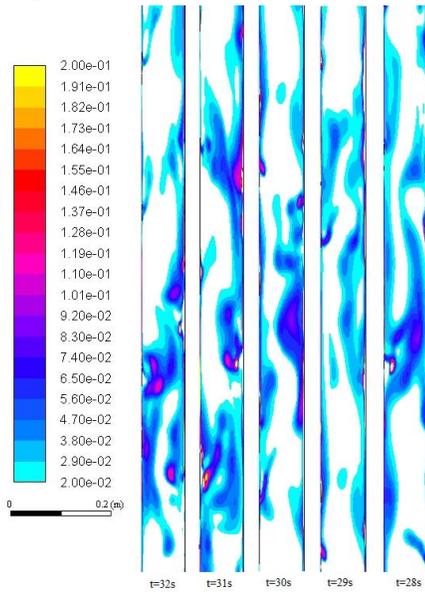
H=3-4m
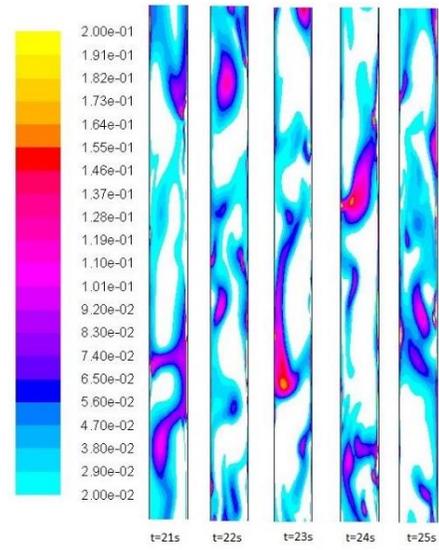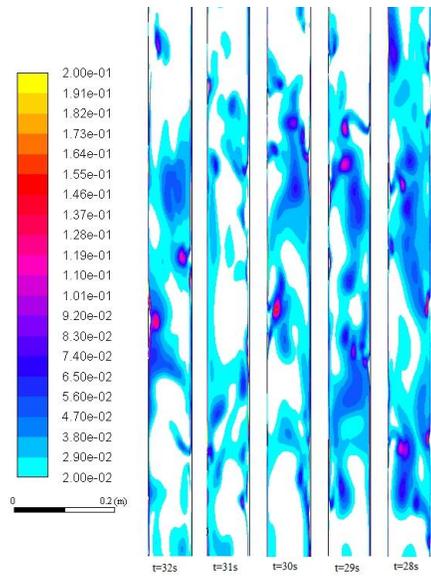
H=5-6m
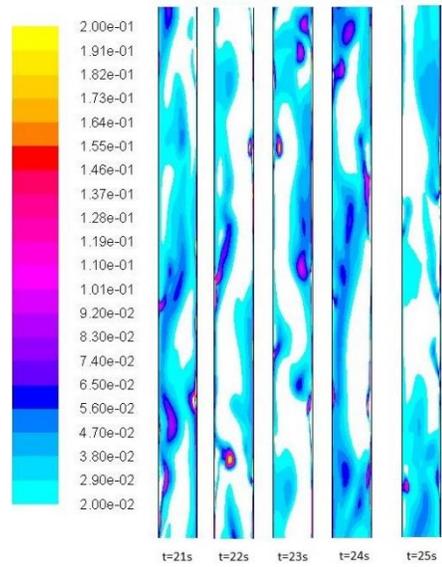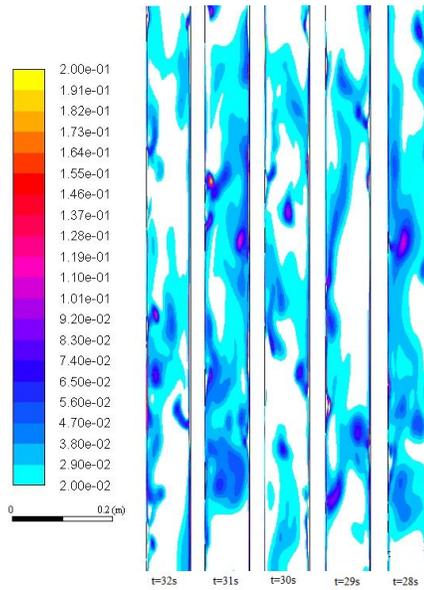
H=7-8m
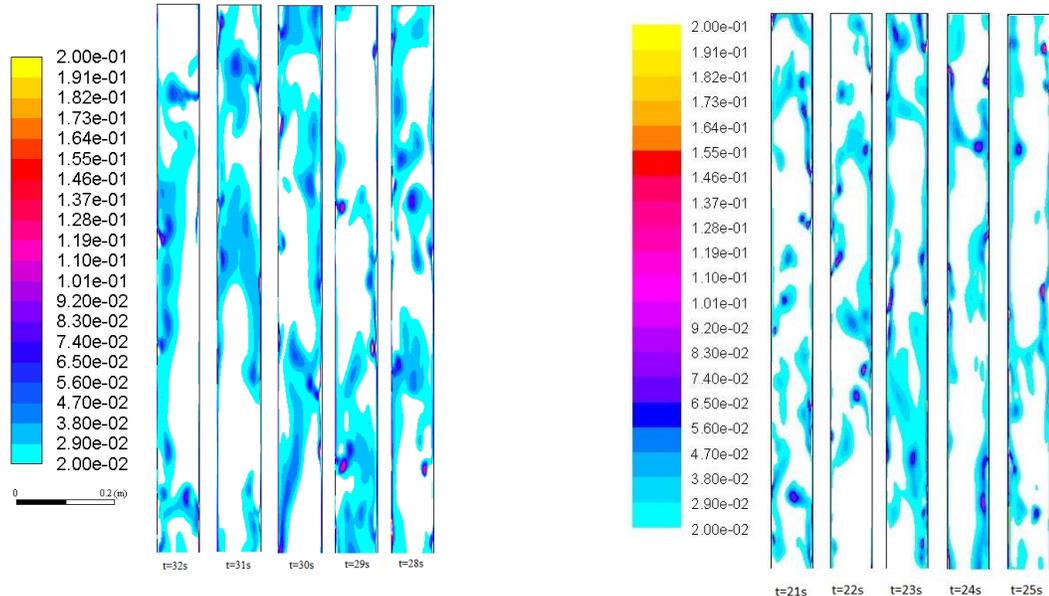
H=9-10m
(a): results from the cluster-driven model   (b): results from the Syamlal-O'Brien model

Figure 7-6: Instantaneous solids holdup contours of the riser (U_g = 5 m/s, G_s = 300 kg/m²s)

The contours of the solids holdup of a high-density flow case (U_g = 5 m/s, G_s = 300 kg/m²s) using the cluster-driven drag model is compared with the results from the Syamlal-O'Brien drag model as shown in Figure 7-6. The area with solids holdup less than 0.02 is cut off as the white regions as shown in Figure 7-6 to better display the denser regions, which indicate the locations of clusters. Clearly, both the cluster-driven drag model and Syamlal-O'Brien model predict various highly concentrated regions inside the CFB riser, indicating the existence of particle clusters as shown in Figure 7-6. However, the cluster behaviors are quite different from these two drag models as shown in Figure 7-6 although the solids holdup profiles are similar as shown in Figure 7-4. In the upper zone of the riser, similar contours of the solids holdup are obtained by both the cluster-driven model and Syamlal-O'Brien model as shown in Figure 7-6. The solids concentration of the denser regions reduces with smaller "core" clusters in the upper fully developed zone indicating the clustering effects are mitigated due to the flow development. However, in the lower part of the riser, elongated streamers and larger pieces of clusters are predicted by the Syamlal-O'Brien model as shown in Figure 7-6 (b). Comparing with the contours of the cluster-

180

driven model where more space in the riser is occupied by denser regions with smaller "core" clusters embedded, the numerical results from the Syamlal-O'Brien model show highly concentrated dense regions that occupy less space in the riser, which are different from that reported by experimental observations.

(a): Cluster-driven drag model
(b): Syamlal-O'Brien drag model
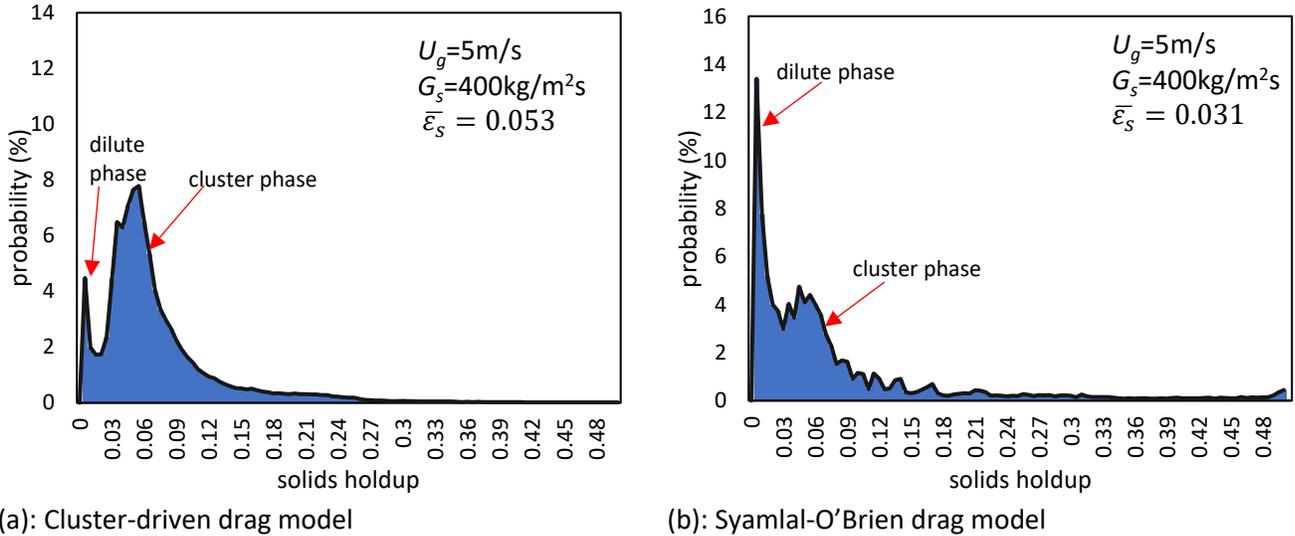
Figure 7-7: Comparison of the probability density distributions of the overall solids holdup in the CFB riser ($U_g = 5$ m/s, $G_s = 400$ kg/m^{2}s) by the cluster-driven drag model and the Syamlal-O'Brien drag model

The time averaged probability density distributions of the overall solids holdup from the cluster-driven model and Syamlal-O'Brien model are compared as shown in Figure 7-7. Generally, two peaks of the solids holdup density distribution can be found in the results from both the cluster-driven model and Syamlal-O'Brien model. The first peak is located at a lower solids holdup around 0.01, which represents the dilute solids suspension with freely moving single particles. The second peak of the probability density takes place at a higher solids holdup around 0.06, which can be considered as the cluster phase with a higher solid concentration corresponding to the denser regions as shown in Figure 7-6. A higher and wider peak for the cluster phase is obtained by the cluster-driven drag model as shown in Figure 7-7(a), indicating that more solids are captured inside the denser cluster phase. However, a thinner and lower peak of the solids holdup for the cluster phase and a much higher peak of the dilute phase are obtained by the Syamlal-O'Brien model as shown in Figure 7-7 (b). The numerical result from the Syamlal-O'Brien model indicates that the

181

volume fraction of the cluster phase is lower and there are more freely moving particles in the dilute phase. A higher overall solids holdup of 0.053 is predicted by the cluster-driven model, which agrees with the experimental data better since the clustering effects are enhanced in the drag model. Therefore, higher fidelity is believed to be achieved by the proposed cluster-driven drag model based on the contours of instantaneous solids holdup where the clustering phenomenon is close as the experimental descriptions (Xu & Zhu 2012, Yang & Zhu 2014).

7.3.2.2 Instantaneous cluster behavior

More detailed information on the gas-solids flow structure and cluster behavior can be obtained from numerical results by the cluster-driven model as shown in Figure 7-6 (a). The regions with higher solids concentration, which consist of one or several extremely dense cores with a solids holdup over 0.10 and a surrounding cloud of relatively denser solids suspension as shown in Figure 7-6 (a), can be considered as clusters since they match the typical descriptions of clusters from the experimental observation (Yang & Zhu 2014).

The distribution and concentration of clusters also differ a lot in the axial direction as shown in Figure 7-6 (a). In the bottom zone of the riser, smaller, but more concentrated clusters that are more like elongated streamers appear frequently and an extremely denser core ($\varepsilon_s > 0.1$) of particles is detected as shown in Figure 7-6 (a) (H<3 m). However, the dilute region ($\varepsilon_s < 0.02$) shown as the white area on the contour occupies more space than the denser clustering phase inside the riser at the lower region of the riser. Meanwhile, since a denser bottom region of the riser has already been reported in the literature (Wang, Li, and Zhu 2015), it is believed that more particles are captured inside clusters, i.e. the solids concentration inside clusters is high, although the dilute phase with freely moving individual particles is volumetrically dominant. In the upper zone of the riser, clusters become larger and slightly more dilute inside and the above-mentioned denser core of particles in the center of the clusters does not appear as frequently as the ones in the bottom zone. Unlike the streamer shape clusters in the bottom of the riser, the clusters in the upper zone appear as large pieces with irregular shapes as shown in Figure 7-6 (a) (H>4m). Correspondingly, the volume fraction of cluster phase increases and the solids

concentration inside the cluster drops. Particles inside the clusters in the upper zone are loosely packed and the solids concentration gradients are smoother from the center to the boundary of the clusters compared with the ones in the bottom zone. Large pieces of clusters tend to link together and have blurred boundaries since the concentration of particles at the boundary of the cluster are close to the solids holdup in the surrounding dilute phase. The clusters appear randomly in the riser from the center to the wall and are continuously connected to form large clusters along the riser as shown in Figure 7-6 (a). Also, the shape, size, and the solids concentration of the denser regions changes greatly in the axial direction as shown in Figure 7-6 (a), indicating the dynamic nature of the clusters and the vigorous interactions between the gas and particles in the high-velocity CFB riser.
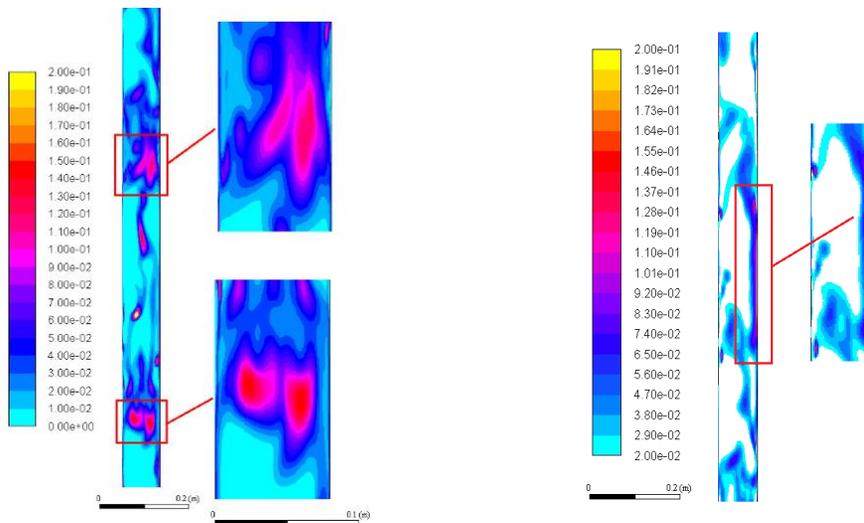
Figure 7-8: Example of typical clusters at the bottom zone of the riser (h=1-3 m)
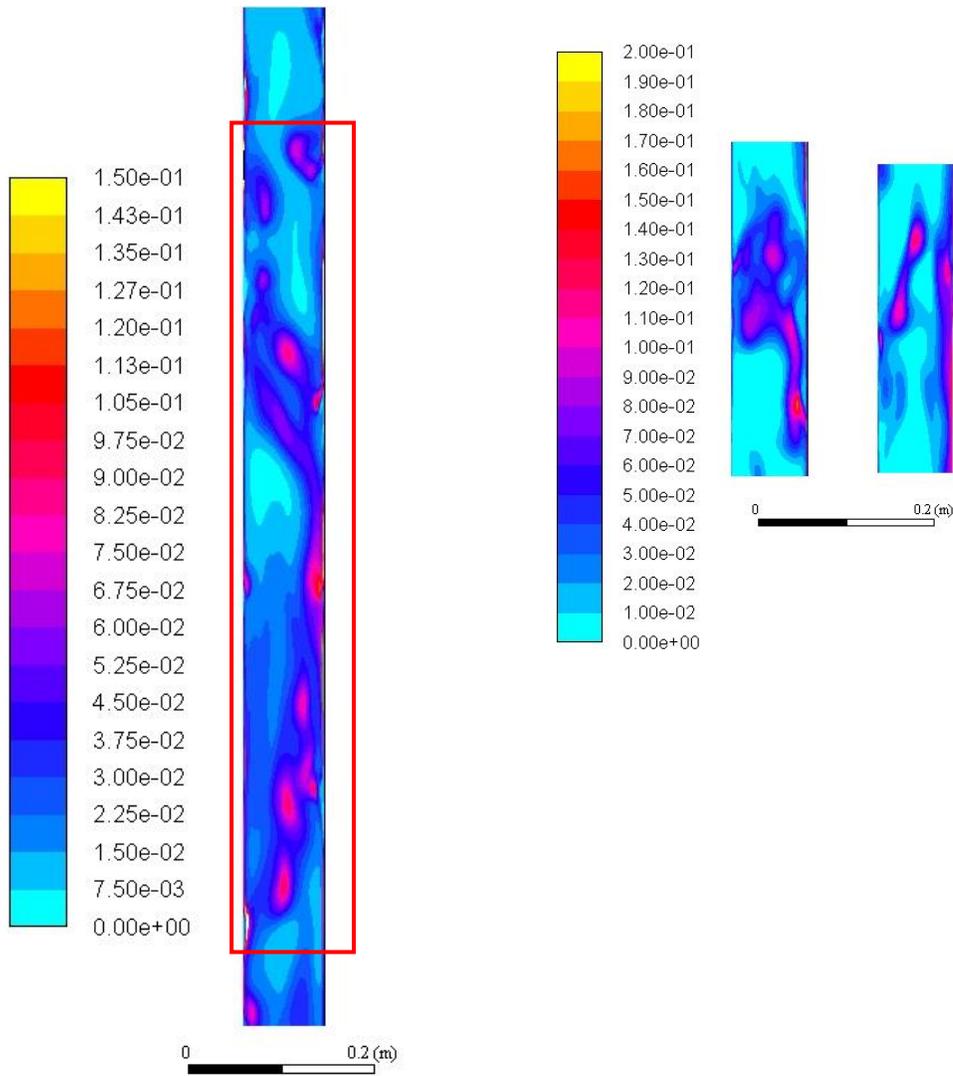
Figure 7-9: Examples of typical clusters in the middle of the riser (h>5m)

Figure 7-8 and Figure 7-9 show some typical structures of clusters in the CFB riser and provide more details in the shape, size, and other dynamic behavior of clusters under a high-density condition. In the lower part of the riser, a long and narrow streamer type of cluster is more likely to appear at the wall of the riser as shown in Figure 7-8. Clearly, the elongated streamer is highly concentrated with a higher solids holdup than the surrounding suspension which can be considered as a typical type of particle clusters inside CFB risers as reported in the literature (Sharma et al. 2000). Typical U-shaped clusters with a clear boundary from the surrounding dilute solids suspension occur at the bottom of the riser as shown in Figure 7-8. The U-shaped cluster is also highly concentrated and more packed

with a solids holdup as high as 0.15 at the core. The upward gas flow tends to bypass the U-shaped cluster due to the large flow resistance inside the cluster, which means the captured particles inside the cluster have less opportunities to contact with the bypassing fresh gas. In the higher part of the riser, oval-shaped clusters are found where the gas-solids flow is more developed and solids suspension becomes dilute as shown in Figure 7-8. The oval-shaped cluster is also highly concentrated like the U-shaped cluster, but the high-velocity gas flow elongates the cluster to a more oval and stretched-out shape. Both the U-shaped and oval-shaped clusters are mostly formed in the center of the riser and usually have a large size close to the radius of the riser, which agrees with the statistical equilibrium diameter of clusters (d_{cl}=0.0052m, U_g=5m/s, G_s=300kg/m^{2}s) from the image analysis based on the experimental data under the same operating condition as shown in Table 7-3.

Series of much smaller "core clusters" are more commonly seen in the upper zone of the riser as shown in Figure 7-9. Small "core" clusters are more spherical and also highly concentrated with a size around a quarter of the riser diameter. The small "core" clusters appear more frequently and tend to link together to form a long and denser streamer of solids as shown in Figure 7-9. Unlike the streamers seen in the lower part of the riser in which the particles are more homogeneously distributed, streamers in the upper part usually consist of several cores with much higher solids concentration, which agrees with the description of the large and unstable "cluster of clusters" mentioned by Royer et al. (2009). The volume fraction of the cluster phase increases in the upper zone of the riser due to the streamers and large pieces of particle clouds as shown in Figure 7-6, which indicates that there is less space for the bypassing gas and the dilute phase. However, the high-velocity field in the upper part of the riser results in an irregular and blurred boundary of the streamers and causes a large gradient for the concentration of the streamer from the "core" clusters to the surrounding dense layer of particles. Therefore, although the "core" clusters embedding in the streamers are stable and highly concentrated, the concentration of the surrounding dense layer is much lower and the shape and size of the streamers also change greatly while moving up in the riser. Consequently, the interactions between the gas and particles in the denser layer are actually more vigorous since the gas flow is more likely to penetrate into the cluster.

The dynamic behavior and characteristics of clusters in the riser can be further explained by combining the local profiles of solids holdup, and the gas and particle velocities from Figure 7-4 and Figure 7-5. The formation of a cluster usually relates with the local velocity field. An increase in the slip velocity between the surrounding fluid and the cluster is expected since a cluster rises slower than the freely moving individual particles due to its higher density. The more power-law and narrower velocity profiles of both the gas and solids phases in the lower part of the riser as shown in Figure 7-5 indicates that the gas-solids flow is developing in the entrance region of the riser resulting in a much denser wall region where long streamers of clusters occur as shown in Figure 7-8.

In the lower part of the riser, larger clusters such as U-shaped and oval-shaped clusters tend to generate in the center of the riser where a larger slip velocity is found as shown in Fig. 8 since the particles are still in the acceleration stage by the gas flow. On the other hand, the large clusters with lower rising velocity also contribute a higher local solid holdup as shown in Figure 7-5. Comparing with the smaller clusters linking together inside a long streamer in the upper part of the riser, the U-shaped or oval-shaped clusters are more dispersed because the dilute phase consisting of gas and freely moving particles is dominant in this region. In the upper zone of the CFB riser, the gas-solids flow is fully developed with a more uniform velocity distribution, smaller and more uniform slip velocity allows smaller clusters to form either in the center or at the wall region of the riser. On the other hand, small clusters rise faster than the large U-shaped and oval-shaped clusters and have more irregular trajectories while moving up so that having more opportunities to collides with each other or interact with the surrounding dilute suspension.

It is difficult to tell whether the dilute phase with freely moving particles or the cluster phase dominates the gas-solids flow in the upper part of the riser due to the lower and uniform slip velocity distribution and more dilute local solids distribution for the fully developed flow. For the behavior of clusters in the upper part of the riser, large pieces of denser regions of solids suspensions occupy much space of the riser, however, the gradients of solids holdup between the dense and dilute regions is not as obvious as the one in the lower part. Therefore, more gas can penetrate the relatively dilute region of the loosely packed large pieces of clusters except for the highly concentrated "core" clusters packed

in the streamers. Under such a circumstance, the clustering phenomenon is welcomed in chemical processes because a higher conversion can be achieved with the help of more contacting between gas and solids in the relatively dilute region of clusters, which actually has a higher solids concentration than the dilute phase, especially under a high-density operating condition for CFB riser.

7.3.3 Clustering phenomenon difference between HDCFB and LDCFB
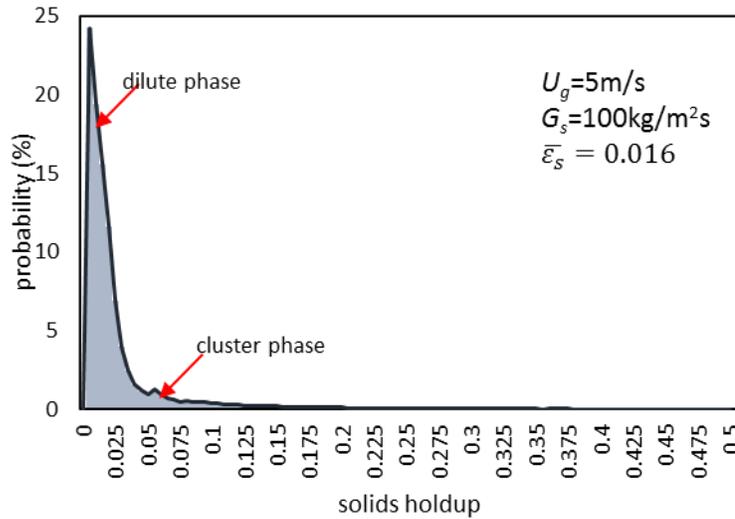
(a) U_g=5 m/s and G_s=100 kg/m^{2}s
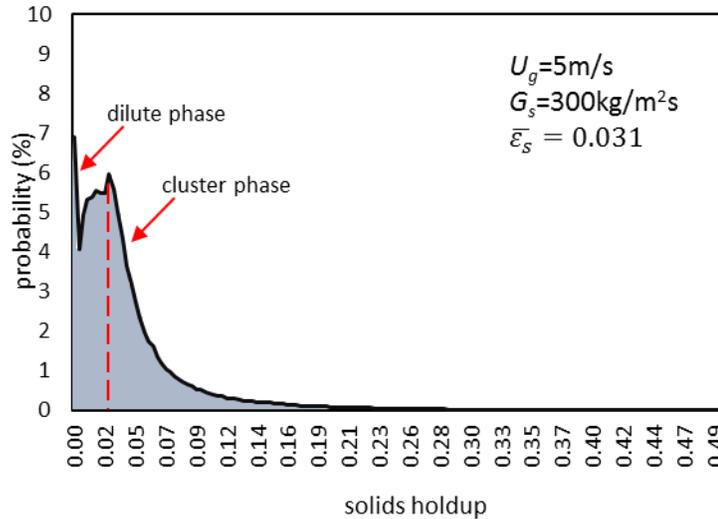
(b) U_g=5 m/s and G_s=300 kg/m^{2}s

(c) U_g=7 m/s and G_s=400 kg/m²s
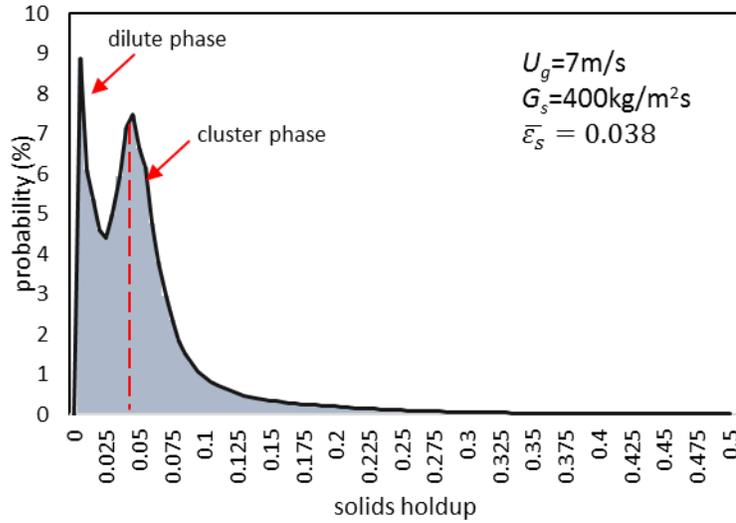
Figure 7-10: Probability distribution function (PDF) of the solids holdup in LDCFBs and HDCFBs

The clustering phenomena in CFB riser are also different between low-density conditions and high-density conditions as the probability distributions function (PDF) of solids holdup shown in Figure 7-10.

In a LDCFB, the phase separation between the dilute phase and cluster phase is not as obvious as the one in a HDCFB. The PDF curve of the solids holdup for a LDCFB is more unimodal with a narrow and concentrated peak representing freely moving single particles located at a lower solids holdup around 0.01 as shown in Figure 7-10 (a). The reason might be that the average solids concentration of clusters in the LDCFB is only a bit higher than the surrounding dilute suspensions due to the low solids circulation rate. The boundary of the dense layers surrounding with the "core" clusters is unclear from the dilute phase. As a result, only a very small peak around ε_s=0.05 is found in Figure 7-10 (a) which might represents the "core" clusters in the LDCFB. The unimodal PDF curve also indicates a more uniform gas-solids flow structure in the LDCFB since less clustering effect is found.

In the HDCFB, phase separation is clear and than the LDCFB two peaks of the solids holdup are found as shown in Figure 7-10 (b) and (c). A thinner peak with lower solids holdup around ε_s=0.01 represents the dilute phase for freely moving single particles in the

188

HDCFB. A wider peak with a higher solids holdup indicates the existence of the cluster phase in a HDCFB. More space is covered by the wider peak of the PDF curve with higher solids holdup suggesting that more solid particles are captured in clusters. The solid holdup of the peak for the cluster phase can be considered as the solid concentration of the "core" clusters. The area under the cluster phase peak can also be recognized as the volume fraction of the solids in clusters corresponding to the denser regions as shown in the solids holdup contours (Figure 7-6 (a)). When the CFB becomes denser with a higher bed density, the peak for cluster phase of the PDF curve swifts to the right for a higher solids holdup compared with Figure 7-10 (b) and (c), which indicates that the solid concentration of the "core" clusters increases with the increase in the bed density. In the meanwhile, the clustering effects are more severe under higher density conditions as the volume fraction of the cluster phase also increases with the increase of the bed density.

7.4 Conclusion

A cluster-driven drag model is applied into the Eulerian-Eulerian two-fluid model to numerically study the gas-solids circulating fluidized bed riser. The drag force in a gas-solids CFB riser can be obtained by the summation of the drag force from freely moving single particles and the drag from clusters. Statistical data of the particle clusters such as cluster diameter, average solid concentration of clusters, and the portion of solids in clusters are from the image processing of the experimental data and are employed into the drag model of clusters. CFD results show that the clustering effects are more severe near the wall region where the slip velocity is larger and the solids holdup is higher. Instantaneous contours of solids holdup in the CFB riser from CFD simulations show that typical types of clusters are strands, U-shaped, and spherical clusters are found in the CFB riser. Larger and more clusters tend to appear at the bottom developing region of the CFB riser. Elongated denser streamers consisting of several small "core" clusters are more likely to occur in the upper fully developed zone of the CFB riser. More severe clustering phenomenon is found under high-density conditions of the CFB riser compared with low-density CFB risers. A clear phase separation between the dilute single particles and denser clusters is found based on the probability distribution function of the solids holdup in the CFB riser.

Nomenclature

$A_p = \dfrac{\pi \cdot d_p^2}{4}$ Reference area of a particle projecting to the fluid, m^2

C_{D_cl} Drag coefficient of clusters in the gas-solid system

C_{D_p} Drag coefficient of single particles in the gas-solid system

C_d Drag coefficient for a single particle in a fluid

C_d' Drag coefficient in the homogeneous dilute gas-solids system

F_D Total drag force per unit volume in the homogeneous gas-solids suspension

P_{cl} Percentage of the total solids captured in the cluster phase

Re_{cl} Reynolds number of clusters

Re_p Reynolds number of single particles

U_{slip} Slip velocity between fluid and particle, m/s

U_{slip_cl} Slip velocity between clusters and surrounding fluid, m/s

$V_{g,in}$ Inlet gas velocity, m/s

$V_{s,in}$ Inlet velocity of the solid phase, m/s

d_{cl} Equivalent cluster diameter, m

d_{en_cl} Solid concentration in the cluster

d_p Particle diameter, m

$n_p = \dfrac{6(1 - \varepsilon_g)}{\pi \cdot d_p^3}$ Number of the particles per unit volume

α_g Gas phase volume fraction

α_s Solid phase volume fraction

$\beta_{cluster}$ Momentum transfer coefficient between clusters and the bypassing gas

β_{gs} Total momentum transfer coefficient between gas and solids

β_p Momentum transfer coefficient between freely moving individual particles and pure gas

ε_{cl} Portion of the captured particles inside the clusters in the gas-solids system

ε_g Gas holdup

ε_{g_cl}	Portion of the captured gas inside the clusters
ε'_s	Solids holdup in a homogeneously dispersed gas-solids system
ρ_g	Gas density, kg/m^3
ρ_s	Particle density, kg/m^3
ρ_{sus}	Mixture density of the gas-solid suspension, kg/m^3
φ_{cl}	Volume fraction of cluster phase
φ_g	Volume fraction of pure gas phase bypassing the individual particles or clusters
φ_p	Volume fraction of single particle phase
g	Gravity acceleration, m/s^2
G_s	Solids circulation rate, kg/m^{2}s
h	Height from the gas distributor, m
h/H	Relative axial position
r/R	Relative radial position
U_g	Superficial gas velocity, m/s
V_{cl}	Volume of a cluster, m^3
V_{l_p}	Volume of a particle, m^3
ε	Gas voidage
ε_s	Solids holdup in the CFB riser
ϕ	Ratio of the opening area in the gas distributor

References

ANSYS, Inc. 2013. ANSYS Fluent Theory Guide.

Cocco, Shaffer, Hays, Karri & Knowlton (2010). Particle clusters in and above fluidized beds. Powder Technology, 203(1), 3-11.

Grace (1986). Contacting modes and behaviour classification of gas-solid and other two-phase suspensions. The Canadian Journal of Chemical Engineering 64(3): 353-63.

Grace (1990). High-velocity fluidized bed reactors. Chemical Engineering Science 45(8): 1953–66.

Grace, Bi & Golriz. (2003). Circulating fluidized beds. in Handbook of Fluidization and Fluid-Particle Systems, ed. Marcel Dekker Wen-Ching Yang. New York: CRC press, 485-498.

Hori & Clift. (1992). A note on terminology: 'Clusters' and 'Agglomerates.' Powder Technology 70(3): 196.

Lackermeier, Rudnick, Werther, Bredebusch & Burkhardt (2001). Visualization of flow structures inside a circulating fluidized bed by means of laser sheet and image processing. Powder Technology, 114(1-3), 71-83.

Li (2010). Investigation of circulating fluidized bed riser and downer reactor performance for catalytic ozone decomposition. Ph.D thesis, University of Western Ontario.

Mondal, Nandan, Kallio, Saxén & Hassel. (2016). Experimental study of cluster properties in a two-dimensional fluidized bed of geldart b particles. Powder Technology 291: 420–36.

Royer, Evans, Oyarte, Guo, Kapit, Möbius & Jaeger. (2009). High-speed tracking of rupture and clustering in freely falling granular streams. Nature, 459(7250), 1110.

Sharma, Arun, Tuzla, Matsen & Chen. (2000). Parametric effects of particle size and gas velocity on cluster characteristics in fast fluidized beds Powder Technology 111(1–2): 114–22.

Sinclair & Jackson. (1989). Gas-particle flow in a vertical pipe with particle-particle interactions. AIChE Journal 35(9): 1473–86.

Syamlal & O'Brien. (1989) Computer simulation of bubbles in a fluidized bed. AIChE Symposium Series. 85 (1989) 22-31.

Tsuji, Tanaka & Yonemura. (1998). Cluster patterns in circulating fluidized beds predicted by numerical simulation (discrete particle model versus two-fluid model). Powder Technology 95(3): 254–64.

Tsuo, Yuan & Gidaspow. (1990). Computation of flow patterns in circulating fluidized beds. AIChE Journal 36(6): 885–96.

Wang (2013). High-density gas-solids circulating fluidized bed riser and downer reactors. Ph.D thesis, University of Western Ontario.

Wang, Li & Zhu. (2015). Axial solids flow structure in a high density gas–solids circulating fluidized bed downer. Powder Technology 272: 153-64.

Wen & Yu. (1966). A generalized method for predicting the minimum fluidization velocity. AIChE Journal 12(3): 610–12.

Xu & Zhu. 2012. A new method for the determination of cluster velocity and size in a circulating fluidized bed. Industrial & Engineering Chemistry Research 51(4): 2143–51.

Yang & Zhu. (2014). A novel method based on image processing to visualize clusters in a rectangular circulating fluidized bed riser. Powder Technology 254: 407-15.

Yang & Zhu. (2015). Cluster identification using image processing. Particuology 23: 16–24.

Yerushalmi & Cankurt. (1979). Further studies of the regimes of fluidization. Powder Technology 24(2): 187–205.

Yerushalmi, Turner & Squires. (1976). The fast fluidized bed. Industrial and Engineering Chemistry Process Design and Development 15(1): 47–53.

Chapter 8

8 Numerical study on liquid-solid flow characteristics in inverse circulating fluidized beds

8.1 Introduction

Inverse liquid-solid fluidization is an operation in which solid particles with density lower than that of the liquid are suspended downwards by the continuous downward liquid flow in the opposite direction of buoyancy (Renganathan & Krishnaiah, 2004; Jaberi, 2014). Inverse fluidized beds can be used in biochemical processes, catalytic hydrogenation, adsorption, biological wastewater treatment industry, etc. It is characterized by advantages such as higher mass transfer rates, less solids attrition, efficient control and easy refluidization (Fan, 1989).

Previous studies on liquid-solid two-phase inverse fluidized beds focused on the hydrodynamic characteristics such as minimum fluidization velocity, pressure drop and bed expansion. Fan et al. (1982) studied the bed expansion in a liquid-solid two-phase inverse fluidized bed experimentally and found that the bed expansion increases with the increasing fluidization velocity and particle density and decreases with the increasing particle size. Renganathan and Krishnaiah (2005) studied the voidage fluctuations, axial voidage profile and bed expansion by measuring the local void fraction in a liquid-solid inverse fluidized bed, as the quality of fluidization is also elucidated by the local voidage fluctuations. However, most previous studies were carried out in conventional inverse fluidized bed reactors and the heights of the test reactors were lower than 3 meters, which cannot reflect the actual industrial situations.

In the inverse liquid-solid circulating fluidized bed, particles can circulate in the bed. The inverse liquid-solid circulating fluidized bed also has the advantage of controlling a large quantity of particles easily. Sang (2013), Jaberi (2014) and Nan (2019) studied the axial particle distribution, radial structure and solids circulation rate in a downer of a liquid-solid inverse circulating fluidized bed whose height was 5.4 meters under different particle densities and different velocities of liquid and particles.

With the development of mathematical modeling, computational fluid dynamics (CFD) has become an important tool to study the hydrodynamics in fluidized beds (Hartge, et al., 2009; Wang, et al., 2010). Wang et al. (2014; 2018) simulated flow behavior of particles in conventional inverse liquid-solid fluidized beds by means of two-fluid model and found that axial velocities of particles and the bed expansion height increase with the increasing liquid velocity. The granular temperatures increase, reach the maximum and then decrease with the increasing solids volume fraction. Some hydrodynamic characteristics of the inverse fluidized beds, such as pressure drop, solids holdup, and minimum fluidization velocity, have been investigated in previous studies either experimentally and numerically and some empirical correlations have been developed. However, studies related to the hydrodynamic characteristics of the inverse circulating fluidized beds of large size using CFD have not been reported in the literature. Such information is required to design, scale up and operate the inverse liquid-solid continuous systems.

In this study, hydrodynamic characteristics of the large size inverse circulating fluidized beds are investigated numerically using a single type of particles and mixed types of particles. Two-dimensional Eulerian-Eulerian approach incorporating the kinetic theory of granular flow is selected and the CFD software Ansys/Fluent is the numerical platform used in this study. Through CFD simulations, some detailed information on the local holdups and velocities of each phase, which is either impossible or difficult to be measured experimentally, can be captured (Xu, et al., 2017). Such information is of great importance in understanding the hydrodynamics in inverse liquid-solid circulating fluidized beds (Roy, et al., 2014). The simulation results are compared with the experimental data obtained by Jaberi (2014) and Nan (2019).

8.2 Configuration and operating conditions

The configuration of the liquid-solid inverse circulating fluidized bed used by Jaberi (2014) and Nan (2019) in their experiments is used in this work in order to compare the numerical results with the experimental data from Jaberi (2014) and Nan (2019).

Figure 8-1 shows the schematic diagram of the inverse liquid-solid circulating fluidized bed (Jaberi, 2014; Nan, 2019). Along the circulation loop, the liquid-solid inverse

circulating fluidized bed consists of a downer with an inner diameter of 76mm and a height of 5400mm, a liquid-solid separator, a water tank and an upcomer with an inner diameter of 200mm and two connecting pipes. When the liquid velocity in the downer is higher than the transport fluidization velocity, particles from the solids control will flow downwards carried by the downward liquid flow and then be separated from the liquid by the liquid-solid separator at the bottom of the downer. The liquid flows to the water tank and then returns to the inlet of the downer through a pump. The upcomer and connecting pipes are filled with the liquid. The particles move from the separator to the upcomer through the lower connecting pipe. Then the particles move up in the upcomer because of their buoyancy and are stored in the upcomer. The solids flowrate at the top of the downer can be adjusted by the solids control. The temperature of the liquid was monitored during the experiments to make sure that all the experiments were performed under the same condition.
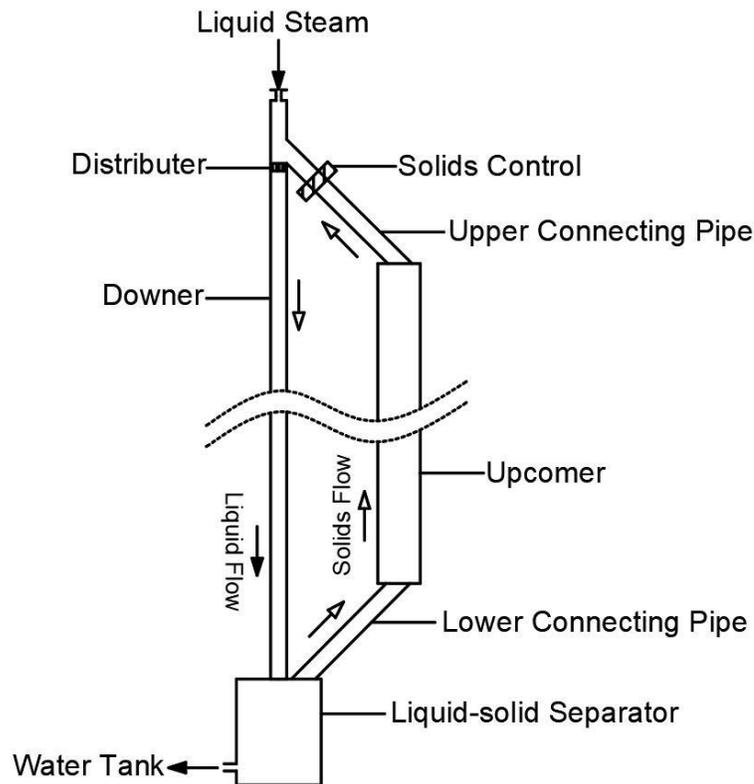
Figure 8-1 Schematic diagram of the liquid-solid inverse circulating fluidized bed

In the study carried out by Jaberi (2014), the solids particles were spherical Styrofoam with a mean diameter of 0.8mm and a density of 28kg/m^3. In the study carried out by Nan (2019), the solids particles are spherical Styrofoam with a mean diameter of 1.1mm and a density of 640kg/m^3. The liquid phase was tap water. Three different operating conditions used by Nan (2019) and four different operating conditions used by Jaberi (2014) are selected to conduct the numerical simulations.

8.3 CFD model

Generally, there are two major approaches to simulate liquid-solid two-phase flows, the Eulerian-Lagrangian approach and the Eulerian-Eulerian approach (Pan, et al., 2016). The Eulerian-Lagrangian approach tracks the motions of individual particles using a Largrangian force balance equation, and the liquid flow is treated as a continuum by two-fluid CFD model (Liu, et al., 2016). The Eulerian-Eulerian approach treats both liquid and solids phases as interpenetrating continua, the motion of each phase is solved using a continuum based CFD approach with suitable closure terms (Feng, et al., 2012). The Eulerian-Lagrangian approach can predict the detailed behavior of the particles but requiring much more computing power. The Eulerian-Eulerian approach costs less computational time, but its accuracy depends on the closure model used to describe properties such as solids viscosity and solids pressure (Zhang, et al., 2012). The former approach is suitable for fundamental research while the latter is for process design (Montastruc, et al., 2009). In this work, the Eulerian-Eulerian approach is employed since the simulated domain is large.

8.3.1 Governing equations

The Eulerian-Eulerian two-fluid model has been adopted for the solids and liquid phases. The kinetic theory of granular flow has been used for closure. The governing equations are given below.

The continuity equation for phase i (i=s for solids phase or i=l for liquid phase) is:

$$\frac{\partial}{\partial t}(\varepsilon_i \rho_i) + \nabla \cdot (\varepsilon_i \rho_i \vec{u}_i) = 0 \qquad (8\text{-}1)$$

where ε_i is the volume fraction, $\vec{u}$ is the velocity vector and ρ is the density.

The momentum equation for the liquid phase is:

$$\frac{\partial}{\partial t}(\varepsilon_l \rho_l \vec{u}_l) + \nabla \cdot (\varepsilon_l \rho_l \vec{u}_l \vec{u}_l) = -\varepsilon_l \nabla p + \nabla(\varepsilon_l \cdot \overline{\overline{\tau_l}}) + \varepsilon_l \rho_l \vec{g} + \beta(\vec{u}_s - \vec{u}_l) \quad (8\text{-}2)$$

where p is the fluid pressure, $\vec{g}$ is the gravity acceleration, β is the interphase momentum transfer coefficient, and $\overline{\overline{\tau_l}}$ is the stress tensor of liquid phase, given by

$$\overline{\overline{\tau_l}} = \mu_f[\nabla \cdot \vec{u}_l + (\nabla \cdot \vec{u}_l)^T] - \frac{2}{3}\mu_f(\nabla \cdot \vec{u}_l)\overline{I} \quad (8\text{-}3)$$

The momentum equation for the solids phase is:

$$\frac{\partial}{\partial t}(\varepsilon_s \rho_s \vec{u}_s) + \nabla \cdot (\varepsilon_s \rho_s \vec{u}_s \vec{u}_s) = -\varepsilon_s \nabla p - \nabla p_s + \nabla(\varepsilon_s \cdot \overline{\overline{\tau_s}}) + \varepsilon_s \rho_s \vec{g} + f_m +$$
$$\beta(\vec{u}_l - \vec{u}_s) \quad (8\text{-}4)$$

where p_s is the particle pressure which represents the particle normal forces due to particle-particle interactions, and $\overline{\overline{\tau_s}}$ is the solids stress tensor given by

$$\overline{\overline{\tau_s}} = \mu_s \left\{[\nabla \cdot \vec{u}_s + (\nabla \cdot \vec{u}_s)^T] - \frac{2}{3}(\nabla \cdot \vec{u}_s)\overline{I}\right\} + \xi_s \nabla \cdot \vec{u}_s \overline{I} \quad (8\text{-}5)$$

The turbulent kinetic energy (k) and dissipation rate (ε) of liquid phase and solids phase are calculated by a per phase standard k-ε turbulence model (Ansys Inc., 2011).

The virtual mass force acting on a particle is given by Drew and Lahey (Roco, 1993):

$$f_m = -0.5\varepsilon_s \rho_l \left(\frac{du_l}{dt} - \frac{du_s}{dt}\right) \quad (8\text{-}6)$$

The granular temperature (θ) is defined as: $\theta = C^2/3$, where C is the particle fluctuating velocity. The equation of solids fluctuating energy can be expressed:

$$\frac{3}{2}\left[\frac{\partial}{\partial t}(\varepsilon_s \rho_s \theta) + \nabla \cdot (\varepsilon_s \rho_s \theta \vec{u}_s)\right] = \left(-\nabla p_s \overline{I} + \overline{\overline{\tau_s}}\right) : \nabla \vec{u}_s + \nabla \cdot (k_s \nabla \theta) - \gamma_s - 3\beta\theta +$$
$$D_{ls} \quad (8\text{-}7)$$

where the conductivity of granular energy (k_s), the collisional energy dissipation (γ_s) and the energy exchange between the liquid and the solids (D_{ls}) are summarized in Table 8-1(Ansys Inc., 2011).

Table 8-1 Closure equations for the solids phase

Solids pressure	$p_s = \varepsilon_s \rho_s \theta + 2\rho_s(1+e)\varepsilon_s^2 g_o \theta$	(8-8)
Solids shear viscosity	$\mu_s = \dfrac{4}{5}\varepsilon_s^2 \rho_s d_p g_o(1+e)\sqrt{\dfrac{\theta}{\pi}} + \dfrac{10\rho_s d_p \sqrt{\pi\theta}}{96(1+e)\varepsilon_s g_o}\left[1+\dfrac{4}{5}\varepsilon_s g_o(1+e)\right]^2$	(8-9)
Solids bulk viscosity	$\xi_s = \dfrac{4}{3}\varepsilon_s^2 \rho_s d_p g_o(1+e)\sqrt{\dfrac{\theta}{\pi}}$	(8-10)
Conductivity of granular energy	$k_s = \dfrac{25\rho_s d_p \sqrt{\pi\theta}}{64(1+e)g_o}\left[1+\dfrac{6}{5}(1+e)g_o\varepsilon_l\right]^2 + 2\varepsilon_s^2 \rho_s d_p g_o(1+e)\sqrt{\dfrac{\theta}{\pi}}$	(8-11)
Collisional energy dissipation	$\gamma_s = 3(1-e^2)\varepsilon_s^2 \rho_s g_o \theta\left(\dfrac{4}{d_p}\sqrt{\dfrac{\theta}{\pi}} - \nabla\cdot\vec{u}_s\right)$	(8-12)
Rate of energy exchange	$D_{ls} = \dfrac{d_p \rho_s}{4\sqrt{\pi\theta}g_o}\left(\dfrac{18\mu_l}{d_p^2 \rho_s}\right)^2 |\vec{u}_l - \vec{u}_s|^2$	(8-13)
Radial distribution function	$g_o = \left[1-\left(\dfrac{\varepsilon_s}{\varepsilon_{s,max}}\right)^{1/3}\right]^{-1}$	(8-14)
Drag model	$\beta = \dfrac{3\varepsilon_s \varepsilon_l \rho_l}{4v_{r,s}^2 d_p}C_D\left(\dfrac{\text{Re}_s}{v_{r,s}}\right)|\vec{u}_s - \vec{u}_l|$ $C_D = \left(0.63 + \dfrac{4.8}{\sqrt{\text{Re}_s/v_{r,s}}}\right)^2$ $v_{r,s} = 0.5\left(A - 0.06\text{Re}_s + \sqrt{(0.06\text{Re}_s)^2 + 0.12\text{Re}_s(2B-A) + A^2}\right)$ $A = \varepsilon_l^{4.14}; B = \begin{cases}0.8\varepsilon_l^{1.28}, & \varepsilon_l \leq 0.85 \\ \varepsilon_l^{2.65}, & \varepsilon_l > 0.85\end{cases}; \text{Re}_s = \dfrac{\rho_l d_p |\vec{u}_s - \vec{u}_l|}{\mu_l}$	(8-15)

The drag force is one of the important terms in the momentum equations (Loha, et al., 2012). A model for the drag force is required to calculate the rate of the momentum transfer between the liquid phase and solids phase. Syamlal-O'Brien drag model (Syamlal & O'Brien, 1989) is employed in the present work, which has been widely used by previous researchers. And a previous research work (Luo, 2017) showed that Syamlal-O'Brien drag

model worked well in liquid-solid fluidization simulations compared with other drag models.

8.3.2 Mesh information

The downer of the inverse liquid-solid circulating fluidized bed shown in Figure 8-1 is simplified to a 2D planar model because of its axial symmetry. In order to correctly represent the complex flow structures at the inlet and near the wall, the mesh in the inlet region and near the wall has been refined. The mesh independence study has been done by other group members for the same bed that is used in this work (Luo, 2017). Two meshes were selected to be applied in this work based on the previous mesh independence study. The information of the selected meshes is given in Table 8-2.

Table 8-2 Mesh information for different operating conditions

Parameters	Domain size (m)	Number of control volumes	Increasing ratio along axis	Increasing ratio along radius	Maximum aspect ratio
Mesh 1	0.076×5.4	50×2000	1.05	1.05	6.9
Mesh 2	0.2×5.4	40×1000	1.03	1.03	2.44

8.3.3 Boundary conditions

The governing equations are numerically solved with appropriate boundary and initial conditions. At the inlet, which is at the top of the downer, both the liquid and solids are of uniform velocities. At the outlet, due to the fully developed flow condition, the outflow condition is used for both liquid and solids phases. At the wall, the no-slip condition is used for the liquid phase and the partial slip Johnson and Jackson boundary condition (Johnson & Jackson, 1987) is used for the solids phase. The particle-particle collision restitution coefficient for the solids phase is set as 0.9 and the specularity coefficient is set as 1×10^{-5}.

The phase coupled SIMPLE scheme is used for the pressure-velocity coupling, the second order upwind is chosen to discretize the convection terms for the k-ε turbulence model, granular temperature and momentum governing equations. The set of governing equations is solved by Ansys Fluent 17. In all simulations, the time step size is set as 1×10^{-5} s and

the convergence criteria are set as 5×10^{-5}. The results are time averaged for 20s after the simulations reaching the stable condition.

Detailed information of the simulation cases is given in Table 8-3. In cases #10, #11 and #12, mixed particles of different densities enter the simulated domain with the same volume fraction as other cases.

Table 8-3 Detailed information of the simulation cases and experiments

Case Number	Particle diameter d_p (mm)	Particle density ρ_p (kg/m^3)	Mesh	Superficial liquid velocity u_l (cm/s)	Superficial solid velocity u_s (cm/s)	Corresponding experiment
#1	1.1	640	Mesh 1	16.68	1.35	Nan # 1
#2	1.1	640	Mesh 1	19.46	0.71	Nan # 2
#3	1.1	640	Mesh 1	19.46	1.35	Nan # 3
#4	0.8	28	Mesh 1	25.09	0.48	Jaberi # 1
#5	0.8	28	Mesh 1	27.84	0.48	Jaberi # 2
#6	0.8	28	Mesh 1	27.84	0.64	Jaberi # 3
#7	0.8	28	Mesh 1	29.2	1.05	Jaberi # 4
#8	3	850	Mesh 2	20	1	
#9	3	950	Mesh 2	20	1	
#10	3	850&950	Mesh 2	20	1	
#11	3	850&950	Mesh 2	12	1	
#12	3	850&950	Mesh 2	12	0.5	

In addition, in Cases #10-#12, two different kinds of particles with densities of 850kg/m^3 and 950kg/m^3 flow into the inverse circulating fluidized bed together. Therefore, the system has three phases, one liquid phase and two solids phases. The flow behavior of the particles is simulated using the Eulerian-Eulerian multi-phase approach incorporating the kinetic theory of the granular flow. In the numerical simulation, the liquid (water) is set as the primary phase. The two solids phases are both set as secondary phases. The Syamlal-O'Brien drag model (Syamlal & O'Brien, 1989) is employed for the interphase interaction between the liquid phase and each solids phase. The drag coefficient for the interphase interaction between the two solids phases is given as follows (Syamlal & O'Brien, 1988):

$$C_{D,ab} = \frac{3(1+e_{ab})\left(\frac{\pi}{2}+C_{f,ab}\frac{\pi^2}{8}\right)\varepsilon_a\rho_a\varepsilon_b\rho_b(d_{p,a}+d_{p,b})^2 g_{0,ab}}{2\pi\left(\rho_a d_{p,a}^3+\rho_b d_{p,b}^3\right)}|\vec{u}_a - \vec{u}_b| \qquad (8-8)$$

The radial distribution function in binary particle system $g_{o, ab}$ is:

$$g_{o,ab} = \frac{d_{p,a}g_{o,b}+d_{p,b}g_{o,a}}{d_{p,a}+d_{p,b}} \qquad (8\text{-}9)$$

Previous studies by Geng et al. (2016) and Khan et al. (2017) showed that this solid-solid drag coefficient performs well in binary particle systems.

8.4 Results and discussion

8.4.1 Flow characteristics of the particles in the inverse liquid-solid flow

8.4.1.1 Solids hold up along the axial direction
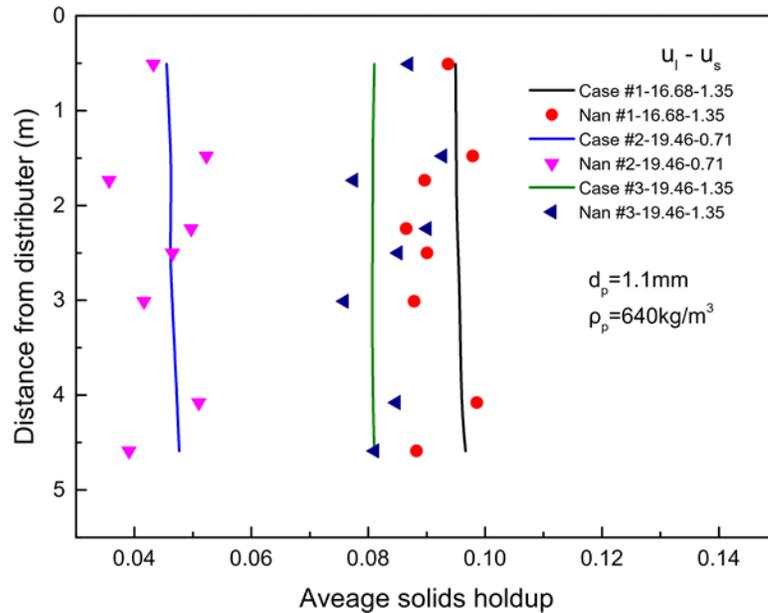
Figure 8-2 Axial distributions of the cross-sectional average solids holdup for Cases #1-#3

In Cases #1-#3, the density of the particles is 640 kg/m^3 and the axial distributions of cross-sectional average solids holdup are shown in Figure 8-2. The numerical results are compared with the experimental data under the same operating conditions. It can be seen that the numerical results and experimental results agree well. It is noticed that the predicted average solids holdup along axis is uniform, as also observed by Liang et al.

(1997) and Zheng (1999). The deviation between the numerical results and experimental data for Cases #1-#3 are 4.3%, 3.5% and 4.1%, respectively. In addition, it can be concluded based on the results from Cases #1 and #3 that under the same u_s, the average solids holdup decreases with the increasing u_l. This is expected since under the same u_s, the amount of the particles entering the fluidized bed is constant. The liquid flow with higher velocity will bring more particles out of the fluidized bed, leading to a lower average solids holdup (Razzak, et al., 2010) Similarly, it can be seen from Cases #2 and #3 that under the same u_l, the average solids holdup increases with the increasing u_s. When the velocity of the liquid is remained the same, higher u_s means more particles flowing into the fluidized bed, resulting in the increase of the solids holdup.
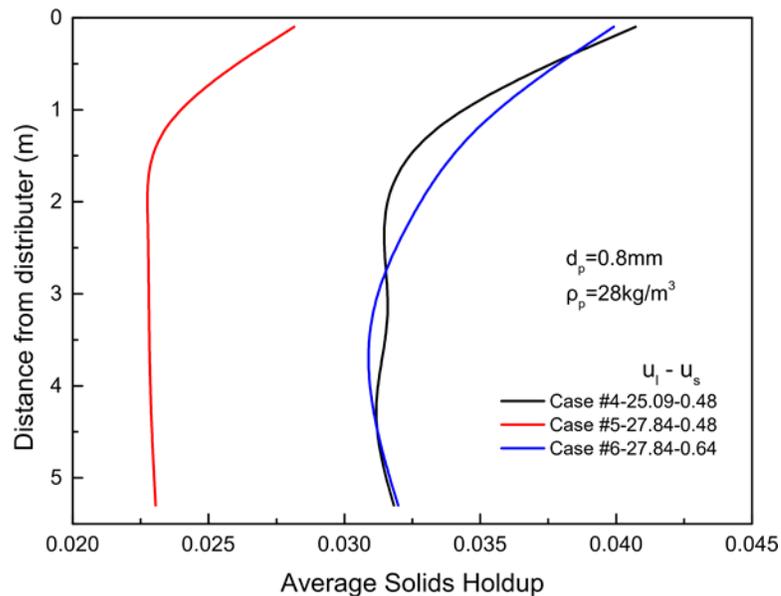
Figure 8-3 Axial distributions of the cross-sectional average solids holdup for Cases #4-#6

Figure 8-3 shows the axial distributions of cross-sectional average solids holdup of Cases #4-#6 where the particles have a density of 28 kg/m^3. Unlike the axial distributions of the cross-sectional average solids holdup in Cases #1-#3, the numerical results of Cases #4-#6 show that the average solids holdup along the axis decreases during the acceleration process, then remains close to being uniform. Due to the large density difference between the solids and liquid, the acceleration caused by the sum of the drag force, gravitational

force and buoyancy acting on the particles with a particle density of 28kg/m^3 is much smaller than that on the particles with a density of 640kg/m^3. Therefore, the acceleration process of the particles with a density of 28kg/m^3 is longer and more evident than that of the particles with a density of 640kg/m^3 before the slip velocity of the particles becomes unchanged. Table 4 shows the average solids holdup of entire bed for Cases #4-#6 and the corresponding experiments, Jaberi #1-#3 (Jaberi, 2014). It can be seen from Figure 8-4 that there is a good agreement between the numerical and experimental results.

Table 8-4 Average solids holdup of the entire bed for Cases #4-#6 and experiments Jaberi #1-#3

Numerical	(Case #4) 0.033	(Case #5) 0.024	(Case #6) 0.034
Experimental	(Jaberi #1) 0.035	(Jaberi #2) 0.026	(Jaberi #3) 0.037
Deviation	5.71%	7.69%	8.11%

8.4.1.2 Solids holdup along the radial direction

(a) Case #1-ρ_p=640kg/m^3-d_p=1.1mm-u_l=16.68cm/s-u_s=1.35cm/s

(b) Case #2-ρ_p=640kg/m^3-d_p=1.1mm-u_l=19.46cm/s-u_s=0.71cm/s

(c) Case #3-ρ_p=640kg/m^3-d_p=1.1mm-u_l=19.46cm/s-u_s=1.35cm/s
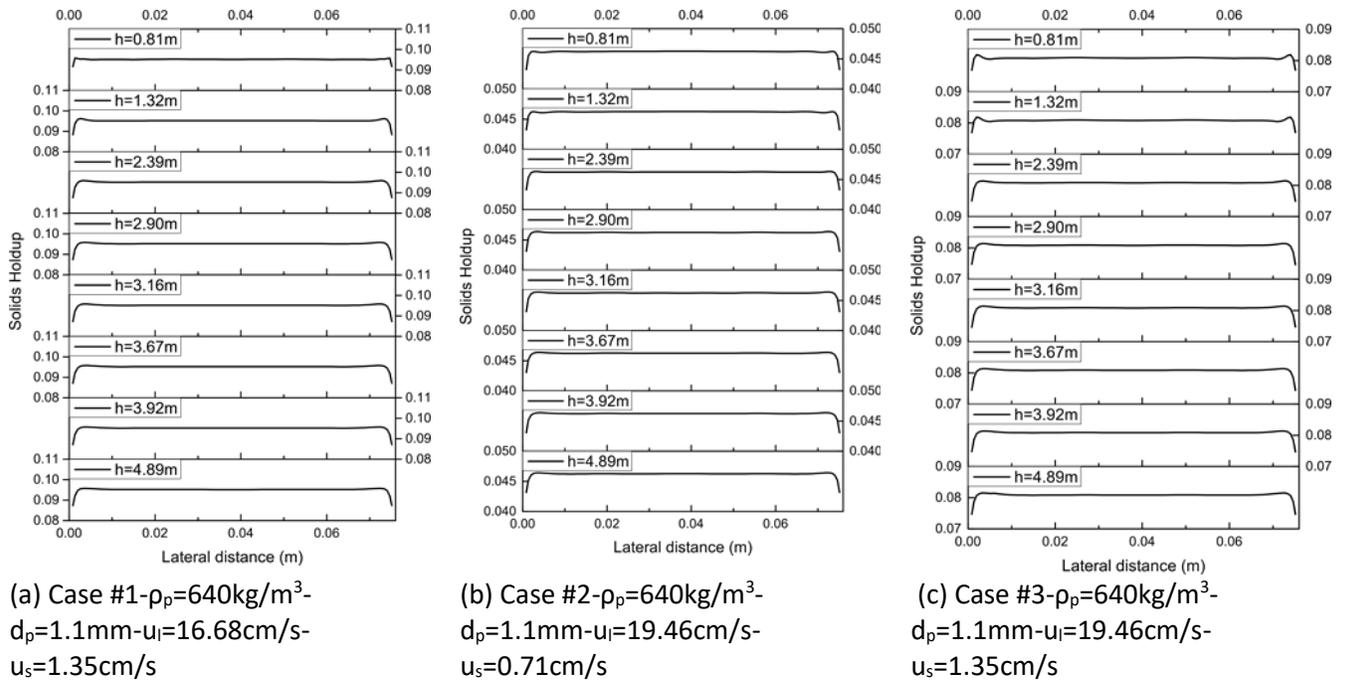
Figure 8-4 Radial distributions of solids holdup at different axial locations
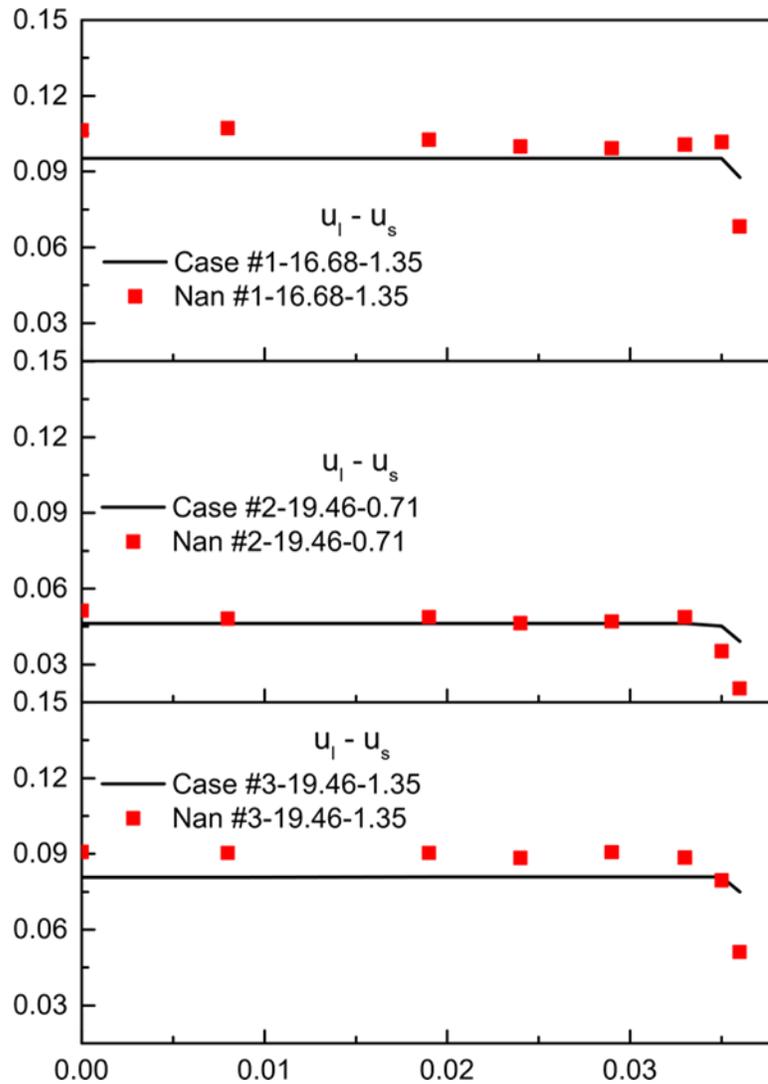
Figure 8-5 Comparisons of the solids holdup radial distributions between the numerical and experimental results at h=2.1m for Cases #1-#3

The solids holdup distributions along the radial direction at different bed heights for Cases #1-#3 are presented in Figure 8-4 and the comparison with the experimental data is given in Figure 8-5. The radial non-uniformity for solids holdup, dilute in the near wall region and dense in the center, can be clearly observed at each bed height. Due to the wall effect, the liquid velocity along the radial direction is higher in the center and lower near the wall. Likewise, the particles will accelerate to the similar velocity as that for the liquid. The wall effect also leads to a lower solids holdup at the wall region and increasing towards to the center (Razzak, 2009). It is shown in Figure 8-4 that the radial non-uniformity is lower at

the inlet region of the bed and increases towards to the exit of the bed. This is because that the liquid and solids velocities are assumed as uniform at the inlet of the bed. In addition, it can be seen in Figure 8-5 that the average solids holdup of case #1 is higher than that of Case #3 and higher than that of Case #2, which is consistent with the results shown in Figure 8-2. Furthermore, it is evident from Figure 8-5 that the agreement between numerical predictions and experimental data is good for solids holdup.

(a) Case #4-ρ_p=28kg/m³-d_p=0.8mm-u_l=25.09cm/s-u_s=0.48cm/s

(b) Case #5-ρ_p=28kg/m³-d_p=0.8mm-u_l=27.84cm/s-u_s=0.48cm/s

(c) Case #6-ρ_p=28kg/m³-d_p=0.8mm-u_l=27.84cm/s-u_s=0.64cm/s

Figure 8-6 Radial distributions of solids holdup at different axial locations
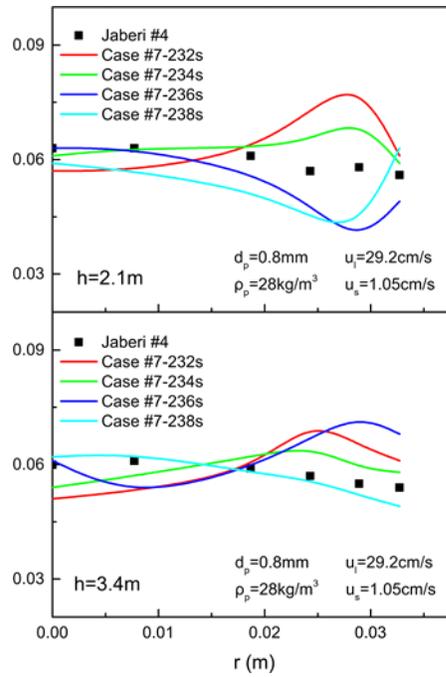
Figure 8-7 Comparisons of the solids holdup radial distributions between the numerical results at different time and experimental results at h=2.1m and h=3.4m for Case #7
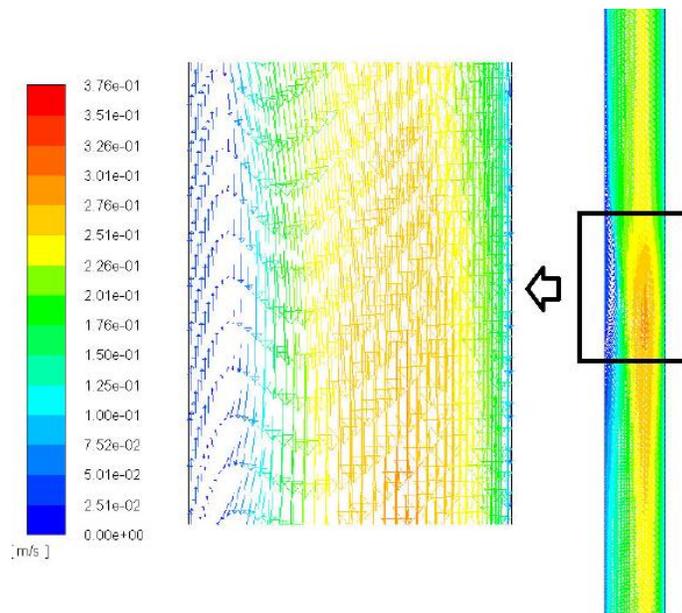
Figure 8-8 Velocity vector of the solids phase for Case #4 at t=232s

The solids holdup distributions along the radial direction at different bed heights for Cases #4-#6 are presented in Figure 8-6 and the comparison between the numerical results at different time for Case #7 with the experimental data is given in Figure 8-7. Unlike the solids holdup radial distributions in Cases #1-#3, the flow structures for Cases #4-#6 at each cross section of the bed are asymmetrical. From the flow structures from 232s to 238s, it can be seen that some vortexes in the solids phase are randomly generated in the bed and the positions of the vortexes change with the time. A vortex is shown in Figure 8-8. This is mainly because of the large density difference between the solids and liquid, the drag force and gravity cannot keep the particles flowing downwards all the time. When a vortex is generated, the velocities of the particles within the vortex become lower, which results in a higher solids holdup in the region of the vortex. As shown in Figure 8-6, because of the randomness and irregularity of the vortexes, the solids holdup radial distributions are irregular.

(a) Case #8-ρ_p=850kg/m³-d_p=3mm-u_l=20cm/s-u_s=1cm/s

(b) Case #9-ρ_p=950kg/m³-d_p=3mm-u_l=20cm/s-u_s=1cm/s
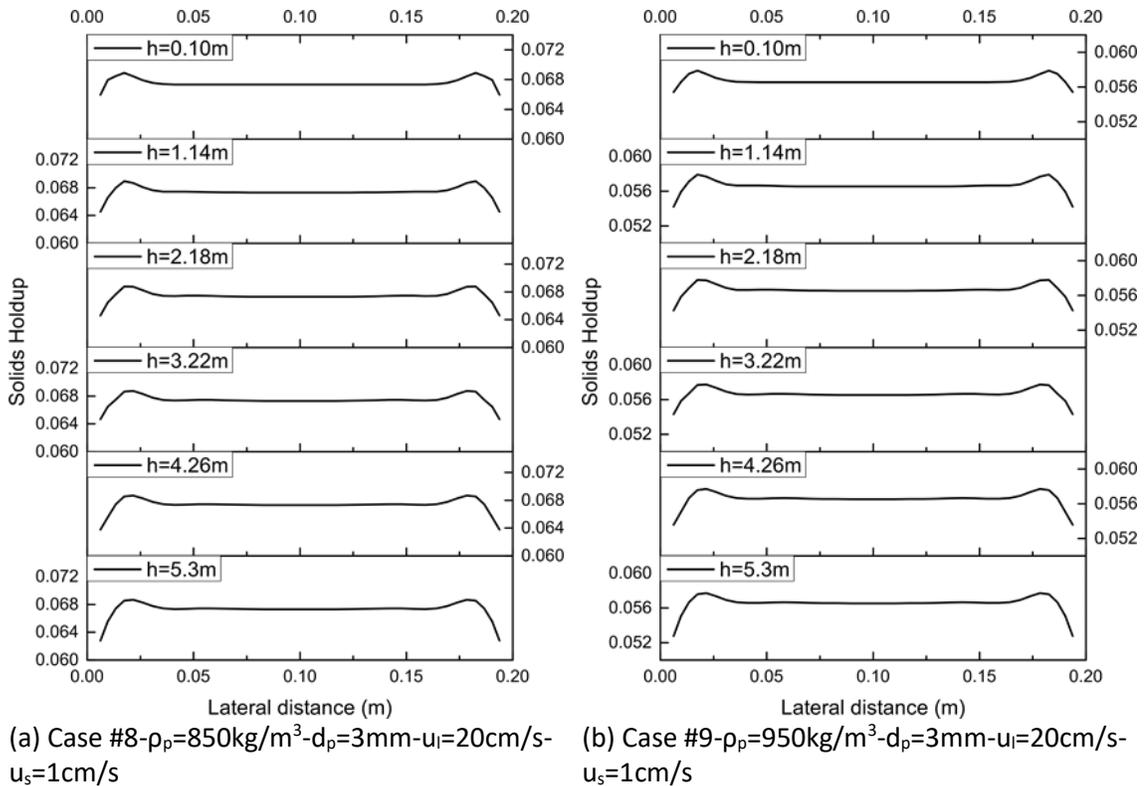
Figure 8-9 Radial distributions of solids holdup at different axial locations

Figure 8-9 shows the radial distributions of solids holdup at different bed heights for Cases #8 and #9. Similar to Cases #1-#3, the solids holdup distributions along the radial direction

for Cases #8 and #9 are dilute in the near wall region and dense in the center. As discussed in Figure 8-4, the wall effect leads to this phenomenon. The radial non-uniformity is lower at the inlet region of the bed and increases along the axial direction. Additionally, it is apparent that the solids holdup in Case #8 is larger than that in Case #9, which is expected since the parti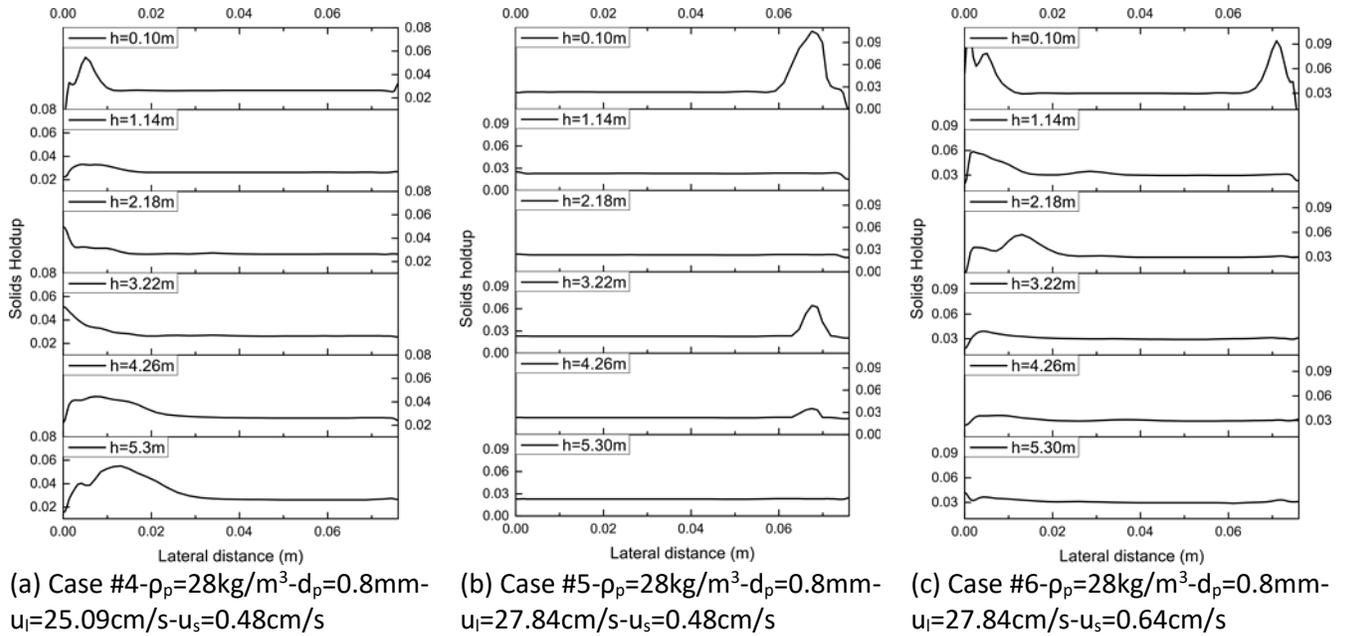cles with higher density have a higher gravitational force. Therefore, it is easier for the particles with higher density to flow out of the bed, resulting in a lower solids holdup.

8.4.1.3 Lateral velocities of particles at different bed heights

Figure 8-10 shows the lateral velocities of particles at different bed heights for Cases #1-#3 respectively. It can be seen from Figure 8-10 that at each bed height, the lateral velocities of solid particles are positive at the left hand side of symmetry axis of bed and negative at the right hand side. That indicates that particles move from the both the left hand side wall and right hand side wall to the centre of the bed, which is also observed by Wang et al. (2014). It is noticed that the lateral velocity of particles increases from zero at the wall to a maximum value, and then decreases to zero at the center due to the boundary conditions. The lateral velocity decreases along the axial direction and becomes zero when the flow is fully developed as shown in the Figure 8-10. This indicates that the transverse mixing of the particles decreases gradually along the axial direction. Based on Cases #1 and #3, it can be concluded that under the same u_s, the lateral velocity of particles increases with u_l. Also, from Cases #2 and #3, under the same u_l, the lateral velocity of particles increases with u_s. This is because the increase in u_l or u_s increases the kinetic energy of the liquid or particles flowing into the bed, leading to the increase in the motion of particles in the bed.

The lateral velocities of particles at different bed heights for Cases #4-#6 are shown in Figure 8-11. Different from Cases #1-#3, the lateral velocities of particles in Cases #4-#6 are random and irregular. Similar to the results shown in Figure 8-6, due to the large density difference between the solids and liquid, vortexes of particles are generated in the bed which leads to the random changes of lateral velocities.
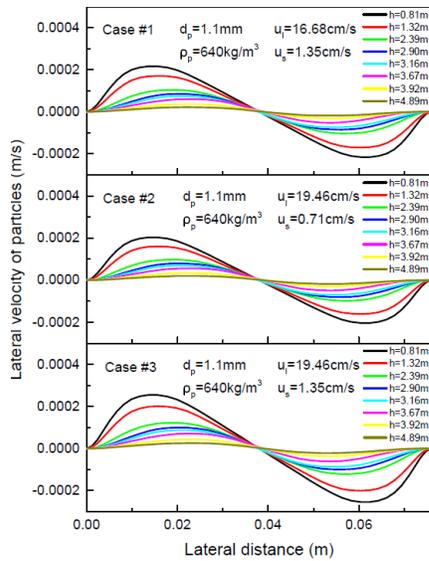
Figure 8-10 Lateral velocities of particles at different bed heights for Cases #1-#3
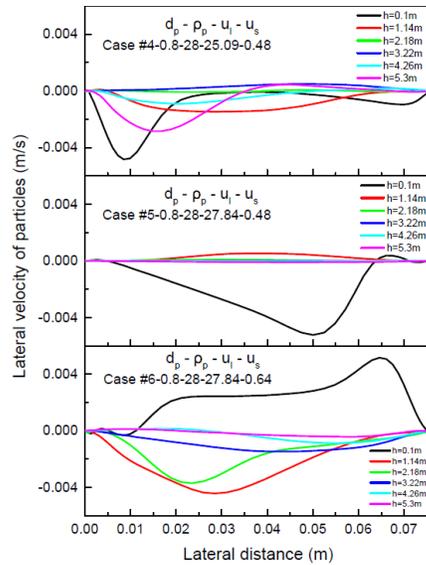
Figure 8-11 Lateral velocities of particles at different bed heights for Cases #4-#6
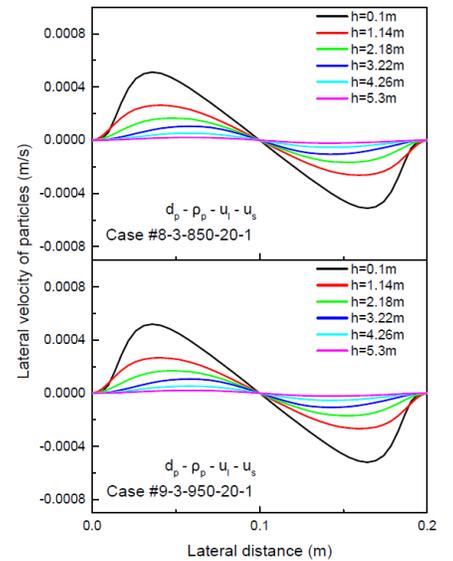
Figure 8-12 Lateral velocities of particles at different bed heights for Cases #8 and #9

Figure 8-12 shows the lateral velocities of particles at different bed heights for Cases #8 and #9. It can be seen from Figure 8-12 that the trend of lateral velocities in Cases #8 and #9 is the same as those of Cases #1-#3. Furthermore, the lateral velocities of Case #9 are a little bit higher than those of Case #8. This is reasonable since under the same u_l and u_s, the kinetic energy of particles increases with the increasing particle density, which further increases the motion of particles in the bed.

8.4.1.4 Axial velocities of particles at different bed heights

Figure 8-13 shows the distributions of the axial velocities of particles at different bed heights for Cases #1-#3. It can be seen that the axial velocities of particles are higher in the center than that near the walls. In the downer of the inverse liquid-solid circulating fluidized bed, the sum of drag force and the gravitational force of the particles is larger than the buoyancy, which causes particles to flow down into the bed, while the friction between particles and wall resists the downward flow of particles. As mentioned before, due to the wall effect, both liquid and solids will have similar axial velocity distributions, which is higher in the center and lower near the wall. Moreover, it can be observed that along the axial direction, the axial velocity distribution of particles becomes steeper as the

solids velocity is assumed as uniform at the inlet of the bed. In addition, from Cases #1 and #3, it is evident that under the same u_s, the axial velocity of particles increases with the increasing u_l. Also, from Cases #2 and #3, it is noticed that under the same u_l, the axial velocity of particles increases with the increase in u_s. This is also due to the fact that the increase in u_l or u_s increases the kinetic energy of the liquid and solids into the bed, leading to an increase in the motion of particles.
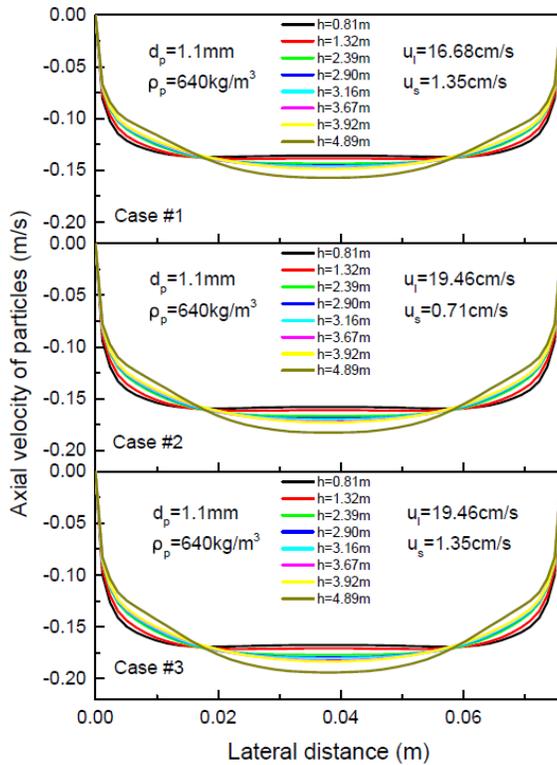
Figure 8-13 Axial velocities of particles at different bed heights for Cases #1-#3
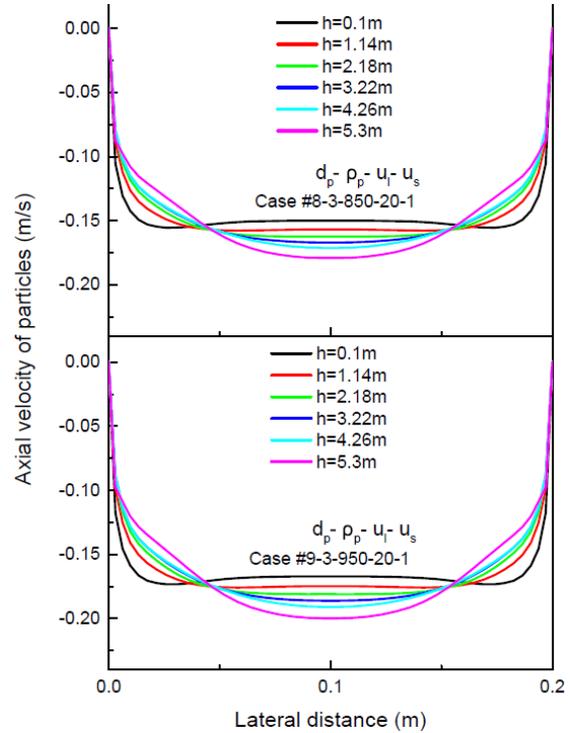
Figure 8-14 Axial velocities of particles at different bed heights for Cases #8 and #9

The axial velocities of particles at different bed heights for Cases #8 and #9 are shown in Figure 8-14. The trend of axial velocities in Cases #8 and #9 is the same as that in Cases #1-#3. Additionally, the values of the axial velocities of Case #9 are higher than those of Case #8, which is due to the fact that higher particle density leads to higher gravity and further increases the acceleration.

211

8.4.2 Liquid-solid flow characteristics of mixed particles

8.4.2.1 Solids hold up along the axial direction
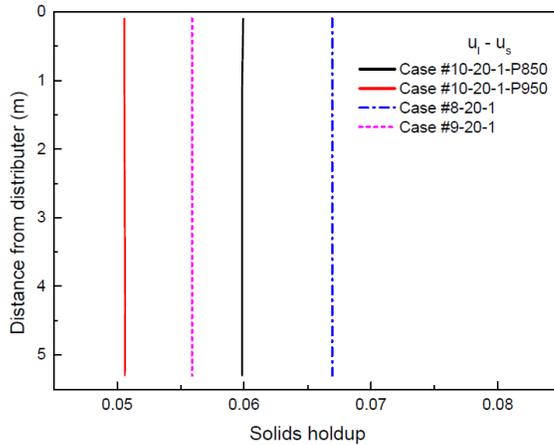
Figure 8-15 The distributions of the average solids holdup along axis for Cases #8-#10
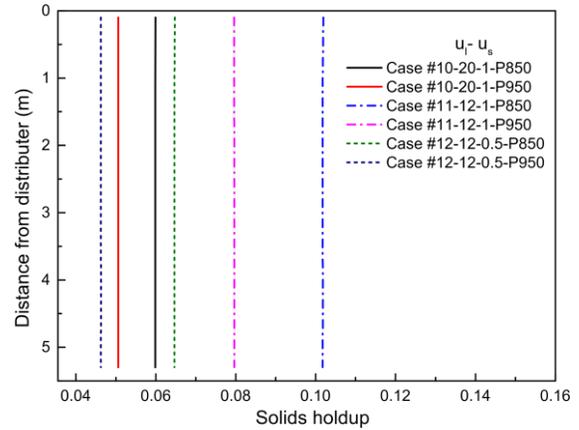
Figure 8-16 The distributions of the average solids holdup along axis for Cases #10-#12

Figure 8-15 shows the distributions of the average solids holdup along axis for Cases #8-#10. In Cases #8 and #9, single-density particles are used with a density of 850kg/m^3 and 950kg/m^3, respectively. The volume fractions of solids phase at the inlet are both 30% in Cases #8 and #9. In Case #10, mixed particles, which are composed of two different particles with a density of 850kg/m^3 (P850) and 950kg/m^3 (P950) are used. The volume fractions of P850 and P950 at the inlet are both 15% in Case #10. It can be seen from Figure 8-15 that the cross-sectional average solids holdups along the axis for these cases are all uniform. In Case #10, the cross-sectional average solids holdup for P850 is larger than that of P950, which is expected since the higher particle density leads to higher gravity. Therefore, it is easier for P950 to flow out of the bed, resulting in a lower solids holdup [23]. The total solids holdup of P850 and P950 in Case #10 is higher than the solids holdup in Cases #8 and #9.

The distributions of the average solids holdup along axis of P850 and P950 for Cases #10-#12 is shown in Figure 8-16. The cross-sectional average solids holdup of each particle group in these cases is uniform along the axis. From Cases #10 and #11, it is clear that under the same u_s, the average solids holdup of P850 and P950 decreases with the

increasing u_l. And based on Cases #11 and #12, under the same u_l, the average solids holdups of P850 and P950 increase with the increase in u_s, which has the same trend as Cases #1-#3.

8.4.2.2 Solids hold up along the radial direction
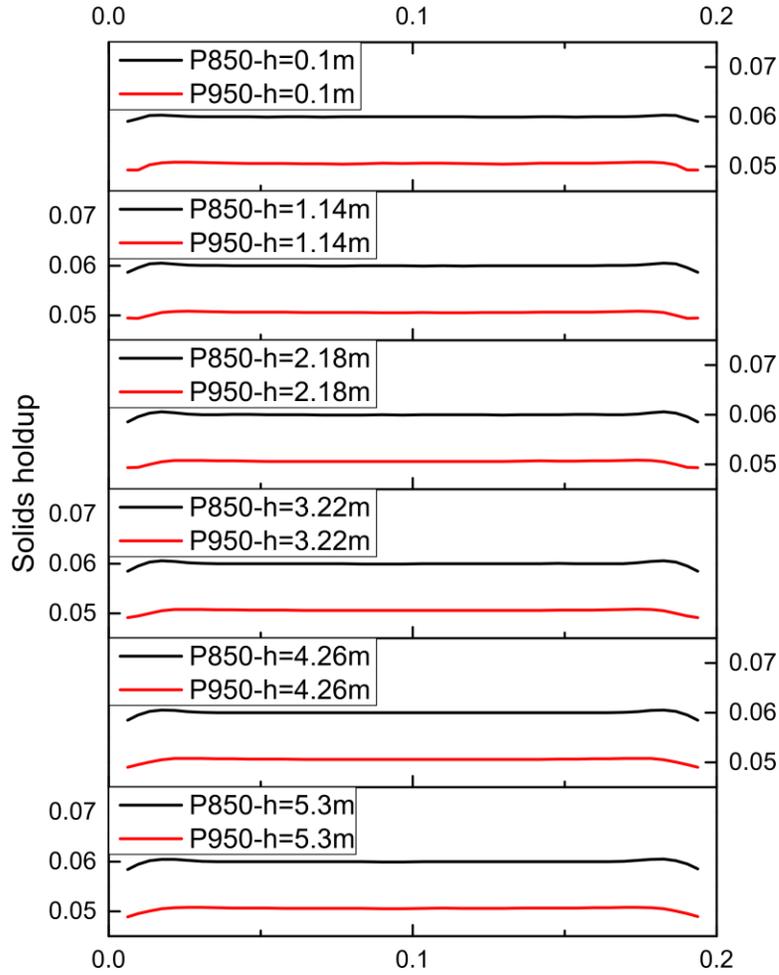
Figure 8-17 Radial distributions of solids holdup at different axial locations for Case#10
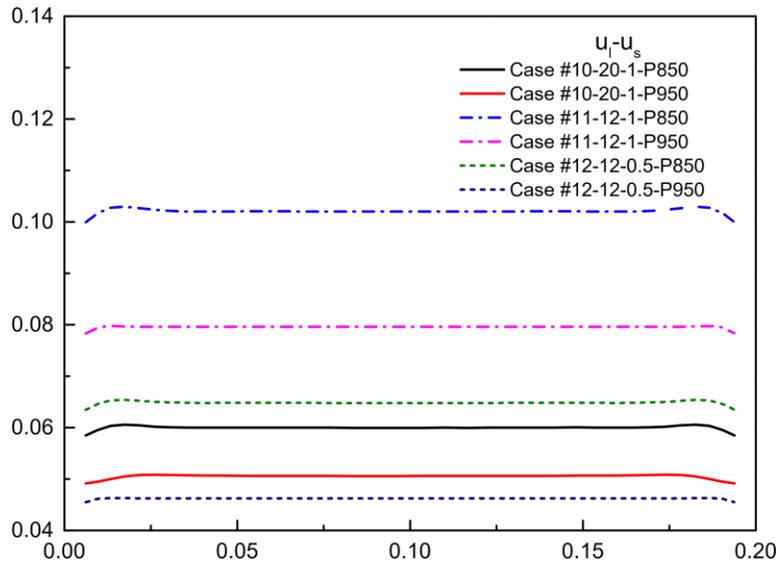
Figure 8-18 Radial distributions of solids holdup for Cases #10-#12 at h=3.22m

Solids holdup radial distributions of P850 and P950 at different axial locations for Cases #10-#12 are shown in Figure 8-17 and Figure 8-18. Evidently, the trend of solids holdup radial distribution of each particle group for the cases using the mixed particles is as the same as that in the cases using the single-density particles. As discussed before, the solids holdup of P850 is higher than that of P950 in each case.

8.4.2.3 Lateral velocities of particles at different bed heights

Figure 8-19 and Figure 8-20 show the lateral velocities of P850 and P950 at different bed heights for Cases #10-#12. It can be seen from Figure 8-19 and Figure 8-20 that the trend of the lateral velocities of each particle group in the case using mixed particles is the same as that in the case using single-density particles. Also, the lateral velocities of P850 and P950 are almost the same at the same bed height in each case. Furthermore, from Cases #10 and #11, it can be concluded that under the same u_s, the lateral velocity increases with the increasing u_l. In addition, it can be seen from Cases #11 and #12, under the same u_l, the lateral velocity increases a little bit with the increasing u_s. As mentioned before, this is due to the higher liquid and solids kinetic energy when increasing u_l or u_s
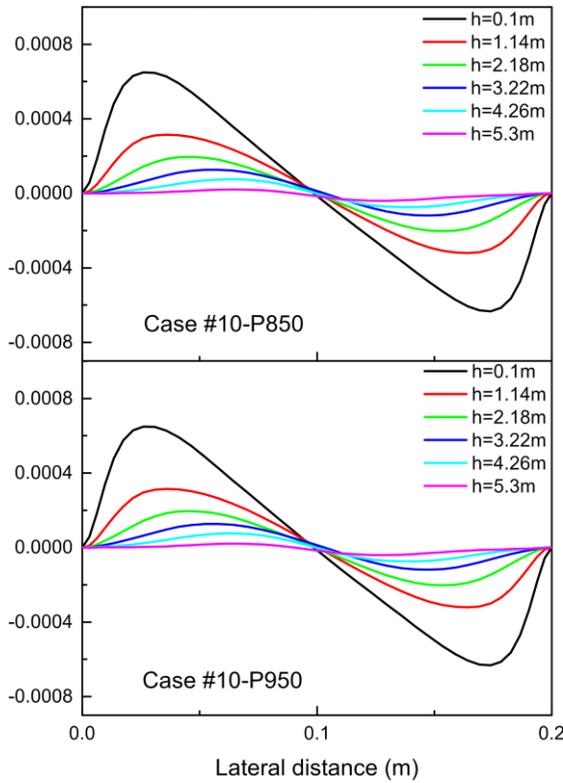
Figure 8-19 Lateral velocities of P850 and P950 at different bed heights for Cases #10
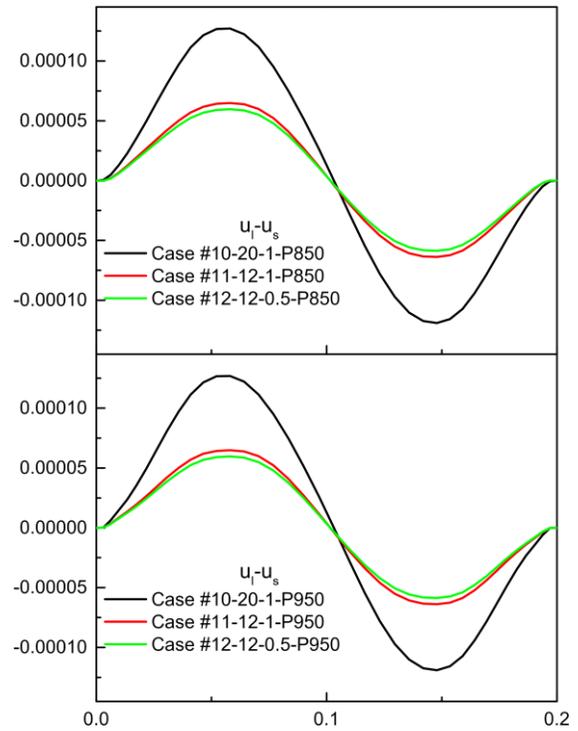
Figure 8-20 Lateral velocities of P850 and P950 for Cases #10-#12 at h=3.22m

8.4.2.4 Axial velocities of particles at different bed heights

Figure 8-21 and Figure 8-22 show the axial velocities of P850 and P950 at different bed heights for Cases #10-#12. The trend of axial velocity for each particle group for the cases using the mixed particles is similar to that for the case using the single-density particles. It can be seen from Figure 8-21 and Figure 8-22 that at the same bed height, the axial velocity of P950 is higher than that of P850. Also, the motion of particles is increased with the increase in u_l or u_s.
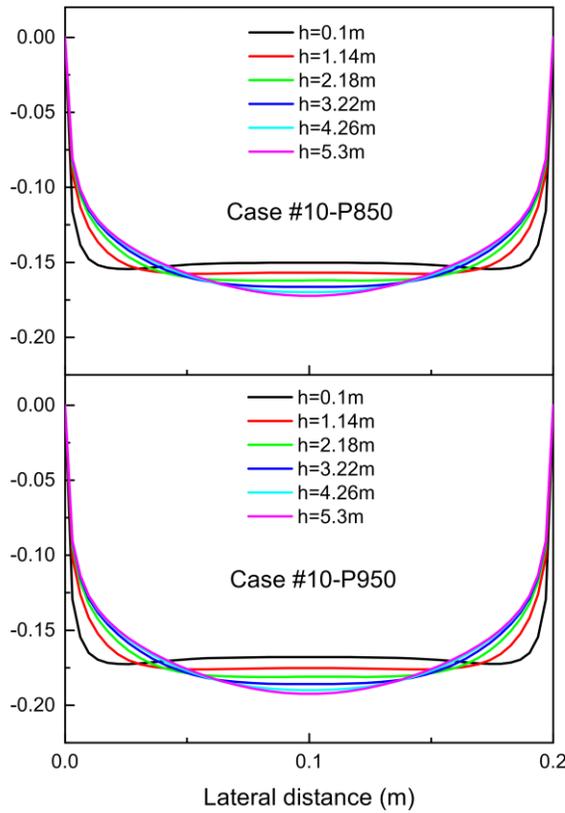
Figure 8-21 Axial velocities of P850 and P950 at different bed heights for Cases #10
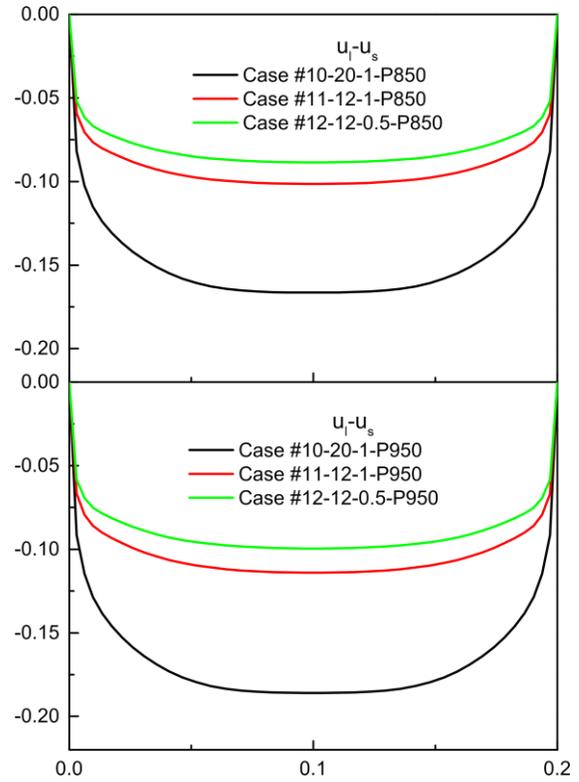
Figure 8-22 Axial velocities of P850 and P950 for Cases #10-#12 at h=3.22m

8.5 Conclusion

A numerical study has been carried out in this work on the liquid-solid multi-phase flow characteristics in inverse circulating fluidized beds using single-density and mixed-density particles. Two-dimensional Eulerian-Eulerian model incorporating the kinetic theory of granular flow is selected as the modeling technique and the CFD package Ansys/Fluent is the numerical platform used in this study. The predictions under different operating conditions are compared with previous experimental data. The following specific conclusions can be drawn from this study:

(1) A good agreement between the numerical simulation results and experimental date has been achieved.

(2) The hydrodynamics of particles with a density of 950 kg/m^3, 850 kg/m^3 and 640 kg/m^3 in the inverse liquid-solid circulating fluidized bed downers under different operations have similar features. The cross-sectional average solids holdup along the axis is uniform and the radial flow structures at different bed heights are similar. For the flow structures in the radial direction, due to the wall effect, the solids holdup is not uniform in the radial direction, which is lower at the wall region and higher in the center of the bed. The radial non-uniformity is lower at the entrance region of the bed and increases towards to of the exit of the bed. Particles move from the wall to the center. Such tendency diminishes as the flow becomes full developed. The axial velocities of particles are higher in the center and lower near the walls. Under the same u_s, the cross-sectional average solids holdup decreases with the increasing u_l, and the lateral and axial velocities of particles increase with the increase in u_l. Under the same u_l, the cross-sectional average solids holdup, the lateral velocity and axial velocity of particles increase with the increasing u_s.

(3) The flow patterns of the particles with a density of 28 kg/m^3 in the inverse liquid-solid circulating fluidized bed downers are irregular. The cross-sectional average solids holdup along the axis decreases during the acceleration process then remains close to uniform. Due to the large density difference between the solids and liquid, the drag force and gravity cannot keep the particles flowing downwards all the time. Therefore, vortexes of particles are randomly generated in the bed and the positions of the vortexes change over time. Because of the randomness and irregularity of the vortexes, the solids holdup radial distributions and the particle velocities are irregular.

(4) Hydrodynamics of mixed particles with a density of 850 kg/m^3 and 950 kg/m^3 in the inverse liquid-solid circulating fluidized bed downer are also studied in this work. The cross-sectional average solids holdup of P850 is higher than that of P950. The radial distribution trend of the solids holdup, the trend of the lateral and axial velocities of each particle group in the simulation using mixed particles are similar to those in the case using single-density particles.

Nomenclature

C_D	drag coefficient
$C_{D,ab}$	solid-solid drag coefficient in binary particle system
$C_{f,ab}$	coefficient of friction between solids in binary particle system
d_p	particle diameter, mm
e	coefficient of restitution
e_{ab}	solid-solid interaction restitution coefficient in binary particle system
f_m	virtual mass force, N
g	gravity acceleration, m/s^2
g_o	radial distribution function
$g_{o,ab}$	radial distribution function in binary particle system
h	distance from the distributer, m
$\bar{\bar{I}}$	unit tensor
K	turbulent kinetic energy, m^2/s^2
P	fluid pressure, Pa
p_s	solids pressure, Pa
r	rayon, m
Re_s	relative Reynolds number
T	time, s
U	superficial velocity, cm/s
β	interphase momentum transfer coefficient, kg/m^{2}s^2
γ_s	collisional energy dissipation, kg/ms^3
ε	turbulent dissipation rate, m^2/s^3
ε_a	volume fraction of particle a
ε_b	volume fraction of particle b
ε_l	volume fraction of liquid
ε_s	volume fraction of solids
$\varepsilon_{s,max}$	maximum solids volume fraction
θ	granular temperature, m^2/s^2
μ_f	effective viscosity of fluid, kg/ms

μ_l	molecular viscosity of fluid, kg/ms
μ_s	solid shear viscosity, kg/ms
ρ	density, kg/m^3
$\overline{\overline{\tau}}_l$	stress tensor of liquid phase, kg/s^2
$\overline{\overline{\tau}}_s$	stress tensor of solids phase, kg/s^2

Subscripts

a	solids particle a in binary particle system
b	solids particle b in binary particle system
l	liquid phase
p	particle
s	solids phase

References

Ansys Inc., Ansys Fluent Theory Guide, available at http://www.ansys.com (accessed in January 1st, 2011).

Fan, Gas-Liquid-Solid Fluidization Engineering, Butterworth Publisher, Stoneham, MA, 1989.

Fan, Muroyama & Chern, Hydrodynamic characteristics of inverse fluidization in liquid-solid and gas-liquid-solid systems, Chem. Eng. J. 24 (2) (1982) 143-150.

Feng, Swenser-Smith, Witt, Doblin, Lim & Schwarz, CFD modeling of gas-solid flow in an internally circulating fluidized bed, Powder Technol. 219 (2012) 78-85.

Geng, Jia, Zhan, Liu & Xu, CFD modeling the hydrodynamics of binary particle mixture in pseudo-2D bubbling fluidized bed: Effect of model parameters, Powder Technol. 302 (2016) 384-395.

Hartge, Ratschow, Wischnewski & Werther, CFD-simulation of a circulating fluidized bed riser, Particuology 7 (4) (2009) 283-296.

Jaberi, The hydrodynamic behavior of an inverse liquid-solid circulating fluidized bed, Master thesis, The University of Western Ontario, 2014.

Johnson & Jackson, Frictional-collisional constitutive relations for granular materials, with application to plane shearing, J. Fluid Mech. 176 (1987) 67-93.

Khan, Evans, Peng, Doroodchi, Moghtaderi, Joshi & Mitra, Expansion behaviour of a binary solid-liquid fluidised bed with different solid mass ratio, Adv. Powder Technol. 28(12) (2017) 3111-3129.

Liang, Zhang, Zhu, Jin, Yu & Wang, Flow characteristics of the liquid-solid circulating fluidized bed, Powder Technol. 90 (2) (1997) 95-102.

Liu, Yu, Lu, Wang & Liao, Z.H. Hao, CFD-DEM simulation of liquid-solid fluidized bed with dynamic restitution coefficient, Powder Technol. 304 (2016) 186-197.

Loha, Chattopadhyay & Chatterjee, Assessment of drag models in simulating bubbling fluidized bed hydrodynamics, Chem. Eng. Sci. 75 (2012) 400-407.

Luo, Numerical simulations of two-phase flows in the liquid solid circulating fluidized bed, Master thesis, The University of Western Ontario, 2017.

Montastruc, Brienne & Nikov, Modeling of residence time distribution: Application to a three-phase inverse fluidized bed based on a Mellin transform, Chem. Eng. J. 148 (1) (2009) 139-144.

Nan, Hydrodynamic in inverse liquid-solid circulating fluidized bed, Ph.D thesis, The University of Western Ontario, 2019.

Pan, Chen, Liang, Zhu & Luo, CFD simulations of gas-liquid-solid flow in fluidized bed reactors-A review, Powder Technol. 299 (2016) 235-258.

Razzak, Barghi & Zhu, Axial hydrodynamic studies in a gas-liquid-solid circulating fluidized bed riser, Powder Technol. 199 (1) (2010) 77-86.

Razzak, Hydrodynamic studies in liquid-solid and gas-liquid-solid circulating fluidized beds. Ph.D thesis, The University of Western Ontario, 2009.

Renganathan & Krishnaiah, Liquid phase mixing in 2-phase liquid-solid inverse fluidized bed, Chem. Eng. J. 98 (3) (2004) 213-218.

Renganathan & Krishnaiah. Voidage characteristics and prediction of bed expansion in liquid-solid inverse fluidized bed, Chem. Eng. Sci. 60 (10) (2005) 2545-2555.

Roco Eds., Particulate Two-Phase Flow, Butterworth-Heinemann, Boston, MA, 1993.

Roy, Sai & Jayanti, Numerical simulation of the hydrodynamics of a liquid solid circulating fluidized bed, Powder Technol. 251 (2014) 61-70.

S.Y. Wang, J. Sun, Q. Yang, Y.Q. Zhao, J.S. Gao, Y. Liu, Numerical simulation of flow behavior of particles in an inverse liquid-solid fluidized bed, Powder Technol. 261 (2014) 14-21.

Sang, Particle fluidization in upward and inverse liquid-solid circulating fluidized bed, Ph.D thesis, The University of Western Ontario, 2013.

Syamlal & O'Brien, Computer Simulation of Bubbles in a Fluidized Bed, AIChE Symp. Ser. 85 (1989) 22-31.

Syamlal & O'Brien, Simulation of granular layer inversion in liquid fluidized beds, Int. J. Multiph. Flow 14 (1988) 473-481.

Wang, Lu, Zhang, Shi & Li, A review of multiscale CFD for gas-solid CFB modeling, Int. J. Multiph. Flow 36 (2) (2010) 109-118.

Wang, Wang, Wang, Shao, Ma, Sun & Zhao, Numerical simulation of flow behavior of particles in an inverse liquid-solid fluidized bed with a jet using CFD-DEM, J. Taiwan Inst. Chem. E. 82 (2018) 214-225.

Xu, Zhong, Yuan & Yu, CFD-DEM study on cohesive particles in a spouted bed, Powder Technol. 314 (2017) 377-386.

Zhang, Wu, Brandani, Chen & Yang, CFD simulation of dynamic characteristics in liquid-solid fluidized beds, Powder Technol. 227 (2012) 104-110.

Zheng, Flow structure in a liquid-solids circulating fluidized bed, Ph.D thesis, The University of Western Ontario, 1999.

Chapter 9

9 Experimental and numerical studies on a bubble-induced inverse gas-liquid-solids fluidized bed

9.1 Introduction

The expansion of the fluidization technology resulted in many new types of the fluidized bed reactors from gas-solids to liquid-solids and even gas-liquid-solids three-phase fluidization by changing the fluidizing agent since the 1940s (Werther, et al., 2014). Also, by using the lighter particles with a lower density than the liquid, the inverse liquid-solid fluidization with particles downward flowing from the top of the fluidized bed has been developed in the 1980s (Fan, et al., 1982; Wen & Xu, 1998). Further by introducing gas bubbles into the inverse liquid-solid fluidization system from the bottom of the column, the packed light particles at the top of the fluidized bed will be fluidized when gas bubbles reach the bottom layer of the particles due to the reduced gas-liquid mixture density or the turbulence induced by the gas bubbles (Grevskott, et al., 1996; Wei, et al., 2005; Comte, et al., 1997; Cho, et al., 2002; and Buffière, et al., 1999). Such a new type of fluidized bed is called a bubble induced inverse gas-liquid-solid fluidized bed (BIFB) in which a three-phase fluidization is operated. Compared to the upward flow three-phase fluidization, the inverse three-phase fluidization can reduce energy consumption and minimum solids attrition as the solid phase can be fluidized under low liquid and gas velocities, and the particle entrainment problem can be eliminated without using any external equipment (Ibrahim et al. 1996). In addition, since the particles can be simply fluidized by the gas bubbles in the BIFB, only a very small or even a zero liquid velocity is needed which makes the BIFB very favourable in the wastewater treatment because a long residence time of the liquid is achieved. Compared with the traditional methods of the wastewater treatment such as activated sludge process which requires longer retention time and large space, the retention time can be reduced in fluidized bed reactor due to high biomass concentration, and another problem of excessive growth of biomass on particles can be fixed by using light particles in inverse fluidized beds as well (Sokół & Korpal, 2006; Lee, et al., 2000).

With the rapid development of computer technology, CFD has become a powerful tool to simulate the multiphase flow and provide more details on the three-phase fluidization process. In addition, CFD is considered to be more time and economic efficient to simulate complex flows compared with the experimental method. Two approach are mainly used to simulate the multiphase flow in fluidized bed, which are the Eulerian-L Eulerian (E-E) approach and Eulerian-Lagrangian (E-L) approach. The E-L approach treats the liquid and gas as a continuous phase by solving the Navier-Stokes equations, and the solid phase is treated as a discrete phase. which can be solved by tracking the trajectories of each particle based on the Lagrangian force balance equation (ANSYS, 2014). The E-E approach treats all phases as the interpenetrating continuum, and all phases are solved using governing equations which are closed by additional closure laws and constitutive relations. Compared to the E-E approach, the computational resource needed for the E-L approach to simulate multiphase flows will be high if the discrete phase volume fraction is high (Pan et al. 2016). Therefore, the E-E approach will be used in the present study, since the volume fraction of the solid phase is higher than 10% in BIFB.

Hamidipour et al. (2012) developed a CFD model for the simulation of the three-phase inverse fluidized bed based on a three-fluid model combined with the kinetic theory of granular flow (KTGF) to investigate the performance of different turbulence models and solid wall conditions. The results showed the dispersed RNG k–ε model gives a better performance on predicting the axial solids velocity and gas velocity than the other k–ε models. According to this study, it was also found that both the three-dimensional and two-dimensional models are capable of predicting the flow field, but the three-dimensional model is slightly more accurate than the two-dimensional model. However, the computational cost of the three-dimensional simulation is also high. The no-slip wall condition for the liquid phase, and free-slip for the gas and solids phases were recommended. Li and Zhong (2015) investigated the performance of different drag models on predicting the hydrodynamics of the three-phase phase bubble columns. The study found that the best drag model for the liquid and gas phases is the Zhang-Vanderheyden model (Zhang & Vanderheyden, 2002), between liquid and solid phases is the Schiller-

Naumann drag model (Schiller & Naumann, 1935), and the drag force between the gas and solid phases was not considered.

It is noticed that the hydrodynamics of the inverse fluidized bed has been studied experimentally by many researchers, but most studies were focused on the flow characteristics, such as the average phase holdup, axial phase holdup, and minimum fluidization velocity. However, few of them reported the details of the flow patterns and local flow characteristics, such as local radial phase holdup, radial solid phase velocity etc. In addition, few researchers investigated the development process of the inverse three-phase fluidization process.

For CFD models, only a few models were developed and validated for the three-phase fluidization process based on the three-fluid E-E approach (Wu & Gidaspow, 2000; Renganathan, et al., 2008; Li, et al., 1999). The complicated interactions between each phase are still not well understood, and there is no clear guideline to follow when setting up a CFD model for the simulation of the three-phase fluidization process. In addition, few CFD models has been developed to predict the hydrodynamics and flow structures in the BIFB.

Therefore, the objective of this study is to develop a CFD model for the simulation of the inverse three-phase fluidized bed based on the three-fluid Eulerian-Eulerian approach in order to study the flow details and fluidization development process in the BIFB, which have not been reported by experimental studies.

9.2   Experimental setup and operating conditions

The configuration of the BIFB used by Sun (2017) is shown in Figure 9-1. The column is made of PVC with 0.153 m in diameter and 3 m in height. The ring shape porous quartz gas distributor with an 8.7 cm outer diameter and a 2.7 cm inner diameter, which can generate very small bubbles, is placed at the bottom of the column.

The tap water, air and light particles are used as liquid, gas and solid phases in the experiment. The tap water and particles are injected into the column before the experiment starts, resulting in the floated particles at the top surface of the water because the particle

density is lower than the density of water. During the experiment, only the gas is continuously introduced into the column through the gas distributor, and there is no outflow for particles and liquid. The gas phase is injected into the column as small bubbles from the bottom of the column through the gas distributor, and bubbles leaves the column through the top of the column. The superficial gas velocity at the inlet is from 0 mm/s to 60 mm/s. With an increase in the inlet superficial gas velocity, the coalescence of small bubbles can be observed. The experiment is carried out under ambient temperature and pressure.

In this study, the hydrodynamics in the BIFB will be simulated under different inlet superficial gas velocities, which will results in different bubble sizes. Therefore, different bubble sizes will be used in the simulations under different inlet superficial gas velocities. The summary of the operating conditions and properties of each phase are shown in Table 9-1.
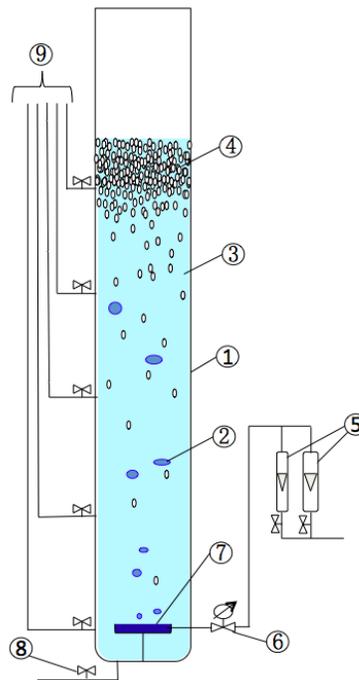
Figure 9-1: Schematic diagram of gas-driven inverse gas-liquid-solid fluidized bed. (1) column, (2) bubble, (3) liquid, (4) solid particles, (5) rotameters, (6) pressure gauge, (7) gas distributor, (8) liquid inlet/outlet valve, (9) manometer.

Table 9-1: Operating conditions and physical properties of each phase

	Bubble column size (m)	Diameter: 0.153
		Total height: 3
	U_l (mm/s)	0
	U_g (mm/s)	9-60
	U_s (mm/s)	0
	Liquid phase	water
	Liquid phase density (kg/m^3)	998
	Liquid phase viscosity (kg/m^{-s})	0.001003
Sun (2017)	Gas phase	Air
	Gas phase density (kg/m^3)	1.225
	Gas phase viscosity (kg/m^{-s})	1.7984×10^{-5}
	Solid phase	Polypropylene
	Particle diameter (mm)	3.5, 4.6
	Particle density (kg/m^3)	904, 930, 950
	Solid phase loading	5%, 10%, 15%, 20%, 25%
	Pressure	Atmospheric pressure
	Temperature	Ambient temperature

9.3   CFD model

9.3.1 Governing Equations

The CFD model developed in this study to simulate the inverse gas-liquid-solid three-phase fluidized bed is based on the three-fluid E-E approach coupled with the KTGF. Each phase is treated as interpenetrating continua. The liquid phase is selected as the primary phase because it is the continuous phase with the volume fraction of the liquid is over 70% in the BIFB. Gas and solid phases are considered as the secondary phases in the simulation. A constant gas bubble diameter of 3mm which is obtained from the experimental observation is set for the simulation. The governing equation for each phase and corresponding closure law and constitutive relations are shown as following.

Conservation equation of mass for the liquid phase

$$\frac{\partial}{\partial t}(\alpha_l \rho_l) + \nabla (\alpha_l \rho_l \overrightarrow{v_l}) = 0 \qquad (9\text{-}1)$$

Conservation equation of mass for the gas phase

$$\frac{\partial}{\partial t}(\alpha_g \rho_g) + \nabla (\alpha_g \rho_g \overrightarrow{v_g}) = 0 \qquad (9\text{-}2)$$

Conservation equation of mass for the solid phase

$$\frac{\partial}{\partial t}(\alpha_s \rho_s) + \nabla (\alpha_s \rho_s \overrightarrow{v_s}) = 0 \qquad (9\text{-}3)$$

where α, ρ, and v are the volume fraction, density and velocity of each phase. The subscripts of l, g land s represent liquid, gas and solid phase respectively. The sum of volume fraction for each phase should be equal to one.

$$\alpha_l + \alpha_g + \alpha_s = 1 \qquad (9\text{-}4)$$

Conservation equation of momentum for the liquid phase

$$\frac{\partial}{\partial t}(\alpha_l \rho_l \overrightarrow{v_l}) + \nabla (\alpha_l \rho_l \overrightarrow{v_l}\, \overrightarrow{v_l}) = -\alpha_l \nabla p + \nabla \overline{\overline{\tau_l}} + \alpha_l \rho_l \vec{g} + M_l \qquad (9\text{-}5)$$

$$\overline{\overline{\tau_l}} = \alpha_l \mu_l (\nabla \overrightarrow{v_l} + \nabla \overrightarrow{v_l}^{T}) - \alpha_l \frac{2}{3} \mu_l (\nabla \overrightarrow{v_l}) \overline{\overline{I}} \qquad (9\text{-}6)$$

Conservation equation of momentum for the gas phase

$$\frac{\partial}{\partial t}(\alpha_g \rho_g \overrightarrow{v_g}) + \nabla (\alpha_g \rho_g \overrightarrow{v_g}\, \overrightarrow{v_g}) = -\alpha_g \nabla p + \nabla \overline{\overline{\tau_g}} + \alpha_g \rho_g \vec{g} + M_g \qquad (9\text{-}7)$$

$$\overline{\overline{\tau_g}} = \alpha_g \mu_g (\nabla \overrightarrow{v_g} + \nabla \overrightarrow{v_g}^{T}) - \alpha_g \frac{2}{3} \mu_g (\nabla \overrightarrow{v_g}) \overline{\overline{I}} \qquad (9\text{-}8)$$

Conservation equation of momentum for the solid phase

$$\frac{\partial}{\partial t}(\alpha_s \rho_s \overrightarrow{v_s}) + \nabla (\alpha_s \rho_s \overrightarrow{v_s}\, \overrightarrow{v_s}) = -\alpha_s \nabla p + \nabla p_s + \nabla \overline{\overline{\tau_s}} + \alpha_s \rho_s \vec{g} + M_s \qquad (9\text{-}9)$$

9.3.2 Drag model

Only the drag force and virtual mass force will be considered in the present study since the other two forces are negligible. Regarding the drag force between the liquid and gas phases, the equation is written as the following

$$F_{drag,gl} = K_{gl}(\overrightarrow{v_g} - \overrightarrow{v_l}) \tag{9-10}$$

where K_{gl} is the momentum exchange coefficients between the liquid and gas phases, which is calculated by

$$K_{gl} = C_{D,gl} \frac{3}{4} \rho_l \frac{\alpha_g \alpha_l}{d_b} |\overrightarrow{v_g} - \overrightarrow{v_l}| \tag{9-11}$$

where d_b is the diameter of bubble or droplet, and $C_{D,gl}$ is the drag coefficient between the gas and liquid phases, and the Schiller-Naumann drag model (Schiller and Naumann 1935) is used to calculate $C_{D,gl}$, which is shown as

$$C_{D,gl} = \begin{cases} 24(1 + 0.15Re_1^{0.687})/Re_1 & Re_1 \leq 1000 \\ 0.44 & Re_1 > 1000 \end{cases} \tag{9-12}$$

$$Re_1 = \frac{\rho_l d_b |\overrightarrow{v_g} - \overrightarrow{v_l}|}{\mu_l} \tag{9-13}$$

The drag force between the liquid and solid phases can be expressed as

$$F_{drag,ls} = K_{ls}(\overrightarrow{v_s} - \overrightarrow{v_l}) \tag{9-14}$$

$$K_{ls} = C_{D,ls} \frac{3}{4} \rho_l \frac{\alpha_l \alpha_s}{d_p} |\overrightarrow{v_s} - \overrightarrow{v_l}| \tag{9-15}$$

where d_p is the diameter of the particles, and the drag model used to calculate the drag force between liquid and solid phases is also based on the Schiller-Naumann model (Schiller and Naumann 1935). The equations are listed as following

$$C_{D,ls} = \begin{cases} 24(1 + 0.15Re_2^{0.687})/Re_2 & Re_2 \leq 1000 \\ 0.44 & Re_2 > 1000 \end{cases} \tag{9-16}$$

$$Re_2 = \frac{\rho_l d_p |\overrightarrow{u_s} - \overrightarrow{u_l}|}{\mu_l} \tag{9-17}$$

The drag force between the solid and gas phases is shown as

$$F_{drag,gs} = K_{gs}(\overrightarrow{v_g} - \overrightarrow{v_s}) \tag{9-18}$$

$$K_{gs} = C_{D,gs}\frac{3}{4}\rho_g\frac{\alpha_g\alpha_s}{d_p}|\overrightarrow{v_g} - \overrightarrow{v_s}| \tag{9-19}$$

$$C_{D,gs} = \begin{cases} 24(1 + 0.15Re_3{}^{0.687})/Re_3 & Re_3 \leq 1000 \\ 0.44 & Re_3 > 1000 \end{cases} \tag{9-20}$$

$$Re_3 = \frac{\rho_g d_p |\overrightarrow{v_s} - \overrightarrow{v_g}|}{\mu_g} \tag{9-21}$$

9.3.3 Turbulence model

In this work, the dispersed RNG k-ε turbulence model is used for the liquid phase, since it performs better than the standard and realizable k-ε models and per-phase RNG k-ε model (Hamidipour, Chen and Larachi 2012).

$$\frac{\partial}{\partial t}(\alpha_l\rho_l k_l) + \nabla(\alpha_l\rho_l k_l\overrightarrow{v_l}) = \nabla\left(\alpha_l\left(\frac{\theta_k\mu+\mu_t}{\sigma_k}\right)\nabla k\right) + \alpha_l G_{k,q} - \alpha_l\rho_l\varepsilon_l + \Pi_k \tag{9-22}$$

$$\frac{\partial}{\partial t}(\alpha_l\rho_l\varepsilon_l) + \nabla(\alpha_l\rho_l\varepsilon_l\overrightarrow{v_l}) = \nabla\left(\alpha_l\left(\frac{\theta_{1,\varepsilon}\mu+\mu_t}{\sigma_\varepsilon}\right)\nabla\varepsilon\right) + \alpha_l\frac{\varepsilon_l}{k_l}(C_{1\varepsilon}\theta_{2,\varepsilon}G_{k,q} - C_{2\varepsilon}\theta_{3,\varepsilon}\rho_l\varepsilon_l) +$$

$$C_{3,\varepsilon}\alpha_l\rho_l\Pi_k - \alpha_l R_\varepsilon \tag{9-23}$$

where $\mu_t = \rho C_\mu\frac{k^2}{\varepsilon}$, k is the turbulence kinetic energy, ε is the turbulence kinetic energy dissipation, and Π_k is the source term to account for the turbulence interaction between phases which is neglected in the dispersed model, and G_k is the turbulence kinetic energy generated by mean velocity gradient is given as

$$G_k = \mu_t S^2 \tag{9-24}$$

$$S = \sqrt{2S_{ij}S_{ij}} \tag{9-25}$$

$$S = \frac{1}{2}(\nabla\vec{v} + (\nabla\vec{v})^T) \tag{9-26}$$

The RNG k-ε model has a better performance on predicting rapid strained flows and swirling flow, and the RNG k-ε model can simulate the flow in a low-Reynolds region accurately by using an analytical formula to calculate the effective viscosity (ANSYS,2014). The parameters of the standard k-ε turbulence model will be modified as following when it is used as a dispersed RNG k-ε turbulence model

θ_k is set to one and σ_k is calculated based on σ_{eff} which is the effective Schmidt number, and it is shown by equation

$$\left|\frac{\left(\frac{1}{\sigma_{eff}}\right)-1.3929}{\left(\frac{1}{\sigma_0}\right)-1.3929}\right|^{0.6312} \left|\frac{\left(\frac{1}{\sigma_{eff}}\right)+2.3929}{\left(\frac{1}{\sigma_0}\right)+2.3929}\right|^{0.3679} = \frac{\mu}{\mu+\mu_t} \tag{9-27}$$

where $\frac{1}{\sigma_0} \approx 1$ and $\theta_k = 1$

Then $\theta_{1,\varepsilon}$ is also set to one and σ_ε is defined based on σ_{eff} as well which can be also calculated by Eq (9-27). R_ε is the addiction model parameter calculated by

$$R_\varepsilon = \frac{\rho C_\mu \eta^3 (\frac{1-\eta}{\eta_0})}{1+\beta\eta^3}\frac{\varepsilon^2}{k} \tag{9-28}$$

where η is the dimensionless strain rate coefficient, which is calculated by

$$\eta = \frac{Sk}{\varepsilon} \tag{9-29}$$

So the equations for the RNG k-ε turbulence model can be write as following

$$\frac{\partial}{\partial t}(\rho_l k) + \nabla(\rho_l k_l \vec{v_l}) = \nabla\left(\alpha_k \mu_{eff}\nabla k\right) + G_k + G_b - \rho\varepsilon - Y_M + S_k \tag{9-30}$$

$$\frac{\partial}{\partial t}(\rho_l\varepsilon) + \nabla(\rho_l\varepsilon_l\vec{v_l}) = \nabla\left(\alpha_\varepsilon\mu_{eff}\nabla\varepsilon\right) + C_{1\varepsilon}\frac{\varepsilon}{k}(G_k + C_{3\varepsilon}G_b) - \rho C_{2\varepsilon}\frac{\varepsilon^2}{k} - R_\varepsilon + S_\varepsilon \tag{9-31}$$

The relevant parameters of the dispersed RNG k-ε model is listed in Table 9-2.

Table 9-2: Parameters of the RNG k-ε models

Parameters	θ_k	$\theta_{1,\varepsilon}$	σ_ε	σ_k	$C_{1\varepsilon}$	$C_{2\varepsilon}$
Values	1	1	Eq. (9-27)	Eq. (9-27)	1.42	1.68
Parameters	C_μ	R_ε	$\theta_{3,\varepsilon}$	$\theta_{2,\varepsilon}$	$C_{3,\varepsilon}$	Π_k
Values	0.085	Eq. (9-28)	1	1	0	0

9.3.4 Kinetic theory of granular flow for the solid phase

To describe the solid phase motion, the KTGF is used in the E-E approach in order to close the solid phase governing equations. The granular temperature is introduced in the KTGF, which is related to the particle random motion, and solid phase stress and pressure can be calculated by using the granular temperature (Gidaspow & Ding, 1990). The constitutive equations related to the KTGF are shown as following:

Table 9-3 Constitutive equations of the solid phases

Solid pressure (Lun et al. 1984)	$P_S = \alpha_S \rho_S \Theta_S + 2\rho_S(1 + e_{ss})\alpha_s^2 g_{0,ss}\Theta_S$	(9-32)
Radial distribution function (Gidaspow & Ding 1990)	$g_{0,ss} = \left[1 - \left(\dfrac{\alpha_s}{\alpha_{s,max}}\right)^{1/3}\right]^{-1}$	(9-33)
Solid shear stress	$\mu_s = \mu_{s,col} + \mu_{s,kin} + \mu_{s,fr}$	(9-34)
Collisional viscosity (Gidaspow 1994)	$\mu_{s,col} = \dfrac{4}{5}\alpha_s \rho_s d_s g_{0,ss}(1 + e_{ss})\sqrt{\dfrac{\Theta_s}{\pi}}$	(9-35)
Kinetic viscosity (Syamlal, et al., 1993)	$\mu_{s,kin} = \dfrac{\alpha_s \rho_s d_s \sqrt{\Theta_s \pi}}{6(3+e_{ss})}\left[1 + \dfrac{2}{5}(1 + e_{ss})(3e_{ss} - 1)\alpha_s g_{0,ss}\right]$	(9-36)
Frictional viscosity (Schaeffer 1987)	$\mu_{s,fr} = \dfrac{P_s \sin\phi}{2\sqrt{I_{2D}}}$	(9-37)
Bulk viscosity (Lun et al. 1984)	$\lambda_s = \dfrac{4}{3}\alpha_s^2 \rho_s d_s g_{0,ss}(1 + e_{ss})\sqrt{\dfrac{\Theta_s}{\pi}}$	(9-38)
Granular conductivity (Syamlal, et al.,1993)	$k_{\Theta_s} = \dfrac{15 d_s \rho_s \alpha_s \sqrt{\Theta_s \pi}}{4(41 - 33\eta)}\left[1 + \dfrac{12}{5}\eta^2(4\eta - 3)\alpha_s g_{0,ss} + \dfrac{16}{15\pi}(41 - 33\eta)\alpha_s g_{0,ss}\eta\right]$	(9-39)
Collisional dissipation of energy (Lun et al. 1984)	$\gamma_{\Theta_s} = \dfrac{12(1 - e_{ss}^2 g_{0,ss})}{d_s \sqrt{\pi}}\rho_s \alpha_s^2 \Theta_s^{3/2}$	(9-40)

9.3.5 Mesh set up and boundary conditions

The gas inlet is located at the bottom of the column, and the uniform velocity is used as the inlet boundary condition for the gas phase based on the inlet superficial gas velocity used in the experiment. For the liquid and solid phases, the inlet velocity is zero for a batch liquid mode operation. The outflow is selected as outlet boundary condition for all three phases on the top of the column. The no-slip boundary condition is set for the liquid phase as wall the boundary condition, and the free-slip condition on the wall is used for both the gas phase and solid phase, so the specularity coefficient of solid phase is set to zero which corresponds to the free-slip boundary condition. The particle-particle restitution coefficient is set as 0.95.

The particles have a mean diameter of 3.5 mm. A total of 9 CFD cases as listed in Table 9-4 are used to study the effects of the superficial gas velocity, particle density, and the solids loading on the flow development.

Table 9-4: CFD cases under different operating conditions

Case #	U_g, mm/s	Particle density, kg/m^3	Solids loading, %
1	9	930	15
2	12.5	930	15
3	15	930	15
4	20	930	15
5	40	930	15
6	15	930	5
7	15	930	20
8	15	904	15
9	15	950	15

The initial conditions of the BIFB under the batch liquid operating condition are shown in Figure 9-2, which are different from the conventional or circulating fluidized beds. To mimic the experimental condition, the liquid is initially patched inside the column, and particles are patched at the top surface of the liquid because the density of the particles is less than the density of the liquid phase.

The simulation is conducted using the commercial software Fluent 16.0. The double precision segregated, transient, implicit formulation are used. The phase coupled SIMPLE algorithm is used for the pressure-velocity coupling. The second order upwind scheme is

used to discretize the momentum equations while the first order upwind discretization method is used for all other convection terms. The convergence criterion is set as 5×10^{-4} and the time step size is set as 0.0001 s.
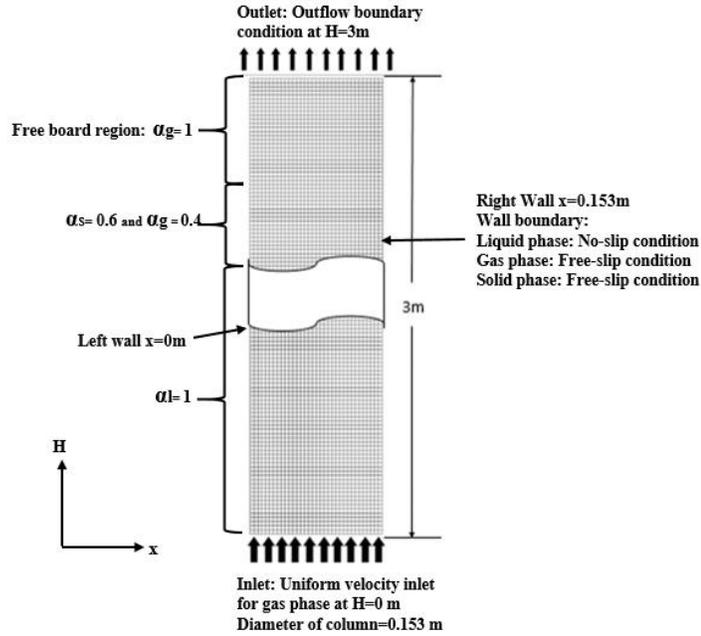
Figure 9-2: Computational domain of the inverse three-phase fluidized bed under the batch liquid mode

9.3.6 Grid independent test

The grid independent study is performed under U_g=20 mm/s. The information on three different meshes is listed in Table 9-5, and the average gas holdup is used to check the grid independence. The results from the three meshes are listed in Table 9-6. The difference of average gas holdup between the medium mesh and fine mesh is less than 1%. Therefore, the medium size mesh is selected in this study for further simulations since it can give grid independent results.

Table 9-5: Mesh information of the computational domain

	Size	Coarse	Medium	Fine
Mesh info	Face	44815	73906	286680
	Node	22750	37400	144000
	Cell	22066	36507	142681

Table 9-6 Average gas holdups from different meshes

Mesh	Average gas holdup	Difference% of gas holdup
Coarse mesh	0.0856	
Medium mesh	0.0819	4.5%
Fine mesh	0.0816	0.4%

9.4 Results and discussion

9.4.1 Experimental observations of the flow regimes

Three flow regimes are observed in the BIFB during the experiment when increasing the gas flowrate as illustrated in Figure 9-3. Initially, light particles are packed as a fixed bed on the top of the column when there is no gas flow or only a few gas bubbles are introduced into the BIFB. With more bubbles rise up from the bottom gas distributor and reach the bottom of the packed particles, the lowest layer of the pecked particles in the fixed bed began to fluidize and a bed expansion regime is characterized in the BIFB. An initial fluidization velocity (U_{g1}) marking the onset of the bed expansion regime in the BIFB is defined as the minimum superficial gas velocity required to break the fixed bed, while the particles in the lower position begin to fluidize.

By gradually increasing the superficial gas velocity in the bed expansion regime, the packed particles are fluidized layer by layer with more particles moving downward to the bottom of the BIFB when more gas bubbles reach the top of the column. In the bed expansion regime, the solids distribution is not uniform in the BIFB with more particles concentrated at the upper zone of the BIFB and less particles at the lower region of the BIFB. A full expansion velocity (U_{g2}) is defined when a few particles first reached the bottom of the column while the distribution of solids concentration is still not uniform in the BIFB. Beyond U_{g2}, the BIFB goes into the complete fluidization regime where the particles gradually become uniformly distributed along the BIFB when increasing U_g.

A complete fluidization velocity (U_{g3}) is defined to mark the stable stage when all the particles are maintained a uniform distribution in the BIFB. Further increasing U_g to a very high value, particles tend to accumulate at the lower part of the BIFB resulting in a freeboard with a gas-liquid two-phase only region occurs at the top of the BIFB. A freeboard velocity (U_{g4}) is defined once the freeboard with a gas-liquid two-phase only

region appears, which marks the transition of the BIFB from the complete fluidization regime to a freeboard regime.
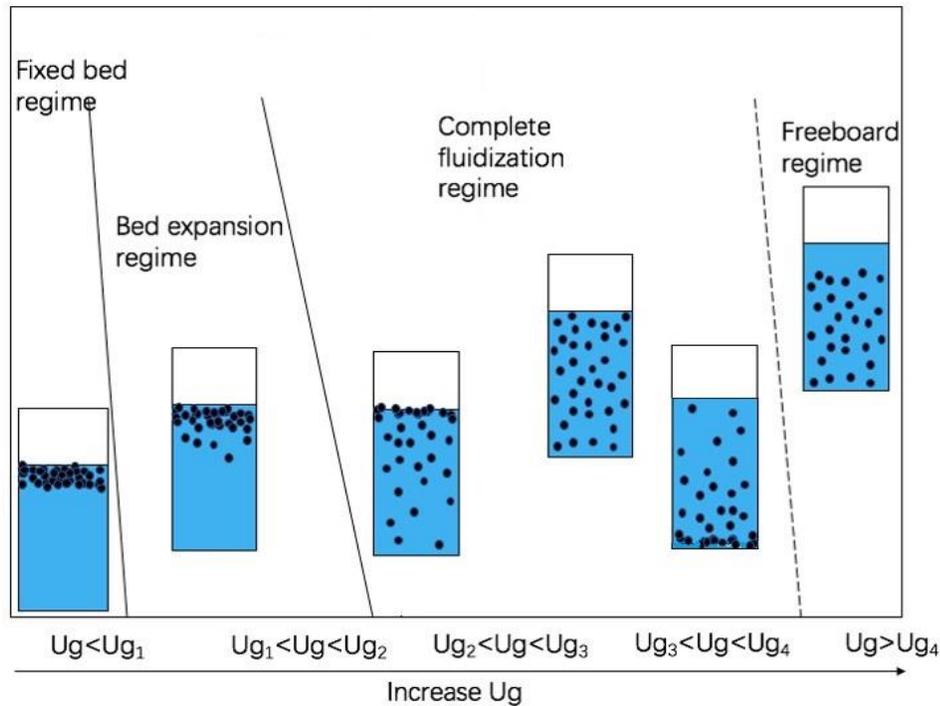
Figure 9-3: Flow regime map in the bubble-induced inverse fluidized bed

Contours of the solids holdup in the BIFB under a wide range of the superficial gas velocity from 5 mm/s to 40 mm/s are plotted in Figure 9-4. Those contours are the average values after the simulations reach the steady (t=160 s to 200 s). Different flow regimes can be clearly seen in Figure 9-4.

For a BIFB with 15% solids loading and the particle density of 930 kg/m^3, the superficial velocity is found to have a significant effect on solids axial distribution. At $U_g \leq 9$ mm/s, the BIFB is in the fixed regime where the particles remain packed as shown in Figure 9-4 because the sum of the gravity and drag force acting on the particles is too small to overcome the buoyance force. The operating window of the bed expansion regime is quite narrow with the initial fluidization velocity (U_{g1}) around 10mm/s and full expansion velocity (U_{g2}) around 12.5mm/s based on the simulation results. Particles are partially

fluidized in the bed expansion regime of the BIFB when increasing U_g to 12.5 mm/s and most particles are still in the packed bed state.

The complete fluidization velocity (U_{g3}) is around 15 mm/s, thus, a uniform distribution of the solid phase can be seen at this U_g as shown in Figure 9-4. By further increasing U_g beyond 20 mm/s, the axial solids distribution becomes less uniform where the solid phase is dense at the lower section and dilute at the upper section of the column as shown in Figure 9-4 although all the particles are still fluidized in the entire column. The stable operating window to maintain a uniform flow structure within the complete fluidization regime of the BIFB ranges from U_g =15-20 mm/s as shown in Figure 9-4, which is narrower than the experimental observation because the actual turbulences induced by the gas bubbles are underestimated in the simulation. When U_g increases to 40mm/s, a distinct freeboard region can be found from the contours of the solids holdup as shown in Figure 9-4. The non-uniformity of the particle distribution becomes worse in the freeboard regime where more particles are accumulated at the bottom of the column when U_g= 40 mm/s.
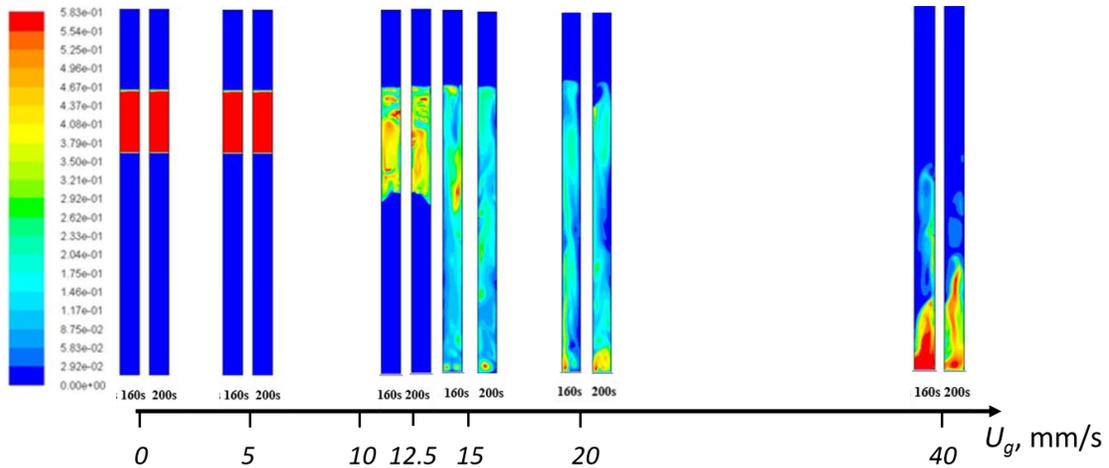
Figure 9-4 CFD contours of the solid phase volume fraction under different U_g with 15% solids loading and ρ_s=930 kg/m³

9.4.2 Regime transitions under different solids loadings
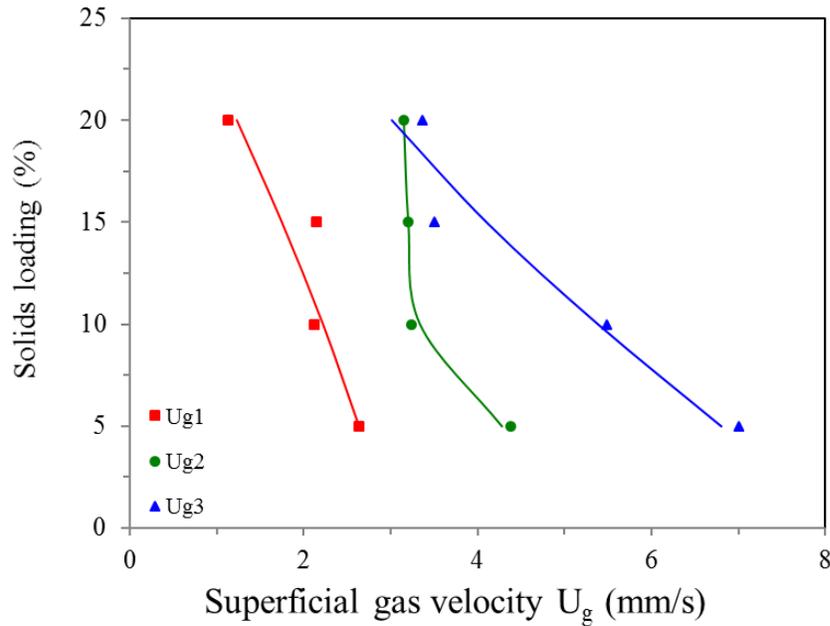
Figure 9-5: Experimental results of the variation of the transition superficial gas velocities with the solids loadings

The transition superficial gas velocities, U_{g1}, U_{g2} and U_{g3}, vary with the particle loading as shown in Figure 9-5. All the three transition gas velocities (U_{g1}, U_{g2} and U_{g3}) decrease with the increase of the solids loading. The reason is that when more particles are immersed into the water, a greater downward force due to the weight of the particles is exerted on the particles at the lower position when the loading is larger. Therefore, less amount of gas is required to reduce the upward buoyance to achieve a force balance on the particles, so U_g is smaller. A larger solids loading also results in a faster transition for the three-phase flow to the complete fluidization regime as shown in Figure 9-5.
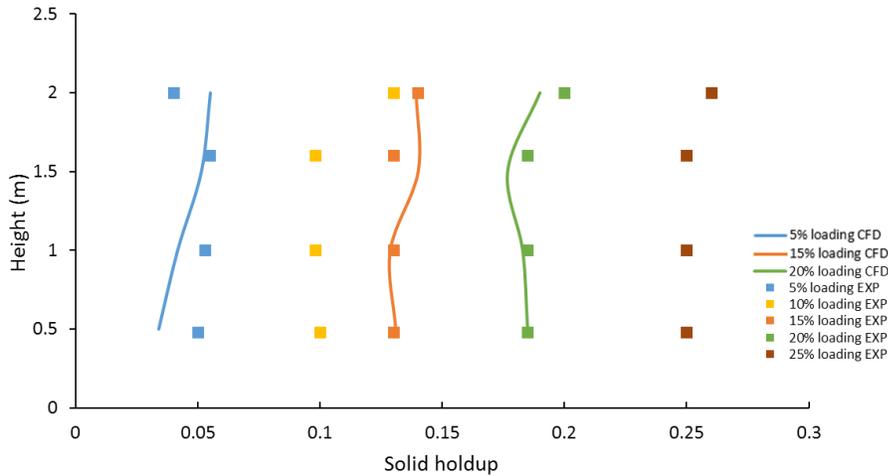
Figure 9-6: Comparison of the axial solids holdup profiles under different solids loadings in the complete fluidization regime between the CFD results and experimental data

Numerical and experimental results of the axial solids holdup profiles under different solids loadings in the complete fluidization regime are plotted in Figure 9-6. A good agreement between the CFD results and the experimental data is achieved. Generally, the solids particles are uniformly distributed along the BIFB in the complete flow regime. The overall solids holdup in the BIFB increases with the increase in the solids loading, which is expected since all the particles are dispersed in the BIFB in the complete flow regime.

9.4.3 Regime transitions under different particle properties

The effects of the types of the particles on the flow regime transitions are experimentally studied as shown in Figure 9-7. Particles with a density of 930 kg/m^3 has the lowest transition superficial gas velocities, which indicates this type of the particles are the easiest to be fluidized in the BIFB. The underlying reasons still need to be investigated with more experimental work in the future.
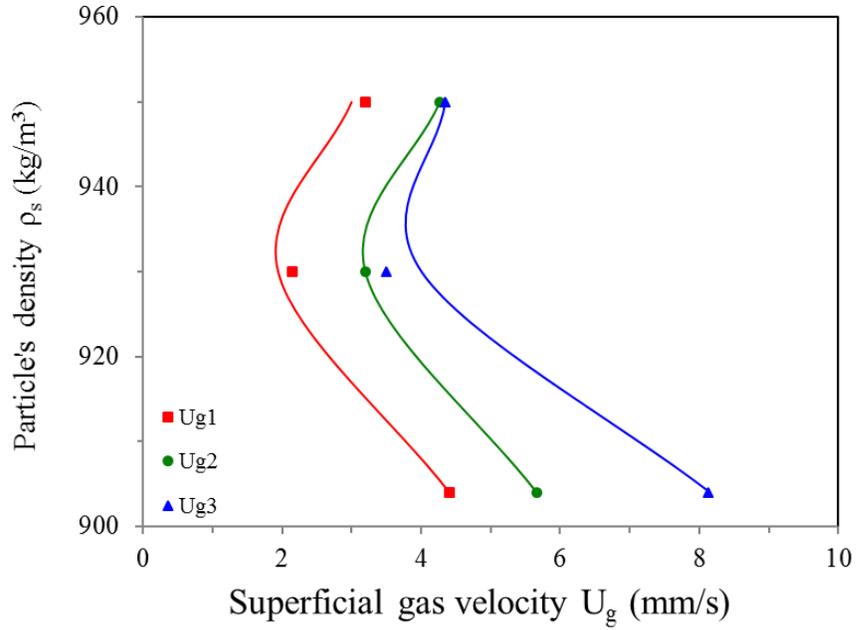
Figure 9-7: Experimental results of the variation of the transition superficial gas velocities with particle densities at solids loading=15%

(a) 904 kg/m³   (b)   930 kg/m³   (c)   950 kg/m³
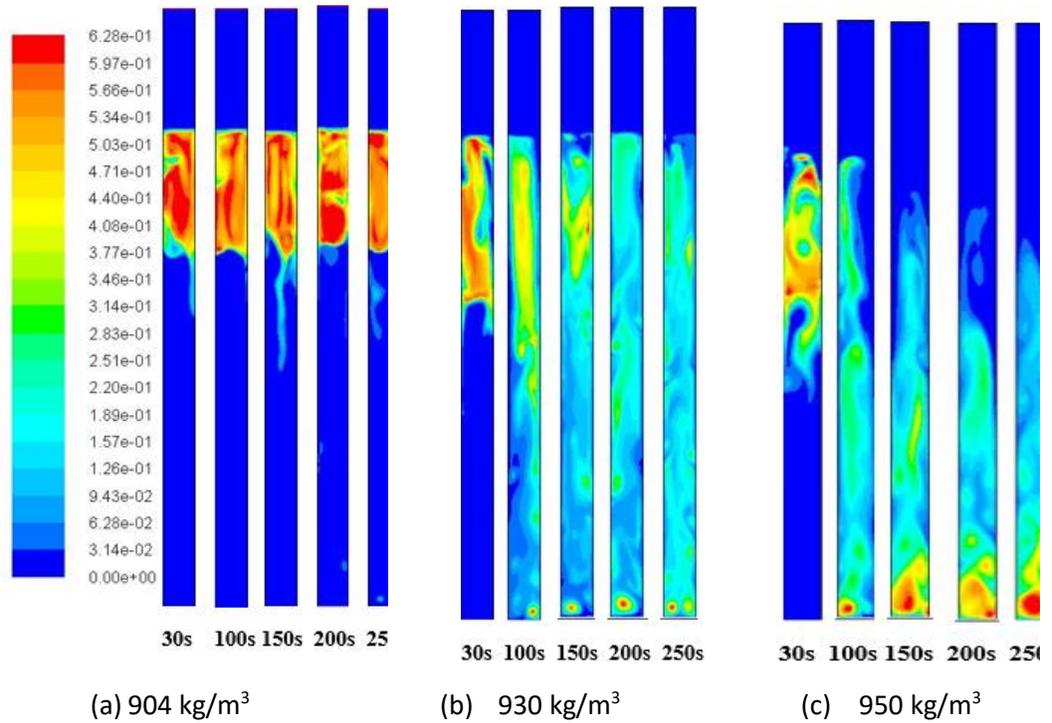
Figure 9-8: CFD contours of the solid phase volume fractions for different particle densities at U_g =15 mm/s and 15% solids loading

Figure 9-8 shows the contours of the solid phase volume fraction from t=30 s to 250 s with different particle densities under U_g =15 mm/s and 15% solids loading. It is noted that particles with a mean density of 904 kg/m^3 are only partially fluidized, and most particles still remain packed as shown in Figure 9-8 (a). The particles with a mean density of 930 kg/m^3 are uniformly distributed along the column shown in the Figure 9-8 (b). The contours of the volume fraction of particles with a mean density of 950 kg/m^3 (Figure 9-8 (c)) indicate that the concentration of the solid phase is dense at the lower section and dilute at the upper part of the column. Thus, the particles with a higher density are easier to be fluidized in the BIFB.

9.4.4 Local flow structures under complete fluidization regime

9.4.4.1 Flow development in the BIFB

The complete fluidization regime in the BIFB is of critical importance in the applications of the BIFB especially in the wastewater treatment because the distribution of the particles along the entire column provides a good contact between the biomass and the liquid. While during the operation, the flow developments in the complete fluidization regime also attracts increasing interest in the industrial uses because a quick development to the uniform flow condition in the BIFB saves the cost and energy. Instantaneous contours of the solids phase volume fraction at different time are extracted from the CFD results as shown in Figure 9-9. The simulation was carried out for a total of 300 s. Particles are firstly fluidized layer by layer when gas bubbles reach the packed particles at the top of the BIFB, which can be considered as the developing stage and agrees with the experimental observations. The developing stage takes about 60 s for the particles to break the packed bed state and reach the bottom of the BIFB time at U_g =15mm/s with 15% solids loading as shown in Figure 9-9. All the particles are fully fluidized at about 80 s with a higher solids concentration around 0.40 in the upper zone and a much diluter suspension with a solids concentration less than 0.15 in the lower zone of the BIFB. At the time of 200 s, a uniform distribution of the particles along the entire BIFB is formed as shown in Figure 9-9. After 200 s, the three-phase flow in the BIFB can be considered as fully developed which can maintain a uniform flow structure under a constant gas flow rate.
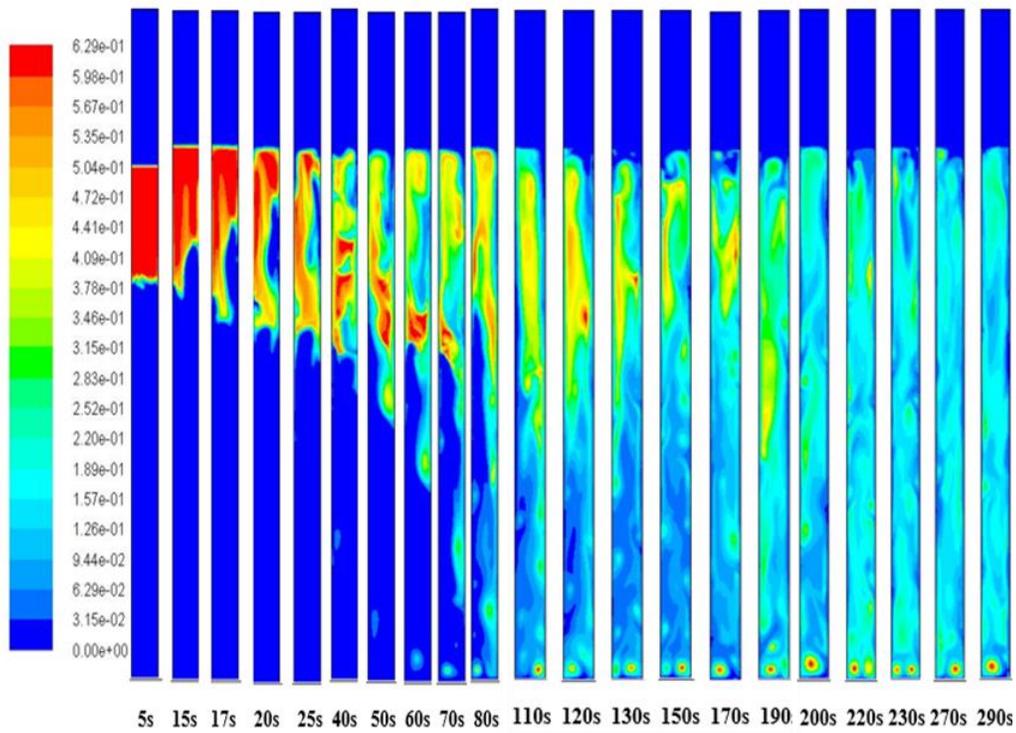
Figure 9-9: CFD contours of the solid phase volume fraction VS. time at U_g =15mm/s, 15% solids loading, and ρ_s=930 kg/m^3
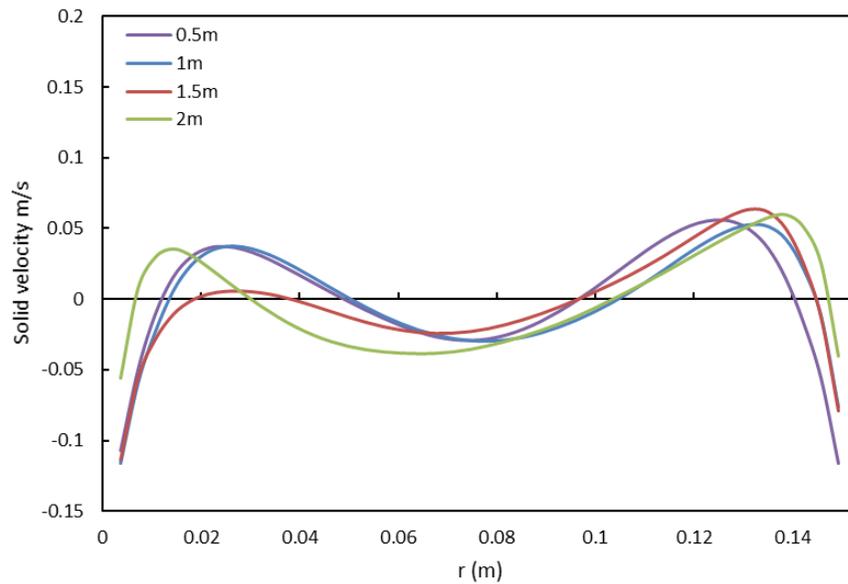
Figure 9-10 Time averaged (t>200 s) radial velocity profile of the solid phase at different heights at U_g =15mm/s, 15% solids loading, and ρ_s=930 kg/m^3
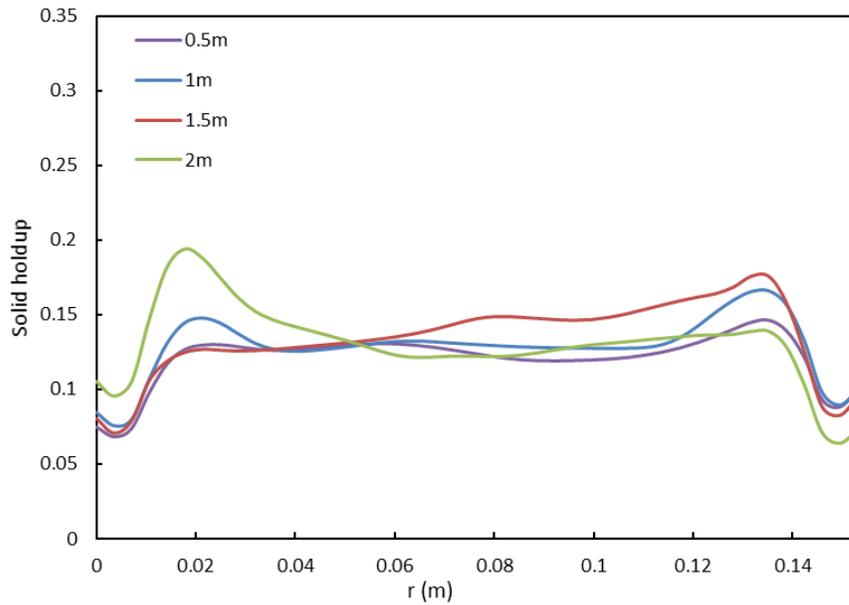
Figure 9-11 Time averaged radial profile of the solid volume fraction at different heights at U_g =15mm/s, 15% solids loading, and ρ_s=930 kg/m³

The radial profiles of the particle velocity, solids holdup at different heights along the BIFB after the three-phase flow is fully developed are plotted in Figure 9-10 and Figure 9-11 respectively. In the axial direction, both the particle velocity and the solids holdup profiles are similar at different heights in the BIFB, which indicates a uniform flow structure along axial direction in the BIFB. In the radial direction, the flow is less uniform due to the wall effects, therefore, the velocity magnitude is higher at the near wall region and lower at center region, while the solid holdup is dense at center and dilute at the near wall region. From the radial velocity profile shown in Figure 9-10 and the solid holdup profile shown in Figure 9-11, it can be seen when particles move downward with a large velocity, the concentration of the solid phase is low. By contrast, when particles with large velocity move in the upward direction, the corresponding concentration of the solid phase is high. These radial non-uniform velocity and holdup profiles are different with the profiles in traditional inverse liquid-solid circulating fluidized bed where a high solid velocity leaded to a low solid concentration. The reason lies in that the existence of particle inner circulation.
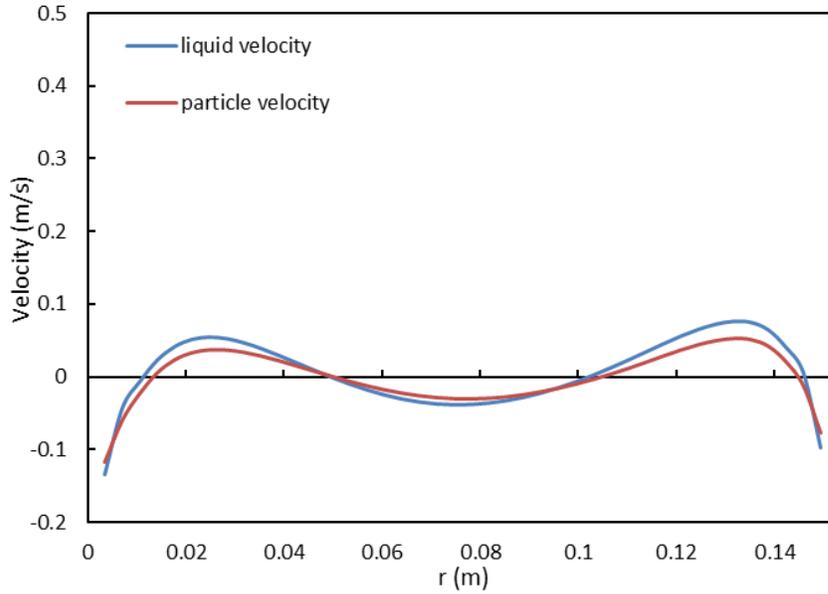
Figure 9-12 Time-averaged radial velocity profile of the solid phase and liquid phase at H=1 m, U_g =15 mm/s, 15% solids loading, and ρ_s=930 kg/m³

The comparison between liquid velocity and solid velocity at same height (H=1 m) is shown in Figure 9-12. It is found that the velocity of the liquid phase and solid phase are almost identical. Therefore, particles are considered to move with liquid circulation once the three-phase flow in the BIFB is fully developed.

The investigation on the effect of the solids loading on the flow development and hydrodynamics in the BIFB is carried out under U_g =15 mm/s and ρ_s=930 kg/m³. Figure 9-13 shows the time required for the three-phase flow under development and to reach the fully developed state under different solids loadings. It is found that a larger solids loading takes a longer time for the development of the three-phase flow. The possible reason lies in that with higher inventory of particles, it will take longer time to fluidize all particles. In addition, a high solids loading also hindered the liquid flow, which results in a higher fraction loss.
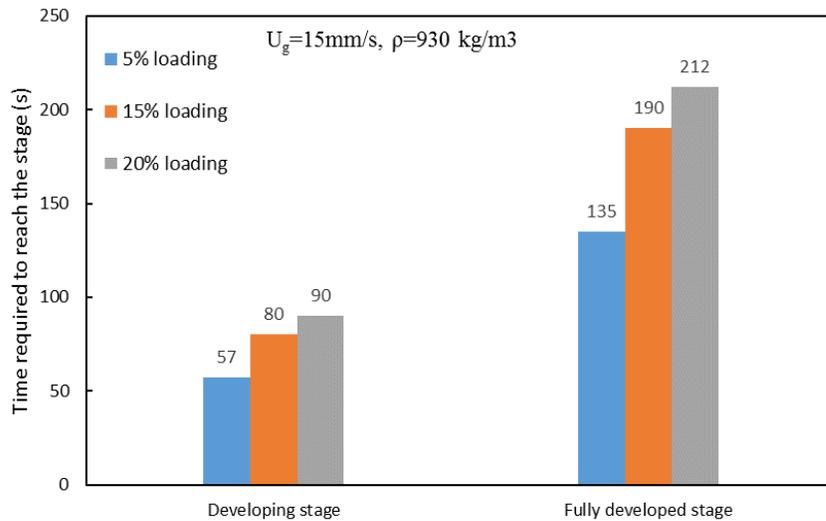
Figure 9-13: Effects of the solids loading on the flow development time

9.4.4.2 Internal circulation

In an inverse three phase fluidized bed under batch liquid model (U_l=0), the gas phase is injected from bottom into the reactor as bubbles, and the bubbles flow upward. The rising gas bubbles induced turbulence, which are considered to cause inner circulation of liquid and solid phase. Thus, internal circulation of liquid and solid phase is an important characteristic of the flow pattern that can influence the heat and mass transfer. The vortex and particle circulation is also observed in the experiment by Sun (2017). Therefore, the investigation of the internal circulation of particles through CFD modeling is carried out. The simulation is conducted with 15% solid loading and 930 kg/m^3 particle density at different superficial velocities.

Figure 9-14 is the time averaged radial profile of solids velocity at the fully developed stage. The radial non-uniform distribution of the solids velocity can be seen under all superficial gas velocities. At U_g=15 mm/s, particles are found to descent at the near wall region and the core region of column, but the particle rising phenomenon can be found at the region between wall and center of column. Particles flow upward at core region and flow downward at the near wall region at U_g=20 mm/s, and particles under U_g=40 mm/s also move in both upward and downward direction. The internal circulation of particles

244

can be observed under all superficial gas velocities through the radial profiles of the solids velocity. Besides, the case at U_g=40 mm/s has the most non-uniformity in the solid velocity in the radial direction. Thus, when increasing the superficial gas velocity, the radial non-uniformity of the solid velocity increases. The maximum solid velocity magnitude is observed under U_g= 40 mm/s at H=1.5 m because with the increase in the superficial gas velocity, the liquid and solid phases get more momentum from the gas phase. The radial profile of the solid velocity under different solids loadings as shown in Figure 9-14 also shows that the internal circulation of particles exists under different solid loadings.
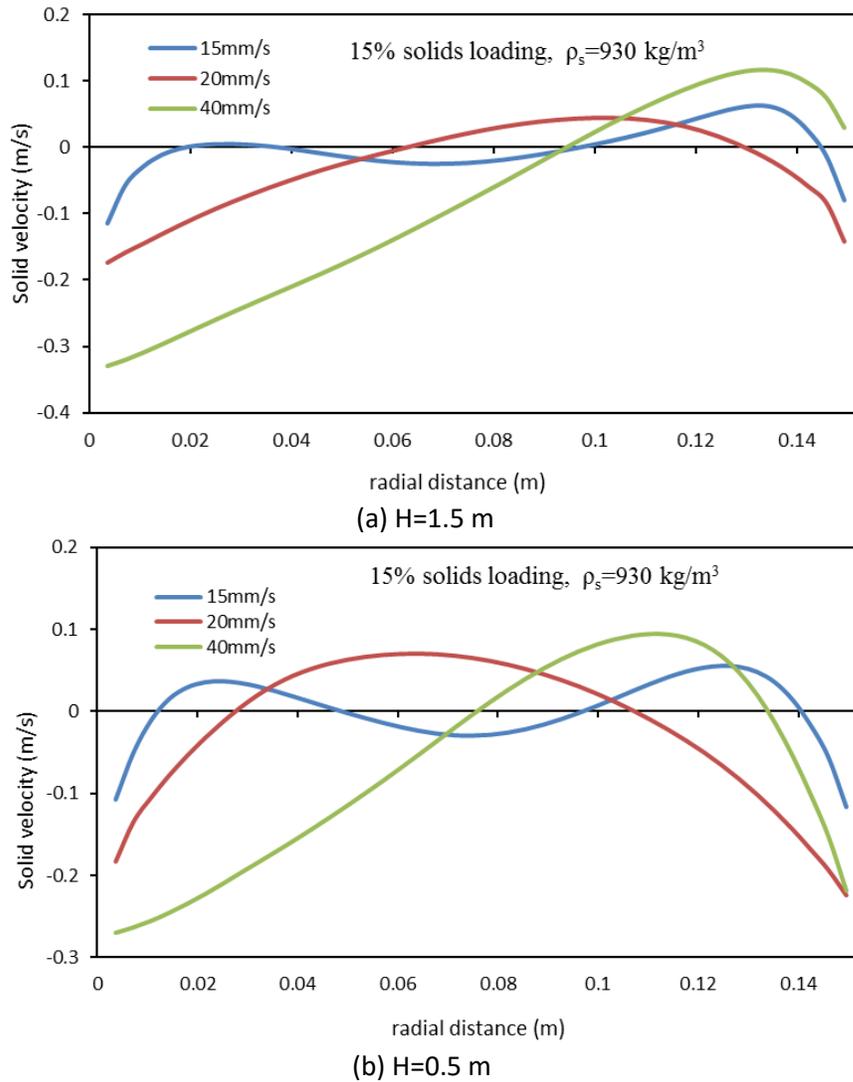
(a) H=1.5 m

(b) H=0.5 m

Figure 9-14 Radial velocity profiles of the solid phase under different U_g (a) H=1.5m; (b) H=0.5m

To further investigate the internal circulation in an inverse three phase fluidized bed, the flow details at different times of the flow development, which is under the condition of U_g=15 mm/s, 15% solid loading and 930 kg/m^3 particle density, are also studied. Figure 9-15 (a) is the veolcity vector of the solid phase at t = 17 s, where only a few particles are fluidized in the BIFB. An inner circulation of particles can be observed at the bottom part of the packed bed, which descend at the near wall region and rise at the center of the column, and the particle velocity at the bottom part of the packed bed is higher than that at the middle part of the packed bed. It implies that particles at the near wall region are fluidized first in the inverse three phase fluidized bed. The instanenous velocity vectors of the solid phase at t = 60s, where all the particles are fluidized with a non-uniform distribution in the BIFB, is shown in Figure 9-15 (b). A large circulation of particels can be seen at the middle and upper part of the reactor. Besides, more vortex is found at the lower section of the column closed to the gas distributor, so the flow of particles is more disordered and the cirulation is more intense at the region close to gas inlet. Figure 9-15 (c) is the instantons velocity vector of the solid phase which revealed to flow details at the fully developed stage at t = 270 s in the inverse three phase fluidized bed. It can be seen clearly that the large inner circulations of particles in the column. Therefore, it can conclude that internal circulations of particles exist at all three stages of the flow development process.

(a)

H=2.1 m

H=0.3 m
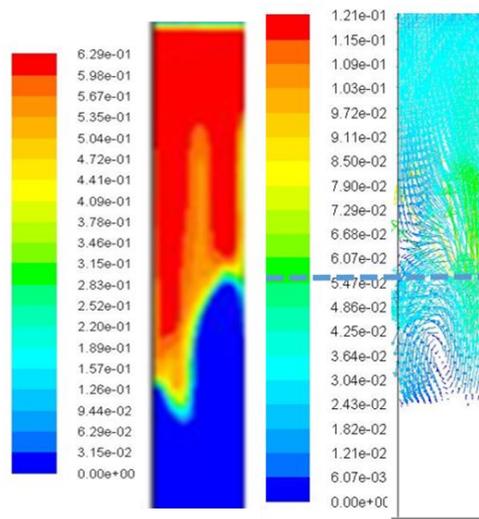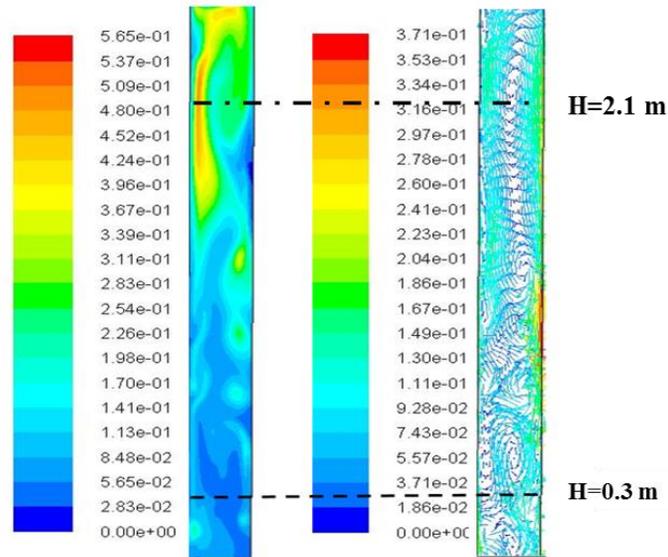
(b)
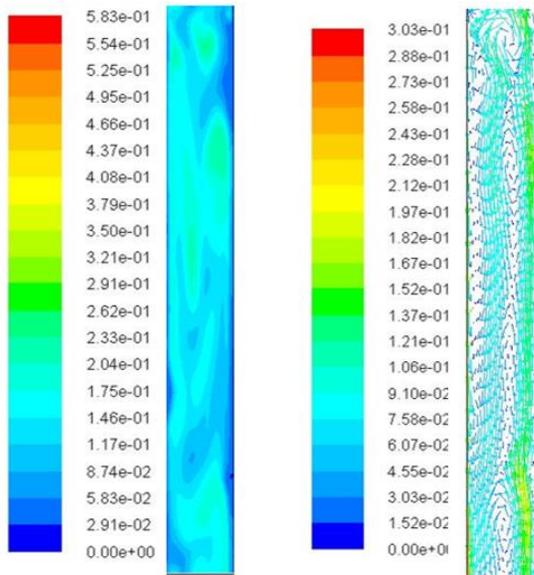
(c)

Solid volume fraction   Solid velocity vector

Figure 9-15 Instantaneous volume fraction contour (left) and particle velocity vector contour (right) at (a) t=17 s (b) t = 60 s (c) t = 270 s

9.5 Conclusions

The bubble induced inverse fluidized bed is experimentally studied in this work. Three flow regimes from the bed expansion regime, the complete fluidization regime, to the

freeboard regime due to the increase in the superficial gas velocity are defined in the BIFB. Four transition gas velocities: the initial fluidization gas velocity (U_{g1}) when the packed bed of particles first breakups, the full expansion gas velocity (U_{g2}) when a few particles first reach the bottom of the BIFB, the complete fluidization gas velocity (U_{g3}) when all the particles are uniformly distributed, and the freeboard fluidization velocity (U_{g4}) when a gas-liquid only two-phase region occurs at the top of the BIFB, are also defined to mark the characteristics in each flow regime of the BIFB based on the observations from the experiments.

A three-phase Eulerian-Eulerian CFD model is developed to simulate the hydrodynamics in the BIFB. Numerical results show a good agreement with the experimental data. Both the experimental and numerical results show that a larger solids loading leads to an easier fluidization operation and a faster flow development to the complete fluidization regime. Local flow structures in the BIFB are studied by the CFD modelling and the numerical results show that the radial flow structure is less uniform compared with the axial flow structure in the BIFB and inner circulation of the liquid exists after introducing bubbles into the BIFB.

Nomenclature

$C_{1\varepsilon}$	Turbulence constants, dimensionless
$C_{2\varepsilon}$	Turbulence constants, dimensionless
$C_{3\varepsilon}$	Turbulence constants, dimensionless
C_D	Drag coefficient, dimensionless
G_b	Generation of turbulence kinetic energy due to buoyancy, m^2/s^2
G_k	Generation of turbulence kinetic energy due to the mean velocity gradients, m^2/s^2
d_p	Mean particles diameter, m
k_{Θ_s}	Granular conductivity, kg/m^3s
α_g	Gas phase volume fraction

α_l	Liquid phase volume fraction
α_s	Solid phase volume fraction
ε_g	Gas holdup, dimensionless
ρ_g	Gas density, kg/m^3
ρ_l	Liquid density, kg/m^3
ρ_s	Particle density, kg/m^3
D	Column diameter, m
h	Height from the gas distributor, m
H	Column height from bottom to top, m
U_g	Superficial gas velocity, mm/s
U_{g1}	Initial fluidization velocity, mm/s
U_{g2}	Full expansion velocity, mm/s
U_{g3}	Complete fluidization velocity, mm/s
U_{g4}	Freeboard velocity, mm/s
U_l	Superficial liquid velocity, mm/s
U_s	Superficial solids velocity, mm/s
Θ	Granular temperature, m^2/s^2
e	Restitution coefficient for particle-particle collision, dimensionless
γ	Collision dissipation rate of energy, kg/ms^3
ε	Turbulent energy dissipation rate, m^2/s^2
λ	Bulk viscosity, kg m/s
μ	Dynamic viscosity, kg/m-s
ρ	Density kg/m^3
τ	Stress sensor, Pa

Subscripts

g	Gas phase
l	Liquid phase
s	Solid phase

References

Ansys. Inc. 2014. "Fluent 16.0 User's Guide."

Buffière, Pierre and Moletta. 1999. "Some Hydrodynamic Characteristics of Inverse Three Phase Fluidized-Bed Reactors." Chemical Engineering Science 54 (9): 1233–42.

Cho, Park, Kim, Kang and Kim. 2002. "Heat Transfer and Hydrodynamics in Two- and Three-Phase Inverse Fluidized Beds." Industrial and Engineering Chemistry Research 41 (8): 2058–63.

Comte, Bastoul, Hebrard, Roustan and Lazarova. 1997. "Hydrodynamics of a Three-Phase Fluidized Bed - The Inverse Turbulent Bed." Chemical Engineering Science 52 (21–22): 3971–77

Ding and Gidaspow. 1990. "A Bubbling Fluidization Model Using Kinetic Theory of Granular Flow." AIChE Journal 36 (4): 523–38.

Fan, Muroyama and Chern. 1982. "Hydrodynamic Characteristics of Inverse Fluidization in Liquid—solid and Gas—liquid—solid Systems." The Chemical Engineering Journal 24(2): 143–50.

Feng, Wei, Wen, Fan, Yuan, Jia and Sun. 2005. "Local Hydrodynamics of Gas–liquid-Nanoparticles Three-Phase Fluidization." Chemical Engineering Science 60 (24): 6887–98.

Gidaspow, 1994. Multiphase Flow and Fluidization: Continuu and Kinetic Theory Descriptions. Boston: Acad. Press.

Gidaspow and Ding. 1990. "A Bubbling Fluidization Model Using Kinetic Theory of Granular Flow." AIChE Journal 36(4): 523–38.

Grevskott, Sannaes, Dudukovic, Hjarbo and Svendsen. 1996. "Liquid Circulation, Bubble Size Distributions, and Solid Movement in Two- and Three-Phase Bubble Columns." Chemical Engineering Science 51 (10): 1703.

Hamidipour, Mohsen, Chen and Larachi. 2012. "CFD Study on Hydrodynamics in Three-Phase Fluidized Beds — Application of Turbulence Models and Experimental Validation." Chemical Engineering Science 78: 167–80.

Hillmer and Weismantel. 1994. "Investigations and Modelling Columns of Slurry Bubble." Science 49 (6): 837–43.

Ibrahim, Yasser, Briens, Margaritis and Bergongnou. 1996. "Hydrodynamic Characteristics of a Three-Phase Inverse Fluidized-Bed Column." AIChE Journal 42(7): 1889–1900.

Wen and Xu. 1998. "Local Hydrodynamics in a Gas-Liquid-Solid Bubble Column Reactor." Science 70 (97): 81–84.

Lee, Dong Hyun, Norman Epstein, and John R. Grace. 2000. "Hydrodynamic Transition from Fixed to Fully Fluidized Beds for Three-Phase Inverse Fluidization." Korean Journal of Chemical Engineering 17 (6): 684–90. https://doi.org/10.1007/BF02699118.

Li and Zhong. 2015. "CFD Simulation of Hydrodynamics of Gas-Liquid-Solid Three-Phase Bubble Column." Powder Technology 286: 766–88.

Li, Yong, Zhang and Fan. 1999. "Numerical Simulation of Gas–liquid–solid Fluidization Systems Using a Combined CFD-VOF-DPM Method: Bubble Wake Behavior." Chemical Engineering Science 54 (21): 5101–7.

Lun, Savage, Jeffrey and Chepurniy. 1984. "Kinetic Theories for Granular Flow: Inelastic Particles in Couette Flow and Slightly Inelastic Particles in a General Flowfield." Journal of Fluid Mechanics 140(1): 223–56.

Pan, Chen, Liang, Zhu & Luo, CFD simulations of gas-liquid-solid flow in fluidized bed reactors-A review, Powder Technol. 299 (2016) 235-258.

Renganathan, Thiruvengadam and Krishnaiah. 2008. "Prediction of Minimum Fluidization Velocity in Two and Three Phase Inverse Fluidized Beds." The Canadian Journal of Chemical Engineering 81 (3–4): 853–60.

Schaeffer and David 1987. "Instability in the Evolution Equations Describing Incompressible Granular Flow." Journal of Differential Equations 66(1): 19–50.

Schiller and Naumann. 1935. "A Drag Coefficient Correlation." Z. Ver. Deutsch. Ing 77: 318–20.

Sokół, Włodzimierz and Korpal. 2006. "Aerobic Treatment of Wastewaters in the Inverse Fluidised Bed Biofilm Reactor." Chemical Engineering Journal 118(3): 199–205.

Sun. 2017. "Bubble Induced Inverse Gas-Liquid-Solid Fluidized Bed." M.Sc. thesis, University of Western Ontario.

Syamlal, Rogers and O`Brien. 1993. MFIX Documentation Theory Guide. United States.

Werther, Hartge and Heinrich. 2014. "Fluidized-Bed Reactors-Status and Some Development Perspectives." Chem. Ing. Tech. 86(12): 2022–38.

Wu and Gidaspow. 2000. "Hydrodynamic Simulation of Methanol Synthesis in Gas Liquid Slurry Bubble Column Reactors." Chemical Engineering Science 55 (3): 573–87.

Zhang and Vanderheyden. 2002. "The Effects of Mesoscale Structures on the Disperse Two-Phase Flows and Their Closures for Dilute Suspensions." Int. J. Multiphase Flows 28(5): 805–822.

Chapter 10

10   Conclusions and recommendations

10.1 General discussion

In contrast with the conventional fluidized bed reactor that mostly contains particles in a defined space, the circulating fluidized bed operates at high velocities and entrain the particles out of the bed continuously while adding more particles at the same time. Circulating fluidized beds have some unique advantages over other types of fluidized bed, such as high throughput and reduced back-mixing for both fluid and particles, albeit still having its own limitations. Among the various CFB systems studied in this work, the gas-solid CFB system has seen the most successful applications in the chemical industry. Gas-solid CFB systems are usually designed for two types of chemical reactions: gas-solid reactions if solids act as reactant such as the coal combustion and gas-phase catalytic reactions if solids act as catalyst such as the FCC process.

There are two types of gas-solids CFB, the riser and downer. The GSCFB riser has been more popular in industrial applications so far as a chemical reactor than the downer, mostly based on a fact that it has relatively higher overall solids holdup. This may, however, be a mishap, as detailed investigation on the solids holdup distributions inside the CFB riser and downer conducted in this work shows that the GSCFB riser and downer could have similar overall solids holdups or even the same axial solids holdup distribution by adjusting the U_g-G_s pair as shown in Figure 10-1. Comparing CFB riser with the downer, by increasing U_g by 2 m/s at the same G_s or lowering G_s by 200 kg/m^{2}s at the same U_g seems, deriving from the studies conducted in Chapters 4 & 5, to make the riser and downer share the same axial profiles of solids holdup. Thus, the performance of the GSCFB reactors is only determined by the radial distribution of the solids which relates to the degree of back-mixing of the particles and the clustering effects on the local distribution of solids.

Since the radial solids holdup profiles in the CFB riser are less uniform compared with that in the CFB downer, as shown in Chapters 4 & 5, due to the more severe clustering effects, the conversion and selectivity of the reactions are believed to be lower in the CFB riser due

to less contacting efficiency when compared with the downer with the same overall solids holdup. Therefore, the use of the GSCFB downer reactor can potentially bring more benefits if it is designed to have the same overall bed density with the riser while having a relatively more uniform flow condition.
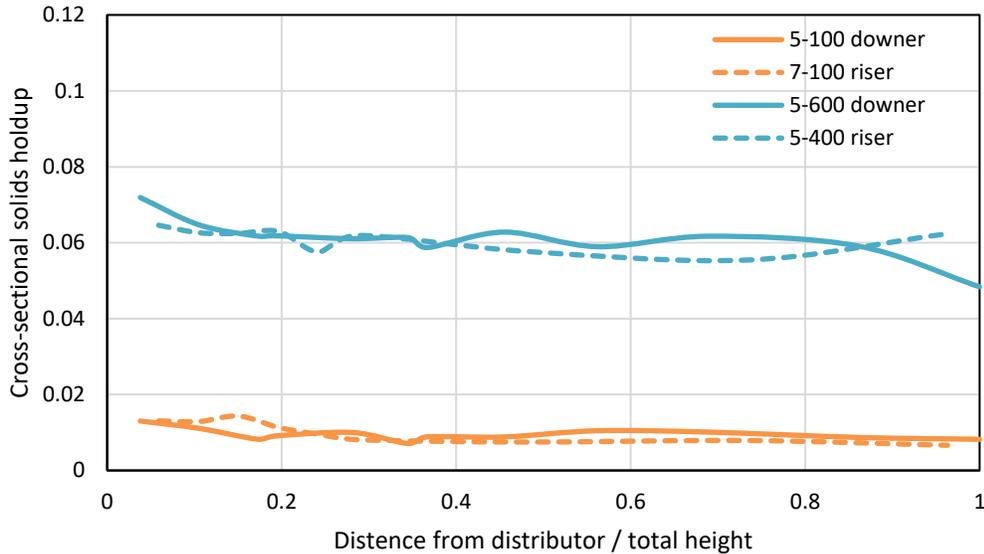
Figure 10-1 Axial solids holdup distributions between gas-solid CFB riser (U_g = 5, 7 m/s, G_s = 100, 400 kg/m²s) and downer (U_g = 5, 7 m/s, G_s = 100, 600 kg/m²s)

The application of the CFD approach has allowed us to examine the flow conditions in the riser and downer covering a wider operating window from low-density to high-density conditions, which helps revisit the flow structures in the GSCFB system and reveal the similarity of the solids holdup distributions between the riser and downer. The improvements on the CFD model which considered the entrance geometric structure effect that is critical and the cluster-driven drag model that is more realistic also provide more reliable simulation results for comparing the uniformity of the gas-solid flow between the riser and downer. The similarity shared by the riser and downer in the overall bed density and axial solids distribution by adjusting the U_g-G_s pair demonstrates a new possible strategy to the future design of a CFB reactor.

Building on the strength accumulated through the GSCFB work and utilizing the large amount of the experimental data from the same group, CFD models under the same framework are firstly constructed in this work for the liquid-solid and three-phase inverse

fluidized bed. When compared with the GSCFB system, the liquid has a density closer to the particles and has a larger viscosity than the gas at the meantime, leading to a lower terminal velocity of the particles in the liquid. The fluidization of the particles can be initiated at a low liquid velocity and go through a smoother expansion in the LSCFB. Both the axial and radial profiles of solids holdup are generally uniform and only a thin but denser layer of particles near the wall is found, which may be considered as a minor clustering of the particles. Therefore, it is easier to predict the overall solids holdup and manipulate similar flow conditions in the upward and inverse fluidization systems.

The introduction of gas bubbles into the inverse liquid-solid fluidized bed decreases the system uniformity and leads to inner circulations of the liquid and solids, resulting in the three-phase fluidized bed possessing a heterogeneity in between the particulate LSCFB system and the aggregative GSCFB system. It is possible that by increasing the gas flow rate and enlarging the density difference between the particles and liquid, the three-phase system will become less uniform because the flow conditions transit to be closer to the gas-solid system. The inverse fluidized beds are typically designed for wastewater treatment because a high overall bed density and a high bed expansion ratio at low U_l can be achieved. The CFD work carried out in this work is paving the way for the design in future industrial applications of the inverse LSCFB and BIFB because it allows the properties of the fluid and particles to change freely.

The CFB reactor also has higher fluid-particle contact efficiency given the relatively higher inter-phase slip velocity. But the utilization of this advantage also depends on the uniform distributions of the local and overall solids holdups. A higher overall solids holdup with relatively uniform solids distribution under high superficial fluid velocity in the CFB systems is ideal for chemical reactions. Higher overall solids holdup contributes to a higher total specific area of the particles, and the uniform distribution of the particles results in a higher contact efficiency due to reduced back-mixing of the solids. Furthermore, the CFB systems allow the fluid phase to have a higher throughput given the high-velocity fluidization operation. Therefore, the overall solids holdup and the uniformity of the multiphase flow are the two key parameters for judging the performance of a CFB reactor.

Multiple factors play a role in determining the effectiveness of a fluidized bed reactor not only including the overall operating conditions such as the superficial fluid velocity, solids circulation rate and particle properties, but also relating to the fluctuations of the multiphase flows in a fluidized bed reactor. How and how much impacts for all these factors on the contacting efficiency in the fluidized bed are still unclear. Extensive amount of the experimental and modelling work done on the CFBs in our group including the CFD studies in this study allows us to extract the similarity of dynamic behavior of the particles among the fluidization systems and better understand the effects of the surrounding fluid and particles from the simulation results.

A system uniformity index combining with the above-mentioned factors either obtained from experiments or simulations is proposed to describe the effectiveness of a fluidized bed reactor. The system uniformity should reflect the flow conditions in a fluidized bed from multi-levels including overall distribution of the fluid and solids from macro scale, the instantaneous features such as the fluctuating velocity, inner circulations, clustering effects, etc. from the meso and micro scales.

The general idea of the system uniformity of the fluidized bed is that it is a function of multiple factors as shown in Eq (10-1).

$$I_u = f\left(S_{tk}, \frac{\overline{\varepsilon_s}}{\varepsilon_s}, \theta_s, G_s, U_f, \Delta\rho, \Delta P_{im}\right) = 1 - \left(S_{tk}^{\ a} \cdot \left(\frac{\overline{\varepsilon_s}}{\varepsilon_s}\right)^b \cdot \theta_s^{\ c} \cdot G_s^{\ d} \cdot U_f^{\ e} \cdot \Delta\rho^f \cdot \Delta P_{im}^{\ g}\right) \qquad (10\text{-}1)$$

where $S_{tk}\ (= \frac{t_0 u_0}{l_0})$ is Stokes number, $t_0\ (= \frac{\rho_p d_p^2}{18\mu_g})$ is the particle relaxation time, $u_0 = (U_f)$ is the fluid velocity, l_0 is the characteristic length of the fluidized bed. $\overline{\varepsilon_s}$ and ε_s are the overall solids holdup and the cross-sectional solids holdup. θ_s is the granular temperature of the particles associating with the particle fluctuations from CFD results. G_s is the solids circulation rate, U_f is superficial fluid velocity, $\Delta\rho$ is the density difference between the particle and fluid, and ΔP_{im} is the pressure imposed in the system.
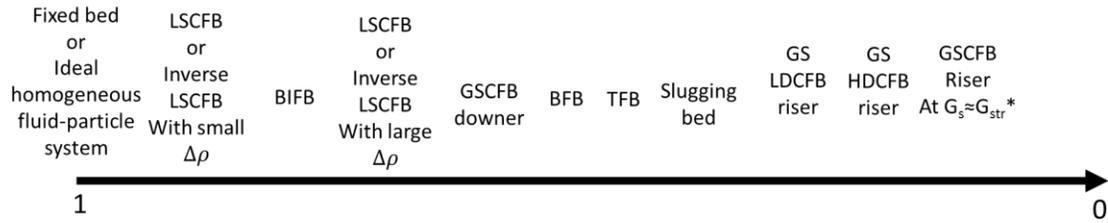
Figure 10-2 The general idea on the system uniformity among various types of fluidized beds

The system uniformity among various types of fluidized beds is briefly sketched as shown in Figure 10-2. Certainly, the ideal homogeneous fluid-particle system can be considered to have the highest uniformity, while the fixed bed is also considered as a perfect uniform state in which $I_u = 1$ at $S_{tk} = 0$, $U_f = 0$, $G_s = 0$, $\frac{\overline{\varepsilon_s}}{\varepsilon_s} = 1$ and $\theta_s = 0$. The LSCFB system with a small density difference between the particles and fluid is close to a homogeneous fluid-particle system because almost all particles are uniformly distributed in the fluidized bed, so that it has a high I_u. However, as the results show in Chapter 8, when the density difference becomes larger, the uniformity of the LSCFB decreases with more inner circulations occurring. The gas-liquid-solids systems such as the BIFB at the complete fluidization velocity can be considered to have a system uniformity in between the LSCFBs with a smaller $\Delta\rho$ and with larger $\Delta\rho$ because all the particles are uniformly distributed and the only turbulence introduced from the gas bubbles is slight. While being less uniform when compared with the LSCFB system, the GSCFB downer has a slightly more uniform flow structure than the GSCFB riser reactor. The LDCFB riser is considered to have better uniformity than the HDCFB riser because the local flow structure is relatively more uniform. The GSCFB riser under the solids circulation rate around $G_{s,tr}^*$ is considered to have the least uniformity among all the fluidized beds because it is under the transition from the LDCFB riser to the HDCFB riser and the changeover between the dense phase and dilute phase is very dynamic. More future work is needed on the detailed correlation with more simulation and experimental data collected.

10.2 Conclusions

This thesis work covers the numerical work on various circulating fluidized bed systems including gas-solid, liquid-solid, and gas-liquid-solid three-phase fluidization systems. The hydrodynamics in different types of fluidized bed reactors under a wide range of operating conditions are numerically studied.

To have a deeper understanding of the underlying flow mechanisms at different scales in the gas-solid fluidization system, a numerical study was initially comprehensively carried out in a gas-solid circulating fluidized bed (CFB) riser reactor. The effects of the inlet boundary conditions on the flow structures in a gas-solid CFB riser are investigated. A more realistic inlet boundary condition which considers the real geometry structure of the gas distributor and the solids returning pipe is applied in the CFD model. The unrealistic squeeze effects with air jets along the entire CFB riser are eliminated and are replaced with a small jet region in the entrance region of the riser by the modified inlet boundary condition.

Hydrodynamics under high-density operating conditions and low-density operating conditions in a gas-solid CFB riser are further studied via the CFD model with the modified inlet boundary conditions. A good agreement with the experimental results is achieved. The exponential shape of the axial solids holdup profile is found either under the very dilute or extremely dense flow condition in the GSCFB riser However, the S-shape profile of the solids holdup distribution is more likely to be found under the intermediate solids circulation rate. Compared with the low-density CFB riser, the overall bed density is higher in the high-density CFB riser with a wider and denser wall region. An index is developed as a function of the superficial gas velocity and solids circulation rate to predict the relationship of the overall bed density under different U_g-G_s operating conditions.

The hydrodynamics in the gas-solid CFB downer reactor are also numerically studied and the results agree well with the experimental data. Compared with the GSCFB riser, the flow structures are relatively uniform in the GSCFB downer, however, the gas-solids suspension is much more dilute. The axial solids holdup distribution is relatively uniform in the CFB downer, while the radial solids holdup distribution is generally uniform from

the center to the wall of the downer but with a slight increase at the wall due to the wall effects. The flow development can be divided into the first and second acceleration stages and a fully developed stage along the downer reactor. A correlation of the overall bed density inside the downer is proposed. The scale-up effects are also numerically studied, and the results show that a higher solid holdup at the wall is achieved in the scaled-up downer while the overall bed densities are similar.

The gas-solid flow structures under high-density operations are found to have distinct characteristics from the low-density conditions in both the GSCFB riser and downer reactors. A higher overall bed density is achieved in both HDCFB riser and downer when compared with the LDCFB operations, which contributes a higher conversion for chemical reactions. For both the HDCFB riser and downer, a longer and denser developing region in the entrance part close to the gas distributor is found along the axial direction, and a wider and denser wall region with higher local solids holdup is found in the radial direction.

A cluster-driven drag model is developed for the gas-solid CFB riser reactor. With the help of the image processing and the wavelet analysis approaches, the size, solids concentration of the clusters, and the solids volume fraction of the cluster phase can be obtained and then directly included into the calculation of the drag force in the gas-solid system. An agreement with the experimental data and an improvement of the solids holdup at the wall comparison with the commonly used Syamlal-O'Brien drag model are achieved by the proposed cluster-driven drag model. Higher slip velocity and higher granular temperature of the particles are predicted by the cluster-driven model, which indicates more intensive gas-particle interaction due to the clustering phenomenon. Further study shows that the clustering effects are more severe in the lower part or near the wall region of the CFB riser. Typical types of clusters such as strands, U-shaped, and spherical clusters are found in instantaneous contours of the solids holdup in the CFB riser. The effects of cluster size, and the distribution of the clusters are further discussed, and still needs more investigations in the future.

To provide more supplementary discoveries to the experimental studies, CFD models in Eulerian-Eulerian approach are developed for two new types of circulating fluidized bed

reactors: an inverse liquid-solid CFB reactor and a bubble induced inverse three-phase fluidized bed reactor.

CFD approach is applied to the hydrodynamic study of the inverse liquid-solid CFB system in which light particles are used, and achieves a good agreement with the experimental data. Numerical results from the ILSCFB show that the general flow structure is uniform in the inverse LSCFB downer. In the radial direction of the inverse LSCFB downer, the major part of the solids holdup distribution is uniform with a slight decrease at the wall due to the wall effects. Radial profiles of particle velocity from simulation results show that the solids suspension has a larger velocity in the center and a lower velocity near the wall in the inverse LSCFB. The flow structures become irregular when very light particles with a density of 28 kg/m^3 is used in the inverse LSCFB because the density difference between the liquid and the particles is too large, resulting in more irregular vortexes. A binary-particle system in the inverse LSCFB is also studied via numerical simulations and the results show similarities in flow structures with the single-particle system. A further study on the comparison of the flow structures between the ILSCFB riser and downer is carried out by numerical simulations and is included in the Appendix.

A bubble induced inverse fluidized bed is studied both experimentally and numerically. A three-phase CFD model is developed for the BIFB using EE approach in which the gas phase is treated as the primary phase and both the liquid and solids phases are treated as secondary phases. With increasing superficial gas velocity, the BIFB will go through a bed expansion regime, a complete fluidization regime, and a freeboard regime. An initial fluidization gas velocity (U_{g1}), a full expansion gas velocity (U_{g2}), and a freeboard fluidization velocity (U_{g4}) are defined as the onsets of the three flow regimes. A complete fluidization gas velocity (U_{g3}) is also defined to characterize the optimized operating condition of the BIFB when all the particles are uniformly distributed. Numerical results show a good agreement with the experimental observations. In the complete fluidization regime, the three-phase flow is generally uniform, however, numerical results show that the radial solids holdup distribution is slightly less uniform than the axial one due to the inner circulation of the liquid. CFD results also show that a larger solids loading helps an

easier fluidization operation with a smaller complete fluidization gas velocity and a faster flow development.

10.3 Recommendations

The underlying physics inside the gas-solid CFB system is still unclear although much of the numerical and experimental works have been done. The proposed cluster-driven drag model provides a more direct way to include the information of the clustering phenomenon obtained from the experiments into the CFD models. That said, however, more future work on the refinery of the proposed drag model is needed:

Firstly, a proper description of the cluster slip velocity is needed. The cluster slip velocity is assumed be the same as the terminal velocity of the cluster in the current cluster-driven drag model since the actual slip velocity of clusters is not readily available from the experiments. With further analysis on the signals of the optical fiber probe, it is possible to extract the absolute velocity of the clusters and then the slip velocity of clusters can be derived. Secondly, a more meticulous size and density distribution of the clusters should be added into the calculation of the drag force. Numerical results from the modified cluster-driven model which use smaller and diluter clusters in the center and larger and denser clusters in the wall region of the CFB riser has already show some improvements for a more accurate prediction. In the future, a correlation on the size and density of the clusters based on the position in the riser can be taken into account for the drag model.

Although it is widely accepted that little clustering phenomenon occurs in the CFB downer in the past due to its very dilute flow conditions with less back-mixing, particles still tend to agglomerate resulting in a clustering effect under the high-density operations in the downer reactor. With more data collected by the experiments, the cluster-driven drag model can likely be used in the gas-solid CFB downer reactors.

With enough hydrodynamics studied in the circulating fluidized bed systems, chemical reactions should be added into the CFD model. The next step after the hydrodynamic study of the fluidized bed reactor is the hot-mode study which investigate the performance of the chemical reactions in the CFBs. With more knowledge obtained on the flow regimes and

the flow development in the CFBs, potential applications need to be studied. For example, a high-density CFB downer could operate the FCC process with less back-mixing, and the BIFB may be welcomed in the wastewater treatment field due to its longer residence time of the liquid. From the view of CFD modelling, an accurate description of the reaction kinetics is of crucial importance and the coupling work of the chemical reactions into the hydrodynamic model deserves more attentions in the future.

Scale-up work on the circulating fluidized bed systems can be continued for industrial uses with the accelerated growth of computational power. Some newly developed algorithms such as the coarse grid approach or the MP-PIC method can be implemented in the simulations. The fundamental study which aims to dig into more advanced theories for the underlying physics can be firstly numerical investigated in the micro-scale with finer grid system and more accurate methods such as the discrete element method (DEM) or direct numerical simulation (DNS) approaches. The scale-up effects can be simulated by some more applied approaches coupled with the initial numerical results from the micro-scale CFD models for saving the time and cost.

More experiments done on the circulating fluidized bed systems especially for some newly invented fluidized beds are still needed to reveal the underlying physics with development of the measuring techniques.

Appendices

Two published articles are included in the appendices part as the supporting materials to present a better integrality of this thesis.

Article 1: Comparison of liquid-solid flow characteristics in upward and downward circulating fluidized beds by CFD approach (published in Chemical Engineering Science)

Authors: Yangfan Song, Jesse Zhu, Chao Zhang, Zeneng Sun, Xiaofeng Lu

This paper is an extended work of **Chapter 8**, in which the hydrodynamics in the inverse liquid-solid CFB riser and downer are compared by CFD approach. A good agreement is achieved between the numerical and experimental results. Similarities and differences are presented between the upward and downward CFB. The previous Sang and Zhu model is proven to be useful in predicting solids holdup.

Article 2: A Consolidated Flow Regime Map of Upward Gas Fluidization (published in AIChE Journal)

Authors: Zeneng Sun and Jesse Zhu

This paper is a review article of the upward gas-solids fluidization systems, which is a supplementary work to **Chapter 3-7**. A consolidated flow regime map is proposed to reflect the expansion of upward gas fluidization. New types of fluidized beds such as CTFB and HDCFB are included and CFB operating region is reclassified. The corresponding transitions between the regimes are discussed. The dynamic changeover of the continuous phase between the flow regimes is discussed.

Comparison of liquid-solid flow characteristics in upward and downward circulating fluidized beds by CFD approach

Yangfan Song [a,c], Jesse Zhu [a,*], Chao Zhang [b], Zeneng Sun [a], Xiaofeng Lu [c]

[a] Department of Chemical and Biochemical Engineering, University of Western Ontario, London, Ontario N6A 5B9, Canada
[b] Department of Mechanical and Materials Engineering, University of Western Ontario, London, Ontario N6A 5B9, Canada
[c] Key Laboratory of Low-grade Energy Utilization Technologies and Systems (Chongqing University), Ministry of Education, Chongqing, 400044, PR China

HIGHLIGHTS

- Hydrodynamics in upward and downward liquid-solid CFB are compared by CFD approach.
- A good agreement is achieved between the numerical and experimental results.
- Similarities and differences are presented between the upward and downward CFB.
- The previous Sang and Zhu model is proven to be useful in predicting solids holdup.

ARTICLE INFO

ABSTRACT

The flow behaviors of the particles in the upward and downward liquid-solid circulating fluidized beds were simulated by Eulerian-Eulerian approach incorporating the kinetic theory of granular flow. The Syamlal-O'Brien drag model was used to account for the interphase interaction between the liquid and solids phases. The numerical results agreed well with the experimental data obtained by other group members, successfully validating the numerical approach. The hydrodynamic characteristics of the particles with different densities and sizes in the upward and downward circulating fluidized beds were compared in detail under different liquid velocities and solids flow rates. The results indicated that there were many hydrodynamic similarities in the upward and downward circulating fluidized beds. However, due to the deviation of the standard drag curve, the drag force on the lighter particles in the downward liquid-solid circulating fluidized bed became different, leading to random and irregular particle flow behaviors. The predicted average solids holdups matched well with the results by an empirical model proposed by Sang and Zhu and the matching degree between the numerical results and the model was larger than 85%, further proving that the Sang and Zhu model is widely applicable.

© 2018 Published by Elsevier Ltd.

1. Introduction

The hydrodynamic characteristics of liquid-solid fluidization systems have attained popularities due to a number of advantages, such as higher heat and mass transfer rates, less solids attrition, improved liquid-solid contact efficiency and easy control of the particle flows (Zhu et al., 2000). Such advantages enable the liquid-solid fluidized systems to be applied in various industries, including biochemical, petrochemical and metallurgical industries.

When the density of the particles is higher than the density of the liquid, the particles are fluidized upwards in the upward liquid-solid fluidized bed (UFB) and the upward liquid-solid circulating fluidized bed (UCFB). When the density of the particles is lower than that of the liquid, the particles are suspended downwards by the continuous downward liquid flow in the opposite direction of the buoyancy, which is referred to as the downward fluidization (Renganathan and Krishnaiah, 2004). Downward liquid-solid fluidized bed (DFB) can be used in biochemical processes and wastewater treatment industry (Sowmeyan and Swaminathan, 2008). In a circulating fluidization system, particles can circulate in the bed. In order to combine the benefits of the DFB and circulating fluidization, the downward liquid-solid circulating fluidized bed (DCFB) has been developed.

* Corresponding author.
  E-mail addresses: jzhu@uwo.ca (J. Zhu), czhang@eng.uwo.ca (C. Zhang), zsun82@uwo.ca (Z. Sun), xfluke@cqu.edu.cn (X. Lu).

Nomenclature

Notation

Ar	Archimedes number defined by $d_p^3 g \lvert \rho_p - \rho_l \rvert \rho_l / \mu_l^2$
C_D	drag coefficient
D	column diameter, m
d_p	particle diameter, m
e	coefficient of restitution
f_m	virtual mass force, N
g	gravity acceleration, m/s^2
g_o	radial distribution function
h	distance from the distributer, m
k	turbulent kinetic energy, m^2/s^2
p	fluid pressure, Pa
p_s	solids pressure, Pa
R	rayon, m
Re_s	relative Reynolds number
Re_t	particle terminal Reynolds number defined by $u_t d_p \rho_l / \mu_l$
r	distance from the center, m
t	time, s
u	superficial velocity, m/s
u_t	particle terminal velocity, m/s

Greek letters

β	interphase momentum transfer coefficient, kg/m^2 s^2
γ_s	kinetic energy dissipation rate, kg/m s^3
ε	turbulent dissipation rate, m^2/s^3
ε_l	volume fraction of liquid
ε_s	volume fraction of solids
$\bar{\varepsilon}_s$	average solids holdup
$\varepsilon_{s,max}$	maximum solids volume fraction
θ	granular temperature, m^2/s^2
μ_f	effective viscosity of fluid, kg/m s
μ_l	molecular viscosity of fluid, kg/m s
μ_s	solid shear viscosity, kg/ms
ρ	density, kg/m^3
τ_l	stress tensor of liquid phase, kg/s^2
τ_s	stress tensor of solids phase, kg/s^2

Subscripts

l	liquid phase
p	particle
s	solids phase

The UFB has been studied extensively by lots of researchers. Couderc (1985) found that the UFB can be considered as a dispersed homogenous fluidization where particles are uniformly distributed in both the axial and radial directions in the dense region. Richardson and Zaki (1997) proposed an important relationship between the operating liquid velocity and the bed voidage, which has been widely adopted and modified for the drag correlation between the liquid and particles.

The hydrodynamics in the UCFB have been widely investigated experimentally in previous studies, such as the axial solids holdup distribution (Zheng, 1999), radial solids holdup distribution (Zheng and Zhu, 2003), liquid velocity distribution (Liang et al., 1997) and particle velocity distribution (Sang, 2013; Roy et al., 2005). Some numerical studies have also been carried out by researchers to investigate the hydrodynamics in the UCFBs. Roy and Dudukovic (2001) simulated the liquid and solids residence time distributions, the solids velocity and holdup pattern in the riser based on the Eulerian-Lagrange model. Cheng and Zhu (2005) simulated the hydrodynamics in the riser of an UCFB under different operating conditions, different particle properties and different riser dimensions based on the Eulerian-Eulerian approach. Later, the same group of researchers (Cheng and Zhu, 2008) investigated the scale-up issue in the UCFB by CFD approach and compared with the similitude method. Dadashi et al. (2014) employed a CFD model based on the Eulerian-Eulerian multi-phase flow with kinetic theory of granular flow to simulate a UCFB reactor and found that both the dispersed and per-phase k-ε turbulence models showed qualitative agreements with the experimental data. Luo (2017) investigated the effect of the drag model, near wall treatment and boundary conditions on the numerical results. The numerical results agreed well with the experimental data and the hydrodynamics of the UCFB under different operating conditions were investigated numerically.

Previous studies on the DFBs focused on the hydrodynamic characteristics such as the minimum fluidization velocity, pressure drop and bed expansion. Fan et al. (1982) studied the bed expansion in a DFB experimentally and found that the bed expansion increased with the fluidization velocity and particle density and decreased with the particle size. Renganathan and Krishnaiah (2005) studied the voidage fluctuations, axial voidage profile and bed expansion by measuring the local void fraction in a DFB, since the quality of fluidization is also elucidated by the local voidage fluctuations. For numerical studies, Wang et al. (2014, 2018) simulated the flow behaviors of particles in the DFBs by means of a two-fluid model and found that the axial velocities of particles and the bed expansion height increased with the liquid velocity. The granular temperature increased, reached the maximum, and then decreased with the increase in the solids volume fraction. The hydrodynamic characteristics of the DFB, such as the pressure drop, solids holdup, and minimum fluidization velocity, have been investigated in previous studies both experimentally and numerically and some empirical correlations have been developed. However, the studies above on the DFB were carried out in the experimental reactors whose heights were lower than 3 m, which cannot reflect the actual industrial situations.

The DCFB combines both the advantages of the DFB and circulating fluidization. Jaberi (2014) and Nan (2019) experimentally studied the axial particle distribution, radial structure and solids circulation rate in a downer of a DCFB whose height was 5.4 m under different particle densities, different liquid velocities and different solids flow rates. Sang (2013) compared the hydrodynamic characteristics in the UFB and DFB by experiments and found that there are many similarities between the upward and downward fluidization.

To design, scale up and operate the liquid-solid continuous systems, the information of the similarities and differences between the UCFB and DCFB is required. In industrial applications, the appropriate flow regime can be selected according to this information. In this study, the liquid-solid flow characteristics in the large size UCFB and DCFB are investigated numerically under different operating conditions, different particle densities and different particle sizes. The hydrodynamics in the UCFB are compared with that in the DCFB. Two-dimensional Eulerian-Eulerian approach with the kinetic theory of granular flow is selected and the CFD software Ansys/Fluent is the numerical platform used in this study. Through CFD simulations, the liquid-solid flow characteristics in large-size fluidized beds can be studied comprehensively and the cost and time of the experiment can be reduced. Moreover, some detailed information on the local holdups and velocities of each phase, which are either impossible or difficult to be measured experimentally, can be captured through CFD approach. Such information is of great importance in understanding the hydrodynamics in the

UCFBs and DCFBs. The simulation results are compared with the experimental data obtained by Sang (2013), Jaberi (2014) and Nan (2019) to validate the CFD models proposed in this study.

2. Configurations and operating conditions of the UCFB and DCFB

The configurations of the UCFB used by Sang (2013) and the DCFB used by Jaberi (2014) and Nan (2019) in their experiments are used in this work in order to compare the numerical results with their experimental data.

Fig. 1(a) shows the schematic diagram of the UCFB (Sang, 2013). Along the circulation loop, the UCFB consists of a riser with an inner diameter of 76 mm and a height of 5 400 mm, a liquid-solid separator, a solids downcomer with an inner diameter of 200 mm and two connecting pipes. When the liquid velocity in the riser is higher than the transport fluidization velocity, particles from the solids flow control will flow upwards carried by the upward liquid flow and then be separated from the liquid by the liquid-solid separator at the top of the riser. The liquid recycles to the inlet of the riser through a pump. The particles move from the separator to the solids downcomer through the upper connecting pipe. Then the particles move down in the solids downcomer because of their gravity and are stored in the downcomer. The solids flow rate at the inlet of the riser can be adjusted by the solids flow control. The temperature of the liquid was monitored during the experiments to make sure that all the experiments were performed under the same condition. Fig. 1(b) shows the schematic diagram of the DCFB (Jaberi, 2014; Nan, 2019). The riser and the solids downcomer in the UCFB are changed to a downer and a solids upcomer in the DCFB respectively. The flow direction of the liquid-solid two phases in the DCFB is opposite to that in the UCFB. In the DCFB, particles from the solids flow control will flow downwards in the downer carried by the downward liquid flow and then move up and be stored in the solids upcomer because of their buoyancy.

In the studies carried out by Sang (2013), the solids particles used were plastic beads whose particle sphericity was 1. And in the studies carried out by Jaberi (2014) and Nan (2019), the solids particles used were spherical Styrofoam. The liquid phase was tap water. Nine different operating conditions used by Sang (2013), Jaberi (2014) and Nan (2019) are selected to compare the numerical results with the experimental data.

3. CFD model

Generally, there are two major approaches to model liquid-solid two phase flows, the Eulerian-Lagrangian approach and the Eulerian-Eulerian approach (Pan et al., 2016). For the Eulerian-Lagrangian approach, the motions of individual particles are tracked by Lagrangian force balance equations and the liquid flow is modeled using a continuum based CFD approach with local properties averaged over a number of computational cells (Liu et al., 2016). The Eulerian-Eulerian approach treats both the liquid and solids phases as interpenetrating continua, the motion of each phase is solved using a continuum based CFD approach with suitable closure terms (Feng et al., 2012). The Eulerian-Lagrangian approach can predict the detailed behavior of the solids, but requires much more computing power. The Eulerian-Eulerian approach costs less computational time, but its accuracy depends on the closure model used to describe properties such as solids viscosity and solids pressure (Zhang et al., 2012). The former approach is suitable for the fundamental research while the latter is for process designs (Montastruc et al., 2009). In this work, the Eulerian-Eulerian approach is employed since the computational domains for the UCFB and DCFB are large.

3.1. Governing equations

A Eulerian-Eulerian two-fluid model has been adopted for both solids and liquid phases. The kinetic theory of granular flow has been used for closure. The governing equations are given below.

The continuity equation for phase i (i = s for solids phase or i = l for liquid phase) is:

$$\frac{\partial}{\partial t}(\varepsilon_i \rho_i) + \nabla \cdot (\varepsilon_i \rho_i \overrightarrow{u}_i) = 0 \tag{1}$$
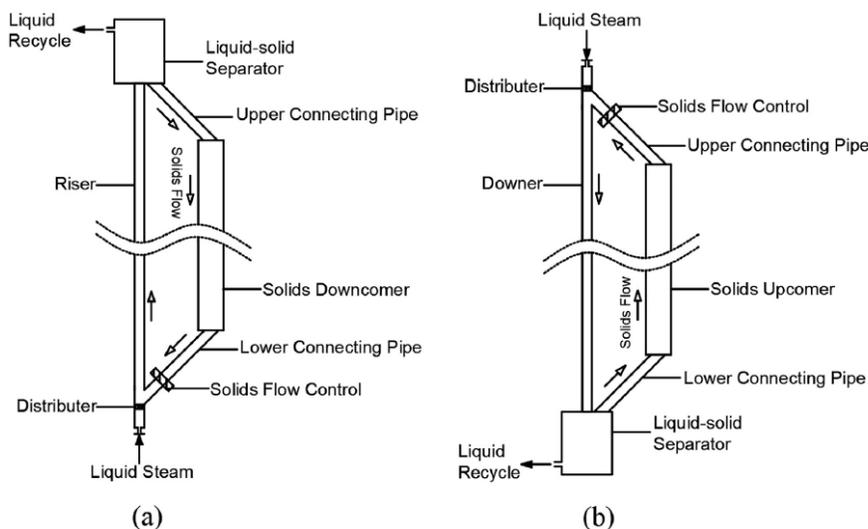

Fig. 1. Schematic diagram of (a) the UCFB (Sang, 2013) and (b) the DCFB (Jaberi, 2014; Nan, 2019).

where ε_i is the volume fraction, $\vec{u}$ is the velocity vector and ρ is the density.

The momentum equation for the liquid phase is:

$$\frac{\partial}{\partial t}(\varepsilon_l \rho_l \vec{u}_l) + \nabla \cdot (\varepsilon_l \rho_l \vec{u}_l \vec{u}_l) = -\varepsilon_l \nabla p + \nabla (\varepsilon_l \cdot \tau_l) + \varepsilon_l \rho_l \vec{g}$$
$$+ \beta(\vec{u}_s - \vec{u}_l) \qquad (2)$$

where p is the fluid pressure, $\vec{g}$ is the gravity acceleration, β is the interphase momentum transfer coefficient, and τ_l is the stress tensor of the liquid phase, given by

$$\tau_l = \mu_f \left[\nabla \cdot \vec{u}_l + \left(\nabla \cdot \vec{u}_l \right)^T \right] - \frac{2}{3} \mu_f \left(\nabla \cdot \vec{u}_l \right) \boldsymbol{I} \qquad (3)$$

The momentum equation for the solids phase is:

$$\frac{\partial}{\partial t}(\varepsilon_s \rho_s \vec{u}_s) + \nabla \cdot (\varepsilon_s \rho_s \vec{u}_s \vec{u}_s) = -\varepsilon_s \nabla p - \nabla p_s + \nabla (\varepsilon_s \cdot \tau_s)$$
$$+ \varepsilon_s \rho_s \vec{g} + f_m + \beta(\vec{u}_l - \vec{u}_s) \qquad (4)$$

where p_s is the particle pressure, which represents the particle normal forces due to particle-particle interactions, and τ_s is the solids stress tensor given by

$$\tau_s = \mu_s \left\{ \left[\nabla \cdot \vec{u}_s + \left(\nabla \cdot \vec{u}_s \right)^T \right] - \frac{2}{3} \left(\nabla \cdot \vec{u}_s \right) \boldsymbol{I} \right\} + \xi_s \nabla \cdot \vec{u}_s \boldsymbol{I} \qquad (5)$$

The solids shear viscosity μ_s and solids bulk viscosity ξ_s are given in Table 1.

The turbulent kinetic energy (k) and dissipation rate (ε) of the liquid phase and solids phase are calculated by a per phase k-ε turbulence model (Fluent, 2011).

The drag force is one of the important terms in the momentum equations (Loha et al., 2012). A model for the drag force is required in order to couple the momentum transfer between liquid phase and solids phase. Syamlal-O'Brien drag model (Syamlal and O'Brien, 1989) is employed in the present work, which has been widely used by previous researchers. And a previous research work (Luo, 2017) showed that Syamlal-O'Brien drag model worked well in liquid-solid fluidization simulations compared with other drag models.

The virtual mass force acting on a particle is given by Drew and Lahey (1993):

$$f_m = -0.5\varepsilon_s \rho_l \left(\frac{du_l}{dt} - \frac{du_s}{dt} \right) \qquad (14)$$

The granular temperature (θ) is defined as: $\theta = C_v^2/3$, where C_v is the particle fluctuating velocity. The equation of the solids fluctuating energy can be expressed:

$$\frac{3}{2} \left[\frac{\partial}{\partial t}(\varepsilon_s \rho_s \theta) + \nabla \cdot \left(\varepsilon_s \rho_s \theta \vec{u}_s \right) \right] = (-\nabla p_s \boldsymbol{I} + \tau_s) : \nabla \vec{u}_s + \nabla \cdot (k_s \nabla \theta)$$
$$- \gamma_s - 3\beta\theta + D_{ls} \qquad (15)$$

where the conductivity of the granular energy (k_s), the kinetic energy dissipation rate (γ_s) and the energy exchange between the liquid and the solids (D_{ls}) are summarized in Table 1 (Fluent, 2011).

3.2. Mesh information

The riser of the UCFB and the downer of the DCFB shown in Fig. 1 are simplified to 2D planar models because of their axial symmetry. In order to correctly represent the complex flow structures at the inlet and near the walls, the mesh in the inlet region and near the walls has been refined. The mesh independence study has been done by other group members for the same beds used in this work (Luo, 2017). Four meshes were selected to be applied in this work for different operating conditions based on the previous mesh independence study. The information of the selected meshes is given in Table 2.

3.3. Boundary conditions

The governing equations are numerically solved with appropriate boundary and initial conditions. At the inlet, which is located at the bottom of the riser in the UCFB or at the top of the downer in the DCFB, both the liquid and solids are of uniform velocities. At the outlet, due to the fully developed flow condition, the outflow condition is used for both liquid and solids phases. At the walls, the no-slip condition is used for the liquid phase and the partial slip Johnson and Jackson boundary condition (Johnson and Jackson, 1987) is used for the solids phase. The particle-particle collision restitution coefficient for the solids phase is set as 0.9 and the specularity coefficient is set as 1×10^{-5}.

The phase coupled SIMPLE scheme is used for the pressure-velocity coupling, the second order upwind is chosen to discretize the convection terms for the k-ε turbulence model, granular

Table 1
Closure equations for the solids phase.

Solids pressure	$p_s = \varepsilon_s \rho_s \theta + 2\rho_s(1+e)\varepsilon_s^2 g_o \theta$	(6)
Solids shear viscosity	$\mu_s = \frac{4}{5}\varepsilon_s^2 \rho_s d_p g_o(1+e)\sqrt{\frac{\theta}{\pi}} + \frac{10\rho_s d_p \sqrt{\pi\theta}}{96(1+e)\varepsilon_s g_o}\left[1 + \frac{4}{5}\varepsilon_s g_o(1+e)\right]^2$	(7)
Solids bulk viscosity	$\xi_s = \frac{4}{3}\varepsilon_s^2 \rho_s d_p g_o(1+e)\sqrt{\frac{\theta}{\pi}}$	(8)
Conductivity of granular energy	$k_s = \frac{25\rho_s d_p \sqrt{\pi\theta}}{64(1+e)g_o}\left[1 + \frac{6}{5}(1+e)g_o\varepsilon_l\right]^2 + 2\varepsilon_s^2 \rho_s d_p g_o(1+e)\sqrt{\frac{\theta}{\pi}}$	(9)
Kinetic energy dissipation rate	$\gamma_s = 3(1-e^2)\varepsilon_s^2 \rho_s g_o \theta\left(\frac{4}{d_p}\sqrt{\frac{\theta}{\pi}} - \nabla \cdot \vec{u}_s\right)$	(10)
Rate of energy exchange	$D_{ls} = \frac{d_p \rho_s}{4\sqrt{\pi}\theta g_o}\left(\frac{18\mu_l}{d_p^2 \rho_s}\right)^2 \left|\vec{u}_l - \vec{u}_s\right|^2$	(11)
Radial distribution function	$g_o = \left[1 - \left(\frac{\varepsilon_s}{\varepsilon_{s,max}}\right)^{1/3}\right]^{-1}$	(12)
Drag model	$\beta = \frac{3\varepsilon_s \varepsilon_l \rho_l}{4 v_{r,s}^2 d_p} C_D\left(\frac{Re_s}{v_{r,s}}\right)\left|\vec{u}_s - \vec{u}_l\right|$	(13)
	$C_D = \left(0.63 + \frac{4.8}{\sqrt{Re_s/v_{r,s}}}\right)^2$	
	$v_{r,s} = 0.5\left(A - 0.06Re_s + \sqrt{(0.06Re_s)^2 + 0.12Re_s(2B - A) + A^2}\right)$	
	$A = \varepsilon_l^{4.14}; \quad B = \begin{cases} 0.8\varepsilon_l^{1.28}, \varepsilon_l \leqslant 0.85 \\ \varepsilon_l^{2.65}, \varepsilon_l > 0.85 \end{cases}; \quad Re_s = \frac{\rho_l d_p \left|\vec{u}_s - \vec{u}_l\right|}{\mu_l}$	

Table 2
Mesh information for different operating conditions.

Mesh name	Domain size (mm)	Number of control volumes	Ratio along the axial direction	Ratio along the radial direction	Maximum aspect ratio
UCFB-1	$76 \times 5\,400$	$50 \times 2\,000$	1.05	1.05	6.9
UCFB-2	$200 \times 5\,400$	$40 \times 1\,000$	1.03	1.03	2.44
DCFB-1	$76 \times 5\,400$	$50 \times 2\,000$	1.05	1.05	6.9
DCFB-2	$200 \times 5\,400$	$40 \times 1\,000$	1.03	1.03	2.44

Table 3
Detailed information of the simulation cases and experiments (Exp.).

UCFB				DCFB				d_p (mm)	u_l (cm/s)	u_s (cm/s)	u_t (cm/s)
Case No.	ρ_p (kg/m^3)	Mesh	Exp.	Case No.	ρ_p (kg/m^3)	Mesh	Exp.				
				#13	950	DCFB-2		3	12	1	4.54
#1	1050	UCFB-2	Sang #S1	#14	950	DCFB-2		3	20	1	4.54
#2	1050	UCFB-2		#15	950	DCFB-2		1.1	20	1	2.75
				#16	850	DCFB-2		3	12	0.5	7.87
				#17	850	DCFB-2		3	12	1	7.87
#3	1150	UCFB-2	Sang #S2	#18	850	DCFB-2		3	20	1	7.87
#4	1360	UCFB-2		#19	640	DCFB-2		3	20	1	12.19
#5	1360	UCFB-1	Sang #S3	#20	640	DCFB-1	Nan #N1	1.1	16.68	1.35	7.38
#6	1360	UCFB-1		#21	640	DCFB-1	Nan #N2	1.1	19.46	0.71	7.38
#7	1360	UCFB-1		#22	640	DCFB-1	Nan #N3	1.1	19.46	1.35	7.38
				#23	28	DCFB-1	Jaberi #J1	0.8	25.09	0.48	10.35
#8	1972	UCFB-1		#24	28	DCFB-1	Jaberi #J2	0.8	27.84	0.48	10.35
#9	1972	UCFB-1		#25	28	DCFB-1	Jaberi #J3	0.8	27.84	0.64	10.35
				#26	28	DCFB-1		0.8	29.2	1.05	10.35
#10	2500	UCFB-2						3	24.89	2	24.89
#11	4000	UCFB-2						3	35.2	2	35.2
#12	8000	UCFB-2						3	53.77	2	53.77

temperature and momentum governing equations. The set of governing equations is solved by Ansys Fluent 17. In all simulations, the time step size is set as 1×10^{-5} s and the convergence criteria is set as 5×10^{-5}. The results are time averaged for 20 s after the simulations reaching the stable condition.

In this work, the liquid phase is water. The detailed information of the simulation cases is given in Table 3.

The particle terminal velocity (u_t) is determined by the following equations (Karamanev, 1996):

$$u_t = \sqrt{\frac{4\left|\rho_p - \rho_l\right|gd_p}{3\rho_l C}} \tag{16}$$

$$C = \frac{432}{Ar}\left(1 + 0.047Ar^{\frac{2}{3}}\right) + \frac{0.517}{1 + 154Ar^{-\frac{1}{3}}} \tag{17}$$

When $Ar > 1.18 \times 10^6 d_p^2$, $C = 0.95$.

4. Results and discussion

In this work, the simulation for twelve cases in the UCFB and fourteen cases in the DCFB under different operating conditions were carried out. The important hydrodynamic characteristics of the liquid-solid two-phase flow, such as the solids holdup and the particle velocities, are discussed below. Understanding the distribution of the solids holdup and the velocities of different particles is helpful to predict the intensity of reaction and heat transfer in the industry process.

4.1. Average solids holdup along the axial direction

Fig. 2 shows the cross-sectional average solids holdup along the axial direction for the particles with a density of 640 kg/m^3 in the DCFB and the particles with a density of 1360 kg/m^3 in the UCFB. The numerical results for the particles with a density of 640 kg/m^3 are compared with the experimental data from Nan (2019) under the same operating conditions. Obviously, the
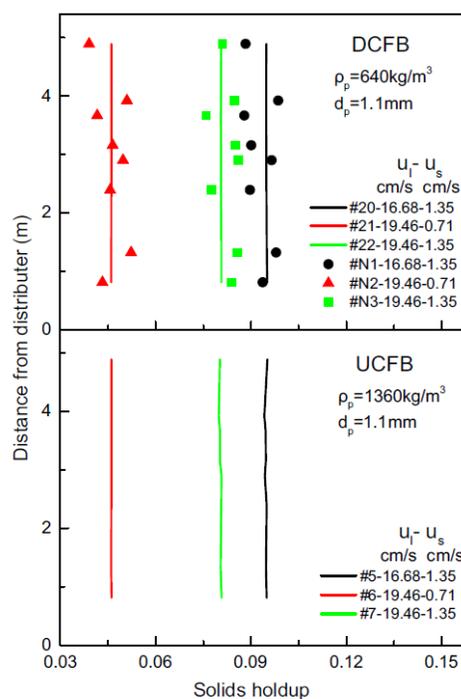

Fig. 2. Axial distributions of the cross-sectional average solids holdup for cases #5–#7 in the UCFB and cases #20–#22 in the DCFB.

numerical results and the experimental results agree well. The deviation between the numerical results and the experimental data for cases #20–#22 are 4.3%, 3.5% and 4.1% respectively.

It is noticed in Fig. 2 that the predicted average solids holdups along the axial direction in the DCFB and UCFB are uniform, as also observed by Liang et al. (1997) and Zheng (1999). The axial distribution of the average solids holdup of the particles with a density of 640 kg/m³ in the DCFB is almost as the same as that of the particles with a density of 1360 kg/m³ in the UCFB under the same operating conditions. Besides, it can be concluded based on the results from cases #20 and #22 in the DCFB and cases #5 and #7 in the UCFB that under the same u_s, the average solids holdup decreases with the increasing u_l. This is expected since under the same u_s, the amount of the particles entering the fluidized bed does not change. The liquid flow with a higher velocity will bring more particles out of the fluidized bed, leading to a lower solids holdup (Razzak et al., 2010). Similarly, it can be seen from cases #21 and #22 in the DCFB and cases #6 and #7 in the UCFB that under the same u_l, the average solids holdup increases with the increasing u_s. When the liquid velocity is remained the same, a higher u_s means more particles flowing into the fluidized bed, resulting in an increase in the solids holdup.

Fig. 3 shows the cross-sectional average solids holdup along the axial direction for the particles with different densities and sizes in the DCFB and UCFB. It is obvious that the average solids holdups along the axis are uniform both in the DCFB and UCFB except for the cases using particles with a density of 28 kg/m³ (#24 and #25). Also, under the same operating condition, the axial distribution of the solids holdup in the DCFB is almost the same as that with the same liquid-solid density difference in the UCFB except for cases #24 and #25. Comparing the upward and downward fluidizations, there are many hydrodynamic similarities. Karamanev and Nikolov (1992) detailedly investigated the liquid-solid flow characteristics of several groups of particles whose densities were lower than 300 kg/m³ and found that when $\rho_P < 300$ kg/m³, the

drag force on the lighter particles became different due to the deviation of the standard drag curve, leading to different particle flow behaviors, which is consistent with the results of this work.

It can be concluded from cases #14, #15 in the DCFB and cases #1, #2 in the UCFB that under the same operating conditions and the same particle densities, the average solids holdup increases with the particle size. This is explainable that the u_t for the particles with the same density but smaller size is lower. Under the same u_l and u_s, particles with smaller sizes are easier to flow out of the fluidized bed, leading to a lower average solids holdup. It can be seen from cases #14, #18, #19 in the DCFB that a lower particle density leads to a higher average solids holdup. This is because that heavier particles have higher gravitational force. Therefore, it is easier for the particles with a higher density to flow out of the bed, resulting in lower solids holdup. This in turn explains the phenomenon of cases #1, #3, #4 in the UCFB.

The numerical results of cases #1, #3 and #4 in the UCFB are also compared with the experimental data from Sang (2013) under the same operating conditions. Table 4 shows the comparison between the predicted average solids holdup of the entire bed of the cases using the particles with a density of 28 kg/m³ (cases#23–#25) and the experimental results from Jaberi (2014). It can be seen from Fig. 3 and Table 4 that there is a good agreement between the numerical and experimental results.

4.2. Solids holdup along the radial direction

The comparison of the radial distributions of the solids holdup between the numerical results for case #5 and the experimental data from Sang (2013) in the UCFB under the same operating condition is given in Fig. 4. The radial distributions of the solids holdup of cases #20–#22 and the comparison with the experimental data from Nan (2019) at h = 2.1 m in the DCFB are presented in Fig. 5. It is obvious from Figs. 4 and 5 that the agreement between numerical predictions and experimental data is good for solids holdup radial distribution both in the UCFB and DCFB. Besides, it can be seen in Fig. 5 that the average solids holdup of case #20 is higher than that of case #21 and case #22, which is consistent with the results shown in Fig. 2.

Fig. 6 shows the radial distributions of solids holdup at different bed heights of the particles with a density of 1360 kg/m³ in the UCFB (case #5) and the particles with a density of 640 kg/m³ in the DCFB (case #20) under the same operating condition. The particle density in case #5 is higher than the liquid density and the particle density in case #20 is lower than the liquid density. However, the density difference between the particles and the liquid is the same for both cases. The radial non-uniformity for the solids holdup in the UCFB, lower at the riser center but higher near the riser wall, can be clearly observed at each bed height in Fig. 6(a). This is mainly because of the wall effect (Luo, 2017). However, as shown in Fig. 6(b), the radial distribution of solids holdup in the DCFB is dilute in the near wall region and dense in the center. This may be due to the fact that the direction of the liquid-solid two-phase flow is changed to the same direction as the gravity in the DCFB. Besides, it is shown that the radial non-uniformity is higher near the inlet of the bed and decreases towards to the outlet of the bed both in the UCFB and DCFB since the flow becomes fully developed at the outlet of the bed (Razzak, 2009).

Fig. 3. Comparison of the cross-sectional average solids holdup along the axis in the DCFB and UCFB.

Table 4
Average solids holdup of the entire bed for cases #23–#25 and experiments #J1–#J3.

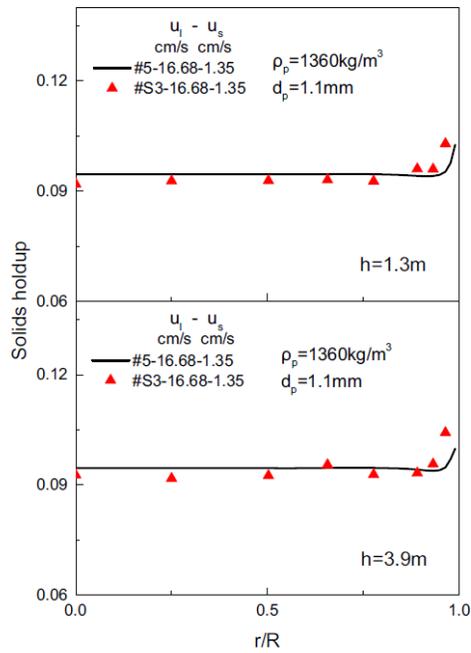|			
Numerical results	(#23) 0.033	(#24) 0.024	(#25) 0.034
Experimental data	(#J1) 0.035	(#J2) 0.026	(#J3) 0.037
Deviation	5.71%	7.69%	8.11%

Fig. 4. Comparison of the radial distributions of the solids holdup between the numerical results for case #5 and the experimental data from Sang (2013) in the UCFB at different bed heights.
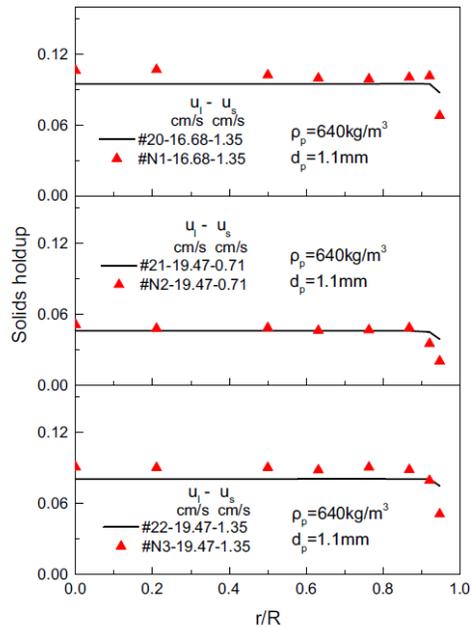

Fig. 5. Comparison of the radial distributions of the solids holdup between the numerical results for cases #20–#22 and the experimental data from Nan (2019) in the DCFB at h = 2.1 m.
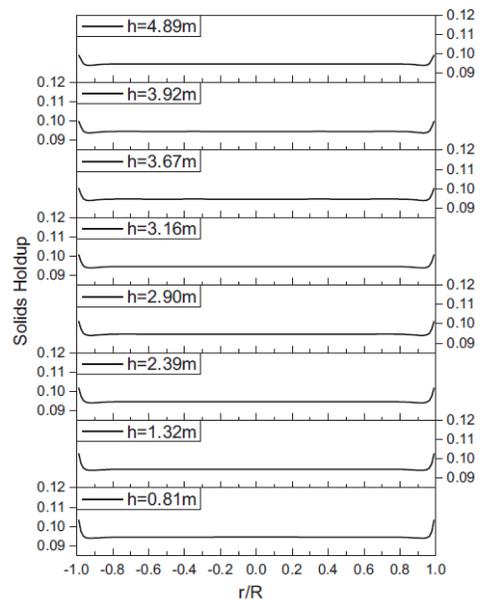
(a) Case #5-ρ_P=1360 kg/m^3 in the UCFB
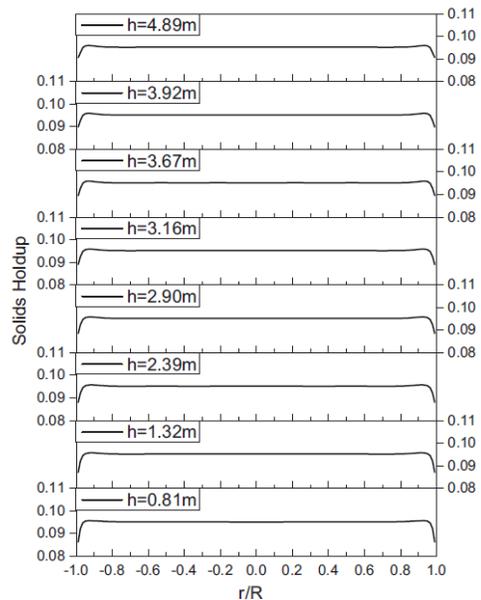
(b) Case #20-ρ_P=640 kg/m^3 in the DCFB

Fig. 6. Radial distributions of the solids holdup at different axial locations.

Figs. 7 and 8 show the radial distributions of solids holdup of different cases at h = 3.16 m in the UCFB and DCFB respectively. It can be seen from Fig. 7 that the radial distributions of the solids holdup for the particles with different densities and sizes have the same trend, lower at the central region and higher near the wall

Fig. 7. Radial distributions of the solids holdup in the UCFB of different cases.

Fig. 8. Radial distributions of the solids holdup in the DCFB of different cases.

(a) Case #9-ρ_p=1972 kg/m^3 in the UCFB

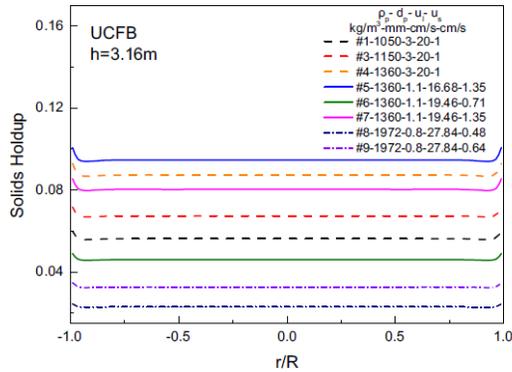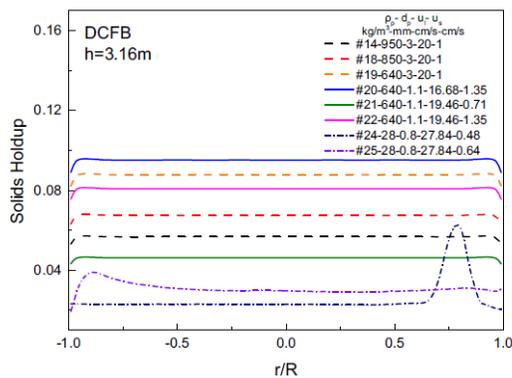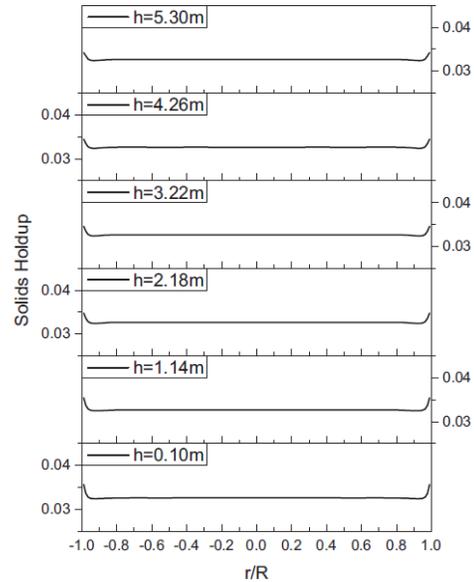(b) Case #25-ρ_p=28 kg/m^3 in the DCFB

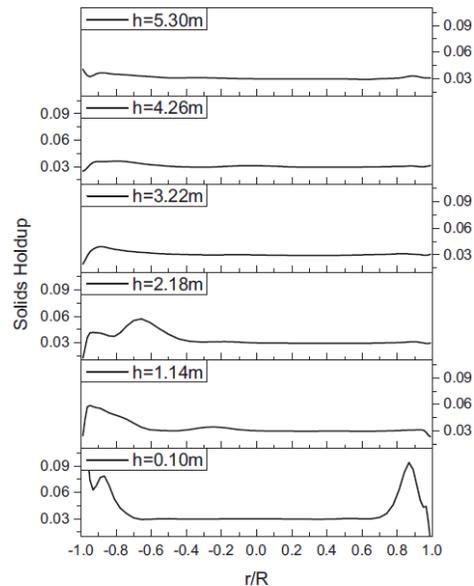Fig. 9. Radial distributions of the solids holdup at different axial locations.

region, in the UCFB. However, the radial distributions of the solids holdup for the particles with different densities and sizes in the DCFB are dilute at the near wall region and dense in the center except for the particles with a density of 28 kg/m^3 (cases #24 and #25). This is due to the fact that when $\rho_p < 300$ kg/m^3, the drag force on the lighter particles becomes different because of the deviation of the standard drag curve, leading to different particle flow behaviors (Karamanev and Nikolov, 1992).

It can be concluded based on the results from cases #1, #3, #4 and cases #14, #18, #19 that under the same operating conditions, the solids holdup increases with the increasing particle density in the UCFB and increases with the decrease of the particle density in the DCFB. Besides, from the cases #5–#7 in the UCFB and the cases #20–#22 in the DCFB, it is clear that under the same u_s, the average solids holdup decreases with the increase in u_l, and under the same u_l, the average solids holdup increases with the increase in u_s. These results are consistent with those shown in Fig. 2.

The radial distributions of the solids holdup at different bed heights for the particles with a density of 1972 kg/m^3 in the UCFB (case #9) and the particles with a density of 28 kg/m^3 in the DCFB (case #25) under the same operating condition are presented in Fig. 9. The particles used in case #9 and case #25 have the same density difference with the liquid. Unlike the results for cases in Fig. 6, there is no similarity for the solids holdup radial distributions between case #9 and case #25. The flow structures at each axial location of the bed for the case using the particles with a den-

sity of 28 kg/m^3 are asymmetrical. As mentioned before, this is mainly because when $\rho_p < 300$ kg/m^3, the drag force on the lighter particles becomes different. Vortexes in the solids phase are randomly generated in the DCFB and the positions of the vortexes change with the time. When a vortex is generated, the velocities of the particles within the vortex become lower, resulting in a
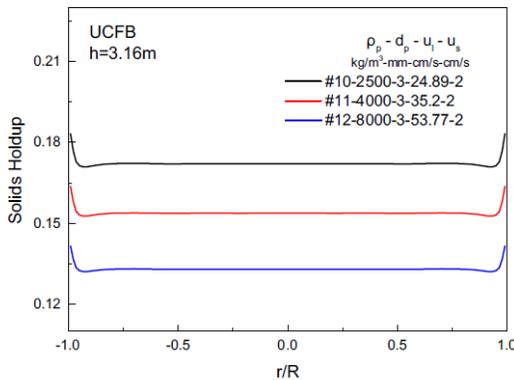
Fig. 10. Radial distributions of the solids holdup in the UCFB based on $u_l = 1 \times u_t$.

higher solids holdup in the region of the vortex. Because of the randomness and irregularity of the vortexes, the radial distributions of the solids holdup are irregular in the cases using the particles with a density of 28 kg/m^3.

Fig. 10 shows the radial distributions of the solids holdup at h = 3.16 m for cases #10–#12 where $u_l = 1 \times u_t$ in the UCFB. The radial non-uniformity for the solids holdup, which is lower at the riser center but higher near the wall region, can be clearly observed. Based on $u_l = 1 \times u_t$ and under the same d_p and u_s, the average solids holdup increases with the decrease in the particle density in the UCFB, which is also observed by Sang and Zhu (2012).
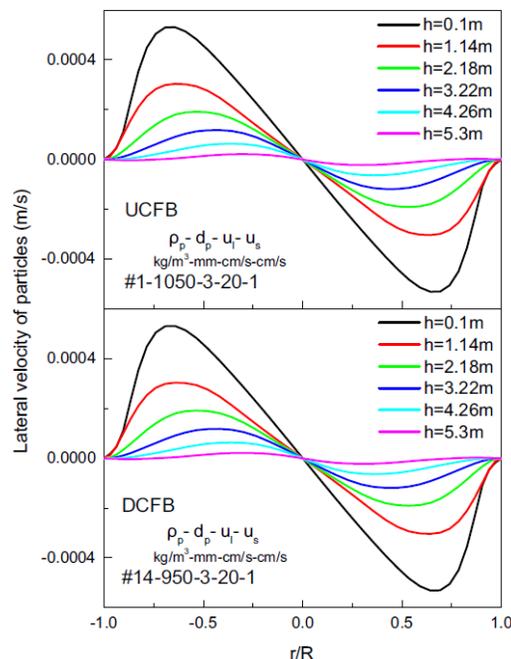

Fig. 11. Lateral velocities of the particles at different bed heights for case #1 in the UCFB and case #14 in the DCFB.

4.3. Lateral velocity of the particles

Fig. 11 shows the lateral velocities of the particles with a density of 1050 kg/m^3 in the UCFB (case #1) and the particles with a density of 950 kg/m^3 in the DCFB (case #14) at different bed heights under the same operating condition. The particles used in case #1 have the same liquid-solid density difference with the particles used in case #14. It is obvious from Fig. 11 that the lateral velocities of the particles at each bed height in case #1 are almost the same as those in case #14. Also, both in the UCFB and DCFB, the lateral velocities of the particles at each bed height are positive at the left hand side of the symmetry axis of the bed and negative at the right hand side. This means that the particles move from both the left hand side wall and the right hand side wall to the center of the bed, as also observed by Wang et al. (2014). Fig. 12 shows the velocity vectors of the lateral velocities of the particles at h = 0.2 m for case #1 and case #14. It is noticed that the lateral velocities of the particles increase from zero at the wall to a maximum value, and then decrease to zero at the center of the bed due to the boundary conditions. Furthermore, as shown in Fig. 11, the lateral velocities decrease along the axial flow direction and become nearly zero when the flow is fully developed. This indicates that the transverse mixing of the particles decreases gradually along the axial flow direction till the flow becomes fully developed.

The lateral velocities of the particles for different cases in the UCFB and DCFB at h = 2.18 m are shown in Fig. 13. It is obvious that the distributions of the lateral velocities of the particles in the UCFB are almost the same as those of the particles with the same liquid-solid density difference in the DCFB. From cases #1, #2 in the UCFB and cases #14, #15 in the DCFB, it can be seen that under the same operating condition and particle densities, the lateral velocities of the particles increase with the decreasing d_p. This is reasonable that under the same particle density, smaller d_p means lighter weight, which makes it easier for the particles to be accelerated to faster velocities by the liquid. Also, it can be concluded from cases #1, #3, #4 in the UCFB and cases #14, #18, #19 in the DCFB that under the same operating condition and particle size, the lateral velocities of the particles increase with the decreasing particle density in the UCFB and with the increasing particle density in the DCFB. Under the same u_l, u_s and d_p, the particles with lower density in the UCFB and the particles with higher density in the DCFB are more easily to be accelerated to higher lateral velocities by the liquid flow. Besides, based on cases #5–#7 in the UCFB and cases #20–#22 in the DCFB, it can be seen that under the same u_s, the lateral velocities of the particles increase with the increasing u_l, and under the same u_l, the lateral velocities of the particles increase with the increasing u_s. This is because that under the same ρ_p and d_p, the increase in u_l or u_s increases the kinetic energy of the liquid or particles flowing into the bed, leading to an increase in the motion of the particles in the bed.

Fig. 14 shows the lateral velocities of the particles with a density of 1972 kg/m^3 in the UCFB (case #9) and the particles with a density of 28 kg/m^3 in the DCFB (case #25) at different bed heights under the same operating condition. The particles used in case #9 and #25 have the same density difference with the liquid. Unlike the results shown in Fig. 13, there is no similarity of the lateral velocities of the particles between case #9 and case #25. The lateral velocities of the particles with a density of 28 kg/m^3 at different bed heights are random and irregular. Similar to the results shown in Fig. 9, due to the deviation of the standard drag curve for the lighter particles whose density is less than 300 kg/m^3, vortexes of the particles are randomly generated in the bed, leading to the irregular distributions of the lateral velocities of the particles (Karamanev and Nikolov, 1992).
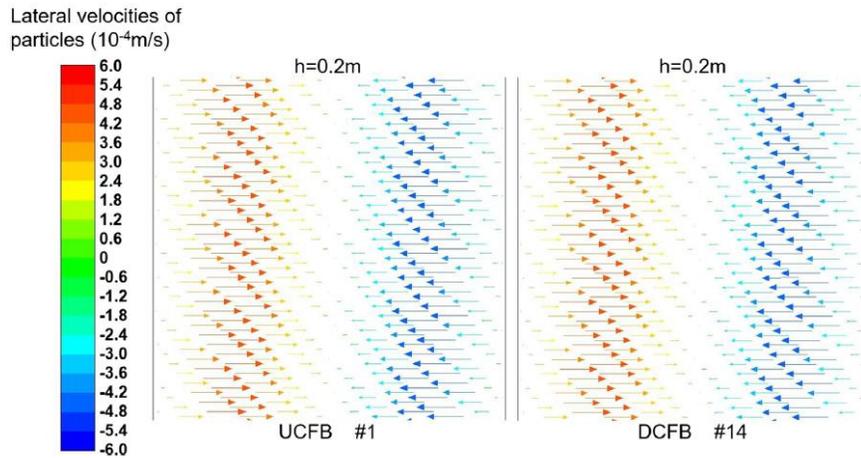
Fig. 12. Velocity vectors of the lateral velocities of the particles at h = 0.2 m for case #1 in the UCFB and case #14 in the DCFB.
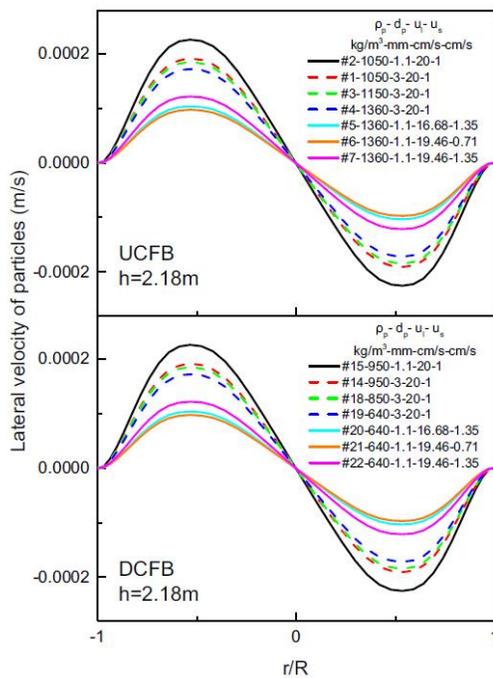
Fig. 13. Lateral velocities of particles in the UCFB and DCFB at h = 2.18 m.

Fig. 14. Lateral velocities of the particles at different bed heights for case #9 in the UCFB and case #25 in the DCFB.

Fig. 15 shows the lateral velocities of the particles for cases #10–#12 in the UCFB at h = 2.18 m based on $u_l = 1 \times u_t$. The distributions of the lateral velocities of the particles for cases #10–#12 have the same trend as the results shown in Fig. 13. Also, it can be observed that under the same d_p and u_s, particles with higher densities have higher lateral velocities in the UCFB based on $u_l = 1 \times u_t$. This is reasonable since under the same d_p and u_s, the kinetic energy of the particles increases with the particle density and the u_l.

4.4. Axial velocity of the particles

The axial velocities for the particles with a density of 1050 kg/ m^3 in the UCFB (case #1) and the particles with a density of 950 kg/m^3 in the DCFB (case #14) at different bed heights under the same operating condition are shown in Fig. 16. The particles used in case #1 in the UCFB have the same liquid-solid density difference with the particles used in case #14 in the DCFB. Obviously, at each bed height, the absolute values of the axial velocities of the

Fig. 15. Lateral velocities of the particles in the UCFB based on $u_l = 1 \times u_t$.

particles in case #1 are almost the same as those in case #14. It can be seen from Fig. 16 that the axial velocities of the particles are higher in the center than that near the walls. Due to the wall effect, both liquid and solids will have similar axial velocity distributions. Additionally, it can be seen that along the axial direction, the axial velocity distribution of the particles becomes steeper since the solids velocity is assumed as uniform at the inlet of the bed.

Fig. 17 shows the axial velocities of the particles for different cases in the UCFB and DCFB at h = 2.18 m. Obviously, the absolute values of the axial velocities of the particles in the UCFB are almost the same as those of the particles with the same liquid–solid den-

sity difference in the DCFB. It can be seen from cases #1, #2 in the UCFB or cases #14, #15 in the DCFB that under the same operating conditions and particle densities, the axial velocities of the particles increase with the decreasing d_p. As discussed before, under the same particle density, particles with smaller d_p have lighter weight, which makes it easier for the particles to be accelerated to faster velocities by the liquid. Also, from cases #1, #3, #4 in the UCFB or cases #14, #18, #19 in the DCFB, it is noticed that under the same operating condition and particle size, the axial velocities of the particles increase with the decreasing particle density in the UCFB and with the increasing particle density in the DCFB. This is mainly because that the particles with lower density in the UCFB and the particles with higher density in the DCFB are more easily to be accelerated to higher axial velocities by the liquid flow. In addition, it can be concluded based on cases #5–#7 in the UCFB or cases #20–#22 in the DCFB that under the same u_s, the axial velocities of the particles increase with the increasing u_l, and under the same u_l, the axial velocities of the particles increase with the increasing u_s. As mentioned before, this is due to the fact that the increase in u_l or u_s increases the kinetic energy of the liquid and solids into the bed, leading to the increase in the motion of the particles.

The axial velocities of the particles for cases #10–#12 in the UCFB at h = 2.18 m based on $u_l = 1 \times u_t$ are shown in Fig. 18. It can be seen that the axial velocities of the particles for cases #10–#12 have the same trend as the results shown in Fig. 17. Besides, it can be concluded that under the same d_p and u_s, the axial velocities of the particles increase with the particle density in the UCFB riser based on $u_l = 1 \times u_t$. As discussed before, under the same d_p and u_s, higher density and higher u_l lead to higher axial velocities of the particles.

Fig. 16. Axial velocities of the particles at different bed heights for case #1 in the UCFB and case #14 in the DCFB.
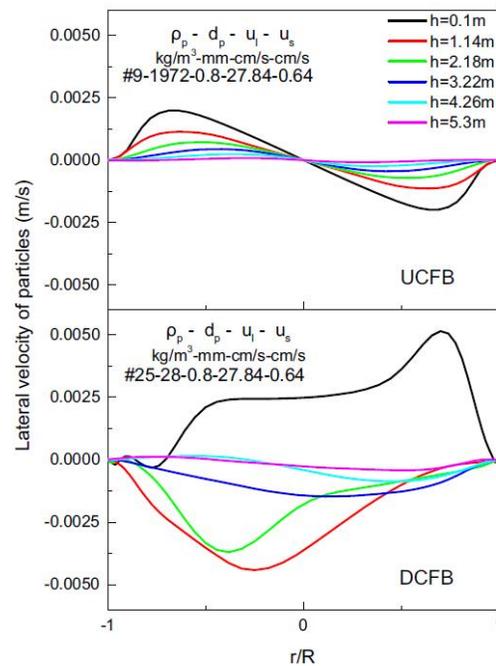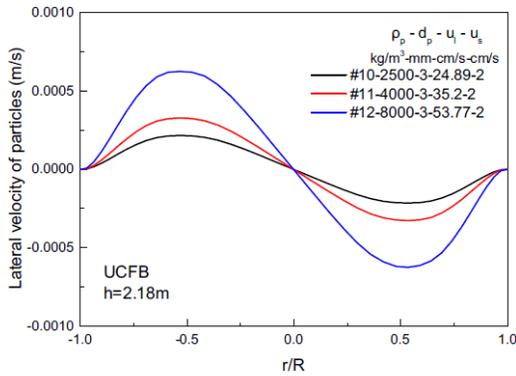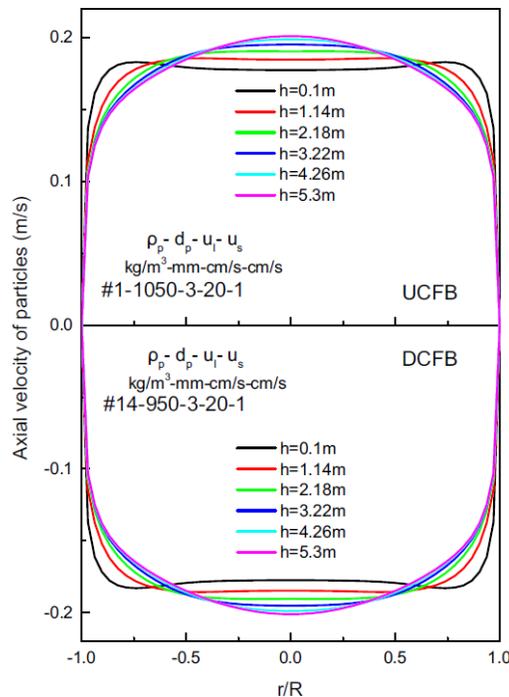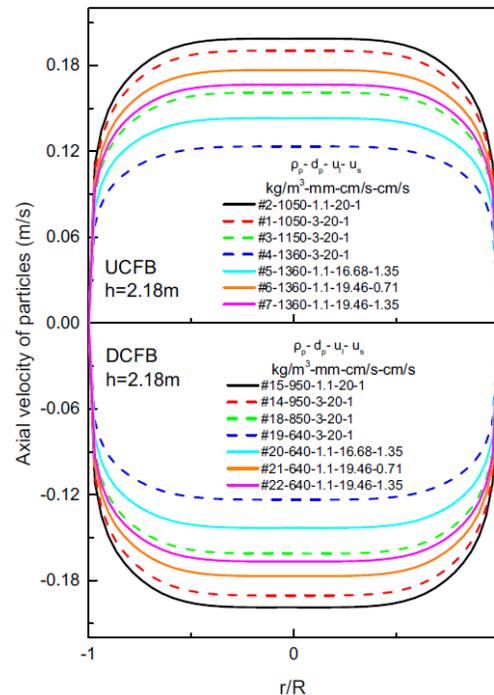

Fig. 17. Axial velocities of the particles in the UCFB and the DCFB at h = 2.18 m.
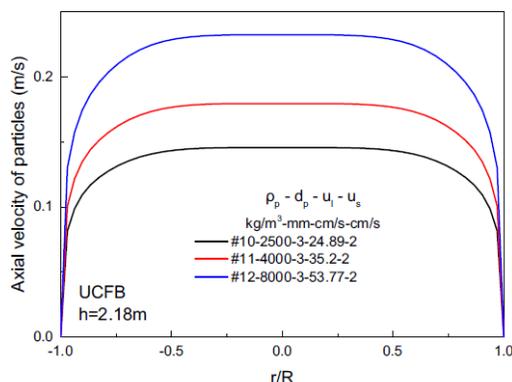
Fig. 18. Axial velocities of the particles in the UCFB based on $u_l = 1 \times u_t$.

4.5. Comparison between the numerical results and the results from the model by Sang and Zhu (2012)

Sang and Zhu (2012) proposed an empirical model to predict the average solids holdups for both the UCFB and DCFB. The model is shown as:

$$\bar{\varepsilon}_s = \frac{u_s}{\frac{u_l}{1-\bar{\varepsilon}_s} - 1.2u_t\left(1 - \bar{\varepsilon}_s\right)^{n-1}} \qquad (18)$$

where the exponent n can be determined from the following correlations:

$$n = \left(4.35 + 17.5\frac{d_p}{D}\right)Re_t^{-0.03} \qquad (19)$$

for $0.2 < Re_t < 1$,

$$n = \left(4.45 + 18\frac{d_p}{D}\right)Re_t^{-0.1} \qquad (20)$$

for $1 < Re_t < 200$,

$$n = 4.45Re_t^{-0.1} \qquad (21)$$

for $200 < Re_t < 500$,

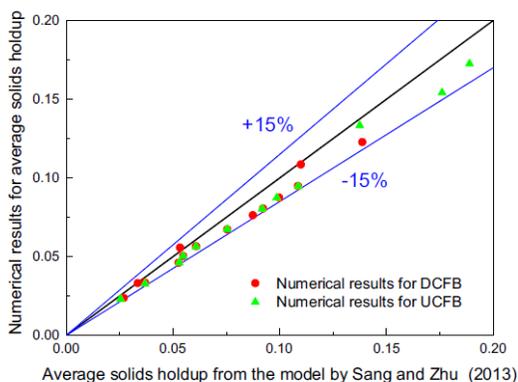$$n = 2.39 \qquad (22)$$

for $Re_t > 500$.

Fig. 19. Comparison between the numerical results and the results from the model by Sang and Zhu (2012).

As shown in Fig. 19, it can be noted that there is a good agreement between the results from the empirical model proposed by Sang and Zhu (2012) and the numerical results for the average solids holdup both in the UCFB and DCFB in this work. The matching degree between the model and the numerical results is greater than 85%, indicating that the model proposed by Sang and Zhu (2012) serves well to predict average solids holdup in both the UCFB and DCFB.

5. Conclusion

The liquid-solid two-phase flow characteristics in both the upward and downward circulating fluidized beds are compared by CFD approach. The two-dimensional Eulerian-Eulerian model incorporating the kinetic theory of granular flow is selected as the modeling technique and the CFD package Ansys/Fluent is the numerical platform used in this work. The following specific conclusions can be drawn from this work:

(1). A good agreement between the numerical results and the experimental data has been achieved.
(2). In this work, for the heavier particles having the same density difference with the liquid in the UCFB and DCFB, the hydrodynamic characteristics, such as the axial distribution of solids holdup, radial distribution of solids holdup, the lateral and axial velocities of the particles, are similar.
(3). Due to the deviation of the standard drag curve, the drag force on the lighter particles in the DCFB becomes different, leading to random and irregular particle flow behaviors.
(4). The numerical results for the average solids holdup in this work agree well with the results by an empirical model proposed by Sang and Zhu (2012). The matching degree between the numerical results and the model is greater than 85%, indicating that the model by Sang and Zhu (2012) serves well in prediction for the average solids holdup both in the UCFB and DCFB.

References

Cheng, Y., Zhu, J.X., 2005. CFD modelling and simulation of hydrodynamics in liquid-solid circulating fluidized beds. Can. J. Chem. Eng. 83 (2), 177–185.
Cheng, Y., Zhu, J., 2008. Hydrodynamics and scale-up of liquid-solid circulating fluidized beds: Similitude method vs. CFD. Chem. Eng. Sci. 63 (12), 3201–3211.
Couderc, J.P., 1985. Incipient fluidization and particulate systems. In: Davidson, J.F., Clift, R., Harrison, D. (Eds.), Fluidization. second ed. Academic Press, London, pp. 1–46.
Dadashi, A., Zhu, J.X., Zhang, C., 2014. A computational fluid dynamics study on the flow field in a liquid-solid circulating fluidized bed riser. Powder Technol. 260, 52–58.
Drew, D.A., Lahey, R.T., 1993. Particulate Two-Phase Flow. Butterworth-Heinemann, Boston.
Fan, L.S., Muroyama, K., Chern, S.H., 1982. Hydrodynamic characteristics of downwards fluidization in liquid-solid and gas-liquid-solid systems. Chem. Eng. J. 24 (2), 143–150.
Feng, Y.Q., Swenser-Smith, T., Witt, P.J., Doblin, C., Lim, S., Schwarz, M.P., 2012. CFD modeling of gas-solid flow in an internally circulating fluidized bed. Powder Technol. 219, 78–85.
Fluent, A., 2011. Ansys Fluent Theory Guide. ANSYS Inc., USA.
Jaberi, A., 2014. The hydrodynamic behavior of an inverse liquid-solid circulating fluidized bed. Master thesis. The University of Western, Ontario.
Johnson, P.C., Jackson, R., 1987. Frictional-collisional constitutive relations for granular materials, with application to plane shearing. J. Fluid Mech. 176, 67–93.

Karamanev, D.G., 1996. Equations for calculation of the terminal velocity and drag coefficient of solid spheres and gas bubbles. Chem. Eng. Commun. 147, 75–84.

Karamanev, D.G., Nikolov, L.N., 1992. Bed expansion of liquid-solid inverse fluidization. AIChE J. 38 (12), 1916–1922.

Liang, W.G., Zhang, S.L., Zhu, J.X., Jin, Y., Yu, Z.Q., Wang, Z.W., 1997. Flow characteristics of the liquid-solid circulating fluidized bed. Powder Technol. 90 (2), 95–102.

Liu, G.D., Yu, F., Lu, H.L., Wang, S., Liao, P.W., Hao, Z.H., 2016. CFD-DEM simulation of liquid-solid fluidized bed with dynamic restitution coefficient. Powder Technol. 304, 186–197.

Loha, C., Chattopadhyay, H., Chatterjee, P.K., 2012. Assessment of drag models in simulating bubbling fluidized bed hydrodynamics. Chem. Eng. Sci. 75, 400–407.

Luo, H., 2017. Numerical simulations of two-phase flows in the liquid solid circulating fluidized bed Master thesis. The University of Western, Ontario.

Montastruc, L., Brienne, J.P., Nikov, I., 2009. Modeling of residence time distribution: application to a three-phase inverse fluidized bed based on a Mellin transform. Chem. Eng. J. 148 (1), 139–144.

Nan, T., 2019. Hydrodynamics in inverse liquid-solid circulating fluidized bed PhD thesis. The University of Western, Ontario.

Pan, H., Chen, X.Z., Liang, X.F., Zhu, L.T., Luo, Z.H., 2016. CFD simulations of gas-liquid-solid flow in fluidized bed reactors-a review. Powder Technol. 299, 235–258.

Razzak, S.A., 2009. Hydrodynamic studies in liquid-solid and gas-liquid-solid circulating fluidized beds PhD thesis. The University of Western, Ontario.

Razzak, S.A., Barghi, S., Zhu, J.X., 2010. Axial hydrodynamic studies in a gas-liquid-solid circulating fluidized bed riser. Powder Technol. 199 (1), 77–86.

Renganathan, T., Krishnaiah, K., 2004. Liquid phase mixing in 2-phase liquid-solid inverse fluidized bed. Chem. Eng. J. 98 (3), 213–218.

Renganathan, T., Krishnaiah, K., 2005. Voidage characteristics and prediction of bed expansion in liquid-solid inverse fluidized bed. Chem. Eng. Sci. 60 (10), 2545–2555.

Richardson, J.F., Zaki, W.N., 1997. Sedimentation and fluidisation: part I. Chem. Eng. Res. Des. 75 (Supplement), S82–S100.

Roy, S., Dudukovic, M.P., 2001. Flow mapping and modeling of liquid-solid risers. Ind. Eng. Chem. Res. 40, 5440–5454.

Roy, S., Kemoun, A., Al-Dahhan, M.H., Dudukovic, M.P., 2005. Experimental investigation of the hydrodynamics in a liquid-solid riser. AIChE J. 51 (3), 802–835.

Sang, L., 2013. Particle fluidization in upward and inverse liquid-solid circulating fluidized bed PhD thesis. The University of Western, Ontario.

Sang, L., Zhu, J., 2012. Experimental investigation of the effects of particle properties on solids holdup in an LSCFB riser. Chem. Eng. J. 197, 322–329.

Sowmeyan, R., Swaminathan, G., 2008. Performance of inverse anaerobic fluidized bed reactor for treating high strength organic wastewater during start-up phase. Bioresour. Technol. 99 (14), 6280–6284.

Syamlal, M., O'Brien, T.J., 1989. Computer simulation of bubbles in a fluidized bed. AIChE Symp. Ser. 85 (1), 22–31.

Wang, S.Y., Sun, J., Yang, Q., Zhao, Y.Q., Gao, J.S., Liu, Y., 2014. Numerical simulation of flow behavior of particles in an inverse liquid-solid fluidized bed. Powder Technol. 261, 14–21.

Wang, S.Y., Wang, X.X., Wang, X., Shao, B.L., Ma, Y.M., Sun, Q.J., Zhao, J., 2018. Numerical simulation of flow behavior of particles in an inverse liquid-solid fluidized bed with a jet using CFD-DEM. J. Taiwan Inst. Chem. E. 82, 214–225.

Zhang, K., Wu, G.Y., Brandani, S., Chen, H.G., Yang, Y.P., 2012. CFD simulation of dynamic characteristics in liquid-solid fluidized beds. Powder Technol. 227, 104–110.

Zheng, Y., 1999. Flow structure in a liquid solid circulating fluidized bed PhD thesis. The University of Western, Ontario.

Zheng, Y., Zhu, J., 2003. Radial distribution of liquid velocity in a liquid-solids circulating fluidized bed. Int. J. Chem. React. Eng. 1, 1–8.

Zhu, J.X., Karamanev, D.G., Bassi, A.S., Zheng, Y., 2000. (Gas-) liquid-solid circulating fluidized beds and their potential applications to bioreactor engineering. Can. J. Chem. Eng. 78 (1), 82–94.

PARTICLE TECHNOLOGY AND FLUIDIZATION

A consolidated flow regime map of upward gas fluidization

Zeneng Sun [ID] | Jesse Zhu [ID]

Particle Technology Research Centre, Faculty of Engineering, The University of Western Ontario, London, Canada

Correspondence
Jesse Zhu, Particle Technology Research Centre, Faculty of Engineering, The University of Western Ontario, London, Canada.
Email: jzhu@uwo.ca

Abstract

A new flow regime map, resulting from more fundamental studies on the hydrodynamics and new flow regimes, is proposed in response to more practical reclassifications of the existing regimes with the development of upward gas-solids fluidization systems. The previously reported flow regime maps and flow structures of some widely used fluidized beds are carefully examined. To better reflect the industrial applications, the fast fluidization regime is reclassified as high-density and low-density circulating fluidization regimes. A consolidated flow regime map is then proposed where the flow regimes of upward fluidization expand to include new types of fluidized beds such as circulating turbulent fluidized bed and high-density circulating fluidized bed. The proposed flow regime map consists of six flow regimes: bubbling, turbulent, circulating turbulent, high-density circulating and low-density circulating fluidization, and pneumatic transport. The transitions between the regimes are discussed with new correlations proposed for fluid catalytic cracking type particles. Analysis on the dominating phase in the different types of fluidized beds reveals the dynamic change-over from solids phase continuous in conventional low-velocity batch/"fixed" fluidization operations to gas phase continuous in high-velocity continuous/"moving" fluidization operations and provides more insights to the transitions between the flow regimes for industrial design and practice.

KEYWORDS
dominating phases, flow structure, gas-solids fluidization, regime map, regime transition

1 | INTRODUCTION

Gas-solid fluidized beds, have been widely applied in chemical, energy and mining industries, biotechnology and pharmaceutical processes, and coating and physical processes.[1] Gas-solid fluidized beds can be categorized as either conventional or circulating fluidized beds (CFBs) distinguishing low-velocity operations from high-velocity operations. Conventional fluidization includes bubbling fluidized beds (BFBs) and turbulent fluidized beds (TFBs). These fluidized beds have been applied in coal gasification operations since the 1920s and later in catalytic processes.[2] The CFB was first proposed in the 1940s but only became fully commercialized in the 1960s for the catalytic cracking process and expanded into coal combustion processes in the 1980s.[3]

Over the years, both conventional and CFBs have become efficient venues for various multiphase reaction processes in the industry.[3,4]

Looking back to the history of fluidization technology, industries have benefited from the advantages of fluidized bed without having to wait for detailed theoretical studies. However, such practice has also resulted in failures and difficulties in some processes such as the scale-up issue in an earlier Fischer-Tropsch process.[4] Recognizing such shortcomings, industrial practitioners began to pay more attention to the hydrodynamic studies and have called for more fundamental understanding on the operating patterns of fluidized beds. Presently, more details have been understood on the operating patterns and the flow regimes inside various types of fluidized beds. A series of classifications and correlations for the upward gas

fluidization flow regimes have been proposed and research has gradually caught up with the pace of industrial developments.[5-8]

The demand for quantifying the transitions between different regimes gave rise to regime mapping with early results being presented as two-dimensional (2D) diagrams of the fluidization regimes.[9-14] Figure 1 shows several typical 2D flow regime maps before 2000 with the coordinate systems based on their own purposes for representing the fluidization regimes. Grace's map[8] with dimensionless superficial gas velocity plotted against dimensionless particle diameter superimposes many gas-solid systems as shown in Figure 1a. However, the use of this map in industrial processes is not always straightforward for high velocity operations of the circulating beds and the transport reactors because it originated from conventional fluidizations so that the solids flux is only used as a secondary parameter. An alternative phase diagram for fluidization regimes is by plotting the solids circulation rate against the superficial gas velocity, which gives a more straightforward representation in term of the operating conditions.[9] Based on the G_s–U_g coordinate system, such maps as shown in Figure 1b,c give more emphases on the higher velocity flow regimes, primarily after fast fluidization, so that the conventional fluidization regimes are not well presented and the higher bed density operations were not included.[12,14]

Moreover, most of the flow regime maps were proposed before 2000 when the definition of the fast fluidization regime was yet to be accurately agreed upon.[9-17]

Firstly, a high-density circulating fluidized bed (HDCFB) has been separately identified and fundamentally studied as a newer type of fluidized bed. The HDCFB operates under higher gas velocity and higher solids flux resembling the fluid catalytic cracking (FCC) conditions.[18,19] Although the commercial applications and the operating patterns of HDCFBs had been fully developed in industry thanks to the bloom of oil refinery in the 20th century, there was not much work on HDCFB reported in the literature prior to the 1990s. Before that, HDCFB has been paid little attention to or largely ignored in academic studies only until Zhu and Bi[19] distinguished it from the conventional low-density circulating fluidized bed (LDCFB) operations suggesting that HDCFB was more representative of the hydrodynamics in the FCC process. Since then, many studies have been carried out on the HDCFB riser reactor leading to many publications such as Isaangya et al,[20] Parssinen and Zhu,[21] Wang et al,[22,23] and Hensler et al.[24] A dense suspension upflow regime has also been proposed by Grace et al[25] to characterize the operations in HDCFB risers.
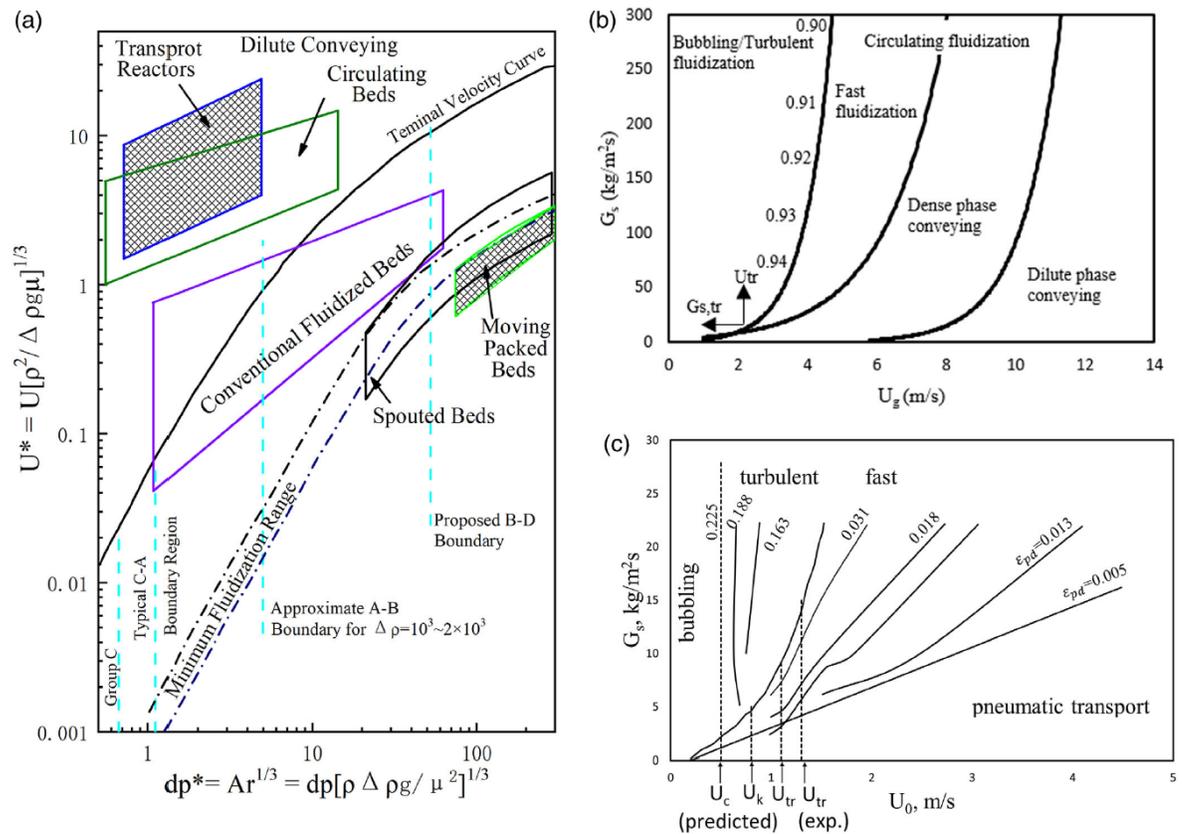
FIGURE 1 Previously reported two-dimensional fluidization regime maps: (a) from Grace[8]; (b) from Bai et al[12]; (c) from Horio and Ito[14] [Color figure can be viewed at wileyonlinelibrary.com]

Another fluidized bed flow regime named circulating turbulent fluidized bed (CTFB) was proposed in 2008.[26,27] CTFB combines the advantages of the denser condition of TFBs with the near plug flow conditions of CFB risers. It is interesting that, unlike the HDCFB risers whose theoretical understanding came after they had been put to practice, CTFB was firstly envisaged in the laboratory prior to any industrial applications. The CTFB was conceived purely from the hypothesis that it is theoretically feasible to combine the TFB and CFB riser in a single unit. The concept was successfully tested in the laboratory,[26-28] and now on its way to potential pilot plant testing. The CTFB fluidization regime was a result of studies showed that such a new type of fluidized bed at high solids fluxes and relatively low superficial gas velocities has much denser and more uniform solids suspensions as well as rather limited solids backmixing. When it comes to the flow regime map, CTFB acts as a new regime which blurs the boundary between the conventional "static" fluidization and circulating fluidization regimes. In industry, CTFB also shows the potential of becoming an ideal gas-solid catalytic reactor for gas-phase catalytic reactions with quick catalyst deactivation such as the FCC process. Representing the desirable high-density operations, HDCFB and CTFB have not yet been well presented in the fluidization regime maps.[28,29] It is important to point out that for the high-density CFB operations, superficial gas velocity alone is not sufficient to distinguish the flow regimes. For example, the transition from HDCFB to LDCFB relies on knowing both the solids flux (G_s) and the superficial gas velocity (U_g). A regime map encompassing both the conventional and high-velocity fluidization regimes and includes the impacts of both the solids flux and the superficial gas velocity would be more practicable for the operations of the fluidized bed.

With the development of higher-density fluidization also comes a desire to remap the flow regimes from the view of the suspension density in addition to the transitional velocity alone. As a wider range of upward gas-solid operations become identified, an improved regime map with more specifics on the high-density conditions is needed. In this work, a consolidated flow regime map with well-defined flow regime boundaries is proposed. The understanding of the underlying phenomena in the flow regimes further allows for successes in design, optimization, and scale-up. Prospects for other potential applications of fluidized beds are improved by the proposed well delineated regime map.

## 2 | THE 2D MAP FOR THE TRADITIONAL FLUIDIZATION REGIMES

Traditionally, a gas-solid fluidized bed goes through particulate, bubbling (in some cases, slugging), turbulent, fast fluidization, and pneumatic transport as the gas velocity increases. The particulate regime which only occurs for Group A particles over a small range of the gas velocity and the slugging regime which only occurs when the reactor size is very small, have no or very limited commercial applications.[4,30] A transport velocity, U_{tr}, is defined as the superficial gas velocity when substantial solids entrainment is observed. U_{tr} divides gas-solid

fluidization into conventional low-velocity fluidization and high-velocity fluidization. Bubbling and turbulent regimes are presented in the conventional low-velocity fluidized beds. Conventional fluidized beds are also called batch or "fixed" fluidized beds because of their relatively low solids entrainment when compared with CFBs. High-velocity fluidization includes the fast fluidization regime and the pneumatic transport regime. CFB riser is the main application of high-velocity fluidization with most of the operations in the fast fluidization regime. The pneumatic transport regime operates beyond a transition gas velocity, U_{tp}, and is more commonly used for physical processes such as solids conveying. The high-velocity fluidized bed is also considered as the continuous or "moving" fluidized bed in contrast to the conventional batch or "fixed" fluidization since solids are continuously carried in and out of the fluidized bed under high U_g. Bubbling, turbulent, fast fluidization and pneumatic transport depicted in Figure 2 are presently considered as the most useful fluidization regimes.

As fluidization expands into the high-U_g regimes, the bed density becomes another important variable in dictating fluidization conditions. In fluidization operations from denser to dilute conditions, the bed density is a function of both the solids flux (G_s) and the superficial gas velocity (U_g). This requires the presentation and the demarcation of the flow regimes in a 2D U_g–G_s coordinate system. Such a 2D map of the flow regimes is proposed (Figure 3) for the upward gas-solid fluidization for Group A particles (FCC). At the bottom of the 2D regime map, a one-dimensional (1D) sketch of the fluidization operations in each flow regime is also plotted based on superficial gas velocities for a better illustration. The average bed solids holdup (ε_s) under different operating conditions from the experiments over the past 20 years are also marked on the map and listed in Table 1.[31-36] Two typical operating parameters, the apparent solids velocity ($U_s = G_s/\rho_p$) and the superficial gas velocity (U_g), are selected as the coordinate system for more direct interpretation. The high-velocity fluidization regimes including the operations of CFB risers and pneumatic transportation, spread over a large range of U_g and G_s. The conventional fluidization regimes including the bubbling bed regime and turbulent bed regime are located in the black squared region near the
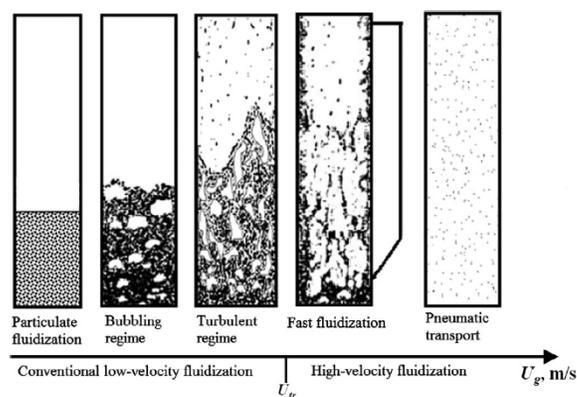
FIGURE 2   The traditional flow regimes for upward gas-solid fluidization systems
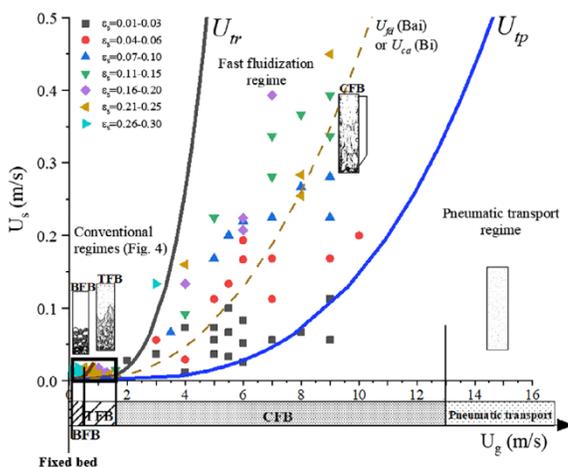
FIGURE 3 Two-dimensional diagram of the fluidization regimes for typical FCC particles with a one-dimensional sketch located at bottom (data sources: Table 1). BFB, bubbling fluidized bed; CFB, circulating fluidized bed; FCC, fluid catalytic cracking; TFB, turbulent fluidized bed [Color figure can be viewed at wileyonlinelibrary.com]

TABLE 1 Data used in Figures 3, 7–8, and 9

| Authors	Solids	d_p, μm	ρ_p, kg/m³	U_g, m/s	G_s, kg/m² s
Issangya[31]	FCC	70	1,600	4–8	14–425
Yan[32]	FCC	67	1,500	3.5–10	50–550
Zhu[33]	FCC	65	1,780	0.06–8	0–400
Li[34]	FCC	60	1,370	2–5	50–100
Wang[35]	FCC	76	1,780	5–9	100–1,000
Liu[36]	FCC	78	1,780	0.3–1.2	0–300

Abbreviation: FCC, fluid catalytic cracking.

origin of Figure 3. Two other transition velocities defined by other researchers are also marked by the dotted line in regime map and will be discussed in detail in later sections.[12,13]

2.1 | The conventional low-velocity fluidization regimes

The conventional low-velocity fluidization regimes (black square in Figure 3 and zoomed in Figure 4) consists of the bubbling bed and turbulent bed operations under low gas velocities (usually less than 1.5 m/s for FCC particles). As there is a very small amount of solids flux in the conventional fluidized bed, they do occupy a small area near the origin with $G_s > 0$ in the upward gas fluidization map as shown in Figure 3. As Figure 4 shows, after minimum fluidization ($U_g > U_{mf}$), and possibly after a short period of particulate fluidization of Geldart Group A particles, the bubbling regime starts with gas bubbles formed above the gas distributor.[37] The transitional velocity, U_c, is the superficial gas velocity that starts the transition from bubbling regime to turbulent regime. At U_c, the fluctuations of bed pressure
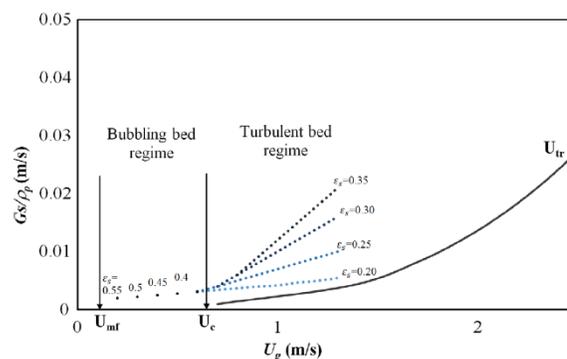
drop reach a maximum.[16,38] Irregular and smaller voids replacing gas bubbles in the turbulent bed provide excellent gas-solid contacting and relatively uniform solids distribution compared to the bubbling bed.[4] Both the bubbling bed and turbulent bed have a higher bed density than the high-velocity fluidized beds. Applications like coking, coal combustion, acrylonitrile production, the Fischer-Tropsch process, and many other catalytic reactions can be carried in the conventional regimes for easier operations and effective mass transfer.[1]

2.2 | The high-velocity fluidization regimes

The fast fluidization regime and the pneumatic transport regime have been considered as the high-velocity fluidization regimes in contrast to the low-velocity conventional regimes. In Figure 3, the fast fluidization regime starts beyond the transport velocity, U_{tr}, when a sharp increase of the particle carryover occurs and the slip velocity reaches a maximum.[16,39] However, the upper boundary of the fast fluidization process is unclear due to the different understandings of the "fast bed" operations, as discussed later.

Although lacking a clear and consistent definition, the major characteristics reported for the fast fluidization regime are similar. Beyond U_{tr}, sufficiently high gas velocity triggers a substantial entrainment of the particles so that continuous solids feeding at the CFB riser bottom becomes necessary. A higher slip velocity and obvious radial non-uniformity are found in the fast fluidized bed due to particle aggregation.[16,40] Also due to particle aggregation, the solids flow still has significant backmixing although much is reduced compared to conventional fluidized beds. The gas flow can be considered to be in plug flow because of the high velocity. The CFB reactor is the key application of the fast fluidization regime. Reactions taking place in the CFB riser not only achieve a high throughput capacity, but also maintain sufficient solids loading and good gas-solid contacting.[41]

Further increasing the gas velocity leads to a very dilute suspension flow in the pneumatic transport regime where both the axial and radial distributions of the solids holdup are uniform. The pneumatic

FIGURE 4 Two-dimensional diagram of the conventional fluidization regimes (for FCC particles, data from Zhu[33] and Liu[36]). FCC, fluid catalytic cracking [Color figure can be viewed at wileyonlinelibrary.com]

transport regime starts at the transition velocity, U_{tp}, beyond the fast fluidization regime as shown in Figure 3. This is similar to V_{mp} as proposed by Bi and Grace,[13] and U_{pt} by Bai et al.[12] The inflection of the pressure gradients is the most remarkable characteristics signifying the start of the pneumatic transport operation when the frictional pressure drop gradually overtakes the dynamic pressure drop.[42] This unique phenomenon in the pneumatic transport process plays an important role in optimizing the design and operation of dilute solids conveying systems.[43-45]

2.3 | Issues on the definitions of the fast fluidization regime

The definition of the fast fluidization regime is still not clear many years after Yerushalmi et al[39] first proposed the concept of fast fluidization in contrast to the conventional low-velocity fluidization operations. The onset velocity of the fast fluidization regime, U_{tr}, is well accepted although its definition is largely experimental. However, there is still no precisely justified upper boundary of the fast fluidization regime due to the various understandings of "fast bed" operations. The 2D diagram of flow regimes can be divided into four regions by the transition velocities as shown in Figure 5. Clearly, region ① and region ④ represent the operations of the conventional fluidized beds with the upper boundary, U_{tr}, and the pneumatic transportation with the lower boundary U_{tp}, respectively. The area between U_{tr} and U_{tp} represents the operations of CFB risers where the conventional fast fluidization regime (region ②) is encompassed with its unclear upper boundary. A number of the upper transition velocities for the fast fluidization regime such as U_{fd} and U_{ca} (dotted lines in Figure 5) have been proposed.[12,13] Although these transition velocities are defined differently, they appear to divide the area between U_{tr} and U_{tp} into two regions (region ② and region ③), and on
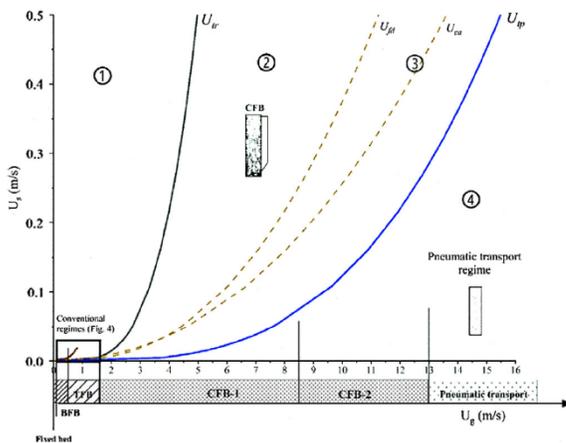
FIGURE 5 Four regions on the 2D diagram of upward gas fluidization for Group A (FCC) particles. BFB, bubbling fluidized bed; CFB, circulating fluidized bed; FCC, fluid catalytic cracking; TFB, turbulent fluidized bed [Color figure can be viewed at wileyonlinelibrary.com]

the 1D sketch CFB-1 and CFB-2 operations are marked for these two regions respectively as shown in Figure 5. Region ② can be considered as the "conventional" fast fluidization regime based on the initial concept from Yerushalmi et al.[39] Region ③ represents CFB risers which are more dilute as they operate at relatively higher U_g. The boundary between region ② and region ③ has never been clearly defined, nor the nature of the flow conditions in region ③.

Region ② has often been taken as the conventional fast fluidization regime, while region ③ is considered as the "dilute phase flow regime" in the contrast to being absence of solids refluxing near the wall in CFB risers as suggested by Bi and Grace.[13] CFB risers in the conventional fast fluidization region (region ②) have intensive solids refluxes near the wall and both axial and radial dispersions. There is little refluxing flow and therefore the absence of solids backmixing in CFB risers operated in region ③.[25] Considering presence or absence of solids backmixing, the boundary between region ② and region ③ was defined as the type A chocking velocity, U_{ca}, by Bi and Grace.[13]

Region ③ was sometimes considered as the "dense phase conveying regime" with an axial uniform but radial core-annulus flow structure as compared to the pneumatic transport regime.[12,30] The shape of axial solids holdup profile has also been used to differentiate the conventional fast fluidization region (region ②) and the "dense phase conveying" region (region ③).[46,47] The conventional fast fluidization (region ②) has a typically S-shaped solids concentration profile with a dense bottom in the fluidized bed. A more uniform axial solids distribution also known as the exponential solids concentration profile is considered as representative in the CFB risers operated in region ③. The boundary between region ② and region ③ has also been correlated by the gas velocity, U_{fd}, by Bai et al.[12]

Table 2 summarizes reported flow conditions for risers in region ② and region ③ as well as in region ① and region ④ and the transitions between the regimes. The different criteria given for the transitions to region ③ lead to considerable confusions on the definitions of the boundary between the conventional fast fluidization regime (region ②) and region ③. Various and sometimes even contradictory terminologies for region ③ such as the "dense phase conveying" or the "dilute phase flow" further aggravated the confusions when characterizing this region. Simply separating out region ③ by the differences from the axial solids holdup profile as proposed from Bai et al[12] is inaccurate because many other factors also affect the flow structure in high-velocity fluidization. For example, although the S-shaped solids concentration profile with a dense bottom is commonly seen in CFB risers, it cannot be considered as an inherent characteristic of CFB risers in the conventional fast fluidization regime (region ②). The presence of the bottom denser region in a CFB riser can be artificially adjusted by changing the pressure head and the solids inventory in the solids returning system.[13,50] Therefore, although it seems like there exists a boundary between region ② and region ③, it is hard to distinguish the operating modes in a CFB between these two regions with such an ambiguous boundary.

From the view of actual operations, any given flow regime has to represent a certain type of fluidized bed with distinctive features and fully developed flow structures.[51] However, the CFB riser reactor, as the main application of fast fluidization, can operate in either region ②

TABLE 2 Literature descriptions of flow regimes in high-velocity fluidization operations

Authors	Regime name and transition mark			
On 2D map	①	②	③	④
In 1D sketch	Conventional fluidization	CFB-1	CFB-2	Pneumatic transport
Lewis et al[48]	Batch fluidization	Continuous fluidization		
Yerushalmi and Cankurt[16]	Conventional fluidization	Fast fluidization	Transport riser reactor/dilute phase flow	Pneumatic transport
	①–② boundary U_{tr}	②–③ boundary $U_{slip,max}$		
Takeuchi et al[10]	Conventional fluidization	Fast bed	Dilute phase flow	Dilute phase flow
	①–② boundary U_{tr}	②–③ boundary $U_{fd}, G_{s,tr}$	③–④ boundary U_{pt}	
Rhodes and Geldart[49]	Conventional fluidization (dense phase transport)	Fast fluidization	Dilute phase transport with reflux	Co-current dilute phase transport
	No correlated transitional gas velocity			
Bai et al[12]	Conventional fluidization	Fast fluidization	Dense phase conveying	Dilute phase conveying
	①–② boundary U_{tr}	②–③ boundary $U_{tf}, G_{s,tr}$	③–④ boundary U_{pt}	
Bi and Grace[13]	Conventional fluidization	Fast fluidization	Core-annular dilute phase flow	Homogenous dilute phase flow
	①–② boundary V_{cc}	②–③ boundary V_{ca}	③–④ boundary V_{mp}	
Grace et al[25]	Conventional fluidization	Fast fluidization and dense suspension upflow (DSU)	Heterogenous refluxing flow	Homogenous dilute phase flow/dilute pneumatic conveying
	①–② boundary U_{dsu} or V_{cc}	②–③ boundary V_{ca}		
Bi and Grace[42]	Conventional fluidization	Dense phase flow	Fast fluidization	Heterogeneous dilute phase flow
	①–② boundary U_{fd}	②–③ boundary U_{ca}	③–④ boundary U_{mp}	
This work	Conventional fluidization	High-density CFB Low-density CFB	Pneumatic transport	
	Transitional velocity U_{tr}	Transitional velocity U_{tp}		

Abbreviation: CFB, circulating fluidized bed; DSU, dense suspension upflow.

or region ③. For example, the operating window of the FCC CFB riser stretches over region ② and region ③ since it typically can operate under a wide range of U_g from 6 to 28 m/s.[19] On the other hand, the operating window of the CFB combustor will extend from the bottom of region ② to region ③ if more bed material is circulated because the increased G_s needs a higher U_g to support.

As a result, neither region ② nor region ③ can be strictly considered as an individual flow regime since both of the two modes are not operationally independent and statistically steady.[11,25] The separation of region ② and region ③ is also not sufficiently useful for industrial design and operations. These confusions in the operating modes have driven us to doubt the practical significances of the fast fluidization regime itself.

3 | REGIMES OF CIRCULATING FLUIDIZED BEDS

3.1 | The definition of the CFB operating region

Based on careful and more in-depth studies on the CFB riser of wide operating ranges, we hereby propose in Figure 6 a combined and single circulating fluidization operating region that includes both region ② and

region ③, which better represent its industrial applications. The two major operations of the CFB reactor, the FCC process and the CFB combustion, both operate across over region ② and region ③ without any sign of transition and with an ambiguous boundary. The FCC CFB riser operates under higher density conditions with higher U_g (6–28 m/s) and higher G_s (400–1,200 kg/m^2 s) so that it is located in the upper area on the regime map between U_{tr} and U_{tp}.[19] In contrast, the CFB coal combustor riser operates under low-density conditions with relatively lower U_g (5–9 m/s) and lower G_s (50–150 kg/m^2 s) so that it occupies the bottom area on the regime map. Clearly both FCC CFB riser and circulating fluidized bed combustor (CFBC) reactor can operate in either region ② or region ③ as Figure 6 shows. The ambiguous boundary between region ② and region ③ becomes really unnecessary in distinguishing the different types of CFBs in industrial uses. On the other hand, the operating modes of the FCC riser and the CFBC reactor on the regime map also actually point to the potential of distinguishing the operating regimes based on the solids suspension density.

To correspond to the two major applications of CFB reactor, it is perhaps more practical and theoretically sounder to characterize the CFB operating region by the average bed density. The CFB operating region can be further "vertically" divided into two regimes on the regime map: the LDCFBs regime and the HDCFBs regime as shown in

Figure 7. The CFBC combustor can be considered as the typical industrial application operating in the LDCFB regime for its low solids circulating rate. Correspondingly, the FCC processes usually operate in the HDCFB regime with higher G_s. The HDCFB regime was originally proposed in the literature in 1995, although the industrial operations of the high-density CFB in the FCC processes have long been implemented since the 1960s.[52] Afterwards, more academic research on gas-solids fluidization turned from covering the LDCFB regime to the HDCFB regime and over 100 papers have been published.

3.2 | HDCFB regime versus LDCFB regime

Although HDCFB and LDCFB share some common characteristics, the evidently different overall bed densities and flow structures make
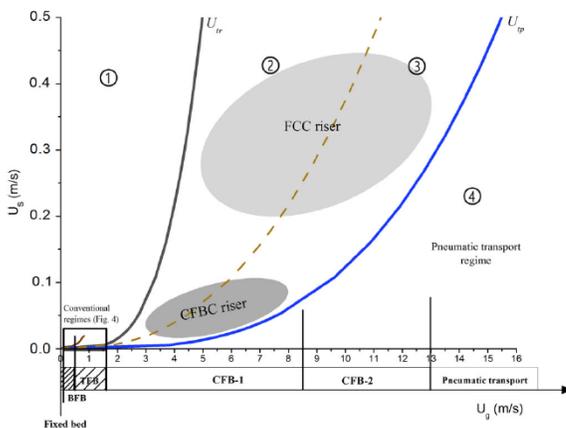

FIGURE 6 Operating windows of the major CFB applications on the 2D diagram. BFB, bubbling fluidized bed; CFB, circulating fluidized bed; CFBC, circulating fluidized bed combustor; FCC, fluid catalytic cracking; TFB, turbulent fluidized bed [Color figure can be viewed at wileyonlinelibrary.com]

it necessary to have a clean distinction between the high-density and low-density operation patterns on the regime map to make it more suitable for commercial use and design. The overall bed solids holdup (ε_s) over the whole height of the riser appears to be a more favorable and more straightforward parameter for separating the HDCFB and LDCFB regimes in regard to the practical operating conditions. A series of fitted average bed solids holdup lines from dilute to denser conditions are also plotted in Figure 7. A transitional average bed solids holdup, $\varepsilon_s = 0.10$, is selected to divide the CFB operating region into the LDCFB and HDCFB regimes[22] with the LDCFB regime located at the bottom and the HDCFB regime occupying the upper area.[22,23,53,54]

The key difference between the two different CFB regimes, HDCFB and LDCFB regimes, lies in the overall bed density and therefore different flow structures in CFB risers. In the LDCFB riser, high-U_g and low-G_s conditions lead to a low overall bed density and a dilute gas-solids suspension flow. The overall bed solids holdup is usually less than 0.10 due to the low solids circulation rate. The axial solids holdup profile in LDCFB risers is found to have an exponential shape, although an S-shape profile is commonly seen in the CFB combustion risers due to the splitting of a portion of the fluidizing airflow with some entering above the bed bottom zone.[50] The radial profile of the solids holdup in the LDCFB riser gives the riser a "core-annulus" structure with a flat concentration profile in a dilute core region and a gradual increase in solids concentration towards the wall. In the HDCFB riser, the high-density operation results in a higher overall bed density and a greater bed pressure drop. The overall riser solids holdup is usually greater than 0.10 under high G_s conditions and even reaches 0.30 when G_s is extremely high (usually $G_s > 700$ kg/m^2 s).[22] The axial profiles of particle velocity and solids holdup in the HDCFB riser become more uniform with increasing G_s. In contrast, the radial profiles of the particle velocity and solids holdup become less uniform with the dilute core region shrinking dramatically. Compared to the LDCFB, the typical radial "core-annulus" profile of the solids holdup described above transitions to a concave parabolic profile where the solids holdup can

FIGURE 7 Expanded two-dimensional diagram of CFB operating region with fitted average bed solids holdup lines (data sources: Table 1). CFB, circulating fluidized bed; HDCFB, high-density circulating fluidized bed; LDCFB, low-density circulating fluidized bed [Color figure can be viewed at wileyonlinelibrary.com]
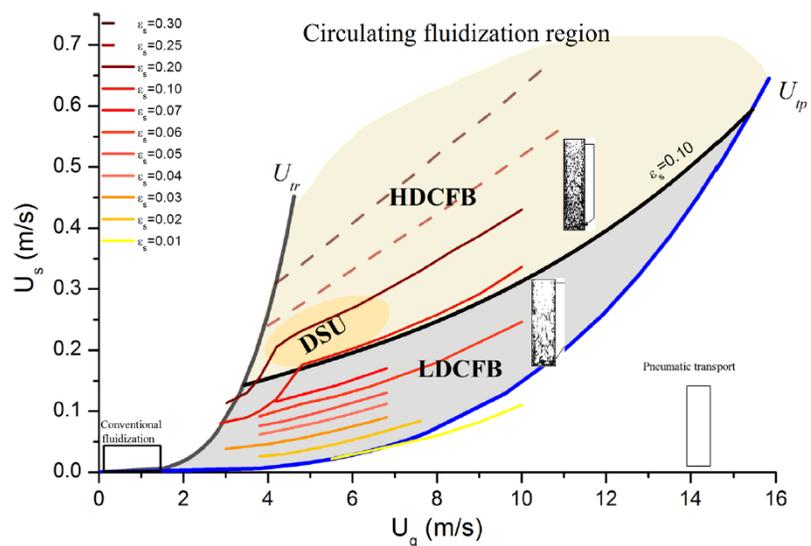
reach as high as 0.35 and even 0.5 at the wall under extremely high G_s in the HDCFB.[22] A higher overall bed density is achieved by HDCFB for its longer entrance region and much wider wall layer with higher solids holdup.[22,41] As far as solids flux pattern is concerned, intensive gas-solids interaction and less net downward flow near the wall are also detected in the HDCFB riser, which are favorable for reducing backmixing and intensifying gas-solids contact.[41,54] Under higher solids flux, more detailed studies on HDCFB revealed significant differences of HDCFB risers from LDCFB risers regarding with the reaction conversions.[41] The overall bed density affected by both U_g and G_s in a CFB riser becomes the dominant factor to the overall conversion of gas-phase catalytic reactions such as FCC process, because a higher solids holdup provides with more gas-solids contacting area and mass transfer.[41,54]

On the other hand, the demarcation of the conventional fast fluidization regime relying more on the increase of superficial gas velocity without a clear upper boundary, is not able to distinguish the operations related to HDCFB and LDCFB which have distinctive differences in hydrodynamics and reaction performance due to the increase of the overall bed density. The replacing of the traditional fast fluidization regime and region ③ on Figure 6 by the CFB operating region adds more practical significances to the regime map. The division between the two CFB regimes, HDCFB regime and LDCFB regime, more clearly distinguishes the two major applications of CFB reactors based on the overall bed density. On the other hand, the high-density conditions of HDCFB regime have broadened the range of the conventional fast fluidization to a higher G_s.
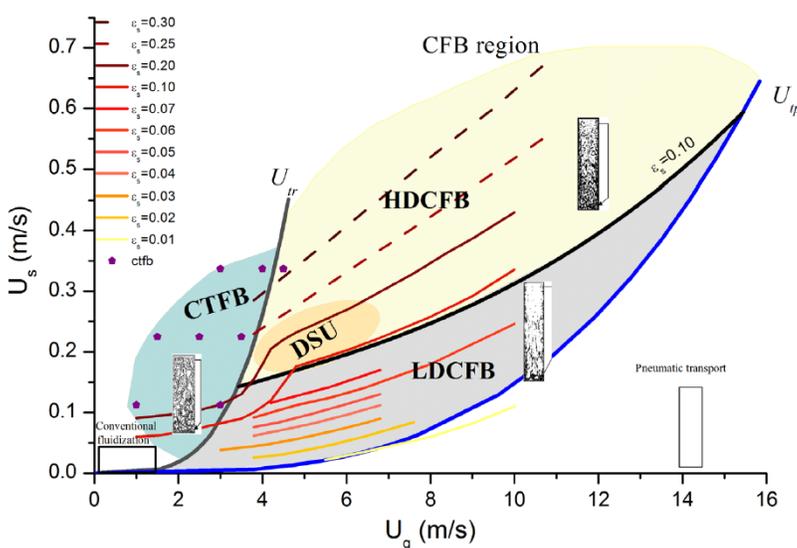
4 | THE CIRCULATING TURBULENT FLUIDIZATION REGIME

A new type of fluidized bed, the CTFB, is added as a new regime connecting the conventional fluidization regimes and the CFB regimes in the regime map in Figure 8. To benefit from the advantages of both the TFB and CFB, the CTFB was firstly proposed in 2008[26] from the theoretical hypothesis that a CFB can be operated below the transport velocity, U_{tr}, if sufficient pressure head is provided. Unlike the HDCFB regime which was only distinguished from the LDCFB regime after being in industrial use for a long time, the operating mode of CTFB regime was first conceived with any industrial practices to "fill in" the "empty area" below U_{tr} with sufficient G_s, and then experimentally studied and proposed for potential industrial applications in the future.[27]

CTFB combines the advantages of CFB and TFB as its name implies: It operates at relatively lower U_g corresponding to the TFB operation but with solids circulation fluxes comparable to that of CFB operations. A high overall bed density is achieved in the CTFB thanks to the denser operating condition, resembling a TFB operation with external solids circulation. On the other hand, CTFB reduces the intensity of solids back mixing and achieves a much more uniform flow structure than the TFB due to the circulation of solids.[26-28] The continuous high-density operation at superficial gas velocities below U_{tr} achieved by the CTFB mode is a fairly recent addition to fluidized bed operation[26,27,29,55] and research in the area is still in the early stages. Thus, on the regime map, the CTFB regime can be considered as the intermediate regime between the conventional fluidization regime and the CFB operating region.

Table 3 compares TFB, CFB, and CTFB.[1,22,28] The gas-solid flow structure in the CTFB is more similar to the one in a TFB but the CTFB has the advantage of offering a large gas-solid throughput with high contact efficiency. The axial solids holdup profile of the CTFB is as high as that of the TFB but it is much more uniform than the CFB. The solids concentration of CTFB and TFB have been found to be as high as 0.30. The circulation of the solids means the CTFB has low axial solids backmixing so that the residence time distribution of the solids is narrowed.[26-28]

FIGURE 8 Expanded two-dimensional diagram of high-velocity fluidization with new and reclassified flow regimes (for typical FCC particles, data sources: Table 1). CFB, circulating fluidized bed; CTFB, circulating turbulent fluidized bed; DSU, dense suspension upflow; FCC, fluid catalytic cracking; HDCFB, high-density circulating fluidized bed; LDCFB, low-density circulating fluidized bed [Color figure can be viewed at wileyonlinelibrary.com]

TABLE 3   Comparisons of TFB, CTFB, and CFB[1,22,28]

	TFB	CTFB	CFB
Advantages	• Higher bed density • Much simpler reactor design and operation • Uniform radial and axial solids distribution	• Higher bed density • More uniform gas-solids contacting and higher reaction intensity • Continuous solids circulation • Uniform flow structure	• Higher gas-solid contacting efficiency • Uniform residence time • Continuous solids circulation
Disadvantages	• Very high solid back mixing • Unsuitable for catalytic reactions with quick catalysts deactivation • Poor chemical reaction selectivity		• Low reaction intensity due to low solids concentration • Non-uniform axial and radial flow structure • Gas by-passing due to solids aggregation

Abbreviations: CFB, circulating fluidized bed; CTFB, circulating turbulent fluidized bed; TFB, turbulent fluidized bed.

Higher density operations in the high-velocity fluidized bed are more favorable in many chemical processes. For reactions of short contact time with rapidly deactivating catalyst involving large amounts of heat introduction or removal such as the FCC processes, usually the HDCFB system is desired. However, the design and construction of a HDCFB system are more complicated and expensive. The CTFB can become an alternative option: It offers high gas-solid throughput and its construction and operation are less complex than the HDCFB system.

5 | THE CONSOLIDATED MAP OF UPWARD GAS-SOLID FLUIDIZATION AND THE SIX FLOW REGIMES

At this point, a consolidated regime map incorporating all the six flow regimes for upward gas-solid fluidization is proposed as shown in Figure 9 with the addition of the new CTFB regime and the reclassification of the CFB operating region into HDCFB and LDCFB regimes. Transition gas velocities, U_c, U_{ctfb}, U_{tr}, U_{hl}, and U_{tp}, representing the onset of each regime, divide the full map into the six flow regimes: bubbling bed, turbulent bed, circulating turbulent bed, HDCFB, LDCFB, and pneumatic transport. The conventional fluidization regimes consisting of the bubbling and turbulent fluidization regimes occupy the smallest area near the origin and along the U_g-axis of the map given their low U_g and insignificant G_s. The CTFB regime fills the blank area between the low-U_g and high-G_s areas connecting the conventional fluidization regimes and the CFB regimes. The middle part between U_{tr} and U_{tp} represents the CFB operating region which enlarges the traditional fast fluidization regime to include the low-density CFB and high-density CFB regimes. Beyond U_{tp} is the pneumatic transport regime.

As shown in the consolidated map (Figure 9), the iso-potential solids holdup lines illustrate a gradually expanding operating window of each flow regime to a wider range of solids throughputs with increasing superficial gas velocity. In other words, the turn-down ratio in terms of solids circulation becomes larger giving more flexibility during the operation towards higher U_g. Higher solids holdup iso-potential lines (ε_s = 0.1 and 0.2) also naturally link the CTFB and

HDCFB regimes together with a seamless transition revealing a coherent nature of the overall bed density across the fluidization regimes under high-density operations. Additionally, a sudden rise of the iso-potential solids holdup lines at the transition velocity, U_{tr}, corresponds well to the type C choking.[13]

In addition to the details discussed above, representative sketches and detailed flow structures of the six fluidization regimes are concluded in Figure 10. Typical local solids holdup profiles across different flow regimes are further illustrated in Figure 11. The characteristics of the transition boundaries between the six flow regimes are also summarized in Table 4. The upward gas-solids fluidization starts from batch or "fixed" fluidized operations, transitions to continuous or "moving" fluidized operations, and then to pneumatic transport. Batch or "fixed" fluidized beds are conventional low-velocity fluidization systems (usually U_g < 1.5 m/s) without external solids circulations, including bubbling and turbulent beds. Continuous or "moving" fluidized beds have external solids circulations under higher gas velocities such as the HDCFB and LDCFB regimes. The newly added CTFB regime can be considered as the bridge over the batch and continuous operations of fluidization with an imposed external solids circulation under otherwise similar operations as the TFB.

With gas-solid flow structures and solids holdup distributions shown in Figures 10 and 11, the dominating flow inside the fluidized bed gradually changes from dense phase continuous to dilute phase continuous as the flow regimes transit from batch to continuous operations. The dense particulate phase takes the dominant role in the conventional low-velocity fluidization systems while the dilute gas phase passes through largely as bubbles or voids. In the continuous high-velocity fluidized beds, the dilute phase replaces the dense phase as the dominating phase while the dense phase drifts through as pieces of clusters. As the connector between the batch and continuous operations, the particulate and dilute phases alternatively dominate in the CTFB.

Such change in the dominating phases can be considered as an important feature characterizing the dynamic nature of the gas-solids contacting modes in fluidized beds. This dynamic changeover in the dominating phase provides a new angle to examine the underlying mechanisms the transitions between the flow regimes and the various
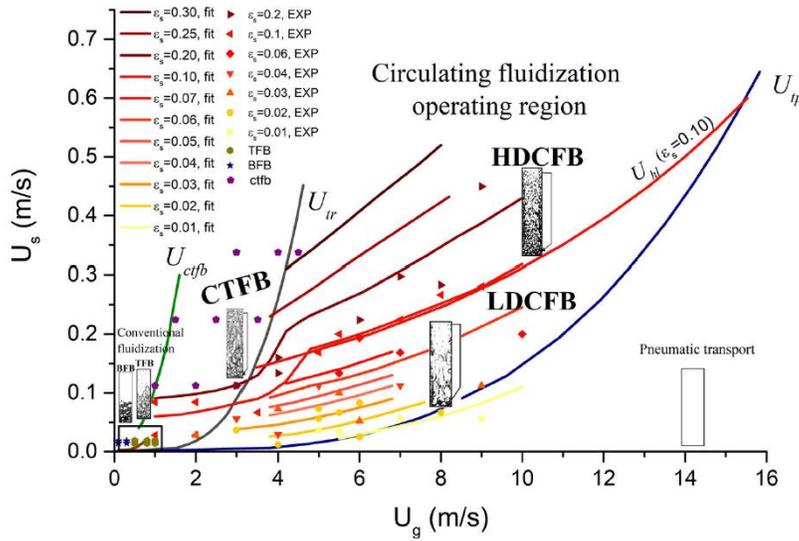
FIGURE 9 The consolidated flow regime map of the upward gas-solid fluidization (for FCC particles, data source: Table 1). BFB, bubbling fluidized bed; CTFB, circulating turbulent fluidized bed; HDCFB, high-density circulating fluidized bed; LDCFB, low-density circulating fluidized bed; TFB, turbulent fluidized bed [Color figure can be viewed at wileyonlinelibrary.com]
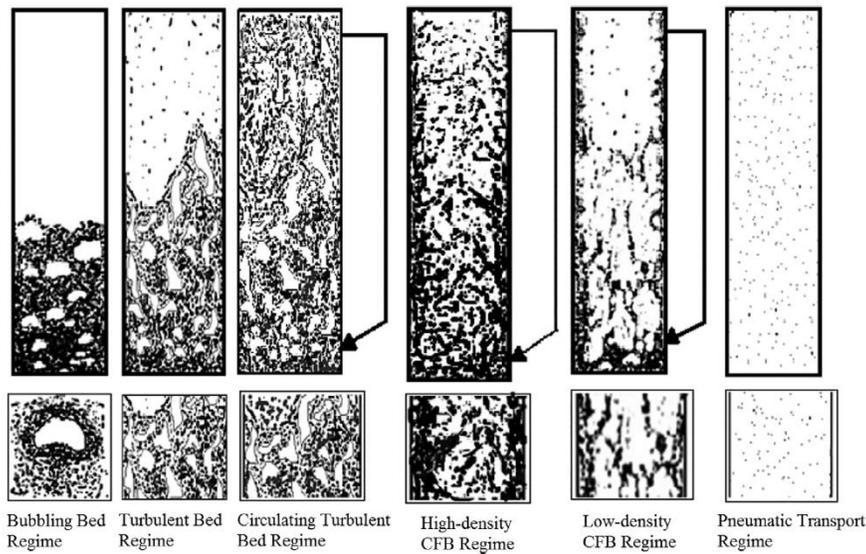
FIGURE 10 Sketches of the six flow regimes in upward gas-solid fluidization

applications of fluidized bed reactors. With the new concept of dynamic changeover in mind, the general classification of the fluidized bed reactors, flow structures and gas-solid contacting modes under different operating conditions, and the demarcation of the six flow regimes are reiterated below:

5.1 | The bubbling bed regime

In the bubbling bed regime at low gas velocity, the dominating particulate phase overtakes the gas phase both in volume and density and the dilute gas phase moves in the forms of gas bubbles that grow up and coalesce while moving up in the bubbling bed. Solids carried by the wake of gas bubbles have more chances to inter-mix with the surrounding particles as the bubbles move up as shown in Figure 10. The

coalescence and the subsequent breakage of gas bubbles play a significant role in gas-solids interactions as well as the mass and heat transfers in BFBs. Bubbles, especially larger bubbles rise quickly, and cause significant gas by-passing, which limits the opportunity for the gas to interact with the particles and hinders chemical reactions. Therefore, the bubbling bed is less favorable for fast gas-solids catalytic reactions but is more suitable for slower gas-solids processes such as drying and combustion[56] because of its lower U_g and much higher bed density and uniform local solids holdup distribution as shown in Figure 11.

5.2 | The turbulent bed regime

With increasing U_g, the instability of the bed increases, resulting in more frequent breakages of the unstable gas bubbles in the bubbling
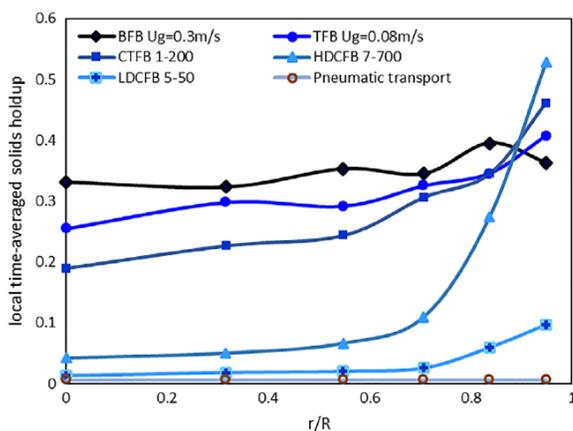
FIGURE 11 Typical local solid holdup profiles across the different flow regimes in upward gas fluidized bed (data sources: Table 1). BFB, bubbling fluidized bed; CTFB, circulating turbulent fluidized bed; HDCFB, high-density circulating fluidized bed; LDCFB, low-density circulating fluidized bed; TFB, turbulent fluidized bed [Color figure can be viewed at wileyonlinelibrary.com]

bed. The fluidized bed goes into the turbulent regime once the breakage rate of the bubbles exceeds the coalescence rate. A relatively larger U_g provides the TFB with a wider operating window and a higher gas holdup in the dense particulate phase than the BFB.[57] The particulate phase still dominates in the TFB as shown in Figure 10, while the impacts from the dilute gas phase gradually enhance as small irregular and unstable voids that form and breakup continuously provide vigorous gas-solid interactions and sufficient lateral mixing with less gas by-passing than in the BFB. Compared to the bubbling bed, the wiggling voids also contain more particles and the dense particulate phase contains more interstitial gas, both enlarging the total effective surface area of the particles and enhances gas-solid contacting.[51]

The role of the TFB in catalytic reactions may seem as somewhat lessened because of its high gas-solid backmixing and the wider residence time distribution profile thus being at a disadvantage to CFB reactors. However, when compared to the CFB, the TFB still enjoys many key advantages including high solids holdup, vigorous gas exchange, and better control of temperature which benefits a high reaction intensity since the dense particulate phase plays a dominating role in the TFB.[26,27] Moreover, easier operation and lower cost make the turbulent bed more favorable than the CFB in many gas-phase catalytic reactions and some gas-solid reactions where solids backmixing and quick catalyst deactivations are not of concern, such as the Fischer-Tropsch synthesis and FCC regeneration.[39,57-60]

5.3 | The CTFB regime

The newly added CTFB regime fills the area between the dense conventional regimes and the CFB operating region in Figure 9. By imposing an external solids circulation in a TFB, relatively higher-U_g

TABLE 4 The characteristics of the six flow regimes of the upward gas fluidization

Flow regime	Fixed system	Conventional fluidization Batch or "fixed" fluidized bed			Circulating fluidization Continuous or "moving" fluidized bed		Transportation system
	Fixed bed	BFB	TFB	CTFB	HDCFB	LDCFB	Pneumatic transport
Superficial gas velocity, U_g (m/s)	0	0.2–0.6	0.6–1.5	1–3	5–25	2–15	≥15
Solids flux, G_s/ρ_p (m/s)	0	≤0.01	0.01–0.03	0.05–0.30	0.1–0.75	0–0.25	–
Average bed solids holdup, ε_s	0.58	0.35–0.55	0.25–0.35	0.20–0.35	0.10–0.30	0–0.10	<0.01
Transition criteria	–	U_{mf} or U_{mb}	U_c or U_k	U_{ctfb}	$U_{tr}, \varepsilon_s > 0.10$	$U_{tr}, \varepsilon_s \leq 0.10$	U_{tp}
Main applications	–	Combustion, drying, coking, and delayed coking	Catalytic gas phase reactions such as Fischer-Tropsch, FCC regeneration	Future applications in FCC type processes	Catalytic cracking	Catalytic cracking, aluminum calcination, combustion	Transportation

Abbreviations: BFB, bubbling fluidized bed; CTFB, circulating turbulent fluidized bed; FCC, fluid catalytic cracking; HDCFB, high-density circulating fluidized bed; LDCFB, low-density circulating fluidized bed; TFB, turbulent fluidized bed.

operations can be achieved in a CTFB but still lower than the transport velocity, U_{tr}, due to the restrictions of the TFB operation. An idealized transitional gas velocity, U_{ctfb}, marks the transition from the conventional fluidization regimes to the CTFB regime on the regime map, is correlated here based on the experimental work form Zhu[33] and Liu[36] as the following for FCC particles:

$$U_{ctfb} = 0.4909 \ln (U_s) + 2.1264,$$

where $0.03 < U_s < 0.3$ (m/s).

As an intermediate flow regime connecting the batch and continuous operations of fluidization, series of elongated voids continuously compose into gas streamers under relatively higher U_g in the CTFB as shown in Figure 10. Consequently, the dense particulate phase with lower density and less volume appears to lose its overwhelming superiority so that the dense and dilute phases alternatively dominate in the CTFB. The CTFB more resembles a TFB since it has a relatively uniform radial profile of solids distribution when compared to the CFB riser as shown in Figure 11. Less downflow of the solids at the wall was found in the CTFB, indicating less backmixing of the solids.[26,55] The external solids circulation in the CTFB promotes a more uniform RTD and allows continuous feeding and removal of particles which are favorable for gas-phase catalytic reactions with quick catalyst deactivations. For typical gas-phase catalytic reactions such as the FCC process where the catalyst regeneration is required and short residence time with narrow distribution are essential, factors including higher solids holdup, vigorous gas-solids contacting, and the presence of more catalyst particles for higher surface area are critical to the design of reactors. While having the advantages of HDCFB for a short contact time with narrow residence time distribution, CTFB has the additional benefits over CFB on higher solids holdup, and more vigorous gas-solids contacting, which could be a better alternative for FCC-type reactions.[1,61]

5.4 | The high-density and low-density CFB regimes

The CFB operating region is the middle area between the two transition gas velocities, U_{tr} and U_{tp} on the regime map, with a high-velocity and various solids fluxes. Once the gas velocity is beyond U_{tr}, TFB or CTFB operations cannot maintain the bed due to excessive entrainment of solids so that a CFB operation with sufficient particle recycling capability is needed. The transition velocity, U_{tr}, marking the onset of the CFB regimes in Figure 9, is determined by the average of the two correlations of the transition velocities, V_{cc} from Bi and Grace[13] and U_{tf}, from Bai et al,[12] which leads to the following equation:

$$U_{tr} = 0.8072 \ln (U_s) + 5.1746,$$

where $U_s > 0.03$ (m/s).

The dilute phase becomes continuous and dominant with solids aggregation occurring under CFB operations. Some solids remain in the dilute phase and more along as individual and interspersed particles while other solids aggregate in the form of smaller particle clusters, or larger descending "particle strands." The presence of clusters/aggregates actually provides a key advantage that more particles can be "preserved" in the CFB riser at higher U_g operation such that very high gas flow rates can be achieved in the CFB column.

The CFB operating region can be further divided into HDCFB and LDCFB regimes based on the bed density.[18,19,35,62] An overall bed solids holdup of 0.10 is selected as the boundary of the HDCFB regime and LDCFB regime and the following equation is correlated for the transition velocities for FCC particles based on the experimental results as listed in Table 1:

$$U_{hl} = 8.4288 \ln (U_s) + 19.837,$$

where $0.14 \leq U_s \leq 0.60$. In the HDCFB, dilute phase dominates the riser center while dense phase in forms of large clustering pieces still maintains a stranglehold in the wall layer as shown in Figure 10. The high gas velocity provides a shorter residence time required for fast reactions and the large solids circulation allows the quickly deactivated catalyst to be easily refreshed. The dynamic formation and breakup of the clusters also provide intensive gas-solid interactions in the HDCFB reactor. The FCC process has been carried out in the HDCFB regime over 50 years for reactions require high intensity and short residence time. In the LDCFB, the dilute phase fully dominates in the entire cross-section where the dense solids phase is cut into disconnected pieces of clusters. Gas-solids reactions such as combustion and alumina calcination which require large amounts of gas throughput but less solids circulation are better operated in the LDCFB regime.

5.5 | The pneumatic transport regime

The pneumatic transport regime starts from the transition velocity, U_{tp}, and is commonly observed in solids transport systems. Based on the experimental work from Issangya,[31] Li[34] and Wang[35] which cover the entire range of the CFB operations, the following equation is proposed to demarcate the upper boundary of CFB operating regimes as the transition gas velocity, U_{tp}, into the pneumatic transport regime for FCC particles:

$$U_{tp} = 2.7555 \ln (U_s) + 16.029,$$

where $U_s > 0.03$ (m/s). In the pneumatic transport regime, the dilute phase completely dominates and the gas-solid suspension can be considered as a homogeneous flow which is too dilute for effective reactions (Figure 10).

From batch to continuous operations in the fluidized bed, the denser particulate phase including particles and interstitial gas reduces both in its density and volumetric fraction in the fluidized bed, and the complementary dilute phase increases both in density and volumetric fraction in the bed with increasing U_g. From the BFB to TFB, the incremental increase in gas flow "drills" into both the dilute bubble/void phase and the dense particulate phase, which increases

the fraction of the dilute phase in the bed and brings down the solids concentration in the dense phase. Meanwhile, more particles from the dense particulate phase are "swept" into the dilute phase through vigorous inter-phase gas exchange with higher U_g. Further increasing the gas velocity to CFB regimes, the dominating dense particulate phase in conventional fluidized beds "breaks" into discrete pieces as the denser cluster phase in the CFB. A gas phase dominant region is found in the center of the CFB riser and expands to a wider cross-section towards the wall, allowing more gas to pass, from the HDCFB to LDCFB. The CTFB acts as the bridge connecting the batch and continuous operations of fluidization with the gas and solids phases alternatively dominating in the bed. Lowering the gas velocity from the CFB to CTFB (below U_{tr}), the relatively low-velocity operations in CTFB cause the clusters to "compound" and interact with gas streams that pulse through. The compounded particle clusters or the extended dense pieces "tangle with" the gas voids or streams, alternately dominating in the entire bed. The competition between dense cluster phase and dilute phase in CTFB reflects and resembles the dynamic and intermittent changeover of the continuous phase in this intermediate regime from batch to continuous operations of fluidization.

The dynamic changeover from dense phase dominant operations to dilute phase dominant operations is further illustrated in Figure 11, through the radial distribution of solids holdups across the six flow regimes. Under conventional low-velocity operations of bubbling and turbulent beds, dense phase dominates the entire cross-section of the fluidized bed, where the bed density is high and the radial solids distribution is uniform. Slightly increasing U_g into the CTFB regime, the dense and dilute phases take the dominating role alternatively in the CTFB, resulting in a similar solids radial distribution as the TFB but with more solids at the wall and lower density in the center region. Further increasing the gas velocity to the HDCFB regime, the dilute phase begins to dominate, at least in the center region, while a wider and denser wall region still appears to be intermittently dense phase dominant, forming a typical core-annulus structure. In the LDCFB, the gas phase dominated region expands to the entire bed leading to a low solids holdup with uniform radial distribution, aside from a small increase in the wall region. From the high gas velocity end, the dilute phase dominates the entire cross-section in pneumatic transport lines where the flow is uniform across the entire bed. Therefore, with the transitions from low-velocity batch operations to high-velocity continuous operations of fluidization, the gas phase gradually becomes continuous and increasing gas flow, and breaks through the center of the fluidized bed, leads to the expansion of the dilute core until it occupies the entire riser. Further increasing gas flow with more gas throughput resulting in a dilute core region.

6 | CONCLUSIONS

A consolidated regime map of upward gas fluidization, which accounts for the gas-solid flow structure under a wide range of operating conditions inside various fluidized beds, is presented with six flow regimes

suitable for different reactions. The new regime map includes the introduction of the new CTFB, and the reclassification of the two CFB regimes, HDCFB regime and LDCFB regime. Therefore, the fluidization map has been expanded to include bubbling fluidization, turbulent fluidization, circulating turbulent fluidization, high-density circulating fluidization, low-density circulating fluidization, and pneumatic transport regimes. The transition gas velocities, U_c, U_{ctfb}, U_{tr}, U_{hl}, and U_{tp}, as the boundaries between those flow regimes are correlated for FCC particles. With increasing gas velocity, wider ranges of operation on solids flux can be achieved in the upward fluidization system. The iso-potential solids holdup lines based on experimental data extending over the consolidated map further reveals the coherency among the flow regimes. In addition to the clearer classifications of the flow regimes that expands the fluidization theory, unique operational characteristics of typical fluidized bed reactors used in the industries are also more intuitionally represented on the consolidated regime map.

The concept of dynamic changeover of the dominating role between the particulate and dilute phases in fluidization systems is proposed to better understand the underlying mechanisms over the transitions between the flow regimes with the help of the new regime map. In conventional fluidized beds, the dense particulate phase is the continuous phase dominating in the fluidized bed with a higher suspension density. In CTFB, the dilute and dense phases compete with each other vigorously and alternate in their level of domination. Further increasing gas velocity to HDCFB, dilute phase dominates the center of the riser and denser cluster phase remains continuous in the wall region. In LDCFB or pneumatic transport system, the gas phase becomes the continuous phase in the whole riser or the transportation line given the high gas velocity.

The consolidated map provides a new view over the operations and underlying mechanisms of the six fluidization flow regimes with detailed demarcation for FCC particles, and furthermore inspires more design optimizations and effective operations of various fluidized bed reactors. More insights over the transitions between the flow regimes can be further benefited by the analysis on the dynamic changeover of the continuous phase across the flow regimes.

NOTATION

Ar	particle Archimedes number, $= \frac{g d_p^3 \rho_f (\rho_p - \rho_f)}{\mu^2}$
d_p	particle diameter, m
G_s	solids circulating rate, kg/m^2 s
U_g	superficial gas velocity, m/s
U_{mb}	minimum bubbling velocity, m/s
U_{mf}	minimum fluidization velocity, m/s
U_c	onset velocity of turbulent regime, m/s
U_{tr}	onset velocity of CFB operating region, m/s
U_{tp}	onset velocity of pneumatic transport regime, m/s
U_{slip}	slip velocity, m/s
U_{ctfb}	onset velocity of CTFB regime, m/s
U_t	particle terminal velocity, m/s

U_{hl} boundary between HDCFB regime and LDCFB regime (ε_s = 0.10), m/s

GREEK LETTERS

ρ_p particle density, kg/m^3

ρ_f fluid density, kg/m^3

μ fluid dynamic viscosity, kg/m s

ε_s average bed solids holdup

ORCID

Zeneng Sun https://orcid.org/0000-0002-4023-7120

Jesse Zhu https://orcid.org/0000-0001-7749-8917

REFERENCES

1. Zhu J, Cheng Y. Fluidized bed reactors and applications. In: Michaelides EE, Crowe CT, Schwarzkopf JD, eds. *Multiphase Flow Handbook*. Boca Raton, FL: CRC Press; 2005:5.55-5.93.
2. Homsy G, Jackson R, Grace J. Report of a symposium on mechanics of fluidized beds. *J Fluid Mech*. 1992;236:477-495.
3. Reh L. New and efficient high-temperature processes with circulating fluid bed reactors. *Chem Eng Technol*. 1995;18(2):75-89.
4. Grace J. Reflections on turbulent fluidization and dense suspension upflow. *Powder Technol*. 2000;113(3):242-248.
5. Kwauk M. Generalized fluidization: II. Accelerative motion with steady profiles. *Sci Sin*. 1964;13(9):1477-1492.
6. Davidson J, Harrison D. The behaviour of a continuously bubbling fluidised bed. *Chem Eng Sci*. 1966;21(9):731-738.
7. Davidson J, Keairns D. In: Davidson JF, Keairns DL, eds. *Fluidization: Proceedings of the Second Engineering Foundation Conference*. Cambridge, England: Trinity College; 1978.
8. Grace J. Contacting modes and behaviour classification of gas-solid and other two-phase suspensions. *Can J Chem Eng*. 1986;64(3):353-363.
9. Matsen J. A phase diagram for gas-particle flow. In: Kunii D, Toei R, eds. *Fluidization IV*. Kashikojima, Mie Prefecture, Japan. 1983; 225-232.
10. Takeuchi H, Hirama T, Chiba T, Biswas J, Leung L. A quantitative definition and flow regime diagram for fast fluidization. *Powder Technol*. 1986;47(2):195-199.
11. Hirama T, Takeuchi H, Chiba T. Regime classification of macroscopic gas-solid flow in a CFB riser. *Powder Technol*. 1992;70:215-222.
12. Bai D, Jin Y, Yu Z. Flow regimes in circulating fluidized beds. *Chem EngTechnol*. 1993;16(5):307-313.
13. Bi H, Grace J. Flow regime diagrams for gas-solid fluidization and upward transport. *Int J Multiph Flow*. 1995;21(6):1229-1236.
14. Horio M, Ito M. Prediction co cluster size in CFBs. *J Chem Eng J*. 1997;30:691-697.
15. Zenz F. Two-phase fluid-solid flow. *Ind Eng Chem*. 1949;41(12):2801-2806.
16. Yerushalmi J, Cankurt N. Further studies of the regimes of fluidization. *Powder Technol*. 1979;24(2):187-205.
17. Kunii D, Levenspiel O. Circulating fluidized-bed reactors. *Chem Eng Sci*. 1997;52(15):2471-2482.
18. Bi H, Zhu J. Static instability analysis of circulating fluidized beds and concept of high-density risers. *AIChE J*. 1993;39(8):1272-1280.
19. Zhu J, Bi H. Distinctions between low density and high density circulating fluidized beds. *Can J Chem Eng*. 1995;73(5):644-649.
20. Issangya A, Bai D, Bi H, Lim K, Zhu J, Grace J. Suspension densities in a high-density circulating fluidized bed riser. *Chem Eng Sci*. 1999; 54(22):5451-5460.
21. Pärssinen J, Zhu J. Particle velocity and flow development in a long and high-flux circulating fluidized bed riser. *Chem Eng Sci*. 2001;56 (18):5295-5303.
22. Wang C, Zhu J, Barghi S, Li C. Axial and radial development of solids holdup in a high flux/density gas-solids circulating fluidized bed. *Chem Eng Sci*. 2014;108:233-243.
23. Wang C, Zhu J, Li C, Barghi S. Detailed measurements of particle velocity and solids flux in a high density circulating fluidized bed riser. *Chem Eng Sci*. 2014;114:9-20.
24. Hensler T, Firsching M, JSG B, Wörlein T, Uhlmann N, Wirth K-E. Non-invasive investigation of the cross-sectional solids distribution in CFB risers by X-ray computed tomography. *Powder Technol*. 2016; 297:247-258.
25. Grace J, Issangya A, Bai D, Bi H, Zhu J. Situating the high-density circulating fluidized bed. *AIChE J*. 1999;45(10):2108-2116.
26. Zhu H, Zhu J. Comparative study of flow structures in a circulating-turbulent fluidized bed. *Chem Eng Sci*. 2008;63(11):2920-2927.
27. Zhu J. Circulating turbulent fluidization—a new fluidization regime or just a transitional phenomenon. *Particuology*. 2010;8(6):640-644.
28. Qi X, Zhu H, Zhu J. Demarcation of a new circulating turbulent fluidization regime. *AIChE J*. 2009;55(3):594-6111502.
29. Geng Q, Zhu X, Yang J, You X, Liu Y, Li C. Flow regime identification in a novel circulating-turbulent fluidized bed. *Chem Eng J*. 2014;244: 493-504.
30. Adidan AA, Yerushalmi J. Bed expansion in high velocity fluidization. *Powder Technol*. 1982;32(2):223-232.
31. Issangya A. *Flow Dynamics in High Density Circulating Fluidized Beds*. Vancouver, BC Canada: University of British Columbia; 1998.
32. Yan A. *Hydrodynamics and Scale-Up of Circulating Fluidized Beds*. London, Ontario, Canada: Univeristy of Western Ontario; 2004.
33. Zhu H. *Turbulent Fluidized Bed vs. High Density Riser-Regimes and Flow Characterizations*. London, Ontario, Canada: University of Western Ontario; 2006.
34. Li D. *Investigation of Circulating Fluidized Bed Riser and Downer Reactor Performance for Catalytic Ozone Decomposition*. London, Ontario, Canada: University of Western Ontario; 2010.
35. Wang C. *High-Density Gas-Solids Circulating Fluidized Bed Riser and Downer Reactors*. London, Ontario, Canada: University of Western Ontario; 2013.
36. Liu J. *Reactor Performances and Hydrodynamics of Various Gas-Solids Fluidized Beds*. London, Ontario, Canada: University of Western Ontario; 2016.
37. Geldart D. Types of gas fluidization. *Powder Technol*. 1973;7(5): 285-292.
38. Lee G, Kim S. Pressure fluctuations in turbulent fluidized beds. *J Chem Eng Jpn*. 1988;21(5):515-521.
39. Yerushalmi J, Turner D, Squires A. The fast fluidized bed. *Ind Eng Chem Process Des Dev*. 1976;15(1):47-53.
40. Bai D, Jin Y, Yu Z, Zhu J. The axial distribution of the cross-sectionally averaged voidage in fast fluidized beds. *Powder Technol*. 1992;71(1): 51-58.
41. Wang C, Wang G, Li C, Barghi S, Zhu J. Catalytic ozone decomposition in a high density circulating fluidized bed riser. *Ind Eng Chem Res*. 2014;53(16):6613-6623.
42. Bi H, Grace J. Flow patterns in high-velocity fluidized beds and pneumatic conveying. *Can J Chem Eng*. 1999;77(2):223-230.
43. Owen P. Pneumatic transport. *J Fluid Mech*. 1969;39(2):407-432.
44. Drahoš J, Čermák J, Guardani R, Schügerl K. Characterization of flow regime transitions in a circulating fluidized bed. *Powder Technol*. 1988; 56(1):41-48.
45. Molerus O. Overview: pneumatic transport of solids. *Powder Technol*. 1996;88(3):309-321.

46. Bai D, Shibuya E, Masuda Y, Nakagawa N, Kato K. Flow structure in a fast fluidized bed. *Chem Eng Sci*. 1996;51(6):957-966.

47. Bai D, Issangya A, Grace J. Characteristics of gas-fluidized beds in different flow regimes. *Ind Eng Chem Res*. 1999;38(3):803-811.

48. Lewis W, Gilliland E, Bauer W. Characteristics of fluidized particles. *Ind Eng Chem*. 1949;41(6):1104-1117.

49. Rhodes M, Geldart D. Upward flow of gas/solid suspensions. Part 2. A practical quantitative flow regime diagram for the upward flow of gas/solid suspensions. *Chem Eng Res Des*. 1989;67(1): 30-37.

50. Bai D, Kato K. Saturation carrying capacity of gas and flow regimes in CFB. *J Chem Eng Jpn*. 1995;28:179-185.

51. Bi H, Ellis N, Abba I, Grace J. A state-of-the-art review of gas-solid turbulent fluidization. *Chem Eng Sci*. 2000;55(21):4789-4825.

52. Squires A, Kwauk M, Avidan AA. Fluid beds: at last, challenging two entrenched practices. *Science*. 1985;230(4732):1329-1337.

53. Bai D, Issangya A, Zhu J, Grace J. Analysis of the overall pressure balance around a high-density circulating fluidized bed. *Ind Eng Chem Res*. 1997;36(9):3898-3903.

54. Wang C, Li C, Zhu J. Axial solids flow structure in a high density gas-solids circulating fluidized bed downer. *Powder Technol*. 2015;272: 153-164.

55. Boonprasop S, Chalermsinsuwan B, Piumsomboon P. Design parameters for performing circulating turbulent fluidization with a single feed stage fluidized bed reactor. *Chem Eng Technol*. 2017;40(1): 177-185.

56. Grace J. In: Hestroni G, ed. *Fluidized Bed Hydrodynamics. Handbook of Multiphase Systems*. Washington, DC: Hemisphere; 1982.

57. Cai P, Jin Y, Yu Z, Wang Z. Mechanism of flow regime transition from bubbling to turbulent fluidization. *AIChE J*. 1990;36(6):955-956.

58. Horio M, Ishii H, Nishimuro M. On the nature of turbulent and fast fluidized beds. *Powder Technol*. 1992;70(3):229-236.

59. Bi H, Grace J, Lim K. Transition from bubbling to turbulent fluidization. *Ind Eng Chem Res*. 1995;34(11):4003-4008.

60. Kim S, Kirbas G, Bi H, Lim C, Grace J. Flow behavior and regime transition in a high-density circulating fluidized bed riser. *Chem Eng Sci*. 2004;59(18):3955-3963.

61. Cheng W-C, Kim G, Peters AW, et al. Environmental fluid catalytic cracking technology. *Catal Rev*. 1998;40(1–2):39-79.

62. Ishii H, Horio M. The flow structures of a circulating fluidized bed. *Adv Powder Technol*. 1991;2(1):25-36.

Curriculum Vitae

Name: Zeneng Sun

Post-secondary Education and Degrees:
Department of Chemical & Biochemical Engineering
University of Western Ontario
London, Ontario, Canada.
2014.09-present
Ph.D. candidate

Department of Chemical Engineering
East China University of Science & Technology
Shanghai, China
2010.09-2014.06
B.Sc.

Honors and Awards:
Honorary graduate of ECUST
Shanghai, China
2014

First-class scholarship of ECUST
Shanghai, China
2013-2014

Award of Shanghai University Student Innovative Experiment Project
Shanghai, China
2012-2014

Related Work Experience:
Research Assistant and Teaching Assistant
University of Western Ontario, London, Canada
2014-2019

Internship
Sinopec Shanghai Engineering co., LTD (SSEC), Shanghai, China
2013.11-2014.05

Internship
3M China co., LTD. R&D center, Shanghai, China,
2013.06-2013.10

Publications:

- Song, Y., **Sun, Z.**, Zhang, C., Zhu, J., & Lu, X. (2019). Numerical study on liquid-solid flow characteristics in inverse circulating fluidized beds. *Advanced Powder*

Technology, *30*(2), 317-329.

- Song, Y., Zhu, J., Zhang, C., **Sun, Z.**, & Lu, X. (2019). Comparison of liquid-solid flow characteristics in upward and downward circulating fluidized beds by CFD approach. *Chemical Engineering Science*, *196*, 501-513.
- **Sun, Z.**, Zhang, C., & Zhu, J. (2017). Numerical Study of the Effects of Inlet Boundary Conditions on Gas-Solids Flows in Circulating Fluidized Bed Risers, *25th CFD-SC Proceedings*.
- **Sun, Z.** & Zhu, J. (2019). A Consolidated Flow Regime Map of Upward Gas Fluidization, *AIChE Journal,* accepted
- **Sun, Z.**, Zhu, J., & Zhang C. (2019). Numerical study on the hydrodynamics in high-density and low-density gas-solid circulating fluidized bed downer reactors, *Powder Technology*, submitted.